

THE UNIVERSITY OF MANCHESTER

DOCTORAL THESIS

Understanding Texture Weakening In
Magnesium Rare Earth Alloys

Author:

David G J GRIFFITHS

Supervisor:

Dr. J ROBSON

*A thesis submitted to the University of Manchester for the degree of Doctor of
Philosophy in the Faculty of Engineering and Physical Sciences*

2014

The School of Materials

Contents

Contents	2
List of Figures	5
List of Tables	10
Abstract	11
Declaration of Authorship	12
Copyright Statement	13
Publications	14
Acknowledgements	15
1 Literature Review	16
1.1 Introduction	16
1.1.1 Magnesium Alloys and their Properties	16
1.1.2 Common Alloying Elements in Magnesium	17
1.2 Deformation of h.c.p Metals	19
1.2.1 Slip Systems	19
1.2.2 Twinning	20
1.2.3 Stacking Faults	21
1.3 Deformation in Magnesium	24
1.3.1 Slip in Magnesium	24
1.3.2 Solid Solution Strengthening	26
1.3.3 Twinning in Magnesium	29
1.3.3.1 Twinning in Single Crystals	29
1.3.3.2 Twinning and Ductility	30
1.3.3.3 Effects of Grain Size & Deformation Temperature	32
1.3.4 Shear Band Formation	33
1.4 Wrought Magnesium	34
1.4.1 Formation of Basal Textures	35
1.4.2 Yield Asymmetry	37
1.4.3 Formability	38
1.4.4 Increasing Magnesium Formability	40
1.5 Recrystallisation of Magnesium Alloys	42
1.5.1 Recovery and Recrystallisation	42

1.5.2	Mechanisms of Recrystallisation	42
1.5.2.1	Strain Induced Boundary Migration–SIBM	43
1.5.2.2	Rotational Recrystallisation–RDRX	45
1.5.2.3	Twin Induced Dynamic Recrystallisation–TDRX	47
1.5.2.4	Shear Band Nucleation	49
1.5.2.5	Particle Stimulated Nucleation–PSN	49
1.5.3	Factors Affecting DRX Behaviour	50
1.5.4	Recrystallisation Textures	51
1.5.4.1	{0001} Basal Textures	53
1.5.4.2	Grain Rotation During Recrystallisation and Grain Growth	53
1.5.5	Summary Of Recrystallisation	55
1.6	Magnesium Rare Earth (RE) Alloys	56
1.6.1	The Rare Earth Texture	57
1.6.2	The Critical Concentration of Rare Earth	59
1.6.3	Rare Earth Texture Deformation or Recrystallisation Effect?	61
1.7	Recrystallisation of Rare Earth Alloys	61
1.7.1	Nucleation of Recrystallisation in Rare Earth Alloys	65
1.8	Deformation in RE Alloys	68
1.8.1	Recovery in Rare Earth Alloys	68
1.8.2	Increasing Non-Basal Slip	69
1.8.3	Mechanism of Increased Non-Basal Slip	71
1.9	The Mechanism of Recrystallisation Retardation	73
1.10	Summary	77
1.11	Focus of the Thesis	79
2	Experimental Methods	81
2.1	Alloy Casting	81
2.2	Rolling	81
2.3	Alloy Compositions	82
2.4	Optical Microscopy	82
2.5	Scanning Electron Microscopy (SEM)	85
2.6	Electron Backscatter Diffraction (EBSD)	85
2.6.1	Processing EBSD Data	86
2.7	Texture Measurement by X-Ray Diffraction	88
2.8	Transmission Electron Microscopy	88
2.9	Generating a Forming Limit Diagram	89
2.9.1	Digital Image Correlation	90
3	Results	92
3.1	Hot Rolling	92
3.1.1	Magnesium-Y Alloys	92
3.1.2	Magnesium-La Alloys	93
3.1.3	Magnesium Ce, Yb, Nd and Eu Alloys	96
3.1.4	Commercial Alloys ZEK100 and AZ31	100
3.1.5	Summary	100
3.2	Static Recrystallisation of Magnesium Sheet	103
3.2.1	Cold Rolling of AZ31 and Dilute Magnesium-La Alloys	103

3.2.2	Cold Rolling of Magnesium-Y Alloys	105
3.2.3	ZEK100	110
3.2.3.1	Straight Cold Rolling (SCR)	112
3.2.3.2	Transverse Cold Rolling (TCR)	113
3.2.3.3	Equal Cold Rolling (ECR)	120
3.3	Grain Growth in ZEK100	128
3.4	Formability of ZEK100 Sheet	129
3.5	Segregation of Rare Earth Atoms	132
3.5.1	Grain Boundaries	132
3.5.2	Precipitates	133
4	Modelling Cold Rolling	140
4.1	Crystal Plasticity Modelling	140
4.1.1	Constitutive Model	140
4.1.2	Mean Field Models	141
4.1.3	Full Field Models	144
4.1.4	Summary	145
4.2	Model Parameters	145
4.3	Benchmark Magnesium Rolling	147
4.4	Contribution of Each Slip System to Deformation Texture	148
4.4.1	Changing Deformation Mode Activities	149
4.4.1.1	Increasing Non-Basal Slip	151
4.4.1.2	Effect of Twin Activity	155
4.5	Simulating Cold Rolling of ZEK100	155
4.5.1	Straight Cold Rolling	155
4.5.2	Transverse Cold Rolling	158
4.5.3	Equal Cold Rolling	160
4.6	Summary	161
5	Discussion	164
5.1	Rare Earth Textures In Binary Magnesium-Rare Earth Alloys	164
5.1.1	Activation of RE Effects	164
5.1.2	Texture Weakening in Binary Alloy Systems	166
5.1.3	Summary	169
5.2	Formation Of Rare Earth Textures In ZEK100	170
5.2.1	Recrystallisation in SCR and TCR Material	170
5.2.2	Recrystallisation in ECR Material	174
5.2.3	Formation of RE Texture Component in ZEK Alloys	175
5.2.4	Grain Growth In ZEK100	179
5.3	Grain Boundary Segregation and Solute Drag	180
6	Conclusions	183
	Bibliography	186

List of Figures

1.1	The most common slip and twinning planes and directions in magnesium.	20
1.2	Schematic of the most important planes and directions within a twin. . .	21
1.3	The variation in twin shear with c/a ratio for a range of twinning systems.	22
1.4	Schematic of the formation of E and I ₁ stacking faults	22
1.5	Schematic for Friedel and double jog mechanisms of cross-slip from basal to prismatic planes.	26
1.6	An alloy design map for the solid solution strengthening of basal slip in magnesium alloys as predicted by DFT calculations.	28
1.7	Flow stress curve for a magnesium single crystal where the c axis is under compressive strains and tensile strains.	30
1.8	Schematic of a {10 $\bar{1}$ 1}-{10 $\bar{1}$ 2} double showing the basal planes along the $\langle 1\bar{2}10 \rangle$ axis.	31
1.9	Proposed mechanism of shear band formation in magnesium under plane strain compression in basally oriented grains.	35
1.10	Proposed mechanism of shear band formation during dynamic recrystallisation.	35
1.11	The {0001} and {10 $\bar{1}$ 0} pole figures of rolled AZ31, with extrusion direction inverse pole figure of extruded AZ31.	36
1.12	Basal texture of AZ31 rolled at 200°C, showing a typical split of the basal texture in the RD.	37
1.13	Flow stress for rolled AZ31 under tension (t) and compression (c) in both normal direction (ND) and rolling direction (RD).	38
1.14	Room temperature forming limit diagram of aluminium 6016 and magnesium AZ31.	39
1.15	Figure showing the mechanism of strain induced boundary migration in aluminium.	44
1.16	Figure showing the growth of the necklace type microstructure characteristic of a variety of recrystallisation mechanisms in magnesium.	44
1.17	TEM image showing the bulging of a grain boundary during straining of a magnesium alloy as a result of high localised shear stress in grain boundary regions caused by dislocation pile up.	46
1.18	Figure showing the rotational or CDRX mechanism of recrystallisation in magnesium.	46
1.19	EBSD map showing twin induced DRX.	48
1.20	Figure showing a schematic digram of two mechanisms of TDRX nuclei formation by twin intersection.	48
1.21	Optical and EBSD micrographs showing PSN within rolled magnesium sheet.	50
1.22	Schematic illustration of the relationship between dominant DRX mechanism temperature and strain.	52

1.23	flow stress curves for pure magnesium over a wide temperature range. . .	52
1.24	Variation in basal intensity and grain size with annealing time in AZ31. .	54
1.25	Extrusion textures for magnesium AZ31 as extruded and annealed for 1800s at 400°C.	55
1.26	Schematic showing the stable and unstable orientations of hcp crystals (relative to prismatic slip) during rolling.	56
1.27	Flow stress curves for a series of grain size normalised magnesium-X at% Gd alloys in tension along the rolling direction.	57
1.28	{0001} basal pole figures of rolled magnesium-Gd alloys and inverse pole figures of an extruded magnesium-Gd alloy, showing the weakening of the basal texture as Gd concentration increases.	58
1.29	Basal, {0001}, pole figures for rolled magnesium 0.374 at% Zn and rolled magnesium 0.374 at% Zn 0.052 at% Ce alloy.	59
1.30	Figure showing peak basal texture intensity against RE concentration, after rolling and recrystallisation, for a number of magnesium-RE binary systems.	60
1.31	Plot of the solubility of each RE element in magnesium at 525°C as a function of atomic mismatch with magnesium.	61
1.32	{0001} pole figures showing the as-rolled 150° and annealed textures for 15 min at 400°C of magnesium 0.371 at% Zn and magnesium 0.442 at% Zn 0.179 at% Ce.	62
1.33	{0001} pole figures calculated from EBSD maps showing the orientations of deformed parent grains and DRX nuclei after plane strain compression at 400°C.	64
1.34	Inverse pole figures relative to the ED of DRX grains of different size in magnesium 0.445 at% Mn and magnesium 0.445 at% Mn, 0.170 at% Nd alloys.	64
1.35	Figure showing the change in {0001} basal pole figure intensity during static recrystallisation at 300°C of magnesium 1.488 at% Zn-0.174 at% Ce, magnesium 0.372 at% Zn-0.173 at% Ce and magnesium 2.70 at% Al-0.372 at% Zn (AZ31) alloys after warm rolling (300°C).	65
1.36	Figure showing regions of high and low shear in a kernel average misorientation of an EBSD map.	67
1.37	EBSD map of grains recrystallising in shear bands of an extruded magnesium 0.24 at% Gd alloy.	67
1.38	Schematic of the mechanism proposed by Basu <i>et.al</i> explaining growth of TD orientations within ZEK alloys.	67
1.39	IGMA plots of basally oriented grains from a series of magnesium-Nd binary alloys.	73
1.40	Plot showing the segregation of different RE atoms to grain boundaries predicted by the Langmuir and McLean model.	75
1.41	Plot of the segregation of Gd to grain boundaries and its relationship with rare earth texture formation during extrusion.	76
2.1	Plot showing the concentration of rare earth element in each alloy studied.	83
2.1	Schematic of specimen producing an Kikuchi patterns and an example of an experimental Kikuchi diffraction pattern.	87
2.2	Inverse pole figure used for colouring EBSD maps.	87
2.3	Schematic of forming press and Nakazima specimen.	89

2.4	a) Schematic diagram of forming press with hemispherical punch. b) Schematic diagram of a Nakazima specimen.	90
3.1	Microstructures of Y alloys after rolling at 400°C in 7 passes pf $\epsilon_T \approx 20\%$ per pass.	94
3.2	$\{10\bar{1}0\}$ pole figures for the binary Y alloy series.	95
3.3	Comparison between the annealed basal texture intensity of the Y alloys with literature data.	95
3.4	Optical micrographs showing shear banding behaviour in the Y alloys above and below the critical rare earth concentration.	96
3.5	Microstructures and $\{0001\}$ pole figure of the La alloys after rolling and annealing for 1hr at 400°C	97
3.6	Figure showing the $\{10\bar{1}0\}$ pole figures for the 0.0050 and 0.0349 at% La alloys in the as hot rolled condition and after annealing for 1hr at 400°C.	98
3.7	Shear banding in the La alloys after rolling at 400°C and quenching.	98
3.8	Microstructures and textures of the Ce, Yb, Eu, Nd and Gd alloys after rolling at 400°C and annealing.	101
3.9	Plot of basal texture strength of the Ce alloy after rolling and full recrystallisation against literature data.	102
3.10	Plot of basal texture strength of the 0.0243 at% Nd alloy (DF013) after rolling and full recrystallisation against literature data.	102
3.11	Microstructures, $\{0001\}$ and $\{10\bar{1}0\}$ pole figures of the as received ZEK100 and AZ31.	103
3.12	Plot of the variation in basal texture intensity with annealing in cold rolled AZ31, 0.017 at% La and 0.08 at% Y.	104
3.13	Textures of magnesium-Y alloys in the as cold rolled and recrystallised conditions.	107
3.14	EBSD maps for magnesium 0.08 at% Y (non-rare earth) and 0.15 at% Y (rare earth) alloys cold rolled and annealed for 4 minutes at 350°C.	109
3.15	IGMA analysis between deformed grains in magnesium 0.08 and 0.15 at% Y alloys.	111
3.16	IGMA analysis of individual deformed grains in 0.15 at% Y alloys.	112
3.17	High magnification images of magnesium 0.15 at% Y cold rolled and annealed for 4 minutes at 350°C.	113
3.18	High magnification images of magnesium 0.08 at% Y cold rolled and annealed for 4 minutes at 350°C.	114
3.19	$\{0001\}$ and $\{10\bar{1}0\}$ pole figures for the cold rolled and partially recrystallised magnesium 0.08 and 0.15 at% Y alloys.	115
3.20	Schematic diagram showing the three paths used when cold rolling ZEK100.	116
3.21	$\{0001\}$ pole figures showing the texture development of a) ZEK100 and b) AZ31 after a hot rolled sheet is straight cold rolled and fully recrystallised at 400°C.	116
3.22	Texture evolution in transverse cold rolled ZEK100 during annealing at 400°C.	117
3.23	Microstructure evolution in transverse cold rolled ZEK100 during annealing at 400°C.	117
3.24	EBSD maps of the transverse cold rolled ZEK100 in the as rolled condition, annealed for one minute, two minutes and five minutes at 350°C.	120

3.25	EBSD maps and textures of transverse cold rolled and annealed ZEK100, separated into regions of deformed and RXed grains.	121
3.26	EBSD maps and textures of recrystallised grains in transverse cold rolled and annealed ZEK100, separated into regions of small and large grains.	122
3.27	high resolution EBSD map of a small area of transverse cold rolled ZEK100 annealed for 1 min at 350°C.	123
3.28	Schematic diagram of rolled billet showing shear bands intersecting ND-RD _{CR} and ND-TD _{CR} planes.	123
3.29	Comparison of recrystallised grains in the ND-RD _{CR} and ND-TD _{CR} cross sections of the transverse cold rolled ZEK100 after annealing.	124
3.30	EBSD map of as transverse cold rolled ZEK100 with the TD _{CR} orientations highlighted.	125
3.31	Pole figures of ZEK100 as equal cold rolled and after annealing.	127
3.32	EBSD maps comparing transverse cold rolled and equal cold rolled ZEK100 after 5 minutes annealing.	127
3.33	Composite EBSD map and corresponding pole figure of ZEK100 annealed for 30days at 400°C	128
3.34	Comparison of the textures and orientations of grains by size in the ZEK100 annealed for 30days.	130
3.35	EBSD map of as received ZEK100 in the fully recrystallised condition. a,b) IPF coloured map and pole figures for the complete map. c,d) map and pole figure for grains larger than 6μm and e,f) map and pole figure for grains smaller than 6μm.	131
3.36	Forming limit diagram for ZEK100, Al6016 and AZ31.	131
3.37	HAADF images showing the segregation of Y to grain boundaries in magnesium-0.15 at%Y after cold rolling and annealing for one hour at 400°C. Two grain boundaries were observed; a,c) grain boundary one and b,d) grain boundary 2, at low and high mag respectively.	134
3.38	EDX map showing the segregation of Y across two different grain boundaries, in magnesium-0.15 at%Y after cold rolling and annealing for one hour at 400°C.	135
3.39	High resolution EDX map showing segregation of Y to grain boundaries in magnesium-0.15 at%Y after cold rolling and annealing for one hour at 400°C. 136	
3.40	High resolution EDX maps showing composition of particles found in magnesium-0.15 at%Y after cold rolling and annealing for one hour at 400°C. Mapped region is indicated by green box in HAADF images a) and e). The regions analysed to to give indicated compositions are shown by red boxes in a) and e)	137
3.41	High resolution EDX map showing composition of particles found in magnesium-0.0243 at% Nd alloy after cold rolling and annealing for one hour at 400°C. 138	
3.42	High resolution EDX map showing composition of particles found in magnesium-0.0243 at% Nd alloy after cold rolling and annealing for one hour at 400°C. 138	
3.43	High resolution EDX map showing composition of particles found in magnesium-0.0243 at% Nd alloy after cold rolling and annealing for one hour at 400°C. 139	
4.1	Benchmark VPSC simulations for rolling of cast material. Including flow stress curve, deformation mode activities and predicted texture development. 148	
4.2	VPSC model predictions of the effect of deactivating each deformation mode during plane strain compression.	150

4.3	VPSC predictions of the effect of changing the CRSS of pyramidal slip during plane strain compression.	152
4.4	VPSC predictions of the effect of changing the CRSS of prismatic slip during plane strain compression.	153
4.5	VPSC predictions of the effect of changing the CRSS of basal slip during plane strain compression.	154
4.6	VPSC predictions of the effect of changing the CRSS of contraction twinning during plane strain compression.	156
4.7	VPSC predictions of the effect of changing the CRSS of tension twinning during plane strain compression.	157
4.8	VPSC simulation of straight cold rolling with pyramidal CRSS set to 63 MPa and 160 MPa.	159
4.9	Percentage Activities of each deformation mode during SCR, TCR and ECR as predicted by the VPSC model.	160
4.10	VPSC simulations of transverse and equal cold rolled ZEK100.	162
5.1	Schematic of proposed texture weakening mechanism in binary magnesium-rare earth alloys and cold rolled non-rare earth alloys.	168
5.2	Schematic of the pinning of a basal edge dislocation by solute Zn and Gd additions.	176

List of Tables

1.1	Table showing the conventional designations for the most common alloying elements in magnesium	17
1.2	Table showing the temper designations for magnesium alloys.	18
1.3	Table showing the c/a ration for common h.c.p systems and the dominant slip system in each case.	19
1.4	Estimated CRSSs for each of the principle deformation modes for polycrystalline magnesium at room temperature.	20
1.5	Possible twinning systems in magnesium together with the associated misorientations about the $\langle 1\bar{2}10 \rangle$ axis	29
1.6	The change in CRSS's τ_0 , (normalised to basal slip) and latent hardening, θ_0 , required to simulate FLCs at 20°C and 200°C using the VPSC crystal plasticity model	41
2.1	Compositions of the range of binary magnesium-RE alloys measured using ICP testing.	83
2.2	Compositions of RE alloys in wt% as measured by XRF and Ni compositions of two alloys measured by ICP-OES.	85
3.1	Cold rolling schedule for AZ31 and magnesium 0.0170 at% La alloy. Prior to cold rolling the AZ31 and hot rolled La alloy were annealed for 1hr at 400°C to fully recrystallise.	105
3.2	Cold rolling schedule for the magnesium-Y binary alloy systems.	106
3.3	Rolling schedule for the transverse cold rolled (TCR) and straight cold rolled (SCR) ZEK100, showing cumulative true strain over nine passes.	114
3.4	Cold rolling schedule for the equal cold rolled ZEK100, all strains true.	124
4.1	Parameters used in the VPSC model, based on the minimum parameters approach by Hutchinson <i>et.al</i>	146
4.2	Table showing the total percentage of strain accommodated by each deformation mode during SCR, TCR and ECR simulations.	158
4.3	Table showing the total percentage of strain accommodated by each deformation mode during ECR simulations to $\epsilon = -0.25$ when the cold rolled RD was parallel and perpendicular to the RD_{HR} respectively.	161

THE UNIVERSITY OF MANCHESTER

Abstract

For the Degree of Doctor of Philosophy in the Faculty of Engineering and Physical Sciences

Understanding Texture Weakening In Magnesium Rare Earth Alloys

by David G J GRIFFITHS September 2014

Magnesium has the lowest density of any structural metal making it a strong candidate for weight savings in the aerospace and automotive industries. However, strong crystallographic textures combine with anisotropic deformation modes to severely limit formability in wrought magnesium alloys. Recently improved formability has been achieved by the addition of small concentrations of solute rare earth elements which reduce the intensity of recrystallisation textures.

In this study the static recrystallisation mechanism of rolled magnesium rare earth alloys, which causes the texture weakening, is examined with a particular emphasis on the contrasting texture weakening effects in binary and tertiary magnesium rare earth alloys. In binary magnesium-rare earth alloys the 'rare-earth' texture is simply a weakened deformation texture, while recrystallisation of magnesium-zinc-rare earth alloys produces unique 'rare-earth' texture components. In the binary alloys weakened recrystallisation textures are attributed to the generation of 'off-basal' orientations within regions of high strain localisation during deformation. These orientations recrystallise and subsequently dominate the recrystallised texture. Texture weakening by this mechanism is also thought to be observed in non-rare earth magnesium alloys where dynamic recrystallisation is suppressed by cold rolling. The unique rare-earth texture components in magnesium-zinc-rare earth alloys are found to be determined by the orientation of shear bands in the material. Similarly to texture weakening in the binary alloys, nuclei for these orientations are thought to develop during deformation as a result of strain incompatibilities within shear bands. The mechanism forming these orientations remains unclear, however it is postulated that a complex change in recovery behaviour within shear bands, as a result of rare earth and zinc additions, may be the cause.

Retarded dynamic recrystallisation is suggested to be of critical importance in the texture weakening mechanisms of all magnesium alloys, both rare earth and non-rare earth. In rare earth alloys dynamic recrystallisation is suppressed by the segregation of rare earth atoms to grain boundaries. A combination of high resolution TEM and EDX shows rare earth atoms form clusters $\approx 2\text{nm}$ in diameter on grain boundaries which are expected to retard dynamic recrystallisation through a solute drag mechanism.

Declaration of Authorship

I, David G J GRIFFITHS, declare that this thesis titled, 'Understanding Texture Weakening In Magnesium Rare Earth Alloys' and the work presented in it are my own. I confirm that:

- This work was done wholly while in candidature for a research degree at this University.
- No portion of this thesis has previously been submitted for a degree or any other qualification at this University or any other institution.
- Where I have consulted the published work of others, this is always clearly attributed.
- Where I have quoted from the work of others, the source is always given. With the exception of such quotations, this thesis is entirely my own work.
- I have acknowledged all main sources of help.

Signed:

Date:

Copyright Statement

- The author of this thesis (including any appendices and/or schedules to this thesis) owns certain copyright or related rights in it (the “Copyright”) and he has given The University of Manchester certain rights to use such Copyright, including for administrative purposes.
- Copies of this thesis, either in full or in extracts and whether in hard or electronic copy, may be made only in accordance with the Copyright, Designs and Patents Act 1988 (as amended) and regulations issued under it or, where appropriate, in accordance with licensing agreements which the University has from time to time. This page must form part of any such copies made.
- The ownership of certain Copyright, patents, designs, trade marks and other intellectual property (the “Intellectual Property”) and any reproductions of copyright works in the thesis, for example graphs and tables (“Reproductions”), which may be described in this thesis, may not be owned by the author and may be owned by third parties. Such Intellectual Property and Reproductions cannot and must not be made available for use without the prior written permission of the owner(s) of the relevant Intellectual Property and/or Reproductions.
- Further information on the conditions under which disclosure, publication and commercialisation of this thesis, the Copyright and any Intellectual Property and/or Reproductions described in it may take place is available in the University IP Policy (see <http://documents.manchester.ac.uk/DocuInfo.aspx?DocID=487>), in any relevant Thesis restriction declarations deposited in the University Library, The University Library’s regulations (see <http://www.manchester.ac.uk/library/aboutus/regulations>) and in The University’s policy on Presentation of Theses.

List of Publications

- D. Griffiths. ‘Explaining texture weakening and improved formability in magnesium rare earth alloys’, *Materials Science and Technology*, **2014** (Accepted).

Winner of the Materials Science and Technology literature review prize 2014.

- D. Griffiths, B. Davis, S. Haigh and J. Robson, ‘Segregation of Rare Earth Atoms to Grain Boundaries’, *Scripta Materialia*, in production.
- D. Griffiths, B. Davis and J Robson, ‘Static Recrystallisation of Cold Rolled ZEK100’, *Materials Science and Engineering: A*, in production.

Acknowledgements

I could not have completed this thesis without the strong support and guidance of my supervisor Joe Robson and the technical supervision and support from Bruce Davis at Magnesium Elektron. The help and expertise of students and staff at School of Materials and the Advanced Metallic Systems Centre for Doctoral Training has also been fantastic. There are far too many names to thank individually, but you know who you are, thank you all very much I couldn't have finished without you!

Chapter 1

Literature Review

1.1 Introduction

1.1.1 Magnesium Alloys and their Properties

Magnesium is increasingly seen as an attractive structural material for use in a wide variety of structural applications from consumer electronics, including laptops and mobile phones, to seat frames and body panelling for automotive and aerospace applications. Interest in magnesium is driven by an exciting range of properties including; low density, high specific strength, good thermal conductivity and low cost processing, particularly in die castings. The growth in magnesium markets is currently driven by these cast components which have been estimated to account for up to 80% of magnesium production [1]. Meanwhile the use of wrought magnesium products is not widespread as a result of low formability limiting the potential applications.

In recent years there has been renewed interest in wrought magnesium as part of the drive to combat climate change by producing greener more fuel efficient vehicles [2]. Mass is a key contributor to fuel consumption with higher mass vehicles burning more fuel to achieve the same velocities as lighter ones. As the lightest structural metal with a density (1.74 g cm^{-3}) 78% lower than steel (7.87 g cm^{-3}) and 37% lower than aluminium (2.70 g cm^{-3}) magnesium is increasingly viewed as a key material required to reduce vehicle mass.

Currently the two primary limitations preventing the widespread uptake of magnesium alloys are low formability and poor corrosion performance. Improving the low formability of these alloys is the focus of this thesis. Fundamentally there are two possible approaches to achieving this goal, adjusting processing route or changing alloy chemistries. Changes

in processing route have had limited success [3–5] however, changing alloy chemistries, particularly the addition of rare earth elements have been far more effective. Rare earth additions are found to significantly improve mechanical properties and the formability of magnesium, in part by weakening strong crystallographic textures which develop during processing. In the following we seek to understand the mechanism facilitating these ‘rare earth’ effects in the hope of leading alloy design towards a new class of industrially viable, highly formable wrought magnesium alloys.

1.1.2 Common Alloying Elements in Magnesium

Traditionally magnesium alloys are labelled by letters designating the two highest concentration alloying elements, followed by the concentration of each element rounded to the nearest wt%. A list of the most common alloying elements and their conventional designating letters is given in Table 1.1. For example the common wrought magnesium alloy AZ31 contains 3 wt% Al and 1 wt% Zn. The temper of magnesium alloys is also indicated by a letter given in Table 1.2.

Alloying elements are typically added to magnesium to increase the yield strength of the material, a primary limiting factor in the majority of magnesium castings. Strengthening occurs by three mechanisms, solid solution strengthening, precipitation hardening and grain refinement. Of particular note are Zn and Al additions common in wrought alloys such as AZ31, which provide strengthening of magnesium alloys through precipitation hardening[6]. Rare earth additions including Y, Ce and Nd are also widely used in magnesium metallurgy providing solid solution strengthening and precipitation hardening especially at high temperatures[7–9]. These rare earth alloys also significantly improve creep resistance[10]. Zr and Al additions also strongly refine grain sizes in magnesium castings, providing hardening through the Hall-Petch relationship[11, 12].

Table 1.1: Table showing the conventional designations for the most common alloying elements in magnesium

Letter	Element	Comment
A	Aluminium	Strengthens
C	Copper	Reduces Corrosion Resistance
E	Rare Earths	Strengthens & Improves Creep Resistance
K	Zirconium	Grain Refinement
L	Lithium	Increases Ductility
M	Manganese	Increases Corrosion Resistance
Q	Silver	Strengthens
S	Silicon	Reduces Strength
Y	Yttrium	Strengthens & Improves Creep Resistance
Z	Zinc	Strengthens

Some elemental additions are highly undesirable in magnesium primarily as they severely compromise the corrosion resistance or strength of the material. Of these elements Ni, Cu and Fe are particularly problematic severely limiting corrosion performance[13]. Inclusions of these elements are typically limited to less than 0.005 wt% in the majority of industrial castings. Corrosion resistance can however, be improved addition of Ca[14] and Mn[15]. Many RE additions are also associated with improved resistance to corrosion, as well as improved creep and strength[16]. As a result many modern magnesium alloys contain significant RE additions which in general have a positive impact on the properties of magnesium.

Table 1.2: Table showing the temper designations for magnesium alloys.

Letter	Description
F	As Fabricated
O	Annealed and Recrystallised
H	Strain Hardened
T	Thermally Treated to Produce a Stable Temper
W	Solution Heat Treated

Also of interest in magnesium metallurgy are Li additions, Li has a lower atomic mass than magnesium and a very high solubility (up to 17 at%). As Li has a lower mass than magnesium it reduces the density of the material further improving the weight advantage of magnesium over other materials. Li addition over 41 at% also induces a body centred cubic β phase in magnesium, offering the opportunity for the development of $\alpha + \beta$ magnesium alloys with high ductility[1, 17]. Unfortunately the improved ductility and weight savings in these alloys also come at the expense of strength and consequently they are not commonly commercially employed.

The most common commercial alloy systems vary by use with AM alloys common in magnesium die castings, providing a good compromise between strength and castability[18]. ZK alloys are typically used in magnesium castings producing a fine grain size which is also strengthened by precipitates. RE alloys such as WE43 are a growing class due to the strong creep resistance and high temperature strength provided by the RE additions. These alloys are also part of a growing collection of wrought magnesium alloys with high ductility. AZ alloys such as AZ31 are also prominent in wrought magnesium metallurgy however, despite reasonable strength these wrought alloys are rarely used commercially due to their low ductility and anisotropic properties.

1.2 Deformation of h.c.p Metals

1.2.1 Slip Systems

H.c.p metals have highly anisotropic mechanical properties, largely as a result of the limited number of deformation modes which are available to accommodate deformation. Like cubic metals dislocation slip is the primary deformation mode however, the low availability of slip systems increases the importance of deformation twinning in magnesium. Slip primarily occurs on the basal $\{0001\}$, prismatic $\{10\bar{1}0\}$ and pyramidal $\{11\bar{2}2\}$ planes indicated in Figure 1.1, the dominant slip plane for a number of h.c.p metals is given in Table 1.3. Typically slip is most active on the close packed plane, which is the basal plane in h.c.p crystals, the inter-planar spacing is also critical in determining the activity of each slip system. Increasing the spacing of slip planes will reduce the Peierls-Nabarro stress required for dislocation motion. Inter-planar spacing is controlled by the ratio of lattice constants or c/a ratio, assuming perfect atomic packing the ideal c/a ratio of a h.c.p crystal is 1.633 which is very close to that of magnesium 1.62. The inter-planar spacing of the prismatic planes becomes larger than basal planes where $c/a < \sqrt{3} = 1.73$, in theory this should favour prismatic slip in cobalt, magnesium, zirconium and titanium on the basis of a Peierls-Nabarro stress argument. Table 1.3 shows that prismatic slip is indeed favoured in zirconium and titanium systems but not magnesium and cobalt[19]. Basal slip is reported to be favoured in these systems due to the formation of stable stacking faults on the basal plane, which reduce the critical resolved shear stress (CRSS) required for basal slip[20], Section 1.2.3.

Table 1.3: Table showing the c/a ration for common h.c.p systems and the dominant slip system in each case[21]

Metal	c/a	Slip System
Cd	1.89	Basal
Zn	1.88	Basal
Co , Mg	1.62	Basal
Zr	1.59	Prismatic
Ti	1.59	Prismatic

Slip on both basal and prismatic planes occurs in the $\langle 11\bar{2}0 \rangle$, $\langle a \rangle$ directions, within the basal plane. As a result both basal and prismatic slip planes contain only two independent slip systems which accommodate strain only the $\langle a \rangle$ directions. Combined these two $\langle a \rangle$ systems give three independent slip systems which does not meet the Von Mises criterion [22], requiring five independent slip systems to accommodate an arbitrary shape change. However, deformation may occur in the $\langle c + a \rangle$ directions by slip on the pyramidal planes, most commonly the pyramidal 2 ($\{11\bar{2}2\}$ $\langle 11\bar{2}\bar{3} \rangle$) system, which gives five independent

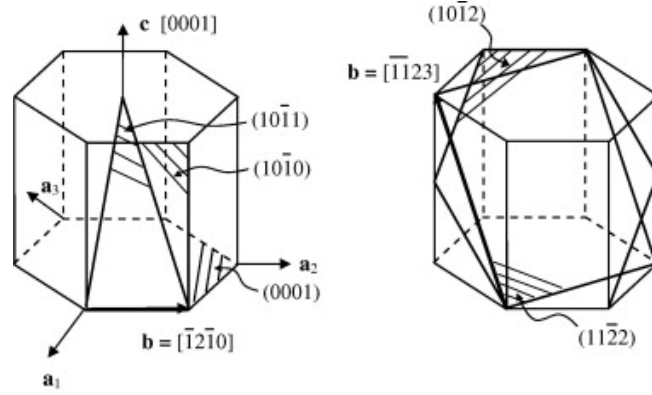


Figure 1.1: The most common slip and twinning planes and directions in magnesium, see Table 1.4 for identification [25].

Table 1.4: Estimated CRSSs for each of the principle deformation modes for polycrystalline magnesium at room temperature, as calculated by the VPSC model[26]. The CRSS of slip modes measured using single crystals is also included, with average values from[27] and estimates of twin CRSSs from [28]. The misorientation axis of each slip system is also given, for use in IGMA analysis, Section 1.8 [29].

Deformation Mode	System	CRSS (MPa)		Misorientation Axis
		Polycrystal Model	Single Crystal	
Basal $\langle a \rangle$ Slip	$\{0001\} \langle 11\bar{2}0 \rangle$	9	1	$\langle 1\bar{1}00 \rangle$
Prismatic $\langle a \rangle$ Slip	$\{10\bar{1}0\} \langle 11\bar{2}0 \rangle$	79	46	$\langle 0001 \rangle$
Pyramidal $\langle a \rangle$ Slip	$\{01\bar{1}1\} \langle 2\bar{1}\bar{1}0 \rangle$			$\langle 10\bar{1}2 \rangle$
Pyramidal $\langle c + a \rangle$ Slip 1	$\{01\bar{1}1\} \langle 11\bar{2}3 \rangle$			$\langle \bar{2}5 \ 41 \ \bar{1}69 \rangle$
Pyramidal $\langle c + a \rangle$ Slip 2	$\{11\bar{2}2\} \langle 11\bar{2}3 \rangle$	100	65 [28]	$\langle \bar{1}100 \rangle$
Tension Twin	$\{10\bar{1}2\} \langle 10\bar{1}1 \rangle$	47	7 [28]	
Compression Twin	$\{10\bar{1}1\} \langle 10\bar{1}2 \rangle$		85 [28]	

slip systems, enough to achieve the Von Mises criterion. At room temperature the critical resolved shear stress for slip on these pyramidal planes is very high and pyramidal slip generally only becomes highly active at elevated temperature where the CRSS is reduced [23, 24]. Table 1.4 gives the range of slip systems possible in h.c.p materials together with typical CRSS values for single crystal and polycrystalline magnesium.

1.2.2 Twinning

In addition to slip twinning also plays a crucial role in accommodating deformation in h.c.p systems. During twinning the crystal shears reorienting the twinned crystal into a mirror image of the un-twinned crystal along a mirror plane. Unlike slip, which occurs via the motion of individual atoms forwards or backwards on the slip plane, twinning may only occur in one direction and involves the simultaneous movement of a large number of atoms on the shear plane (P) in direction η_1 (Figure 1.2), shuffling of atoms within the

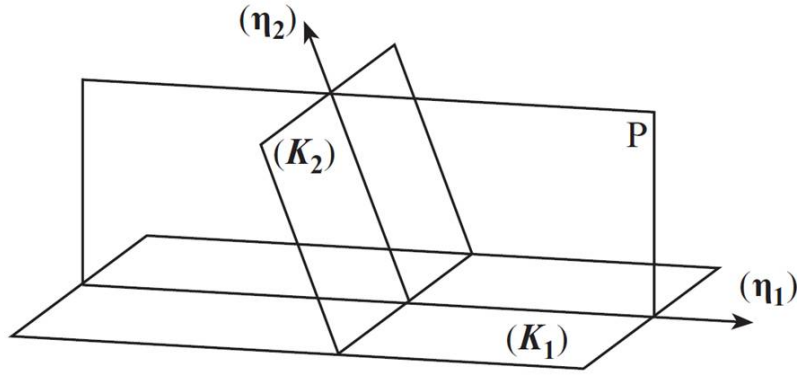


Figure 1.2: Figure showing a schematic of the most important planes and directions within a twin. K_1 represents the twinning (habit plane) and K_2 is the reciprocal twinning plane, P is the shear plane. η_1 and η_2 are the twinning and reciprocal twinning directions[32].

twin is also reported to be necessary to generate the correct twin structure within the twin[30]. The relationship between parent grain and twin is explicitly defined by the plane K_1 which is invariant in both twinned and un-twinned crystals and the direction of shear η_1 . In h.c.p crystals twinning primarily occurs on the $\{10\bar{1}2\}$ and $\{10\bar{1}1\}$ planes with the direction of shear dependent on the c/a ratio[31]. Figure 1.3 plots the magnitude of twinning shear as a function of c/a ratio, the gradient of the curve indicates shear direction; A positive gradient gives contraction in the c direction and negative gradient extension in the c direction. Where $c/a < \sqrt{3}$ as for magnesium, titanium and zirconium twinning on the $\{10\bar{1}2\}$ plane causes extension along the $\langle c \rangle$ axis, it is thus known as tension twinning. While for $c/a > 1.5$ $\{10\bar{1}1\}$ twinning causes a contraction in the $\langle c \rangle$ axis and so is known as contraction twinning in the same systems. Twinning in magnesium is discussed in detail in Section 1.3.3.

1.2.3 Stacking Faults

Stacking Faults (SFs) are planar defects common in crystalline materials in which the regular stacking order of the atomic planes is interrupted. In h.c.p metals the close packed basal planes are packed in an ABABABAB formation, in which A and B represent basal planes of atoms occupying alternate sites on top of each other. There are three possible SFs on the basal plane, the intrinsic I_1 and I_2 faults and the extrinsic E fault. Intrinsic SFs describe a situation in which the stacking sequence is interrupted by one break in the stacking order and in extrinsic faults the order is disrupted in more than one location;

$$(I_1) ABABABAB \longrightarrow ABABCBCB \quad (1.1)$$

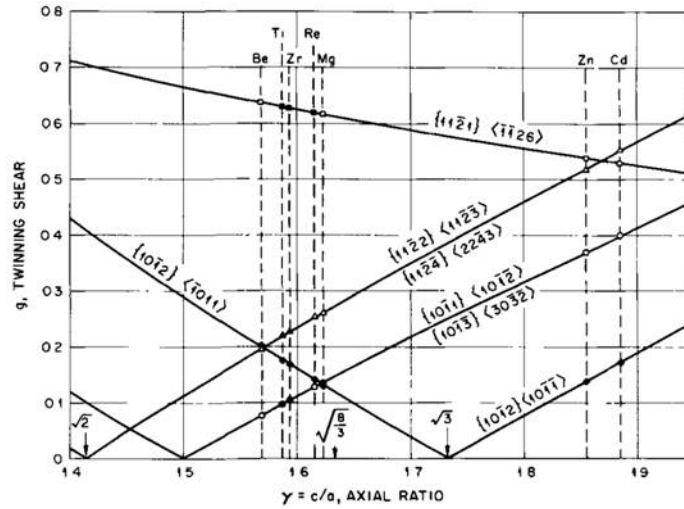


Figure 1.3: Figure showing the variation in twin shear with c/a ratio for a range of twinning systems. The direction of twinning shear is given by the gradient of the curve, positive gradient gives contraction of c axis and a negative gradient gives extension. The c/a ratio of a range of elements is indicated [31].

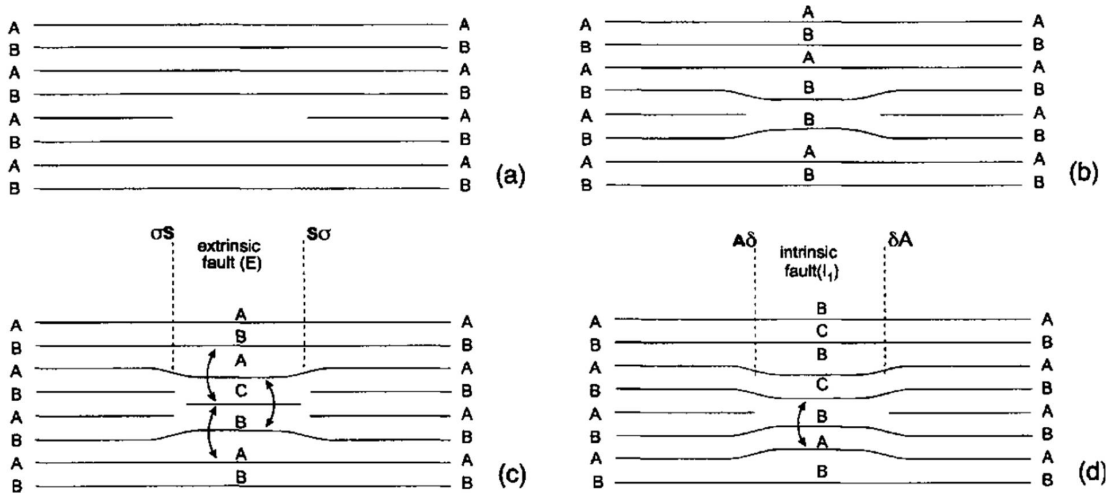


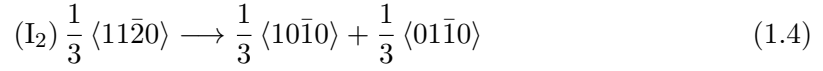
Figure 1.4: Figure showing the formation of E and I_1 stacking faults by the removal of an atomic plane. a) vacancies condense on a C plane removing part of it, b) the cavity collapses, c) the collapsed cavity forms an E type fault, d) cavity forms an I_1 fault[20].

$$(I_2) ABABABAB \rightarrow ABABCACA \quad (1.2)$$

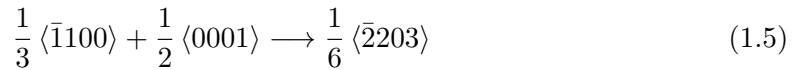
$$(E) ABABABAB \rightarrow ABABCABAB \quad (1.3)$$

The I_1 fault is formed by the removal of basal layer (A in this case) and slip of $\frac{1}{3} \langle 10\bar{1}0 \rangle$ above the fault to form the C layer. The I_2 or ‘deformation fault’ is formed by slip of $\frac{1}{3} \langle 10\bar{1}0 \rangle$ above the fault. Finally the E fault is caused by inserting an extra C plane.

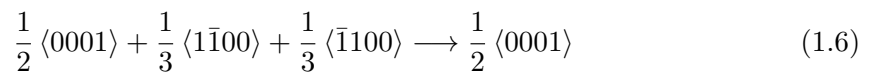
Stacking faults are separated from the unfaulted matrix by partial dislocations, there are two types of partial dislocation Shockly partials and Frank partials. Shockly partials are glissile as the Burgers vector lies within the glide plane, Frank partials are sessile as the Burgers vector is normal to the glide plane, fixing the partial in place. The most common stacking fault in h.c.p crystals is the I_2 stacking fault which is formed by the dissociation of a $\frac{1}{3} \langle 11\bar{2}0 \rangle$ perfect dislocation into two Shockly partials



The I_1 and E faults are caused by removing or inserting an atomic layer of material, this can occur by the condensation of vacancies or interstitial loops on atomic planes. For example vacancies may condense on a basal plane effectively removing a layer, Figure 1.4a). The planes above and below the void may then slip to fill the gap left by the condensed vacancies, however two planes with the same packing have high energy, Figure 1.4 b). To reduce the energy a stacking fault of I_1 or E type forms. An I_1 stacking fault forms if one layer glides by $\langle 10\bar{1}0 \rangle$ above the vacancy and $\frac{1}{3} \langle \bar{1}010 \rangle$ below, effectively changing a B layer to a C layer and shifting the stacking to BCBCBCBC above the fault (Equation 1.1), Figure 1.4 d). The associated dislocation reaction;



leaving a Frank partial preventing glide of the dislocation. Alternatively an E stacking fault may form if a B layer is changed to a C layer without changing the stacking above the fault. With dislocation reaction



leaving an extrinsic Frank partial loop surrounding the fault Figure 1.4c).

The stacking fault energy γ_E is determined by the separation of the partial dislocations surrounding the stacking fault. Dislocations are elastically repelled by each other driving an expansion of the SF however, this expansion is limited as increasing the separation of partials requires an increase in the size of the SF which requires energy to form. So γ_E is inversely proportional to the separation of partial dislocations in the SF which have reached an equilibrium between the elastic repulsion of the dislocations, driving expansion, and the energy required to form the SF forcing the partials to come together. Materials with a high γ_E either do not form SFs or have very small SFs.

The SFE has a significant effect on the recovery of the material because once a perfect dislocation has separated into partials the partials are confined to a particular slip plane.

In order to cross slip onto other planes the partials must constrict reforming a perfect dislocation. The energy required to form this constriction is larger the greater the separation of the partials as the partials must move a larger distance to recombine. As a lower SFE increases the separation of the partials it also means cross slip is less likely. If dislocations are unable to cross slip this significantly reduces recovery rates.

1.3 Deformation in Magnesium

1.3.1 Slip in Magnesium

As discussed in Section 1.2.1 and shown in Table 1.1 basal slip is the most active deformation mode in magnesium. This was first observed in slip trace analysis of single crystals[33, 34] and has since been confirmed by direct observation of basal dislocations in TEM studies[35]. The CRSS of basal slip in single crystal studies has been estimated at ≈ 1 MPa [36], in comparison to ≈ 50 MPa [37, 38] for prismatic and up to ≈ 100 MPa for pyramidal slip[27, 39, 40]. With such a low CRSS the dominance of basal slip is unsurprising, however basal slip only affords two independent slip systems both with burgers vectors in the $\langle a \rangle$ direction, which suggests only very limited formability. When tested in tension magnesium sheet typically demonstrates a room temperature tensile elongation of $> 10\%$ (Section 1.4.2), much larger than what would be expected with basal slip alone[25, 41]. Crystal plasticity modelling predicts prismatic and pyramidal slip must be active during deformation [25, 26] in order to reproduce such experimental ductilities. Significant prismatic and pyramidal slip has also been experimentally observed in TEM analysis of deformed magnesium[25, 41].

Significant activity of prismatic and pyramidal slip was until recently thought unlikely due to the high CRSS values of these systems measured by single crystal studies. However in polycrystalline material high localised incompatibility stresses develop in the microstructure as a result of grains favourably aligned for basal slip being constrained by neighbouring grains which have a hard orientation for basal slip. This can lead to local stresses at grain boundaries up to five times larger than the applied stress[42], large enough to activate non-basal slip. These incompatibility stresses also result in the CRSS values predicted by polycrystal plasticity models being higher than those measured in single crystal experiments[25–27, 43, 44]. In fact Hutchinson, Jain and Barnett [45] argue that the relative polycrystalline CRSSs will converge in magnesium as deformation proceeds because the work hardening term grows larger than the relative differences between the deformation modes.

The true CRSS's of all slip systems are also strongly dependent on the deformation temperature, with lower yield stresses and better ductilities associated with high temperatures [25, 33, 34, 46, 47]. Higher temperatures increase non-basal slip activity by two primary effects; reducing the CRSS for slip on each system and reducing the activation energy required for cross slip. Falling CRSS's at high temperatures are due to the increased thermal energy which allows dislocations to overcome energy barriers of the order $\approx kT$ (thermal energy) with a lower applied shear stress[20]. The fall in CRSS with rising temperature saturates once the energy barrier to dislocation motion is $\ll kT$, this will happen at lower temperatures for basal slip due to its lower energy barrier, one reason why basal slip is relatively insensitive to temperature in comparison to prismatic and pyramidal slip[28].

The sensitivity of prismatic and pyramidal slip to temperature is primarily thought to be a result of a reduced activation energy for cross slip of basal dislocations onto non-basal planes at these temperatures. Prismatic dislocations form due to cross slip of basal dislocations onto the prismatic plane, this occurs by one of two mechanisms depending on the deformation temperature; At $T < 400\text{K}$ [48, 49] an extended basal dislocation may constrict at two points allowing it to bow on the prismatic plane, Figure 1.5 a)[50–52]. At $T > 400\text{K}$ [48] another mechanism is observed the Friedel-Escaig, jog or kink pair mechanism shown in Figure 1.5 b). In this mechanism a basal dislocation cross slips onto the prismatic plane where the prismatic dislocation then re-dissociates onto basal planes parallel to the original slip plane[49, 52, 53]. The prismatic dislocations are present effectively as a pair of jogs between two basal stacking faults, in this mechanism the activation energy for cross slip is therefore dependent on the activation energy for nucleating and propagating the jog pairs on the prismatic plane[49].

The formation of pyramidal dislocations is not as well understood as the prismatic case, however pyramidal slip is still reported to be strongly temperature dependent[39] also relying on a cross slip mechanism[54, 55]. Two cross-slip mechanisms nucleating pyramidal dislocations have been proposed; in the first, similarly to prismatic slip, basal $\langle a \rangle$ dislocations cross slip onto the prismatic plane. The $\langle a \rangle$ component of the prismatic dislocation then interacts with a sessile $\langle c \rangle$ dislocation forming a $\langle c+a \rangle$ dislocation which resultantly cross slips onto the pyramidal plane[55]. In another recently proposed mechanism pyramidal dislocations are suggested to form without the need of cross slip from the basal plane[54]. In this mechanism pyramidal dislocations nucleate on the pyramidal I $\{10\bar{1}1\}$ plane and subsequently cross slip onto the pyramidal II $\{10\bar{2}2\}$ plane[54]. In either case cross slip of dislocations is believed to be a critical factor in determining the activity of pyramidal slip in magnesium.

In summary basal slip dominates magnesium deformation, however significant prismatic and pyramidal slip do occur. The formability of magnesium can be greatly improved

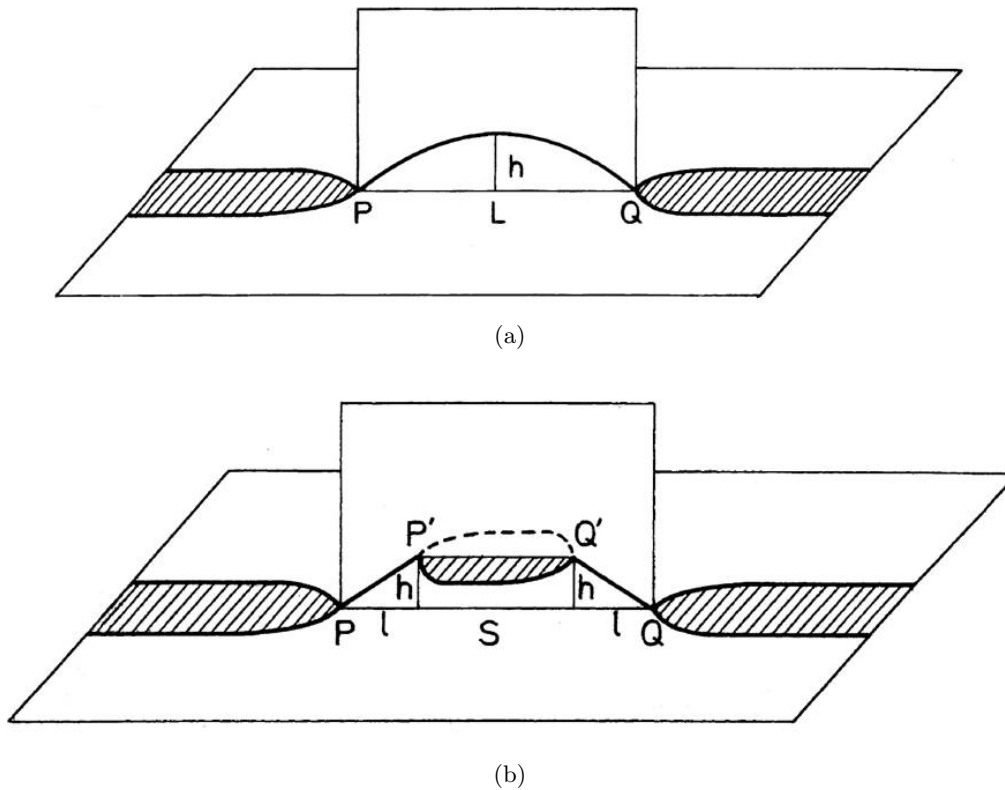


Figure 1.5: Figure showing two possible mechanisms for cross-slip of basal dislocations onto prismatic planes. a) Friedel mechanism when cross slip occurs at a constriction of a basal stacking fault and b) the double jog mechanism where a cross slipped dislocation re-dissociates onto a parallel basal plane to the original slip plane, the jogs between basal planes being the prismatic dislocations[52].

by deforming at temperatures above 400K where the prismatic and pyramidal activation energy for dislocation cross slip, required to activate prismatic and pyramidal slip, is low. At high temperatures the CRSS's for these slip systems are also reduced, increasing their activity. A change in the activity of non-basal slip can also be achieved by solute addition, which may harden or soften prismatic and pyramidal slip systems.

1.3.2 Solid Solution Strengthening

The CRSS for slip is also controlled by solute addition, with both solid solution strengthening and softening possible. Solid solution strengthening can be broadly considered in two regimes; where solute diffusion occurs Cottrell atmospheres[56–59] may form around dislocations pinning them in place, if solutes are not able to diffuse individual solutes may be considered to pin dislocations as they glide past the solute[60–62].

Where solute diffusion is not possible solid solution strengthening is commonly described by either the Friedel-Fleischer[62] or Labusch models[60]. Within each model the solute-dislocation interaction energy is caused by a size misfit and a chemical misfit between the

solute atom and the matrix[61]. The size misfit accounts for a change in local volume of the matrix as a result of solute addition and chemical misfit accounts for chemical interaction between the solute atom and dislocation core. The Friedel-Fleischer model considers each solute atom as an individual pinning entity with an associated pinning force meaning dislocations must bow around every solute. This model finds solution strengthening is $\propto C^{\frac{1}{2}}$, where C is the concentration of solute. The Labusch model considers the effect of many solute atoms forcing the dislocation to find a low energy configuration bowing around many solutes at the same time giving $CRSS \propto C^{\frac{2}{3}}$. Leyson and Curtin [61] review both approaches in a variety of materials finding the Labusch type model is more relevant to engineering problems at typical processing temperatures and where solute concentrations exceed 10^{-4} at%.

Solid solution strengthening of basal slip occurs in magnesium by a variety of solute additions including Al, In, Pb, Bi[47, 63], Zn[34, 64], Sn [65] and Cd [66]. In these systems the athermal component of strengthening is also found to be best represented by a $C^{\frac{2}{3}}$ relationship of Lebusch[61]. Strengthening was concluded to be dependent on size and chemical misfits between solute and matrix atoms by the Labusch theory and the interaction between solutes and edge dislocations was reported to be particularly significant[47]. More recent studies have applied *ab initio* modelling techniques together with the Friedel-Fleischer model to predict the strengthening of basal slip over a variety of magnesium alloying systems[67] which can predict the strengthening of a variety of solutes in magnesium. Figure 1.6 shows the models prediction that the greatest strengthening is achieved by alloys with large size or chemical misfits.

At high temperatures where solute atoms are able to diffuse in the matrix solid solution strengthening may also occur by the formation of Cottrell atmospheres of solute atoms around dislocations[56, 57]. Diffusing to dislocations relaxes lattice strains around both the dislocations and solute atoms causing the dislocation to be pinned in place, raising the yield stress for slip. Once the dislocation is free of the atmosphere the CRSS for slip drops as there is no longer a pinning effect. At high temperatures or low strain rates solute atoms may diffuse fast enough to keep up with the dislocation continuing to retard dislocation motion. Repeated pinning and release of dislocations is one cause of dynamic strain ageing (DSA) which produces a characteristic serrated flow stress curve. DSA effects have been observed in a number of magnesium systems; magnesium-Ag[68, 69], magnesium-Li-Al[70], magnesium-Gd [71], magnesium-Li-Al[72], magnesium-Th[73] and magnesium-Y-Nd[74]. However, DSA effects have not been extensively studied in magnesium alloys and it has been commented[71] that alloying additions which do not produce DSA in binary systems do show DSA when alloyed with each other in tertiary or quaternary systems, for example Zn and Al[63, 72]. This suggests a complex relationship between solute atoms and dislocations in tertiary and higher order systems that is not yet understood in magnesium.

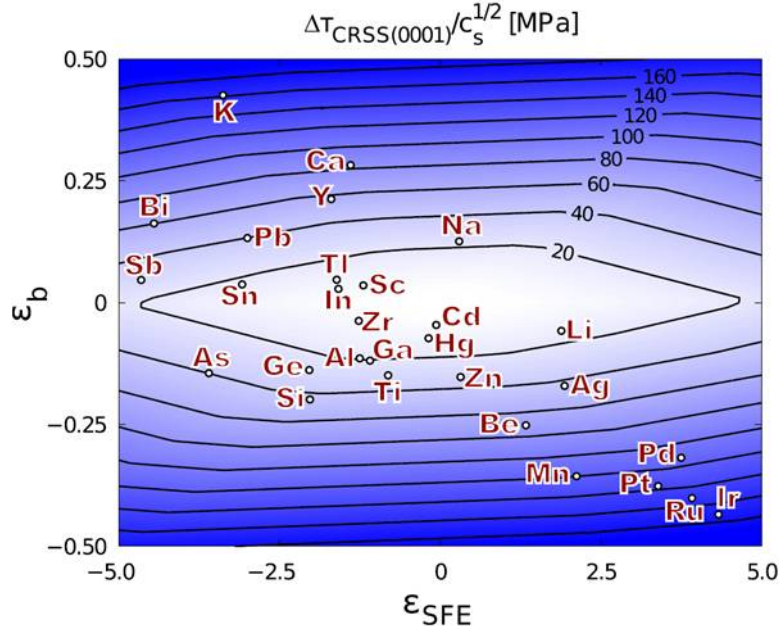


Figure 1.6: Figure showing an alloy design map for the solid solution strengthening of basal slip in magnesium alloys as predicted by DFT calculations. Contours represent concentration normalised CRSS, the chemical misfit (ϵ_{SFE}) and the atomic size misfit (ϵ_b) of the solute atoms[67].

In addition to solid solution strengthening solute additions can also cause softening of slip systems, Al, Zn[46] and Li [75] atoms for example are found to reduce the CRSS for prismatic slip. As discussed in Section 1.3.1 prismatic slip occurs as a result of cross slip of basal dislocations primarily by the jog pair mechanism (Figure 1.5b)), solid solution softening is thus attributed to a reduced cross-slip stress in solid solutions[64, 76]. Using DFT approach Yasi *et.al* predict that K, Na, Sc, Ca, Y and Zr will lower the cross-slip stress in magnesium, raising the activity of prismatic slip[76, 77]. The cross-slip stress is also found to be a function of temperature with stress falling with rising temperature. For each deformation temperature solute concentration can be optimised to minimise the cross-slip stress and thus soften prismatic slip[77]. Of course the CRSS for slip is also influenced by grain size through the Hall-Petch effect. Stanford and Barnett only observe solute softening in a magnesium-Zn alloy at grain sizes larger than $30\mu\text{m}$ [64]. They argue that at smaller grain sizes Hall-Petch hardening exceeds the CRSS for activation of prismatic slip by cross-slip, preventing the solute softening effect from being significant until the grain size exceeds a critical value.

In summary basal slip is the most active deformation mode in magnesium having a CRSS that is far lower than competing slip and twinning systems. While various alloying additions have been found to soften prismatic slip through solid solution softening, basal slip remains the dominant system.

1.3.3 Twinning in Magnesium

1.3.3.1 Twinning in Single Crystals

Twinning is also a key deformation mode in h.c.p materials, particularly in magnesium as the $\{10\bar{1}2\}$ tension twin has a CRSS of approximately 33 MPa [26] (according to polycrystal plasticity modelling), making it the most easily activated deformation mode after basal slip. There are various other twinning modes possible in h.c.p magnesium, listed in Table 1.5, each with a characteristic misorientation between the twin and parent grain. As discussed in Section 1.2.2 the c/a ratio of magnesium means the $\{10\bar{1}2\}$ twin allows c axis extension while $\{10\bar{1}1\}$ and $\{10\bar{1}3\}$ twin modes both cause c axis compression. Also listed in Table 1.5 are two commonly observed double twin systems in magnesium, in which a secondary twin forms within a primary twin[33, 78, 79], Figure 1.8.

Table 1.5: Table giving the possible twinning systems in magnesium together with the associated misorientations about the $\langle 1210 \rangle$ axis. Also listed are two observed double twinning systems[78]

Twin Plane	Misorientation	Shear
$\{10\bar{1}2\}$	86°	0.131
$\{10\bar{1}1\}$	56°	0.138
$\{10\bar{1}3\}$	64°	0.138
$\{10\bar{1}1\}$ - $\{10\bar{1}2\}$	38°	0.208
$\{10\bar{1}3\}$ - $\{10\bar{1}2\}$	22°	0.192

As each twinning system only operates in one direction the activity of each twin type is dependent upon straining direction. Tension twins are active where c axis extension is required and compression twins are active under c axis compression. Figure 1.7 shows the flow stress curve for a magnesium single crystal under c axis extension and compression. Under extension, tension twinning is activated producing an s shaped flow stress curve characteristic of twinning[80, 81]. A low yield stress is due to the low CRSS and high Schmid factor for tension twinning in this orientation. Immediately after yielding there is little work hardening due to the majority of strain being accommodated within twins. After twinning is exhausted significant work hardening is observed as a result of the operation of slip. Under c axis compression the majority of strain is accommodated by slip due to the high CRSS for compression twins, so the flow stress curve shows hardening behaviour expected for deformation primarily by dislocation slip.

The anisotropic flow stress behaviour described above is successfully predicted by crystal plasticity modelling treating twinning similarly to slip; with twin activity governed by Schmid factor and a characteristic CRSS [26, 82–84]. While the majority of twinning events in magnesium can be understood by this Schmid factor approach[81] recent studies have observed the formation of some double twin variants with sub-optimal Schmid factors

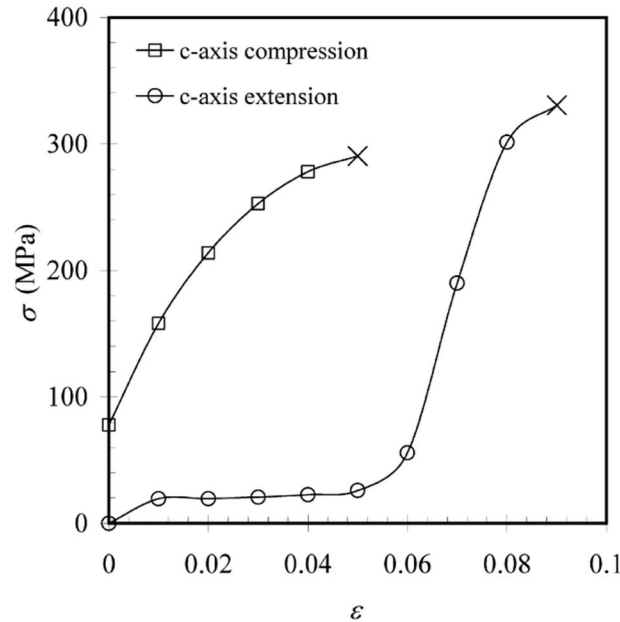


Figure 1.7: Figure showing the flow stress curve for a magnesium single crystal where the c axis is under compressive strains and tensile strains[87, 88].

in polycrystalline magnesium. It is proposed these non-Schmid twins form in order to maximise strain compatibility with the surrounding matrix[79, 85]. However it serves as a reminder that while macroscopic effects of twinning are quite well understood a full mechanistic understanding of twinning remains incomplete[86].

1.3.3.2 Twinning and Ductility

The activity (or inactivity) of twinning systems during deformation has strong effects on the ductility of magnesium alloys. Activation of tension twinning provides an extra easily accessible deformation mode within these grains increasing ductility, Figure 1.7. Improved ductility is not only provided by the additional deformation mode but also by changes in work hardening behaviour when tension twinning is operational. Figure 1.7 shows that magnesium work hardens more under c axis extension after twinning is complete than under c axis compression where no twinning occurs. The full complexities of this effect are still poorly understood however the additional twin boundaries in a heavily twinned material effectively refine the grain size contributing to hardening by a Hall-Petch type effect[83, 89]. Hardening due to some tension twins having relatively harder orientations for basal slip than the parent grains has also been considered to account for increased work hardening[89]. The increased uniform elongation that might be expected as a result of better hardening (Section 1.4.3) has been predicted by a constitutive modelling approach [80]. This suggests that tension twinning is beneficial to ductility not just because it offers an additional deformation mode but also by improving work hardening.

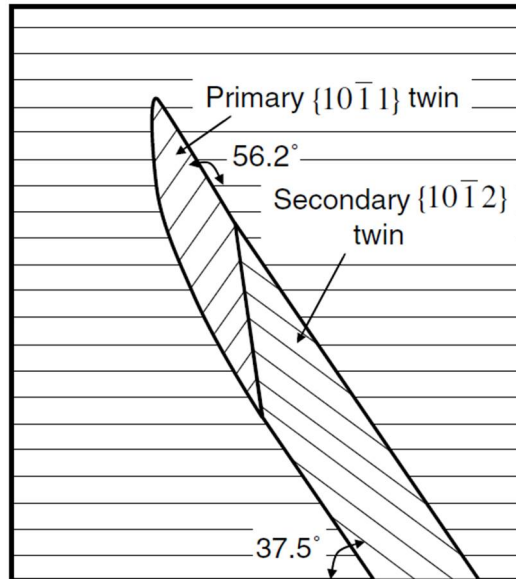


Figure 1.8: Schematic of a $\{10\bar{1}1\}$ - $\{10\bar{1}2\}$ double showing the basal planes along the $\langle 1\bar{2}10 \rangle$ axis. Taken from [79] after [91].

Not all twinning modes are beneficial to ductility with contraction and double twinning often thought to reduce ductility of magnesium. Contraction twinning has a less significant effect on the flow stress curve of c axis compression, where the s shape twinning curve is not observed, Figure 1.7. However some contraction twins do form under c axis compression, rotating the matrix inside the contraction twin into a favourable orientation for secondary tension twin formation, Figure 1.8. These double twins are favourably aligned for basal slip [79] within the twin (unlike the matrix) and once activated this basal slip can lead to flow stress softening due to the low CRSS required for basal slip[33]. This softening reduces the work hardening in the overall material which is expected to reduce material ductility (see Section 1.4.3). Indeed constitutive modelling also predicts a reduced uniform elongation in double twinned material as a result of work softening within double twins.[90].

The effect of twinning on mechanical properties is not only determined by the rate of twin nucleation (as discussed above) but also the rate of twin growth. The strain accommodated by a twin is proportional to the twin volume fraction, larger twins accommodating more shear strain[31, 86, 92]. Typically immediately post nucleation twins have a narrow lenticular shape, which may grow depending on the mobility of the twin boundary. Twin boundary mobility varies strongly between twin types, contraction twins have very immobile boundaries while tension twin boundaries are very mobile. This means that contraction and therefore double twins are often observed as very thin twins while tension twins grow much wider[87], often consuming the entire grain[78]. The easy nucleation and fast growth of tension twins when a material is strained in c axis tension contribute to the s shape of the flow stress curve which is not observed under c axis compression.

1.3.3.3 Effects of Grain Size & Deformation Temperature

Twin activity is also sensitive to deformation temperature and grain size with tension twinning suppressed at both high temperatures and small grain sizes[89, 93]. At high temperatures ($> 150^{\circ}\text{C}$ depending on grain size) the CRSS of competing slip systems falls more than that of tension twinning, reducing the tension twin activity in magnesium. Indeed, the actual CRSS for twinning is reported to be relatively insensitive to temperatures[89, 93]. The reduced twin activity at high temperatures is clearly observed in optical micrographs as a fall in twin volume fraction and in flow stress curves, where the twinning s shape flow stress curve is replaced with a typical flow stress curve at high temperatures. A similar transitional behaviour is observed as grain size is reduced, below a critical grain size deformation becomes slip dominated showing a similar transition in flow stress curve morphology and twin volume fraction. The transition is accompanied by a change in Hall-Petch slope (k) at the critical grain size, with the dislocation dominated region having a much lower k value than the twin dominated region[89, 92, 93]. The reason for the dependence of twin activity on grain size is not fully understood although it has been proposed to be due to the reduced twin size possible in smaller grains. A small grain size limits the size of twins, as each twin cannot grow beyond the grain boundary. As a result, the same number of twins accommodate less strain at smaller grain sizes. Thus in order to accommodate the same strain at small grain sizes, more twins must be activated, which raises the yield stress and k value for the material[92].

The temperature dependence of compression twins is more difficult to elucidate due to the less influential role these twins play in magnesium deformation. Indeed, unlike tension twinning at room temperature, other deformation modes such as prismatic and pyramidal slip are often active along with compression twinning[28, 33]. However, high temperatures are expected to reduce the CRSS for compression twinning and there is some evidence from studies of single crystals that increased compression and double twinning are observed at higher temperatures up to 350°C [28, 33]. In any case at higher temperatures the activity of non-basal slip systems increases and these systems come to dominate deformation, severely reducing all twin activity.

1.3.4 Shear Band Formation

Compression and double twinning have also been associated with the formation of shear bands in magnesium alloys during deformation[90, 94–98]. Shear bands are regions of high localised strain, often traversing many grains. Optical micrographs of shear bands in magnesium are shown in Figure 3.4. Shear bands might be expected to form at 45° to the compression direction during plane strain compression (the plane of highest shear

stress) however, shear bands are often observed at angles $<_{\pm} 35^{\circ}$ to the RD[99]. The reason for this is not clear but, strong rolling textures have been suggested as a possible explanation[100]. Investigations of shear band angles are complicated by difficulties in identifying new shear bands because once a shear band has formed continued plane strain compression will reduce the inclination of the band as the material is compressed. Thus old shear bands will be inclined at reduced angles to the RD compared to new bands. Regardless of the shear band angle, strain in magnesium shear bands is generally thought to be accommodated by basal slip, as this is the most easily activated slip system. Thus basal planes within shear bands are thought to be parallel to the band[101], maximising the Schmid factor for basal slip.

Shear bands are often seen as a precursor to failure in magnesium because they typically form once the soft deformation modes in a material are exhausted. At the start of an arbitrary deformation, strain is distributed evenly in the microstructure between many grains with favourable orientations for basal slip and tension twinning. As these soft orientations are exhausted, deformation continues in grains with unfavourably low Schmid factors, requiring greater applied stresses to allow deformation. Eventually shear bands form because the shear stress required to force slip in the remaining hard orientations is less than that required to form a shear band. This occurs first at locations of stress concentration (such as twins). Once formed the CRSS for slip within the band is low, due to a high Schmid factor for basal slip[99]. The low CRSS for basal slip once a shear band forms is associated with a drop in flow stress during processing; this is known as texture softening[101, 102]. Once strain is concentrated in this way failure is thought to be imminent as shear bands can only accommodate a finite amount of strain before incompatibility stresses and void formation cause the material to fail[103, 104]. If compression twinning were to initiate shear banding at low applied strains, it could cause further localisation of deformation and premature failure of the material, reducing ductility.

Shear bands are thought to form as a result of strain localisation within the matrix, with twins identified as a primary source of this localisation. Some twins, particularly compression and double twins, have a softer orientation for basal slip than the matrix. Strain is thus preferentially accommodated within such twins, concentrating strain in this area. Some argue this strain concentration ultimately nucleates shear band formation[33, 94, 98, 101]. Sandlöbes *et.al.* suggest that the strain localisation within the twin triggers the formation of further fine twins which constitute the shear band Figure 1.9 [94]. Other mechanisms have been proposed to account for shear band formation. At high temperatures Ion *et.al.* propose shear bands form due to dynamic recrystallisation around grain boundaries, Figure 1.10[105]. Recrystallised grains with soft orientations for basal slip concentrate slip in the necklace region of recrystallised grains around grain boundaries, ultimately forming shear bands

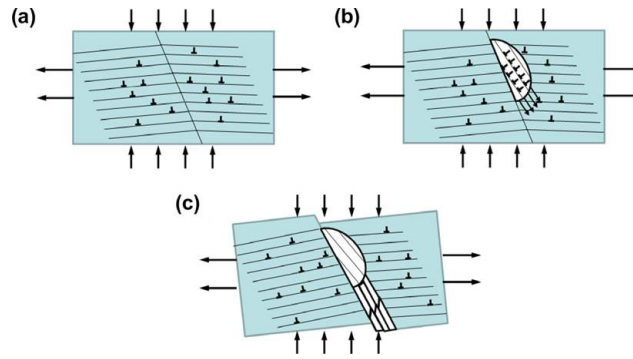


Figure 1.9: Proposed mechanism of shear band formation in magnesium under plane strain compression in basally oriented grains. a) Basal planes are perpendicular to compression direction and so basal slip cannot accommodate compression. b) This forces a compression twin to form, the basal planes within the twin are favourably oriented for basal slip. c) Strain localisation within the twin triggers formation of multiple fine twins starting a shear band[94].

While shear bands are considered a precursor to failure, they contribute significantly to the ultimate tensile elongation of magnesium. Sandlöbes *et.al.* argue that increased ductility in a group of magnesium-rare earth alloys can be partly explained by a fine distribution of fine shear bands throughout the deformed microstructure[94]. In other words a fine distribution of low intensity shear bands each accommodating a small amount of strain is likely to result in a higher strain before failure than a small number of very large shear bands which accommodate a lot of strain. In this way the spatial distribution of shear bands is very important in determining their contribution to ductility.

In summary, shear bands are an important deformation feature in magnesium, and their formation is often considered a precursor to the onset of failure. The density and spatial distribution of shear bands is considered critical in determining the final ductility of magnesium; in material where a large number of small shear bands nucleate, strain is shared between many bands allowing greater strains to be accommodated before failure, while in material with a small number of high strain bands strain is concentrated in a small area causing failure at lower strains[94]. In material where compression twins form, the twins are argued to nucleate shear bands which might be expected to induce failure. However if widespread twinning nucleates a larger number of finely distributed shear bands this may actually increase the ductility.

1.4 Wrought Magnesium

Magnesium is very rarely used to construct wrought components, because of the anisotropic properties those components have and the difficulty in manufacturing them. A wrought component is formed by plastic deformation of a material into a desired shape. Commonly

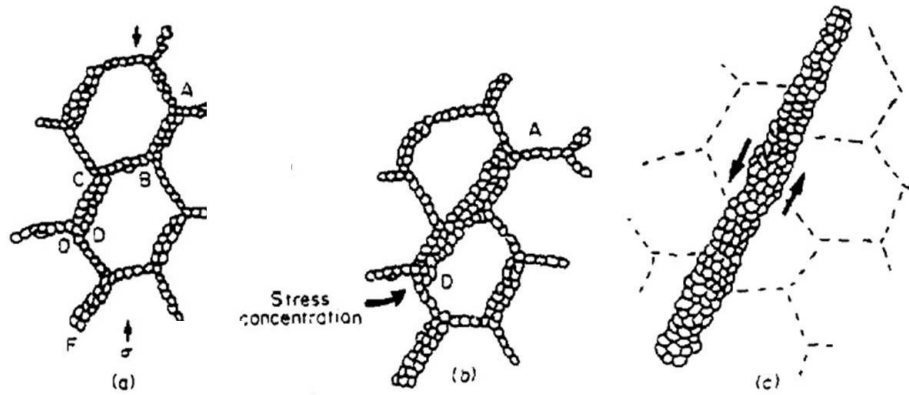


Figure 1.10: Proposed mechanism of shear band formation during dynamic recrystallisation. a) Deformed grains begin to recrystallise at grain boundaries forming a necklace type microstructure. b) Recrystallised grains have soft orientations for basal slip in comparison to parent grains, concentrating slip in bands of interconnected grains around grain boundaries concentrating stress at the ends. c) Continued stress concentration and shear band formation cause shear band formation[105].

this involves rolling or extrusion into sheet or rod product which is subsequently deformed into a component. During rolling or extrusion, magnesium alloys form strong textures which combined with a small number of easily activated deformation modes limits the subsequent room temperature formability, preventing sheet or rod products from being easily deformed into desired shapes. Even in cases where magnesium products are formed they typically demonstrate anisotropic mechanical properties often not desirable in an engineering material. In the following, the origins of the strong textures that form in magnesium are discussed together with the impact these have on mechanical properties and formability. Strategies for optimising the formability of magnesium alloys are also presented.

1.4.1 Formation of Basal Textures

Figure 1.11 gives example pole figures demonstrating the typical strong textures that develop in magnesium during rolling and extrusion. After rolling, the basal plane normals are aligned parallel with the normal direction (ND) of the sheet and after extrusion the basal plane normals are perpendicular to the extrusion direction (ED). These textures are largely formed due to the high activity of basal slip; the Schmidt factor for basal slip during rolling is highest for grains with their c axis at 45° to the ND and lowest for grains with c axis parallel to ND or perpendicular to it. The action of basal slip during compression rotates grains such that basal plane normals become almost parallel to the ND where the Schmid factor for basal slip is very low. Even if grains are unfavourably oriented for basal slip, the low CRSS means that in many cases this mode is activated first in these grains. In grains which are initially oriented perpendicular to the ND, so the

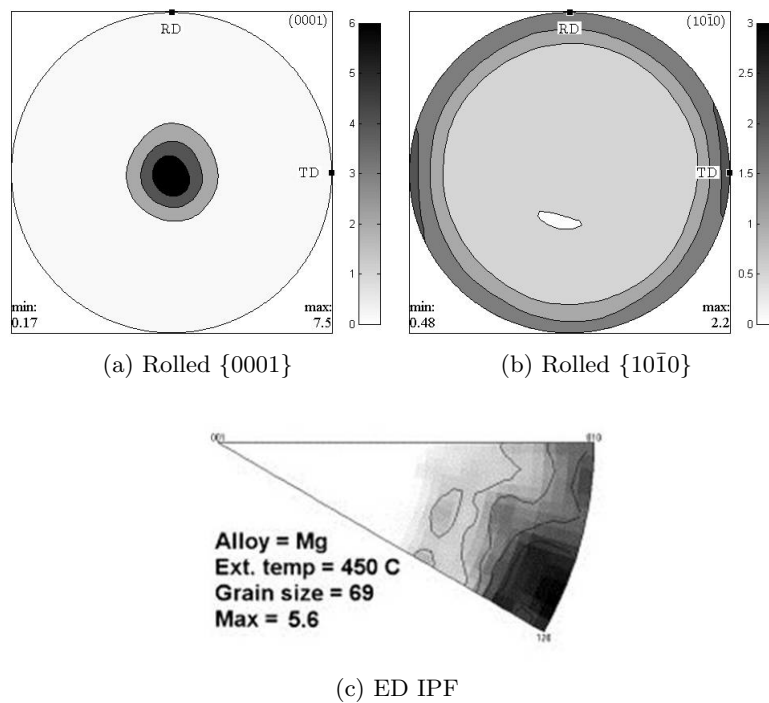


Figure 1.11: Figure showing the a) $\{0001\}$ and b) $\{10\bar{1}0\}$ pole figures of rolled AZ31. c) Extrusion direction inverse pole figure of extruded AZ31[96].

Schmidt factor for basal slip is too low for its activation despite the low CRSS, the Schmid factor for tensile twinning is high so this mode is activated. Tensile twinning reorients the material in the twin by 86° into the ND of the sheet, producing the same alignment of basal poles as produced by basal slip. In this way, predominantly by the activity of basal slip and tensile twinning, strong basal textures develop during rolling with basal plane normals parallel to the principle compression direction. Similarly, during extrusion, basal slip and twinning orient grains so that their c axes lie perpendicular to the extrusion direction and parallel to the compression direction of the extrusion process.

The basal texture of Figure 1.11a) is that typically expected of rolled pure magnesium sheet. However, in practice it is common to find a texture in which the basal pole is split towards the RD, Figure 1.12. The split texture has been associated with increased activity of pyramidal $\langle c+a \rangle$ slip during the deformation[83, 106] and shear band formation (Section 1.5.2.4). These strong basal type textures are key contributing factors causing the yield asymmetry and low formability which are currently significant in preventing the widespread use of wrought magnesium.

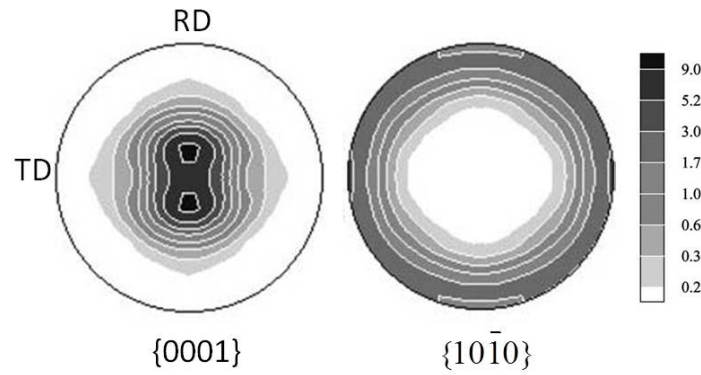


Figure 1.12: Basal texture of AZ31 rolled at 200°C, showing a typical split of the basal texture in the RD [25].

1.4.2 Yield Asymmetry

The low CRSS of basal slip combined with strong textures mean the yield stress of wrought magnesium products varies significantly depending on strain direction [107, 108]. A difference of around ≈ 100 MPa (a factor of three) has been measured in some alloys, as shown in Figure 1.13. The data plotted in Figure 1.13 was derived from a sheet with a basal texture similar to that of Figure 1.11 a), in which the strongly textured polycrystal almost behaves like a single crystal, as all grains are oriented with their c axes nearly parallel to the ND. The yield anisotropy observed occurs as the c axis of these grains moves from compression to tension. The c axis is under tension both when the ND is directly under tension ND(t) and indirectly when the sheet is compressed in the rolling direction, RD(c), due to the Poisson effect. c axis extension under these conditions can be easily accommodated by tensile twinning, which has a low CRSS. This leads to low yield stress (≈ 60 MPa) and a typical s shape flow stress curve caused by twinning. However, when the c axis is compressed (directly by ND(c) and indirectly by RD(t)) very few deformation modes are available to accommodate deformation because, as discussed in Section 1.2.1, the Burgers vectors of both basal and prismatic slip lie in the basal $\langle a \rangle$ plane, leaving only compression twinning and pyramidal slip able to accommodate $\langle c \rangle$ axis compression. The CRSS's of both compression twinning and pyramidal slip are high at room temperature raising the yield stress to ≈ 140 MPa [87, 107, 109]. The inability of magnesium crystals to accommodate $\langle c \rangle$ axis compression is at the heart of magnesium's anisotropic behaviour and, combined with strong textures, severely limits the applications of wrought magnesium products.

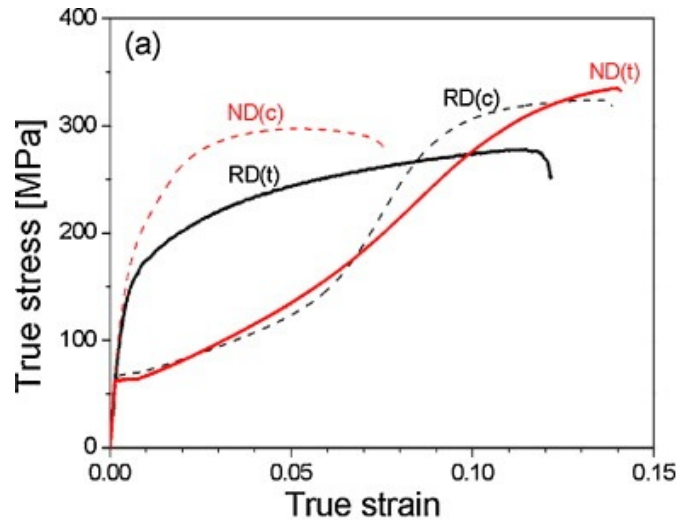


Figure 1.13: Flow stress for rolled AZ31 under tension (t) and compression (c) in both normal direction (ND) and rolling direction (RD). The anisotropic properties of Mg are clearly shown, flow stress strongly dependent on both direction of deformation and orientation of the sample[109].

1.4.3 Formability

Strong basal textures are also the cause of low formability of wrought magnesium products. Formability is a term used to describe the extent to which a material can deform before failure. A sheet with low formability is likely to fail before it can be deformed into a useful shape. The formability of sheet material can be quantified using a forming limit curve (FLC) such as that plotted in Figure 1.14. An FLC plots the strain to failure of a sheet material when strained in a variety of strain states, from uniaxial tension (dotted line) to biaxial tension (dashed line). Effectively, the region below the FLC is “safe”, containing strain states where the material should not fail, while attempting to deform to a strain state above the FLC is “unsafe” and will cause material failure. Figure 1.14 shows that a typical magnesium alloy AZ31 has a significantly lower forming limit strain for all strain states than aluminium 6016 when deformed at room temperature.

Formability of sheet in cubic materials is considered to be controlled by its ability to resist strain localisation which causes necking and ultimately failure[112]. High strain rate sensitivity m and work hardening n values contribute to a highly formable material by resisting strain localisation. A high work hardening coefficient hardens a material in regions of strain localisation, preventing further deformation in that area. Similarly a high strain rate sensitivity causes hardening in a necked region where strain rate is higher than in the bulk of the material. Both parameters delay the onset of strain localisation and failure, increasing formability. While these parameters are specific to each alloy and temper, typical values for aluminium at room temperature are $n = 0.22 - 0.30$ and $m = 0.01$ [113]. Despite much lower formability at room temperature magnesium has

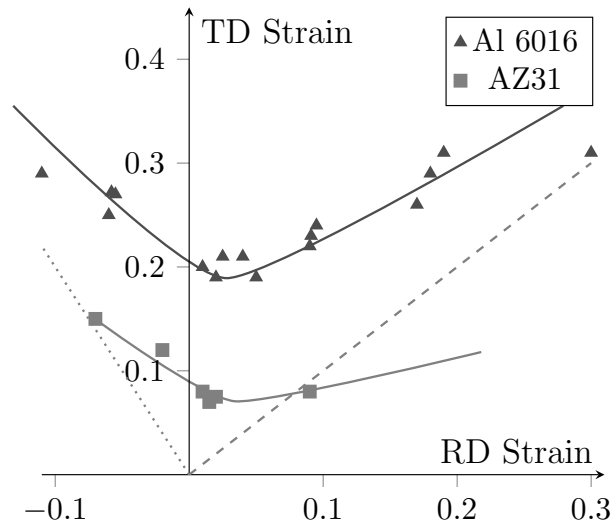


Figure 1.14: Room temperature forming limit diagram of aluminium 6016 [110] and magnesium AZ31 [111]. Curves are added to guide the eye. Uniaxial tension is indicated by the dotted line and biaxial tension by the dashed line.

similar values of $n = 0.2$ [114] and $m = 0.02$ [71]. In principle one would expect magnesium alloys to be significantly more formable based on these parameters. However, failure of magnesium parts is not typically thought of in terms of necking but in terms of a hardening of the material to basal slip[115]. The majority of deformation in magnesium occurs by basal slip as the CRSS for basal slip is so much lower than that of other deformation modes. Strong textures mean that the majority of grains in magnesium sheet have similar orientations ($\langle c \rangle \parallel ND$) and therefore similar Schmid factors for basal slip. A grain with a high Schmid factor for basal slip requires only small applied stress activate basal slip, easily accommodating strain and allowing the material to form. A low Schmid factor for basal slip on the other hand requires a large applied stress to activate basal slip, large stresses are also required to activate non-basal slip (even with a favourable Schmid factor) because the CRSS of these non-basal modes is very high. So in cases where the Schmid factor for basal slip is low applied stresses may exceed that required to form shear bands and/or voids causing the material to fail. This behaviour is markedly different to cubic materials where weak textures and large numbers of slip systems are available to accommodate deformation. Failure in these materials is considered to be more due to local necking rather than hardening of the material to a particular slip system.

In summary, the formability of magnesium is dependent upon the ease with which basal slip is activated. Forming magnesium is possible where grains well oriented for basal slip are available. However, the material rapidly hardens to basal slip due to the rotation of

those grains in which basal slip is active and the fact that strong textures often mean that few grains are favourably oriented for basal slip in the first place. Once the material hardens to basal slip failure is often imminent as the high applied shear stresses, which are required to activate basal slip in unfavourably oriented grains or overcome the high CRSS values of non-basal slip, often exceed the applied stresses required for void or crack formation causing material failure.

1.4.4 Increasing Magnesium Formability

There are two possibilities for increasing magnesium formability; reducing the basal texture strength or reducing the CRSSs of the other deformation modes [108]. Indeed, the two are intrinsically linked since reducing the CRSS of non-basal modes would also lead to texture weakening. Reducing texture strength will increase the number of grains with a high Schmidt factor for basal slip in an arbitrary straining direction and reducing the CRSS of other deformation modes will allow slip on other planes to occur. Both solutions will slow the build up of applied stresses, delaying the activation of failure modes to higher strains, improving formability and raising the FLC. Improved formability as a result of weakening basal textures in magnesium alloys has been successfully predicted by crystal plasticity modelling[115, 116]. Where weaker textures are shown to increase the forming limit without any changes to the CRSS values. Random textures are predicted to provide the maximum improvement in formability[115].

Formability may also be improved by reducing the CRSS of non-basal slip systems. As discussed in Section 1.3.1 one way of reducing the CRSS of non-basal slip systems in magnesium is by forming at high temperatures which shifts the minimum of the AZ31 FLC up to $\epsilon_{\text{major}} \approx 1$ at 250°C [117]. Crystal plasticity simulations of FLCs have also suggested the improvement in formability at high temperatures can be reproduced by reducing the CRSSs and work hardening rates of the prismatic and pyramidal slip systems[118] (see Table 1.6). In particular pyramidal slip is particularly important for improving formability as it offers six independent slip systems which are enough to accommodate an arbitrary shape change in a grain, which explains the increased formability when the CRSS and latent hardening for this mode are significantly lower at high temperatures. Increasing activity of pyramidal slip at high temperatures has also been suggested to explain the reduced planar anisotropy under these conditions[25]. Although increasing deformation temperature is effective at improving formability the temperatures required in practice make the forming process expensive relative to cold forming of aluminium products and so high temperatures are not industrially viable.

Table 1.6: Table showing the change in CRSS's τ_0 , (normalised to basal slip) and latent hardening, θ_0 , required to simulate FLCs at 20°C and 200°C using the VPSC crystal plasticity model (Section 4.1.2)[115].

	Basal	Prismatic	Pyramidal	Tension Twin
$\tau_0^{20^\circ\text{C}}$	1	3.2	5	1.5
$\tau_0^{200^\circ\text{C}}$	1	1.8	1.8	2.1
$\theta_0^{20^\circ\text{C}}$	80	20	500	0
$\theta_0^{200^\circ\text{C}}$	80	20	35	0

In addition to identifying the importance of texture and CRSS for each slip system, crystal plasticity modelling also suggests strain rate sensitivity and work hardening are significant in determining formability. Increasing either factor is predicted to improve formability shifting the FLC up [115, 116]. Neil and Agnew note that improved formability at high temperatures in magnesium may saturate above 150°C due to competition between strain rate sensitivity and work hardening [115]. High temperatures increase strain rate sensitivity, which improves formability, while also reducing work hardening causes a fall in formability. Their simulations suggest these effects balance at around 150°C beyond which increases in temperature do not lead to significant improvements in formability.

We should note the crystal plasticity results quoted here are produced by the VPSC model described in more detail in Section 4.1.2. The model does not account for recovery or DRX, which may significantly impact formability especially at high temperatures. The model also neglects local effects such as grain-grain interactions and shear banding meaning the model predictions should be viewed with caution. Despite these limitations over the temperature range considered the model gives a reasonable explanation of material formability, in particular the predicted role pyramidal slip plays has recently been supported by observations of pyramidal dislocations in TEM studies[25].

In summary. the poor formability of magnesium is the result of a unique combination of strong textures and dominant basal slip in wrought magnesium alloys. Formability can be improved by deformation at high temperatures, which simulations suggest is due to a reduced CRSS for pyramidal slip. Weakening deformation textures also greatly improves formability in both experiment and simulation due to the larger number of grains with soft orientations for basal slip. Although this discussion has focused on the behaviour of sheet material the principles are the same for all wrought magnesium products; Dominant basal slip leading to strong textures during processing and subsequently premature failure during forming processes. It should be noted that strong textures are not always undesirable in finished products but currently in the majority of cases they prevent such products from being successfully formed.

In the remainder of this review the mechanisms for weakening the strong deformation textures in magnesium are considered with a view to increasing formability. The most obvious process for changing the deformation texture is recrystallisation.

1.5 Recrystallisation of Magnesium Alloys

1.5.1 Recovery and Recrystallisation

Recrystallisation occurs either dynamically during deformation (DRX) or statically during an annealing heat treatment post deformation (SRX). DRX in magnesium is very common even at relatively low deformation temperatures $T > 400^\circ\text{K}$. Typically the activation energy for DRX is associated with the stacking fault energy (SFE) of a material. A low SFE corresponds to a high DRX rate because the easy formation of partial dislocations prevents cross-slip. With cross slip prevented recovery is limited, meaning a high stored energy is available causing DRX. However, the SFEs in magnesium and aluminium are very similar [21] and unlike aluminium, where DRX is rare, magnesium alloys frequently show DRX. DRX in magnesium is primarily a result of stress concentrations which build up in the material because of the anisotropies in slip and twinning activities together with strong crystallographic textures. A combination of these factors leads to the build up of dislocations and stored energy in the microstructure particularly at grain boundaries where incompatibility stresses between neighbouring grains are highest. The high stored energy in these locations allows DRX to occur at relatively low temperatures. In contrast deformation in aluminium is far more uniform and strain concentration is thus much lower, which combined with a high SFE prevents DRX. As the majority of industrially processed magnesium undergoes significant DRX we concentrate on DRX in magnesium as SRX normally involves the growth of DRX nuclei or grains.

As deformation mechanisms are critical in generating stored energy in the microstructure, which allows DRX to occur, they also strongly influence the DRX mechanism which in turn controls the texture components nucleated. In the following we discuss the DRX nucleation mechanisms and discuss how these affect the recrystallised texture components.

1.5.2 Mechanisms of Recrystallisation

Recrystallisation in magnesium is commonly associated with five mechanisms; twin induced dynamic recrystallisation (TDRX), continuous dynamic recrystallisation (CDRX), strain induced boundary migration (SIBM), shear band nucleation (SBN) and particle

stimulated nucleation (PSN). In the following we consider each mechanism and the texture components they nucleate.

1.5.2.1 Strain Induced Boundary Migration–SIBM

SIBM is a common recrystallisation mechanism in many metallic materials, occurring at a bulge in a grain boundary. Interaction of a grain boundary with a slip band during deformation causes a build up of stress on one side of the boundary, which is relieved by a bulging of the boundary into a neighbouring grain. The mechanism of SIBM for aluminium alloys is illustrated in Figure 1.15 a). The bulge grows into a grain 2 as $E_2 > E_1$ where E is the stored energy of the grain including energy due to stress build up on the boundary and dislocation density. The region left behind the bulge has a lower dislocation density than both grains as the dislocation substructure is stretched during the bulging process Figure 1.15 b). Rearrangement of the stretched substructure within the bulge forms a low angle boundary bridging the recrystallisation nucleus Figure 1.15 c). Formation of the bridge may also be facilitated by grain boundary sliding, causing stresses to build up at the edges of the bulge which are relaxed by emission of dislocations constituting the bridge[119]. During recrystallisation the nucleus grows into the higher energy grain fastest as the high angle boundary between the bulge and grain 2 has a higher mobility than the low angle boundary between the bulge and grain 1. Grain boundary bulges may also form at large subgrains Figure 1.15 d)[21]. A TEM micrograph showing grain boundary bulges in magnesium (white arrows) is presented in Figure 1.17.

The misorientation between the low angle boundary of the nucleus and grain 1 gradually increases as dislocations are absorbed by the boundary, eventually forming a high angle boundary. Once the nucleus is surrounded by high angle boundaries nucleation is completed and recrystallisation continues by boundary migration of the high angle boundaries. This discrete two step nucleation and growth process is described as discontinuous recrystallisation mechanism in much of the literature. Recrystallisation by SIBM at grain boundaries in this way is one mechanism which leads to the ‘necklace’ type microstructure of recrystallised grains around the edges of prior grain boundaries (Figure 1.16). As the orientation of recrystallising grains is initially only separated from the parent grain (grain 1) by a low angle grain boundary (Figure 1.15c)) SIBM might not be expected to greatly weaken basal textures[120]. However, growth of the low angle boundary into a high angle boundary increases the misorientation between the SIBM grain and the parent grain weakening deformation textures overall[121].

SIBM is only active at high deformation temperatures ($T > 573\text{K}$)[122–124] where higher grain boundary mobility aids bulge formation. Increased non-basal slip, cross-slip and

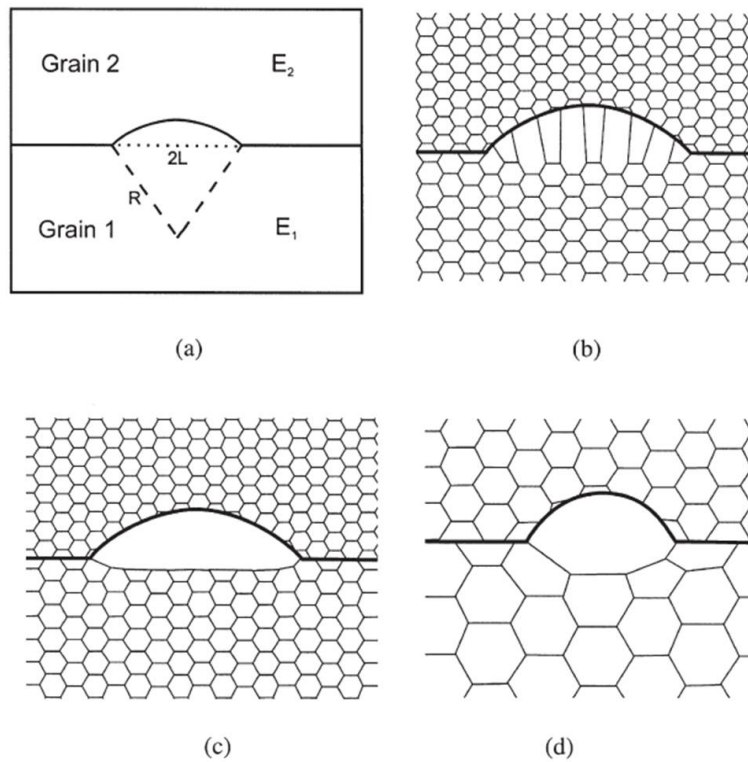


Figure 1.15: Figure showing the mechanism of strain induced boundary migration in aluminium. A similar mechanism operates in magnesium, but the subgrains tend to be less well defined especially in the centre of the grain. a) a bulge forms in a grain boundary as a result of a difference in stored energy $E_1 < E_2$, b) the dislocation substructure is stretched behind the bulging boundary, c) the substructure within the bulge recovers to form a low angle boundary and recrystallised grain. d) SIBM may also occur at large subgrains such that the interior is already substructure free[21].

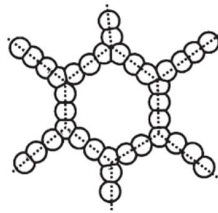


Figure 1.16: Figure showing the growth of the necklace type microstructure characteristic of a variety of recrystallisation mechanisms in magnesium. Nucleation of recrystallisation occurs preferentially at grain boundaries forming a necklace of recrystallised grains in this region [21].

climb are also possible at these temperatures which are required for recovery of the dislocation substructure within the bulge. Thus any process that impedes recovery or grain boundary motion is likely to inhibit the formation of SIBM nuclei.

1.5.2.2 Rotational Recrystallisation–RDRX

Rotational (dynamic) recrystallisation (RDRX) is another recrystallisation mechanism proposed in magnesium alloys which also produces a ‘necklace’ type microstructure around grain boundaries, Figure 1.16 [105]. In this mechanism, shown schematically in Figure 1.18, shear strain is concentrated at grain or twin[125] boundaries due to the build up of dislocations in these regions causing locally high incompatibility stresses. Dynamic recovery of these dislocations forms a subgrain structure next to the grain boundary, Figure 1.18b). With continued straining dislocations are dynamically added to these low angle boundaries eventually rotating them into high angle boundaries, Figure 1.18c). Such rotations are also suggested to be facilitated by grain boundary sliding of both high and low angle boundaries during continued straining[126–128]. In many respects RDRX is a pseudo recovery process as it only requires continued strain and recovery of dislocations rather than migration of high angle boundaries typically observed in other recrystallisation processes. As a result RDRX nuclei are usually small and contain small internal misorientations as the nuclei grow slowly and contain dislocations which are dynamically recovering to the subgrain boundary.

Dynamic recovery and the formation of a 3D subgrain structure requires the activation of non-basal slip and/or cross-slip mechanisms. These processes are believed to be active near grain boundaries because the stress concentration at the boundaries locally exceeds the CRSS for non-basal slip and cross slip[105]. Despite stress concentrations locally raising shear stress at boundaries RDRX only operates at moderate-high temperatures (typically $\approx 473\text{--}623\text{K}$ [105, 122, 123]) where the CRSSs for non-basal slip and cross-slip are low enough for these systems to be active. Climb of basal dislocations, activated at higher temperatures, also aids subgrain formation contributing to the increased activity of RDRX. At these high temperatures RDRX competes with SIBM, where both mechanisms are reported in the vicinity of grain boundary serrations[129]. In general SIBM is thought to be more favourable at the highest temperatures ($> 573\text{K}$ [123]) due to the increased mobility of high angle boundaries. The two processes are significantly different; RDRX is a one step continuous process without discrete nucleation and growth steps, so it is often referred to a continuous recrystallisation mechanism[105, 123, 129]. SIBM has discrete nucleation and growth steps and is described as a discontinuous recrystallisation process.

RDRX nuclei have orientations based upon rotations of the parent grain, continued dynamic recovery increases the misorientation of RDRX grains, in other words rotating the nucleus away from the parent orientation. The magnitude and direction of RDRX rotation is likely to depend upon the applied strain and dominant slip system. Larger strains will generate larger rotations with each slip system having a characteristic rotation. The temperature and strain rate will also determine the activity of each slip system as discussed

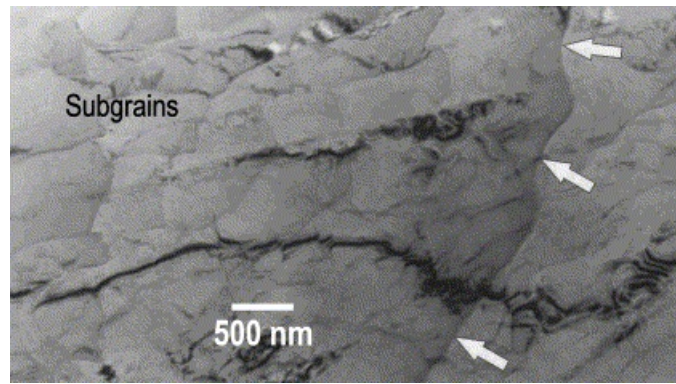


Figure 1.17: TEM image showing the bulging of a grain boundary during straining of a magnesium alloy as a result of high localised shear stress in grain boundary regions caused by dislocation pile up. This bulging and substructure development at grain boundaries is typical of SIBM and RDRX. The dense subgrain structure surrounding the grain boundary becomes more diffuse moving further from the boundary into the grain[129].

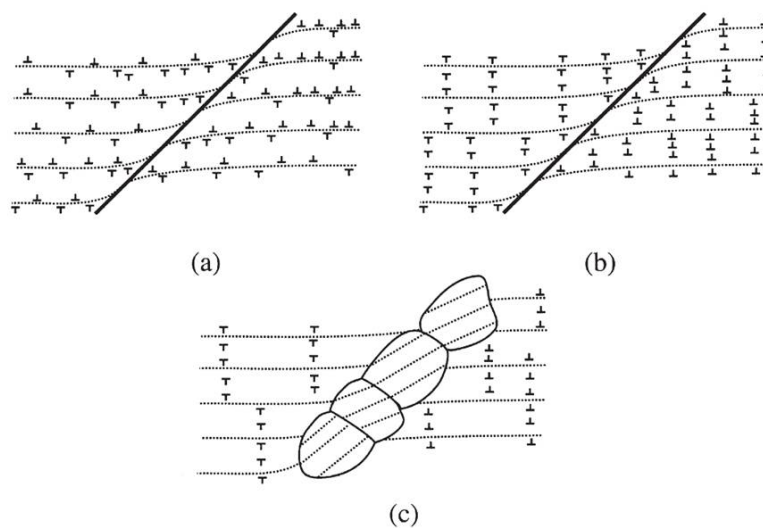


Figure 1.18: Figure showing the rotational or CDRX mechanism of recrystallisation in magnesium. a) Local shearing occurs at grain boundaries due to stress concentration in these regions. b) Dynamic recovery then occurs around these boundaries forming subgrain structures. c) Continued straining and dynamic recovery in these regions forms grains on the boundary[21].

in Section 1.3.1. In practice, where orientations of RDRX nuclei have been observed in magnesium they are found to be close to that of the parent grain [130].

The relative activity of basal and non-basal slip are also reported to affect the morphology of RDRX grains[131]. High basal slip activity is expected to generate rectangular lamellar of low angle boundaries on basal planes. Recovery of these lamellar into subgrains by a small number of non-basal dislocations forms rectangular RDRX nuclei. Likewise if the activity of basal and non-basal slip are similar RDRX nuclei are expected to be more uniform in shape as dislocations are more evenly distributed between the slip planes[128].

1.5.2.3 Twin Induced Dynamic Recrystallisation–TDRX

As well as grain boundaries deformation twins, particularly contraction and double twins[98, 132], nucleate recrystallised grains. Contraction and double twinning have two significant effects, rotation of the matrix into a softer orientation for basal slip (see Section 1.3.3) and generation of twin boundaries which obstruct dislocations. These effects make twins ideal RX sites because basal dislocations are quickly generated within the twin, due to a low Schmid factor for basal slip, and these dislocations are quickly impeded by twin boundaries. The resultant build up of stored energy within the twin is greater than the surrounding matrix, concentrating recrystallisation within the twin. Recovery may then lead to the development of a subgrain structure consisting of high and low angle boundaries developing within the twin, Figure 1.19 [124, 125, 132–134]. Although common in contraction twins, recrystallisation within tension twins is not often observed because the matrix within these twins is frequently poorly oriented for basal slip. This prevents stored energy required for recrystallisation building up and so DRX is less active in tension twins[135].

This mechanism requires the development of a subgrain structure within the twin which requires the activation of non-basal slip systems[95, 132]. Despite this TDRX is frequently reported at low deformation temperatures in magnesium ($T < 473\text{K}$) where non-basal slip activity is low but twinning activity is very high[105, 122, 123, 132]. The activity of non-basal slip at these temperatures is considered to be increased within twins due to areas of stress concentration at twin boundaries[123, 132, 133]. As a result of the recovery required to form a subgrain structure needed for this TDRX mechanism it is referred to as a continuous recrystallisation mechanism[122, 132, 136], like the RDRX mechanism. In particular a recent single crystal study by Molodov *et.al* [132] has shown significant activity of prismatic slip within compression twins, which is proposed to account for texture weakening in TDRX grains by such a CDRX mechanism.

At lower temperatures where the CRSS for non-basal slip is too high for significant recovery, even within twins, an alternative discontinuous TDRX mechanism has been proposed. Where TDRX nuclei form at the intersections of twins and subsequently grow into the deformed matrix. Twin intersections may form by two mechanisms shown in Figure 1.20. The secondary twin may nucleate externally and intersect the primary twin, or the secondary twin may nucleate within the primary twin. In both cases a TDRX nucleus forms bounded by high angle boundaries which may grow into surrounding deformed material[122, 125, 134]. However, the low temperatures at which this mechanism operates and the low mobility of many twin boundaries prevent this discontinuous TRDX mechanism from being considered a significant source of DRX grains in magnesium.

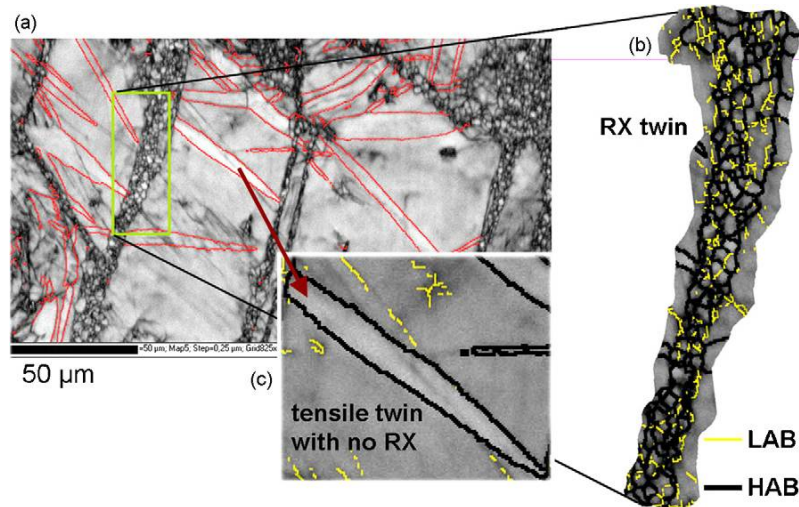


Figure 1.19: Figure showing a) an EBSD map in which TDRX is observed, b) high and low angle boundaries develop within a contraction twin. c) tension twin where no TDRX is observed, some of these tension twins are believed to form during unloading[124].

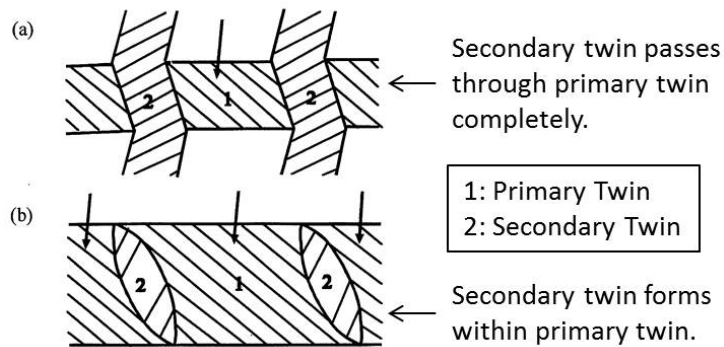


Figure 1.20: Figure showing a schematic diagram of two mechanisms of TDRX nuclei formation by twin intersection. a) in which a secondary twin completely intersects a primary twin and b) where a secondary twin nucleates within a primary twin.

Twins have a fixed orientation relationship with the parent matrix and TDRX grains might be expected to share this relationship, nucleating grains with similar orientations to the parent twin. This is likely to be particularly true for nuclei developed from the discontinuous TRDX mechanism described above, Al-Samman *et.al* have also shown that characteristic twin orientations are retained even where the continuous TRDX mechanism is operational in single crystal experiments[136]. In particular the basal planes in these continuous TRDX grains have the same orientation as the parent twin which is likely to only slightly weaken the macrotexture during recrystallisation. The situation is more complicated in polycrystalline material however, where many authors find TDRX grains with significantly different orientations to the parent twin [98, 124, 134]. Nevertheless even in polycrystalline material, there are examples where characteristic twin boundaries and orientations are maintained in recrystallised grains[135–137]. In either case, TDRX

typically nucleates non-basal textures as the contraction and double twins which recrystallise usually do not have ‘basal’ orientations. In summary recrystallisation is widely reported to nucleate within deformation twins, weakening strong basal deformation textures. TDRX is most active at lower temperatures ($T \approx 473\text{K}$) where twinning is active and significant recovery within twins is possible.

1.5.2.4 Shear Band Nucleation

As discussed in Section 1.3.4 shear bands are regions of high localised strain, nucleated by both twinning and DRX. The high stored energy of shear bands makes them ideal sites for recrystallisation which together with their frequency means that shear band nucleation is a very active recrystallisation mechanism in deformed magnesium [96, 101, 121, 138]. The orientations nucleated by shear bands are complex. In cubic materials shear bands are thought to contain crystallites with a variety of orientations which are typically reported to nucleate weak textures [100], although some of the strong recrystallisation textures, such as the Goss component in certain steels, are also found to nucleate in shear bands [100]. In magnesium grains nucleated within shear bands are thought to have similar orientations to the matrix within the shear band, although measurement of shear band textures is difficult due to the heavy deformation within the band. Barnett *et.al* observe DRX grains which nucleate within shear bands during extrusion have similar orientations to the deformation textures predicted by crystal plasticity modelling of shear band formation [121]. In these simulations, basal slip is expected to be the dominant deformation mode in magnesium, aligning the basal plane parallel to the plane of the shear band. As a result, shear band nuclei are often found to have basal planes parallel to the shear band during both extrusion [96, 121] and rolling [99, 101]. Indeed shear band nucleation during rolling is thought to contribute to the RD split basal texture in Figure 1.12, as during rolling shear bands are oriented $18\text{-}35^\circ$ to the RD [99], which would nucleate the RD texture split if recrystallised grains nucleate within the shear bands with their basal planes parallel to the band. Clearly to be active, shear band nucleation requires the presence of shear bands in the microstructure. This restricts shear band nucleation to material deformed at high strain rates and/or high strains. As shear bands form under most commercial deformation conditions, they are a significant recrystallisation site in magnesium.

1.5.2.5 Particle Stimulated Nucleation–PSN

Localisation of deformation in the matrix can also occur as a result of the presence of particles which are stiffer than the matrix; these particles concentrate deformation by failing to shear with the matrix creating a deformation zone around the particle. Recovery within

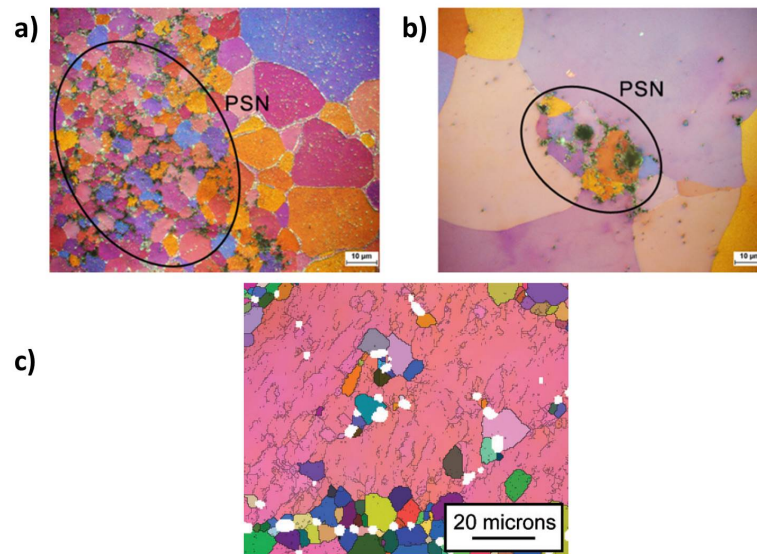


Figure 1.21: a,b) Optical micrographs showing PSN within rolled magnesium sheet [141].
c) An EBSD map in Euler colouring of PSN grains nucleating within a deformed grain in extruded magnesium WE43[142].

the deformation zone leads to development of a subgrain structure of low angle boundaries which gradually grow into high angle boundaries enclosing the PSN nucleus[139, 140]. In cubic materials strain concentration around particles is often greater than other points in the matrix allowing recrystallisation by PSN to dominate recrystallisation textures. In these systems the size and distribution of recrystallised grains is a function of particle size and distribution[21]. PSN nuclei are widely considered to have random orientations generated by the high levels of misorientation (up to 45° [140]) within the deformation zone from which the nuclei grow. Extensive PSN in cubic materials is thus reported to weaken textures by generating recrystallised grains with random orientations. In magnesium alloys while PSN is observed to occur[141–143], Figure 1.21, it is not reported to dominate recrystallisation because of strong competition from other recrystallisation mechanisms[144]. The other recrystallisation mechanisms are more competitive in magnesium because significant strain localisation occurs at various other recrystallisation features, such as grain boundaries, twins and shear bands. These regions prove to be more potent nucleation sites for recrystallisation than particles meaning that while PSN does occur, any grains nucleated by this mechanism make a relatively small contribution to the overall recrystallised texture.

1.5.3 Factors Affecting DRX Behaviour

All of the recrystallisation mechanisms above require the presence of particular deformation features such as twins, grain boundary serrations and shear bands. Deformation conditions are therefore very significant in determining the dominant recrystallisation

mechanism. Broadly speaking, DRX in magnesium is described in three temperature regimes; low temperatures ($< 473\text{K}$), intermediate temperatures ($\approx 473\text{-}623\text{K}$) and high temperatures ($> 623\text{K}$)[105, 122, 123]. A schematic DRX mechanism map is presented in Figure 1.22, it should be emphasised that this is a schematic only and exact operational DRX mechanisms under given conditions are subject to considerable debate Figure 1.22 is merely intended to outline general trends. In the low temperature regime twinning is very active during deformation because non-basal slip is largely inactive. The large twin volume fraction means a large number of TRDX locations are available promoting TDRX activity. At high strains, shear bands form and due to their high stored energy become more favourable DRX sites. At higher temperatures in the intermediate temperature range non-basal slip and cross slip are thought to become active, particularly at grain boundaries, this reduces twin volume fraction and facilitates RDRX. At higher strains (where grain boundary serrations are more common) increased recovery also promotes SIBM. Even at these intermediate temperatures shear bands form at high strains becoming the favourable DRX sites. In the high temperature regime more extensive non-basal slip, cross slip and even dislocation climb are active allowing more extensive recovery. The high temperatures also allow grain boundary serrations to form more easily which combined with high recovery around grain boundaries activates extensive SIBM. Again shear band formation may be possible at very high strains or strain rates, nucleating further DRX.

Increasing deformation temperature and changing DRX mechanism also has a significant impact on the magnesium flow stress curve. Figure 1.23 shows the flow stress curve for magnesium in tension over a various temperatures[122]. The work hardening and subsequent softening before a steady state flow stress is achieved is characteristic of DRX during deformation[21]. The steady state flow stress is a complex balance between hardening caused by dislocation accumulation and softening due to DRX. As a result the flow stress curve is sensitive to temperature as it affects both slip system activity and which DRX mechanism is operational. Strain rate ($\dot{\epsilon}$) is also critically important in influencing both the flow stress curves and dominant DRX mechanism, although little work has examined the effect of changing strain rate on active DRX mechanism in magnesium.

1.5.4 Recrystallisation Textures

Regardless of which mechanism is operational the desired goal is weakening the strong basal texture typical of rolled magnesium. All of the mechanisms described above are expected to nucleate orientations that are slightly different to the basal orientation of deformed parent grain. We now consider the magnitude of the texture weakening during recrystallisation in magnesium.

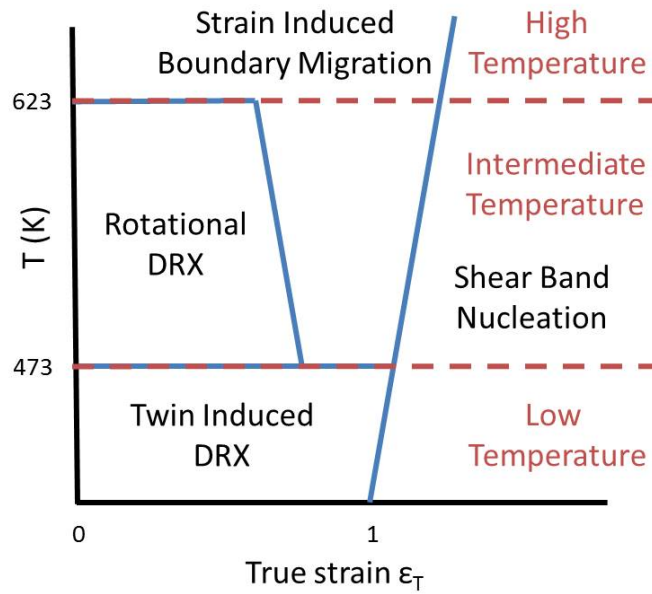


Figure 1.22: Schematic illustration of the relationship between dominant DRX mechanism temperature and strain. The three DRX temperature regimes are highlighted in red. This figure, loosely based on [122, 123], is intended as a **schematic only** to aid discussion, with all indicated temperatures and strains approximate.

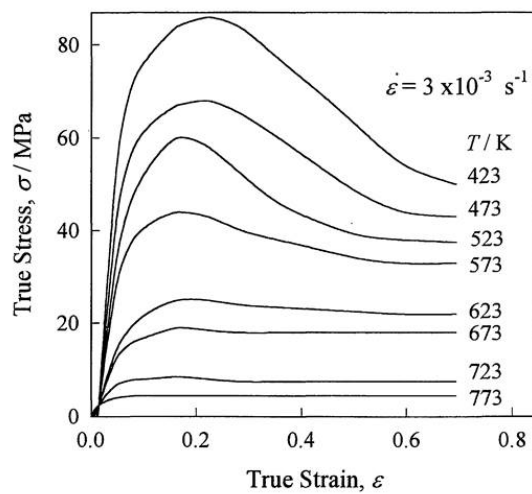


Figure 1.23: Figure showing the flow stress curves for pure magnesium over a wide temperature range. The steady state flow stress characteristic of DRX is clearly observed at temperatures above 473K [122].

1.5.4.1 {0001} Basal Textures

Recrystallisation in magnesium occurs both dynamically during deformation and statically post deformation. Fully recrystallised material that has undergone both SRX and DRX is made up of recrystallised grains that have nucleated and grown under both regimes. The ratio of SRX grains:DRX grains in the fully recrystallised material is a function of deformation temperature, strain and strain rate. The recrystallisation mechanisms are similar in both regimes with the most active mechanisms, such as RDRX and SIBM, nucleating grains which have orientations close to the parent orientation. Resultantly the {0001} basal texture morphology of deformed magnesium does not significantly change during recrystallisation. However, the basal texture intensity does weaken as large numbers of grains with slightly non basal orientations grow[145–148].

Figure 1.24a) plots basal texture intensity of AZ31 sheet rolled at 150°C (blue) and 225°C (red) in the as rolled condition and after annealing for 1hr at a range of temperatures. Both curves show a fall in texture intensity during annealing, by up to 1.6 MRD (multiples of a random distribution) after rolling at 150°C and annealing at 250°C [147]. Figures 1.24b-d) demonstrate that despite the fall in texture intensity the basal texture morphology of the deformed sheet is retained. Texture weakening is due to the consumption of deformed grains (which have strong basal orientations) by recrystallised grains nucleated by the mechanisms described in Section 1.5.2 (which have less strong basal orientations). The texture intensity weakens less in the material rolled at the higher temperature of 225°C because at this temperature more DRX occurs during rolling. Although DRX does nucleate grains with weak basal textures many of these grains are deformed during continued processing. Once deformed, the DRX grains are rotated back into a basal orientation negating the texture weakening effect of DRX[147]. Even where texture weakening is observed after recrystallisation it is often a very small effect. At typical magnesium processing temperatures > 400°C DRX is extensive and in fact the texture is often observed to strengthen during annealing as a result of grain growth[149]. Indeed the effect of grain growth on strengthening basal textures is also shown in 1.24a); where the larger grain sizes and stronger textures are reported after annealing at higher temperatures. Basal textures appear to grow preferentially during this process slightly strengthening the deformation texture[147, 150], however grain growth is found to have an even more significant effect on the orientation and alignment of prismatic planes discussed in the next section.

1.5.4.2 Grain Rotation During Recrystallisation and Grain Growth

Grain growth during and after recrystallisation is associated with a rotation of the prismatic planes by 30° about the <0001> axis. This phenomenon not only occurs in magnesium

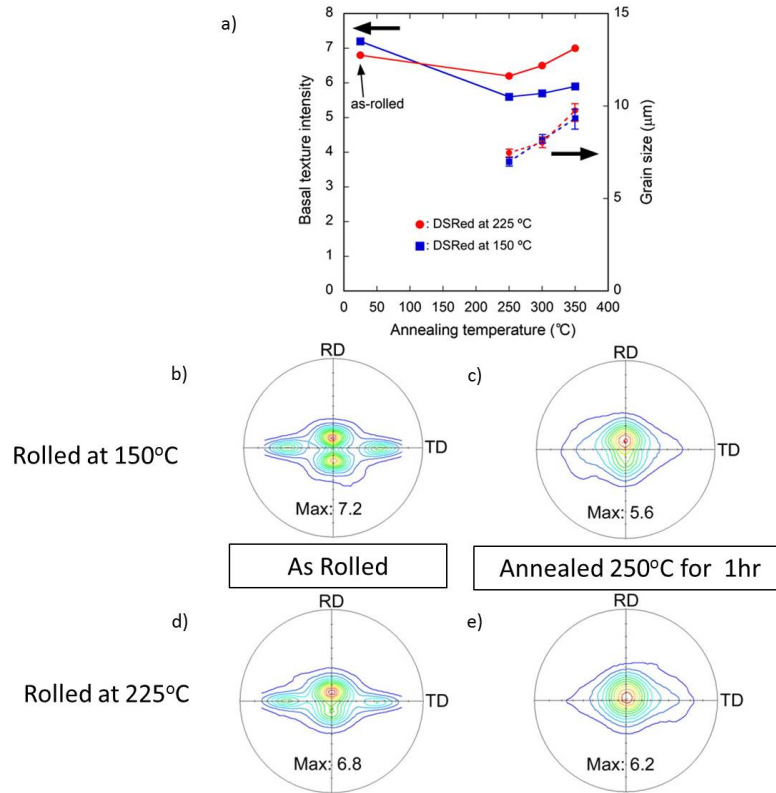


Figure 1.24: a) Basal texture intensity (solid lines) and grain size (dashed lines) as a function of annealing temperature after annealing for 1hr of AZ31 warm rolled at 150 $^{\circ}\text{C}$ (blue) and 225 $^{\circ}\text{C}$ (red). Basal pole figures for the material in the as rolled b,d) condition and after annealed for 1hr at 250 $^{\circ}\text{C}$ c,e). Adapted from [147].

but is also common in many h.c.p metals [151–154]. Figure 1.25 shows the textures of an extruded magnesium alloy recrystallised at 400 $^{\circ}\text{C}$. Figure 1.25a) shows the as extruded material has a fibre texture component with the $\langle 10\bar{1}0 \rangle \parallel \text{ED}$. After recrystallisation the grain orientations have rotated by 30 $^{\circ}$ giving a fibre texture $\langle 11\bar{2}0 \rangle \parallel \text{ED}$, Figure 1.25b). This rotation has not affected the orientation of the basal planes which remain at 90 $^{\circ}$ to the ED before and after annealing. The rotation is considered to be partly due to the activity of prismatic slip during deformation; During extrusion only the $\langle 10\bar{1}0 \rangle$ and $\langle 11\bar{2}0 \rangle \parallel \text{ED}$ fibre orientations are stable. This is shown in Figure 1.26, where the angle (ϕ) between the compression direction and $[10\bar{1}0]$ direction is defined Figure 1.26 a) and the corresponding Schmid factor for basal slip on the three prismatic slip planes is plotted for various angles Figure 1.26 b). Slip will occur on the plane with the highest Schmid factor and Figure 1.26b) shows there are three cases where two prismatic slip planes have equivalent Schmid factors, $\phi = -30, 0, +30^{\circ}$. These orientations are stable because two prismatic slip systems operate in opposite directions cancelling each other out Figure 1.26c). For $0 < |\phi| < 30$ slip on one prismatic plane will be active rotating the crystal about the $[0001]$ axis to a stable position at $\pm 30^{\circ}$ with the $\langle 11\bar{2}0 \rangle \parallel \text{compression direction}$ (in extrusion this corresponds to $\langle 10\bar{1}0 \rangle \parallel \text{ED}$). So while $\phi = 0^{\circ}$ is a stable orientation it is not possible

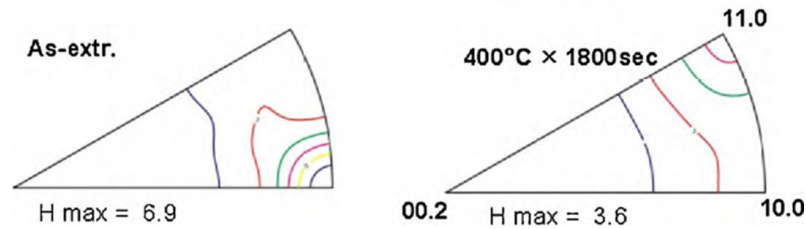


Figure 1.25: Figure showing extrusion textures for magnesium AZ31 a) as extruded and b) annealed for 1800s at 400°C. The as extruded texture is dominated by a $\langle 10\bar{1}0 \rangle$ fiber which is consumed by a $\langle 11\bar{2}0 \rangle$ component which grows during recrystallisation[151].

for a $\phi \neq 0^\circ$ orientation to rotate towards it by prismatic slip alone [155]. As a result during extrusion, the deformation texture is dominated by the $\langle 10\bar{1}0 \rangle \parallel$ ED component however some $\langle 11\bar{2}0 \rangle \parallel$ ED ($\phi = 0^\circ$) orientations are preserved. At the early stages of recrystallisation both orientations are found to nucleate recrystallised grains however the $\langle 11\bar{2}0 \rangle \parallel$ ED orientations have been found to have a growth advantage, growing larger and faster than the $\langle 10\bar{1}0 \rangle \parallel$ ED recrystallised grains [151]. The cause of this advantage is still not completely understood. The higher boundary mobility of the $\langle 11\bar{2}0 \rangle \parallel$ ED orientations, which have the maximum possible misorientation relative the deformed microstructure and has a $\langle 10\bar{1}0 \rangle \parallel$ ED orientation may be a significant contributory factor. As a result of the higher boundary mobility the $\langle 11\bar{2}0 \rangle \parallel$ ED grains grow fast causing a rotation of 30° in the final recrystallisation texture because they recrystallise before the $\langle 10\bar{1}0 \rangle \parallel$ ED grains. The rotation of the deformation texture by 30° during grain growth is also observed in rolled material[147, 152–154].

1.5.5 Summary Of Recrystallisation

In summary there are a range of active recrystallisation mechanisms operational in magnesium. The activity of each mechanism is strongly dependent on the deformation conditions which control not only the number of possible nucleation sites for each mechanism eg twins or shear bands, but also the extent of non-basal slip, which is required to varying extents by each mechanism. Regardless of the dominant mechanism recrystallisation of magnesium is not associated with a significant drop in basal texture intensity needed to improve formability. Slight texture weakening is possible if recrystallisation occurs statically as weak basal orientations consume deformed grains with strong basal orientations. However, under processing conditions where DRX is extensive DRX grains with the weakest basal orientations are deformed into more basal orientations during processing reducing the texture weakening effect. Combined with the strengthening of basal textures during grain growth recrystallisation does not significantly improve the formability of magnesium alloys.

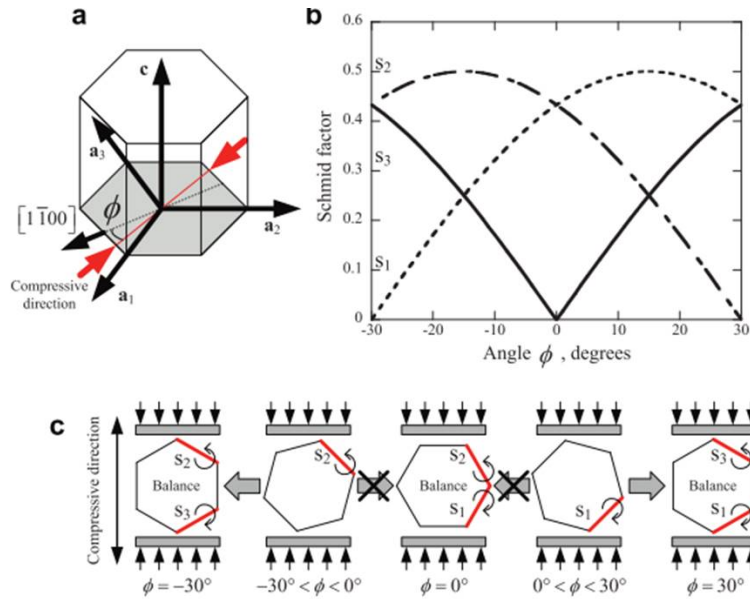


Figure 1.26: Figure showing stable and unstable orientations of hcp crystals during rolling. a) Defines the angle ϕ relative to the compressive direction and the $[1\bar{1}00]$ direction. b) Plots the Schmid factor as a function of ϕ between -30° and 30° , showing there are three stable ϕ values. c) Shows schematically the three stable orientations of the hcp crystal during rolling and indicates the direction of rotation when the crystal is in each orientation [155].

1.6 Magnesium Rare Earth (RE) Alloys

RE elements added to magnesium typically include La, Ce, Nd, Eu, Gd, Yb and Y. Initially magnesium was alloyed with RE elements to provide solid solution strengthening and creep resistance [7, 156]. Weak textures and reduced yield anisotropy of RE alloys were first reported by Ball and Prangnell [157], subsequent investigations have shown significant improvements in ductility also occur with RE addition [141, 158, 159]. Figure 1.27 shows flow stress curves for a series of magnesium-Gd alloys, where ductility increases from 0.06 to 0.26 engineering strain as Gd concentration is increased [114]. The improvements in ductility are accompanied by reduced yield anisotropy, which is nearly eliminated in many RE alloys [25, 158, 160].

Improvements in sheet formability are observed in variety of magnesium-RE alloys [111, 161, 162], in particular the ZEK100 system [111, 162] where the addition of $\approx 0.04\text{at}\%$ Nd raises the FLC, by ≈ 0.2 true strain, giving it a similar formability to Al 6016 [110]. The improved formability is primarily attributed to the significantly weaker texture in the RE alloy [141, 158, 159]. Weaker textures mean a larger spread of grain orientations and so a greater number of grains favourably oriented for basal slip when the material is strained in an arbitrary direction, increasing formability. RE addition is also associated

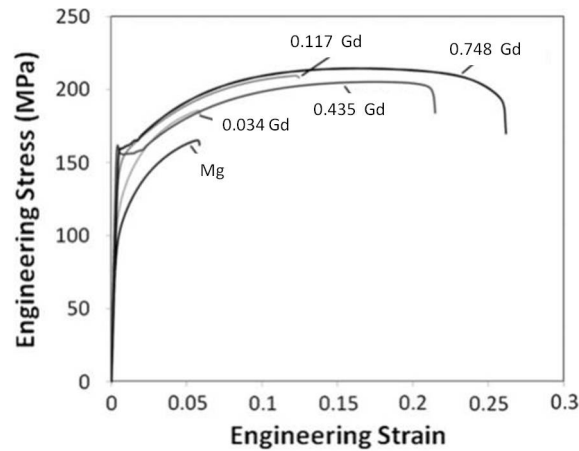


Figure 1.27: Flow stress curves for a series of grain size normalised magnesium-X at% Gd alloys in tension along the rolling direction (RD)[114]. The flow stress curves correspond to the material textures in Figure 1.28a). Increasing Gd concentration increases ductility as a result of weakening textures.

with increased non-basal slip (Section 1.8) which also contributes to improved ductility, but weak textures are considered to be more significant.

1.6.1 The Rare Earth Texture

Examples of typical rolling and extrusion textures of binary magnesium-Gd alloys are shown in Figure 1.28 (see also flow stress curves shown in Figure 1.27). Increasing the concentration of Gd from 0-0.748 at% changes both texture intensity and morphology; Peak texture intensity falls from 11.6 to 2.6 mrd, the strong basal texture spreads slightly in the TD and splits into two lobes in the RD[114, 149, 158]. The RD split of the basal texture is also observed in non-RE magnesium alloys, see Figure 1.12 and Figure 1.29a), and so is not regarded as an exclusive RE effect[25, 83, 138, 158]. The fall in texture intensity and TD spreading of basal poles are however considered unique RE effects[141, 149, 158]. Extrusion textures of pure magnesium and magnesium-0.243 at%Gd are also given in Figure 1.28 b). There is a weakening of peak texture intensity and a characteristic RE texture component is generated with the $\langle 11\bar{2}1 \rangle$ directions parallel to the extrusion direction[96, 159, 163, 164]. All of these wrought textures are very sensitive to tertiary alloying additions[158, 164, 165] and deformation conditions, including temperature and strain rate[166].

In tertiary magnesium-X-RE systems (X=Mn[164] or Zn[158, 165]) the texture intensity is not sensitive to non-RE alloying element concentration[167] but texture is often different to the binary magnesium-RE case described by Figure 1.28. The effects are most striking during the rolling of magnesium-zinc-RE (ZEK) alloys as seen in Figure 1.29, in which the rolled texture of a magnesium 0.374 at% Zn 0.052 at% Ce alloy is split into two lobes

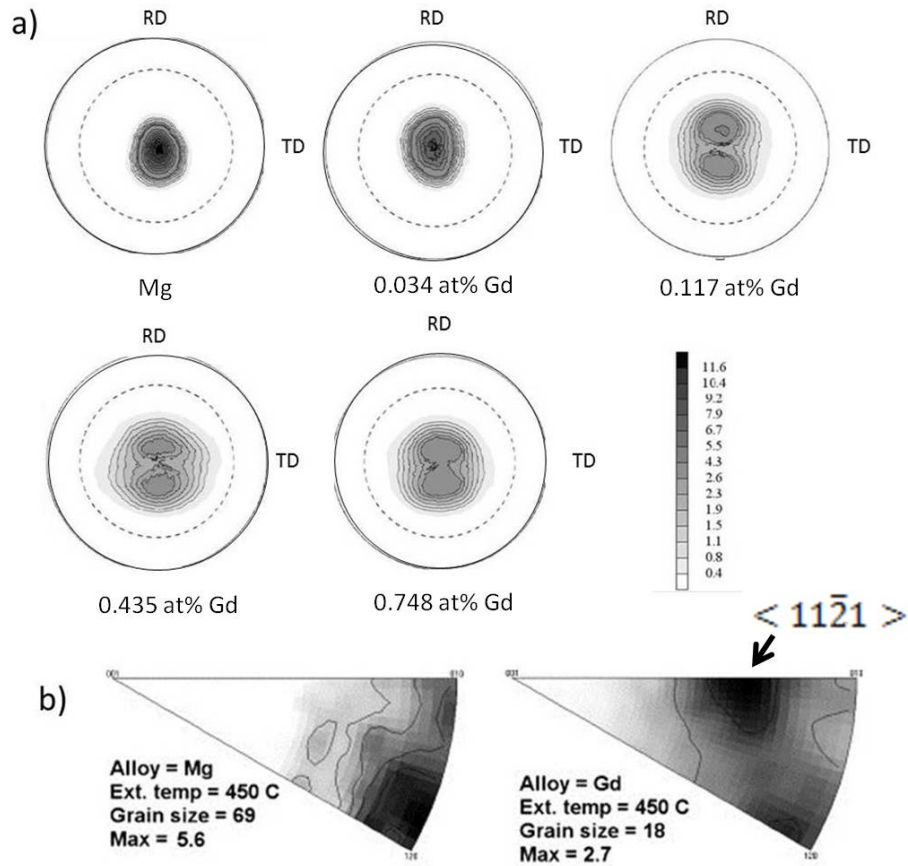


Figure 1.28: a) $\{0001\}$ basal pole figures of rolled magnesium-Gd alloys, showing the weakening of the basal texture as Gd concentration increases. In each case the material is fully recrystallised with normalised grain sizes of $\approx 10\mu\text{m}$ [114]. b) ED (extrusion direction) inverse pole figures comparing extrusion textures of pure magnesium and magnesium-0.243 at%Gd, showing the unique RE extrusion texture component $\langle 11\bar{2}1 \rangle$ directions parallel to ED [96].

in the TD[165], the basal texture intensity is also lower in tertiary alloys in comparison to their binary counterparts[168]. A similar spreading of the rolled texture in the TD is reported in a variety of ZEK alloys including those containing Ce, La, Nd or Gd [141, 168]. Much of the literature focuses on explaining the RE texture weakening effects in binary magnesium-RE alloys and it remains unclear how closely related the texture weakening effects in tertiary alloys are.

Ca additions as low as 0.545 at% have also been reported to reduce the basal texture intensity in binary[169] and tertiary alloys[170]. However, in these systems the reduced basal texture intensity is not always associated with improvements in formability[169–171]. In the magnesium-Ca alloys texture weakening has widely been associated with increased contraction and double twinning behaviour during deformation[170, 171] and importantly, unlike RE alloys where the RE textures only form during recrystallisation (as discussed in Section 1.6.3), the RE textures are observed in the deformation textures of

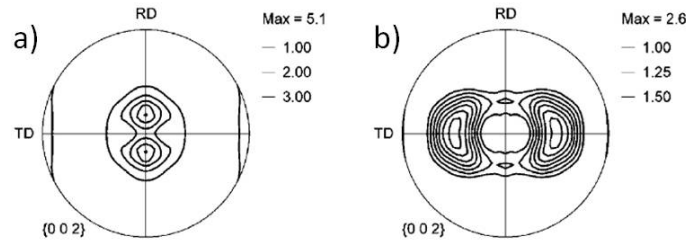


Figure 1.29: Basal, $\{0001\}$, pole figures for a) rolled magnesium 0.374 at% Zn and b) rolled magnesium 0.374 at% Zn 0.052 at% Ce alloy[165]. The TD split of the basal texture is characteristic of magnesium-RE-Zn alloys.

magnesium-Ca alloys. This suggests that texture weakening due to RE and Ca additions may be two different effects, as the goal of this research is the production of more formable magnesium alloys, in addition to those with low texture intensities, the focus of this review is on RE alloying additions.

Wrought magnesium textures are not only sensitive to alloy chemistries but also deformation conditions. For example, RE textures can be deactivated during extrusion at high temperatures ($> 500^{\circ}\text{C}$) restoring typical magnesium basal textures. The TD split in ZEK alloys can also be deactivated in some cases producing a more typical RD split of the basal texture[150, 158]. Texture weakening can even be activated in non-RE alloys in certain deformation conditions; AZ31 produces unusually weak recrystallisation textures during SRX if DRX is significantly suppressed[145, 148, 160], see Section 1.5.4.1. The weak textures in non-RE alloys are best described as weak basal textures which do not show a significant change in texture morphology in comparison to deformation textures. So while the RE textures formed in magnesium-X-RE tertiary alloys are clearly a unique RE effect, owing to the characteristic TD split of the basal texture in these alloys, the situation is less clear in the binary RE case. A TD spread in textures of rolled binary alloys is often difficult to distinguish and the textures often appear of a weak basal type like the non-RE cases described above, although the magnitude of texture weakening is typically much larger in RE alloys. So there is lack of clarity in the term ‘RE texture’; in some cases it refers to a distinct texture morphology, such as the TD split in ZEK100 or the $\langle 11\bar{2}1 \rangle$ directions parallel to ED in extrusions, while in other cases it simply refers to a significant weakening of the basal texture. Similarly the extent to which the mechanism causing texture weakening in non-RE alloys is related to the RE texture weakening is also poorly understood.

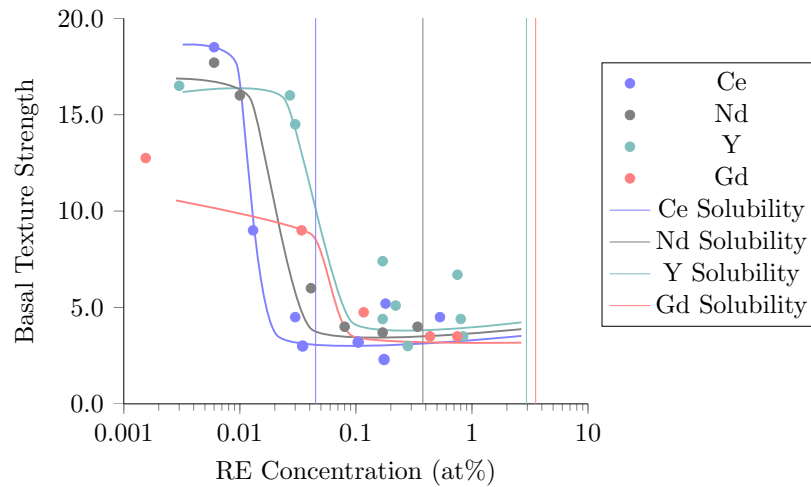


Figure 1.30: Figure showing peak basal texture intensity against RE concentration, after rolling and recrystallisation, for a number of magnesium-RE binary systems. The vertical lines indicate the maximum solubilities of each element in magnesium and the curves, to guide the eye, show the transition between textures occurs at a critical RE concentration for each RE element. The critical concentration appears to scale with solubility of each element in magnesium. Plot after Hantzsche *et.al.*[149] includes data from [95, 114, 149, 165], solubilities are measured at 525°C[172].

1.6.2 The Critical Concentration of Rare Earth

RE textures and improved ductilities are only activated once a critical threshold concentration of RE has been exceeded [95, 114, 149, 163, 165]. Figures 1.27 and 1.28a) clearly show the increase in ductility and a fall in texture intensity occur once Gd concentration exceeds 0.117 at% [114]. A similar relationship has been found in a variety of magnesium-RE binary alloy sheet and extrusions as demonstrated in Figure 1.30. Hantzsche *et.al.*[149] observed that the critical concentration appears to be dependent on the solubility of each RE in magnesium, the critical concentration rising with the solubility of RE. The solubilities of the RE elements at 525 °C are plotted as a function of atomic size mismatch in Figure 1.31, giving an indication of the potency of each RE element.

Figure 1.30 also reveals the very low concentrations of RE needed to activate a fall in texture intensity, in the case of Ce only around 0.01at% Ce is required i.e 1 atom in 10,000. In all cases the critical concentration is below the solubility limit of the RE in magnesium, meaning particles are not essential to activate this effect [95, 149, 163]. We make the assumption that the relative solubilities of each RE are similar at the typical processing temperature of 400°C (solubilities calculated for 525°C Figure 1.31) and that the RE's are still in solution at these temperatures, an assumption supported by thermodynamic calculations [95, 173].

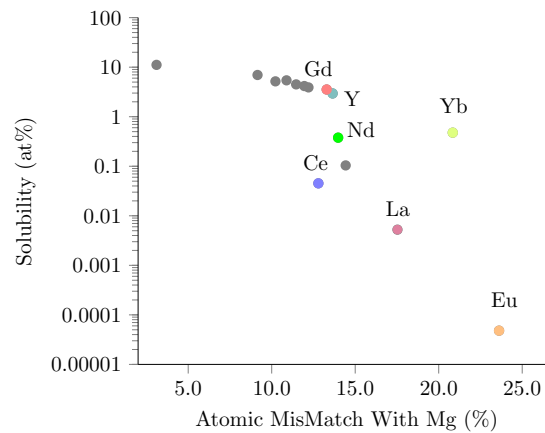


Figure 1.31: Plot of the solubility of each RE element in magnesium at 525°C as a function of atomic mismatch with magnesium[172]. Hatzsche *et.al* propose that lower solubility RE elements are the most potent, requiring the lowest solute additions to activate RE effects, in theory making Eu the most effective RE addition[149].

Continued addition of RE above the critical concentration has very little effect on texture intensity[114, 149, 163], Figure 1.30. Despite this, Figure 1.27 shows the ductility increases considerably from 0.13 to 0.26 engineering strain with continued RE addition[114]. This suggests improvements in mechanical properties in RE alloys are not solely due to weaker textures, the effect of RE additions on deformation mechanisms is discussed in Section 1.8.

As the RE textures above are measured from fully recrystallised material, there are two possibilities for RE texture formation; RE additions change the deformation texture from which the recrystallisation texture grows or RE elements change the recrystallisation mechanism which forms the RE texture.

1.6.3 Rare Earth Texture Deformation or Recrystallisation Effect?

The deformation textures of non-RE magnesium 0.371 at% Zn and magnesium 0.442 at% Zn 0.179 at% Ce after rolling at 150°C are shown in Figure 1.32. During rolling both alloys develop basal textures typical of rolled magnesium with the basal poles parallel to the ND and split slightly in the RD. The RE texture only appears in the RE alloy after annealing for 15 minutes at 400°C where the texture weakens and splits in the TD. In the non-RE alloy the basal texture strengthens during annealing. This example shows the deformation behaviour of the RE alloy is very similar to that of a non-RE alloy[3] and the deviation in texture between the RE and non-RE alloys only emerges during recrystallisation [138, 167].

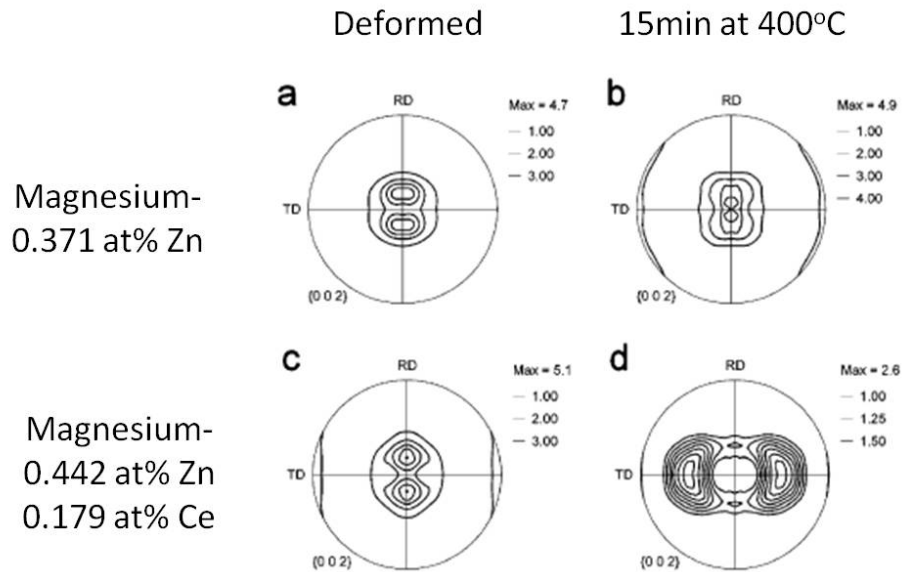


Figure 1.32: $\{0001\}$ pole figures showing the a,c) as-rolled 150° and b,d) annealed textures for 15 min at 400°C of a,b) magnesium 0.371 at% Zn and c,d) magnesium 0.442 at% Zn 0.179 at% Ce. Showing that the rare earth texture only forms during recrystallisation[138].

1.7 Recrystallisation of Rare Earth Alloys

As discussed recrystallisation can occur statically or dynamically and weak RE orientations have been observed to nucleate and grow in both regimes; RE textures are observed in extrusions where DRX dominates [96, 163, 164, 174] (Figure 1.28b)) and after warm, or even cold rolling followed by annealing, where SRX is dominant[95, 114, 149], Figure 1.32a). EBSD analysis of partially DRX material has found that DRX nuclei have weak basal orientations in both non-RE [175, 176] and RE [160, 175, 176] alloys. This is shown in Figure 1.33 where the orientations of DRX nuclei are found to be distributed about the orientation of the parent grain. Further analysis of such EBSD data shows the unique RE texture components such as the $\langle 11\bar{2}1 \rangle$ directions parallel to ED are isolated only in the large DRX grains in RE alloys[160, 164], Figure 1.34. This segregation is not present in non-RE alloys where the orientations of DRX grains are the same regardless of grain size. This suggests that RE orientations preferentially nucleate and grow by a different mechanism to that observed in non-RE alloys where no DRX orientation appears to be favoured. This also suggests that the texture weakening, which is sometimes observed in non-RE alloys, is caused by a different mechanism to the RE effects.

Under typical deformation conditions, where significant DRX occurs, the DRX grains with most non-basal orientations are expected to preferentially deform during processing due to a high Schmid factor for basal slip. These grains are rotated into a more basal orientation as a result of the deformation. This strengthens the texture and leads to the

dominance of basal orientations during subsequent recrystallisation and grain growth, as DRX grains with basal orientations do not deform during DRX and therefore have low stored energy favouring their continued growth[147, 149]. In conditions where DRX is retarded in non-RE alloys nucleation and growth of recrystallised grains with a spread of orientations, such as those in Figure 1.33, do not deform and are all allowed to grow statically post deformation. This weakens deformation textures by recrystallisation of weaker basal orientations which is only possible if DRX is suppressed. In contrast formation of weak RE texture components seems to be possible under all deformation conditions, even where DRX is dominant. This indicates the RE texture weakening mechanism is unique to RE alloys.

Figure 1.35 shows the extent of texture weakening during SRX of RE and non-RE alloys, in rolled material where DRX has largely been prevented. During SRX the texture weakens as annealing takes place, in magnesium 1.488 at% Zn-0.174 at% Ce and AZ31 alloys texture weakening stops after around 10mins and begins to strengthen, while in the magnesium 0.372 at% Zn-0.173 at% Ce texture weakens continually during 60 mins of annealing. The authors attribute the strengthening in basal texture with the completion of SRX and the onset of normal and abnormal grain growth, which they suggest favours the growth of basally oriented grains. In the 0.372 at% Zn-0.173 at% Ce alloy basal texture does not strengthen after 60 mins of annealing as SRX was retarded and thus grain growth has not been active for long enough to strengthen the texture [150].

Abnormal grain growth is observed in many magnesium alloys, both RE[95, 177] and non-RE[150] magnesium. It is caused by particular grains gaining a significant growth advantage over others during annealing. Such advantages can be gained due to the distribution and size of particles, the higher mobility of particular texture components in strongly textured material and even restriction of normal grain growth by free surfaces in thin sheets[21]. Recently solute drag at grain boundaries has also been associated with abnormal grain growth[178]. The many causes of abnormal grain growth make it difficult to associated with a particular effect and so it is not considered in detail when explaining RE textures.

In summary RE additions form weak RE textures during both SRX and DRX[95, 96, 114, 149, 163, 164, 174]. DRX nuclei in both RE and non-RE alloys have orientations distributed about deformed parent grains which are retained in RE alloys after annealing[160, 175, 176]. In special cases the weak orientations are retained in non-RE alloys during SRX[145, 148], this is often attributed to retarded DRX[145, 148]. RE addition is associated with retarding DRX, as segregation of RE atoms to grain boundaries causes solute drag [167, 175, 179], see Section 1.9. However, it must be emphasised that while retarding DRX is considered a key requirement for RE texture formation it alone

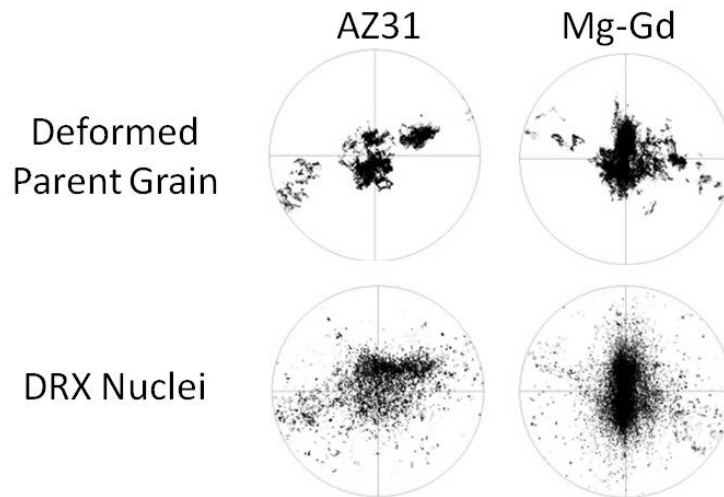


Figure 1.33: $\{0001\}$ pole figures calculated from EBSD maps of AZ31 and a magnesium 0.202 at% Gd alloy, showing the orientations of deformed parent grains and DRX nuclei after plane strain compression at 400°C. In both alloys the orientations of DRX nuclei are spread about the deformed parent grains. Adapted from Stanford[176].

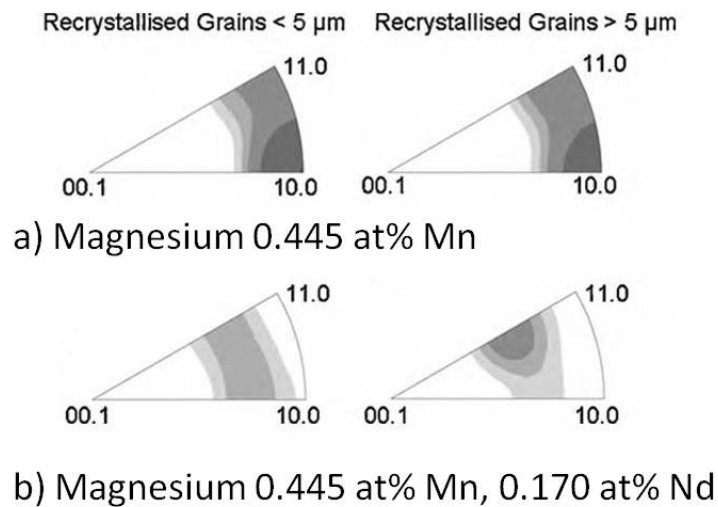


Figure 1.34: Inverse pole figures relative to the ED of DRX grains of different size in magnesium 0.445 at% Mn and magnesium 0.445 at% Mn, 0.170 at% Nd alloys. Levels: 1, 1.5, 2, 3 and 5 MUD, calculated from EBSD maps. The RE orientation ($\langle 11\bar{2}1 \rangle$ directions parallel to ED) is only present in larger recrystallised grains, indicating grains with this orientation have an advantage over basally oriented grains.

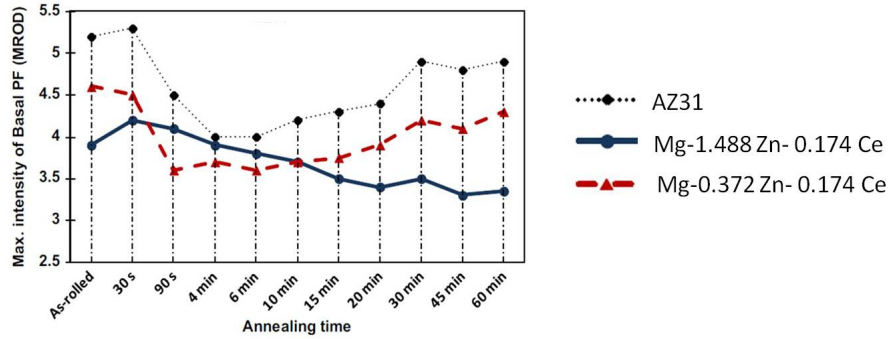


Figure 1.35: Figure showing the change in $\{0001\}$ basal pole figure intensity during static recrystallisation at 300°C of magnesium 1.488 at% Zn-0.174 at% Ce, magnesium 0.372 at% Zn-0.173 at% Ce and magnesium 2.70 at% Al-0.372 at% Zn (AZ31) alloys after warm rolling (300°C)[150].

does not form RE textures, because the unique RE orientations are not nucleated in non-RE alloys where DRX is suppressed. We now consider the nucleation mechanism of these RE texture components.

1.7.1 Nucleation of Recrystallisation in Rare Earth Alloys

Nucleation mechanisms in magnesium alloys are described in detail in Section 1.5.2 where grain boundaries, twins and shear bands are considered important nucleation sites in magnesium. In particular rare earth addition has been associated with increased numbers of twins and shear bands in the microstructure [134, 141, 148, 149, 174]. For example rolling of RE alloys produces fewer tension twins and more compression and secondary twins than non-RE alloys [134, 148, 149]. An increased propensity for twinning in RE alloys has been considered to form the weak textures by TDRX nucleating the weak RE orientations[149]. Indeed, a recent study by Molodov *et.al*[132] suggests texture weakening within a twinned single crystal is the result of prismatic slip within the contraction twin, activating a continuous TDRX mechanism, see Section 1.5.2.3. However, twins are not thought to be the exclusive source of RE nuclei, because despite similar twinning behaviour (after identical deformation conditions) the texture of a magnesium-Gd alloy is still found to be significantly less intense than AZ31 which produced a normal strong basal texture[176]. Even where weak textures are produced in non-RE alloys the twinning behaviour was no different to that observed under rolling conditions which produced the normal strong recrystallisation textures[145].

Twinning and compression twinning in particular, have also been associated with the localisation of strain and the onset of failure[90, 94–96], Section 1.3.4. Some argue that compression twins in particular nucleate shear bands in magnesium, observing that a significant proportion of shear bands have misorientations characteristic of compression

twins[94]. The increased compression twinning in RE alloys is suggested to nucleate a more even distribution of shear bands [94, 95, 134], Figure 1.36. More uniform shear banding partly explains the increased ductility in RE alloys, as shear is spread more evenly throughout the material reducing strain localisation, meaning that higher strains can be reached before failure.

The increased density of shear bands also means that RE alloys have a greater number of sites for shear band nucleation. The matrix within a shear band is reported to be oriented with the basal planes perpendicular to the plane of the shear band (Section 1.3.4), nucleating similarly oriented textures[96, 99, 101] (Section 1.5.2.4). This occurs as the dominant mode of slip within the bands is basal slip, which aligns the basal planes parallel to the direction of shear in the band. Stanford *et.al* observed this in the shear bands of a magnesium-Gd extrusion in which the bands parallel to the ED produce the typical magnesium extrusion texture, with basal planes parallel to the ED, while shear bands 25° to the ED produce the RE texture extrusion component [96], see Figure 1.37. The argument for RE texture formation by this mechanism is that RE addition retards DRX and promotes a greater number of shear bands of different orientations which nucleate the RE texture[96, 149]. Shear band nucleation of RE textures has also been reported by Basu *et.al.* in both binary and tertiary RE alloys[168, 180]. They propose a mechanism shown schematically in Figure 1.38 which attributes the preferential growth of RE orientations to the high mobility of the high angle boundaries between non-basal nuclei and basal parent grains. These boundaries are expected to be more mobile than those between basal nuclei and basal parent grains which have low misorientation angles by comparison. This difference in boundary mobility is suggested to be exacerbated by the pinning effect of solutes on DRX nuclei, which retards DRX. While there is no doubt shear bands nucleate RE textures[96, 138, 148, 168, 176] questions remain about the role of shear bands alone in nucleating it, primarily because significant shear banding is observed in some non-RE alloys without forming RE textures[101, 165]. Weak RE textures are also observed in some RE alloys where shear banding does not appear to be active[95].

As discussed the deformed microstructure in RE alloys contains increased numbers of twins and shear bands [96, 149, 174]. However, these features are not prerequisites for the RE texture, since it is not possible to produce RE textures in non-RE alloys by promoting these features alone [145, 176], despite this both twins and shear bands do nucleate recrystallised grains with RE orientations [96, 138, 148, 176]. To explain the formation of these RE orientations the effects of RE addition on slip system activity must be considered, since even if this does not change deformation texture directly, as already discussed, it may change the recrystallisation mechanism. Particularly if RE orientations are found to nucleate with a lower stored energy than basal orientations, as this would provide a clear driving force for the growth of RE textures.

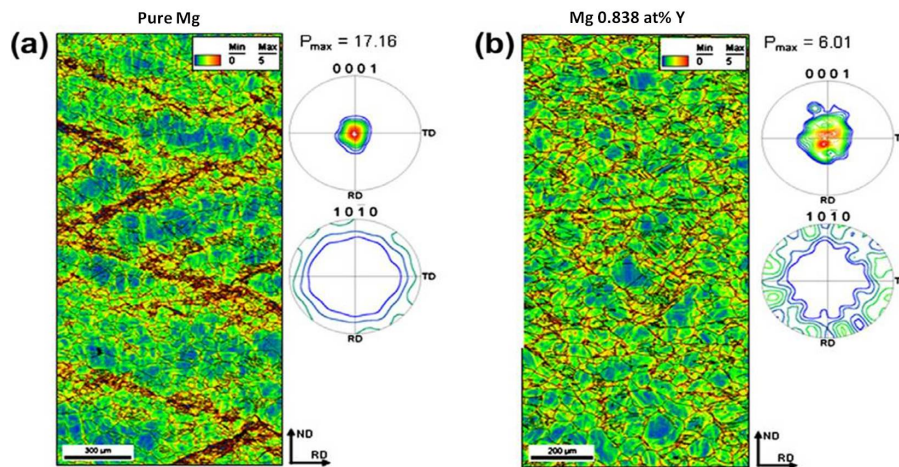


Figure 1.36: Figure showing regions of high shear (red) in an EBSD map, calculated by plotting the average misorientation of a single pixel with respect to neighbouring pixels. a) pure magnesium and b) magnesium 0.838 at% Y after deformation of 10% strain[94]. The shear bands are less intense and more evenly distributed in the Y alloy.

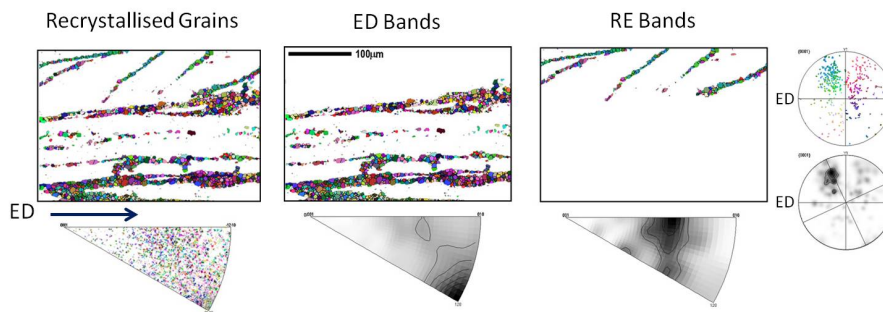


Figure 1.37: Figure showing EBSD map of grains recrystallising in shear bands of an extruded magnesium 0.24 at% Gd alloy[96]. The orientation of the shear bands determines the orientation of the recrystallising grain, Shear bands at 25° to ED appearing to nucleate the RE extrusion texture component.

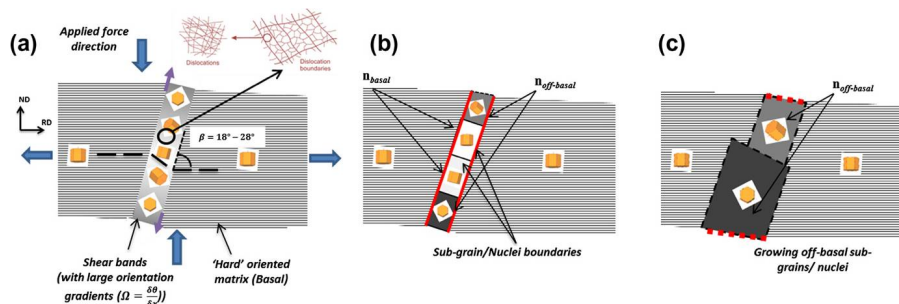


Figure 1.38: Schematic of the mechanism proposed by Basu *et.al* [168]. a) nuclei of various orientations form within shear bands, b) subgrain boundaries form within the shear band, c) off basal orientations have a growth advantage as a result of the higher angle boundaries between them and parent grains having a greater mobility. An effect the authors argue is exacerbated by retarding of DRX due to solute pinning.

1.8 Deformation in RE Alloys

Deformation in pure magnesium is dominated by basal slip, which produces the typical basal textures of wrought magnesium [181] (Section 1.4.1). Early work on RE textures noted the TD spread of basal poles is very similar to the rolled texture of titanium and zirconium[138], both h.c.p materials where prismatic slip is dominant[21, 182]. Naturally, RE textures were suggested to form due to increased prismatic slip in magnesium. However, because the deformation texture in RE alloys is often the same as in non-RE alloys[3, 165, 167] (Section 1.6.3) basal slip is expected to remain the dominant system, although, increased prismatic and pyramidal slip could still be significant in explaining the formation of RE textures.

1.8.1 Recovery in Rare Earth Alloys

Additional non-basal slip systems are likely to change recovery behaviour and subsequently recrystallisation mechanism. Recovery processes reduce the stored energy of a deformed microstructure by the annihilation of dislocations and their rearrangement into subgrain boundaries [21]. Subgrain formation has been observed in many magnesium alloys and commonly occurs through the continuous RDRX mechanism[105, 123](Section 1.5.2.2). RDRX is a pseudo-recovery process in which the typical nucleation and growth steps of recrystallisation occur simultaneously forming a subgrain structure at grain boundaries. As subgrain formation requires the activation of more than one slip system[95], this is typically only observed at higher temperatures where non-basal slip systems are more active[105, 122]. Hadorn *et.al* have postulated that increasing prismatic slip in RE alloys may promote subgrain formation at lower temperatures, rotations produced inside the RDRX grains nucleating the RE orientations[95]. Such a mechanism has recently been observed within contraction twins in a single crystal study, where prismatic slip was identified as a key factor leading to subgrain formation and subsequent texture weakening in CDRX grains within a compression twin[132]. However increased subgrain formation could also be attributed to higher levels of pyramidal slip, as both prismatic and pyramidal slip offer the extra slip systems necessary for easy subgrain formation.

Recovery rates could also be significant in the formation of RE textures as recovery rate determines the stored energy in deformed grains which is proportional to recrystallisation rate[21]. Fazadfar *et.al* propose that differences in stored energy between grains of different orientation could cause grains to SRX at different rates, potentially forming RE textures if grains with RE orientations RX faster than others[160]. The stored energy differences between orientations could be due to differences in recovery rate between grains, non-basal slip promoting faster recovery. Fazadfar *et.al* observe 20 times more

stored energy in basally oriented grains than in grains with the RE orientations between the ND and TD (ND-TD grains), in a magnesium 0.810 at% Y alloy after a 50% rolling reduction in a single pass at 350°C[160]. The high energy basal grains are also observed to contain a much finer substructure than the comparatively low energy ND-TD grains. However, such large differences in stored energy and substructure are not always reported in alloys with low intensity RE textures[179]. For example, Stanford finds no significant differences in stored energy with grain orientation in a magnesium-Gd alloy, after plane strain compression over a variety of strain rates at 400°C [179].

Although differences in stored energy between grains of different orientations are difficult to detect rare earth alloys are found to have a higher overall stored energy than non-RE alloys after equivalent deformation[160, 179]. This is most probably due to retarded dynamic recrystallisation in these alloys (see Section 1.9). The formation of RE textures has often been attributed to retarded recrystallisation however, higher stored energy can lead to RE alloys statically recrystallising faster than non-RE alloys in some cases. In these cases low intensity RE textures are still produced in the RE alloys which recrystallise slower, while intense basal textures form in the non-RE alloys which recrystallise faster[160, 179]. This suggests that retarding DRX alone is not enough to produce RE textures, a change in deformation behaviour may also be required.

In summary changes in slip system activity are believed to be required for RE texture formation and a number of mechanisms have been proposed by which the RE textures form as a result. These range from non-basal slip allowing new orientations to develop during RDRX to non-basal slip changing the recovery rate of grains by orientation. While the currently proposed mechanisms are still speculative they depend on the extent of the increase in non-basal slip and particularly which dislocations types are promoted, as the orientation which develops in a deformed grain or subsequent subgrain is dependent on the slip system operational during deformation.

1.8.2 Increasing Non-Basal Slip

The increased non-basal slip activity required for these recovery mechanisms has been observed in TEM studies of RE alloys, showing high activities of both prismatic and pyramidal slip in basally oriented grains[94, 183, 184, 184, 185]. However, the most significant type of dislocation for RE texture formation is still debated. High prismatic slip activity has been reported in magnesium-Ce alloys showing the RE texture after rolling[183–185] and increased pyramidal $\langle c + a \rangle$ slip has also been observed in both Ce and Y alloys[94, 184] post rolling. In particular, in the magnesium-Y system 65% of dislocations are estimated to be pyramidal after 3% cold rolling [35, 94]. At these low

strains the authors found no evidence of prismatic $\langle a \rangle$ dislocations[35], which they suggest may only become active at higher strains. The type of non-basal slip in basally oriented grains is thus dependent on both alloying additions and the extent of deformation within each grain. These studies have focused on grains with a basal orientation to aid comparison of dislocation activities with non-RE alloys, dislocation activities in non-basal grains have not been extensively investigated using TEM. It is likely that the activity of dislocations in non-basal grains is more significant for RE texture formation as by definition these grains have a non-basal orientations which may grow during recrystallisation. Dislocation analysis in deformed and recovered grains with such non basal orientations is a significant area for future investigations.

A limitation of dislocation observations in the TEM is the small areas studied. Dislocation analysis over larger areas may be achieved using Intra Granular Misorientation Axis (IGMA) analysis, which uses EBSD data to calculate the misorientation axis between neighbouring points within a grain. Each slip system has a characteristic misorientation axis, given in Table 1.4, which can be plotted on an inverse pole figure showing the dominant slip system. Detailed mathematical explanations of the tool may be found in work by Chun *et.al.* [29] and its application to magnesium-RE alloys by Hadorn *et.al*[95]. It is important to note that only geometrically necessary dislocations (GNDs) are detected by this method. GND's are an indicator of dislocation activity during deformation, they represent only the dislocations required to accommodate a given misorientation and do not necessarily represent constituent dislocations which may be observed in the TEM[21].

Various studies have used IGMA analysis to compare the deformation behaviour of RE alloys[95, 134, 179, 184]. In particular, Hadorn *et.al* compare GNDs in a series of hot rolled magnesium-Y alloys with concentrations above and below the critical concentration. The dominant GND type changes as a function of RE concentration. Basal slip is dominant below the critical concentration and prismatic slip is dominant above the critical concentration[95]. Similar IGMA studies on Ce, Nd and Gd alloys show the same increased prismatic GND content with rising RE concentration in basally oriented grains[134, 160, 176, 177, 184]. However, the transition from a high intensity to low intensity texture happens at a lower concentration than the transition in GND content[95, 177]. This suggests that a change in the dominant GND type in these basal grains is not required to activate RE effects[160, 179], but a small increase in prismatic GNDs may be involved, which is observed as a weakening of the $\langle 10\bar{1}0 \rangle - \langle 2\bar{1}\bar{1}0 \rangle$ peak in the IGMA plot[184], see Figure 1.39. The view that prismatic GNDs need not be dominant to activate RE effects, is supported by the observation that prismatic GND's are also dominant in AZ31(a non-RE alloy), which does not produce low intensity RE textures observed in RE alloys after similar processing, plane strain compression at 400°C and strain rates above 0.1s^{-1} [179].

IGMA analysis can also compare GND content in grains with non-basal orientations, which could be significant for the formation of RE texture if GND content was found to be strongly dependent on grain orientation. Some studies do report such a dependence with high prismatic GND populations in grains favourably oriented for prismatic slip and basal GND's in grains oriented favourably for basal slip[95, 160]. In cases where this is observed, increasing RE content is found to increase prismatic GND populations in both cases[95, 160]. However, a dependence of GND content on grain orientation is not found in all IGMA analyses and it is very sensitive to the statistics of the study[177]. This makes it difficult to determine the dependence of GND content on grain orientation however, grain orientation does seem as important in determining the GND content as the RE concentration in these alloys[95, 177].

The GND's detected by IGMA analysis are present after recovery processes such as cross-slip and dislocation annihilation have occurred[29, 95]. So, while increased prismatic slip is detected after RE addition, the argument is merely that prismatic activity has increased, not that it has become more active than basal slip in these alloys[95, 160, 179]. If prismatic slip were more active than basal slip a change in the deformation texture of RE alloys would be expected, which is not observed[138].

Increased levels of prismatic and pyramidal slip are observed in TEM and IGMA studies of RE alloys, however the most significant system for RE texture formation is still unclear. Typically changes in the relative activities of each slip system in magnesium may imply a change in c/a ratio [20, 181] (Section 1.2.1), which does not change significantly with the dilute RE additions considered here[94, 186]. However, there is increasing evidence, based on DFT simulations, that a variety of RE additions do cause a reduction in c/a ratio when present at higher concentrations (> 6 at%) [187, 188]. c/a ratios are predicted to fall from 1.62 (pure magnesium) to < 1.59 in binary magnesium lanthanide or Y alloys where the concentration of RE is greater than > 6 at% [187]. This is significant as a magnesium alloy with a c/a ratio of 1.59 would be expected to behave similarly to titanium and zirconium alloys (where prismatic slip is dominant) as these metals also have $c/a= 1.59$. However, even these DFT simulations do not predict a significant change in c/a ratio at the concentrations where RE effects are observed ($c/a=1.625$ at 0.926 at% Y) [188], thus to explain changes in slip activity other solute based effects must be considered.

1.8.3 Mechanism of Increased Non-Basal Slip

Increasing prismatic slip activity has been attributed to a solid solution softening effect[95] also observed in magnesium-zinc and aluminium solutions[34, 46, 47]. In which the large size of solute RE additions reduces the activation energy for kinking and jogging [189, 190]

which are required for cross slip of basal dislocations onto prismatic planes[48, 191], Section 1.3.2 . As cross slip of basal dislocations is the main source of prismatic dislocations a reduced activation energy for cross-slip would significantly increase prismatic slip and therefore recovery. Indeed recent DFT modelling predicts that Y addition below 1 at% would significantly reduce the cross-slip stress[77].

The increase in pyramidal dislocation activity has been attributed to a reduced I_1 stacking fault energy in RE alloys[188]. The reduced stacking fault energy, which has also been predicted by ab initio DFT studies[192], results in a large number of I_1 stacking faults observed in the TEM[188]. Sandlöbes *et.al* suggest the sessile stacking fault, which is bounded by $\frac{1}{6} \langle \bar{2}203 \rangle$ Frank partial dislocations, forms a defect on the pyramidal plane which acts as a source for pyramidal dislocations[188]. A reduction in SFE would therefore provide more stacking faults and thus more sources for pyramidal dislocations, subsequently accounting for a significant proportion of the increased ductility in RE alloys. A reduced I_1 SFE is predicted and observed in a variety of magnesium-RE systems including the lanthanides, Y and Sc[187]. For a solute atom to reduce the I_1 SFE a large atomic radius ($\gg 145\text{pm}$), similar electronegativity (≈ 1.2) and bulk modulus ($32 - 56\text{GPa}$) to magnesium are required. No other solute elements considered (apart from lanthanides, Y and Sc) fulfil these criteria[187].

Stacking faults are usually thought to impede recovery by restricting glide, cross-slip and climb of dislocations[21], which would be expected to inhibit the mechanisms of RE texture formation by recovery discussed Section 1.8.1. However, while more stacking faults may retard recovery on the basal plane, the pyramidal dislocations nucleated by them might allow subgrains to rotate into RE orientations not possible with only basal dislocations[95]. Indeed significant cross-slip of these pyramidal dislocations has been observed by TEM, which is a critical part of subgrain formation[35].

In summary there is significant evidence for solute additions changing slip system activities in magnesium[35, 95, 160, 177, 183, 188], less clear is which of these changes are required for RE texture formation. TEM studies on RE alloys show an increase in prismatic and pyramidal slip in grains with a basal orientation[35, 183, 185], however neither system has been directly associated with nucleation of RE textures. Changes to slip system activity in non-basal grains may be more significant in nucleating RE textures but remain to be studied with the TEM. IGMA analysis supports TEM observations of increased prismatic slip[35], reporting prismatic GND content increases with RE addition in both basal and non-basal grains[95, 160]. However as texture intensity falls before the prismatic GNDs population is larger than the basal GND population[95], only a small increase in prismatic GND content seems to be required to activate the RE effect. Indeed the role of prismatic

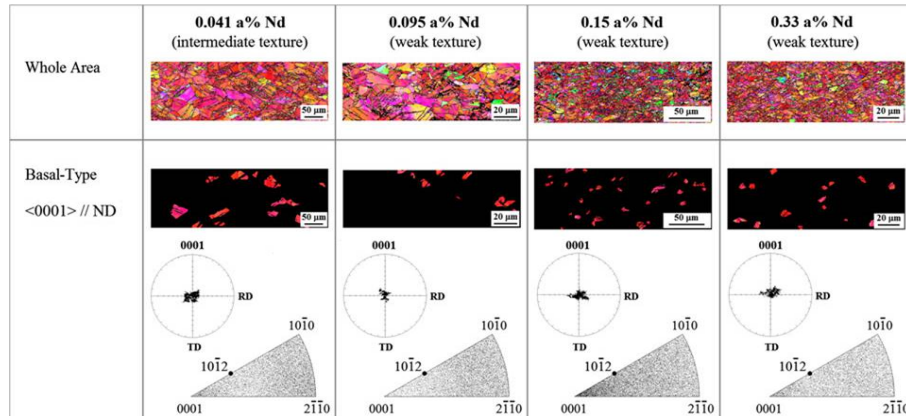


Figure 1.39: Figure showing IGMA plots of basally oriented grains from a series of magnesium-Nd binary alloys. The upper EBSD map shows the whole area and the lower EBSD map shows only the grains considered in the IGMA plot. Increasing prismatic slip with RE addition is indicated by a strengthening of the [0001] peak in the IPF. Figure adapted from Hadorn *et.al*[177]

GND's in RE texture formation is thrown into further doubt as similarly high levels of prismatic GNDs are observed in non-RE alloys that do not produce the RE effects[179].

An increase in non-basal slip, particularly pyramidal slip is expected improve formability even without weak RE textures. However, as basal slip remains the dominant deformation mode, even in RE alloys, weakening of basal textures is also critical in explaining improved formability. Despite the observed changes in slip system activities in RE alloys little modelling has been attempted to predict how significant the change in deformation mode activities could become before causing changes to deformation textures. This is an area for further investigation as changes in slip system activity, particularly increasing non basal slip, are also believed to cause a change in recovery behaviour leading to recrystallisation of RE textures by a change in recrystallisation mechanism. Currently the majority of studies have focused on basally oriented grains, however a renewed focus on deformation in non-basal grains may be needed to observe the nucleation of RE texture component. Of course the deformed microstructure is only preserved by the retarding of DRX in RE alloys, retarded DRX is thus thought to be critical nucleating the RE texture[95, 176, 193]. It is thus important to consider the mechanism of retarding DRX by RE addition.

1.9 The Mechanism of Recrystallisation Retardation

Retarded DRX and a refined grain size after SRX[114, 149, 167, 176] are normally explained by a Zener pinning mechanism, in which precipitates pin grain boundaries[21]. While Zener pinning predicts the limiting grain size well in more concentrated RE alloys[177], DRX is retarded and RE textures formed in many dilute alloys where particles are not

found[95]. This suggests that another mechanism must operate in dilute alloys to retard DRX. A solute drag effect, caused by segregation of RE atoms to grain boundaries has been proposed [95, 193, 194].

Recent studies investigating the distribution of RE atoms in the matrix find there is a strong propensity for them to segregate to grain boundaries, Figure 1.41 b). In the case of a magnesium-Gd alloy the concentration of Gd at the grain boundaries was found to be almost 10 times higher than in the matrix[194], similar results were found in magnesium-Y alloys[95]. Notably, both studies find that non-RE elements, including Zn, do not show significant segregation. This segregation has been reproduced with the Langmuir and McLean model, which assumes that the driving force for segregation is the relaxation of elastic stresses caused by the large size of RE atoms in the matrix[193]. The model predicts high segregation of RE atoms and no segregation of Zn or Al to grain boundaries, purely on the basis of size misfit between the magnesium matrix and solute atom, Figure 1.40. The propensity of each RE atom to segregate is a balance between atomic size and solubility in magnesium. Larger atoms segregate more however, their large size reduces their solubility meaning that there are fewer atoms in the matrix to segregate. Accounting for both factors Gd is estimated have the potential to produce the highest concentrations on grain boundaries (Figure 1.40).

This model can be extended to consider the effect of solute drag on grain boundaries as a result of segregation, using the Cahn-Lücke-Stüwe impurity drag model[193]. This model requires a knowledge of matrix and grain boundary diffusion rates, which are not known for many RE additions apart from Y[193]. The solute drag produced by Y dissolved at its maximum solid solubility is found to be too small to significantly retard SRX at typical processing temperatures. DRX however, is predicted to be significantly retarded by Y segregation. This is consistent with Stanford *et.al's* [176] experimental results which show the RE texture can emerge even when SRX is faster in a RE than in a non-RE containing alloy. These results suggest that retarded DRX may be critical in RE texture formation.

Segregation of RE atoms to grain boundaries is a function of temperature, higher temperatures reducing RE concentration at grain boundaries, reducing the drag effect[21]. Stanford *et.al* find that the RE texture of a magnesium-Gd extrusion reverts to a standard (non-RE) extrusion texture when extruded above 500°C, where RE segregation to grain boundaries drops sharply (Figure 1.41)[194]. This supports the notion that segregation of RE retards DRX and this is critical to RE texture formation.

The segregation of RE atoms is not limited to grain boundaries, atom probe tomography reveals solute atoms also segregate to dislocations[71], forming solute atmospheres around them[195]. Cottrell atmospheres inhibit dislocation motion, raising the CRSS of dislocation slip (Section 1.3.2). When segregated to dislocations the characteristic serrated flow

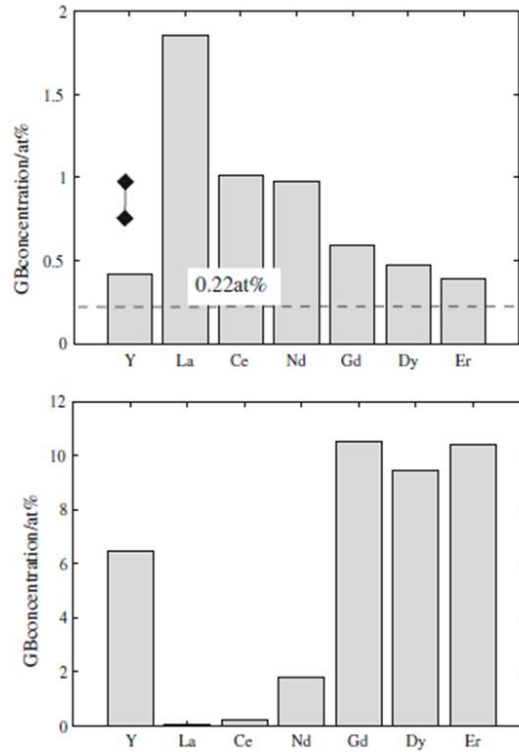


Figure 1.40: Figure showing the segregation of different RE atoms to grain boundaries predicted by the Langmuir and McLean model. a) shows segregation if the RE concentration was 0.22at%. b) shows segregation of RE's to grain boundaries if each element were present at the maximum solubility of that element in the matrix [193]. Also plotted is the experimentally measured Y segregation of Hadorn *et.al* [95] at 0.22at%, which suggests the model underestimates propensity to segregate.

stress curve associated with DSA was observed at deformation temperatures above 200°C, indicating that diffusion of RE atoms to dislocations is active[71]. Dislocation drag by RE atoms at these temperatures may retard recovery leading to a higher stored energy in RE alloys as observed[179].

Partitioning of RE atoms to grain boundaries and dislocations is likely to do more than simply retard recrystallisation, it might be enough to change the dominant recrystallisation mechanism entirely[95, 193, 194]. Hadorn *et.al* note that solute drag is likely to restrict recrystallisation by strain induced boundary migration(SIBM) significantly more than by RDRX[21, 95]. As SIBM requires the bulging of prior grain boundaries to nucleate recrystallisation[21], which would be retarded by solute drag. Basu *et.al.* also propose RE texture formation is favoured due to solute drag[168], the mobility of low angle boundaries between recrystallising grains with a basal texture and basal parent grains is further slowed relative to the growth of recrystallising grains with a non-basal orientation due to boundary pinning. In both mechanisms solute drag may be critical in RE texture formation restricting recrystallisation by normal mechanisms which produce basal textures, thus allowing alternative recrystallisation mechanisms to produce RE textures.

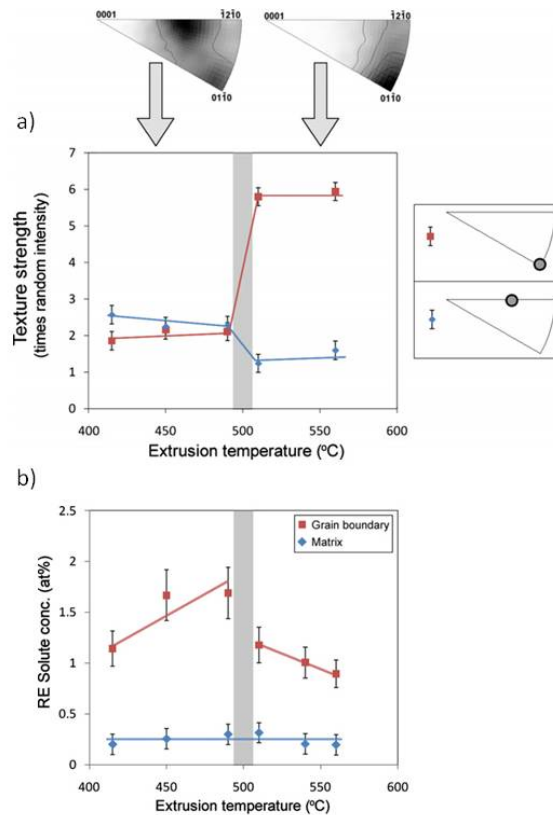


Figure 1.41: a) Figure showing the intensity of the RE texture component (blue) and the normal magnesium component (red) of magnesium-0.234at% Gd alloy extruded at different temperatures. b) The concentration of Gd at grain boundaries at each extrusion temperature, measured by EDS in the TEM. The grey region indicates the transition temperature above which RE effects deactivate [194].

It should also be noted that tertiary magnesium-X-RE alloys, with RE concentrations typically $> 1\text{at}\%$, RE and non-RE solutes are found to form Long Period Stacking Ordered structures (LPSO phases) within the matrix [196–198]. LPSO phases are not reported in the very dilute alloys considered here and neither are the fine particles reported in many similar creep resistant alloys [199] of even higher RE concentration. The dilute RE textures discussed here are not thought to be related to these phases typical of alloys with much higher RE concentrations. However, co-segregation of RE and smaller non-RE atoms (eg Zn and Al) reported in these higher concentration tertiary alloys [197, 199] is likely to be active in the dilute tertiary alloys discussed here such as ZEK100. Segregation of Zn and Nd atoms in the matrix is suggested to reduce the elastic strain fields created by both solutes, as Zn atoms, with a radius of 0.134 nm, are smaller than magnesium atoms (0.150 nm) creating a negative strain field which is relaxed by the positive strain field created by Nd atoms (0.185 nm) which are larger than the magnesium matrix [168]. While this co-segregation of solute atoms is likely to occur in very dilute tertiary RE alloys the significance of this effect in producing RE textures, particularly the TD basal texture split (Figure 1.29), is not yet understood.

In summary RE atoms strongly segregate to dislocations and grain boundaries[95, 194]. This is consistent with a simple model that predicts RE elements segregate more strongly than non-RE atoms as a result of their large atomic size, causing misfit strains in the matrix, which are relieved as the atoms diffuse to boundaries[193]. It is suggested segregation to boundaries retards DRX by grain boundary drag[95, 193]. Modelling suggests that the potential for segregation and thus ability to retard DRX is a balance between atomic size and solubility of RE in magnesium. Larger RE elements may segregate more strongly, but lower solubilities of these large atoms limit the maximum grain boundary concentration[193]. The observation that the RE texture disappears at high extrusion temperatures is consistent with the predicted loss of segregated solute from those boundaries at high temperatures[194]. This suggests that suppression of boundary migration by segregation is a necessary condition to produce the RE texture[95, 193, 194]. The importance of segregation is also suggested by the observation that the RE effect is activated at very low levels of solute addition[149], since through this effect the local concentration of RE (eg on grain boundaries) may be an order of magnitude greater than the average atomic concentration. Importantly however, no high resolution TEM studies have been carried out on this segregation effect to indicate how segregation occurs; do RE atoms exist as a mono-layer or in clusters at grain boundaries for example? Work such as this might help us to understand fundamentally why RE atoms have these effects, is their large size or electronic structure most significant? Current modelling of segregation is based on large atomic size causing RE atoms to distribute as a mono-layer at grain boundaries, if the predictions of RE segregation are accurate it suggests that the size of RE atoms is their most significant property.

1.10 Summary

Very small concentrations of RE elements are found to significantly weaken strong deformation textures in wrought magnesium [149]. Weak textures lead to increased formability and reduced anisotropic properties greatly increasing the applications of magnesium alloys. A critical concentration of RE is required to activate these effects which appears to be a function of RE solubility in magnesium, more soluble elements requiring higher RE concentrations [149]. Although the link between critical concentration and solubility has not been tested in RE elements such as Eu which have extremely low solubilities in magnesium, offering the possibility of weak RE textures requiring ultra low RE concentrations.

RE additions also increase the activity of non-basal (prismatic and pyramidal) slip systems which contribute to the improved formability of RE alloys [35, 95]. However, basal slip

remains the most active deformation mode as deformation textures in RE alloys are typically the same as non-RE magnesium alloys [138]. A reduced cross-slip stress of basal dislocations onto prismatic planes has been proposed to account for increased prismatic slip [95]. While a reduced I_1 stacking fault energy is suggested to increase the number of I_1 stacking faults which nucleate increased pyramidal dislocations [188]. The relative contribution of prismatic:pyramidal slip in RE alloys remains poorly quantified as does the mechanism linking changes in slip system activity with RE texture formation.

The weak RE textures form during both SRX and DRX of the deformed microstructure and these weak textures thought to contribute at least as much as increased non-basal slip to improved formability of RE alloys. The deformed microstructure in RE alloys is reported to contain significantly larger numbers of compression twins and shear bands than non-RE alloys. Higher numbers of compression twins are reported to nucleate many of the increased number of shear bands[94]. Recrystallisation nuclei with RE orientations are observed to nucleate at both shear bands and twins however, neither feature is thought to exclusively nucleate RE texture components[96] because shear bands and twinning may be promoted in non-RE alloys without nucleating the characteristic RE textures[176]. Texture weakening during SRX is possible in non-RE alloys where DRX is suppressed however, this does not produce characteristic RE orientations such as the TD split in the basal texture of rolled material. Also in these non-RE alloys weak textures are not observed during DRX [145], so while retarding DRX does cause some texture weakening it alone does not explain RE texture formation.

Despite this RE addition is found to retard DRX and this is believed to be critical in explaining RE textures[179]. Retarded DRX raises stored energy in the microstructure which could increase the activity of recovery processes changing recrystallisation mechanism. In particular the activity of continuous recrystallisation mechanisms, such as RDRX, might increase with RE addition as they require the formation of a subgrain structure which is facilitated both by retarded DRX and increased non-basal slip. The RDRX mechanism could nucleate RE orientations by differences in recovery rates between deformed grains of different orientations or due to the new rotations possible during RDRX as a result of high levels of non-basal slip[95]. Currently such a mechanism is still speculative and its increased activity has not been directly reported in RE alloys. This is partly as many studies focus on partially DRXed material where many of the RDRX nuclei may already have nucleated or been consumed making their identification difficult.

Retarding DRX has been associated with the segregation of solute atoms to grain boundaries [194] which reduces grain boundary mobility by a solute drag effect[193]. Segregation of RE atoms to grain boundaries is directly associated with RE texture weakening as at high temperatures, where solute segregation is reduced, RE textures are deactivated[194].

Basic modelling of this effect has suggested that the solute drag on boundaries is enough to retard DRX but not SRX, exactly as is observed and hence the importance of retarded DRX on RE texture formation is highlighted.

Solute drag on grain boundaries is also thought to be important in determining the most active RX mechanism, as it is likely to retard some recrystallisation mechanisms more than others[95]. For example SIBM, which requires the bulging of prior grain boundaries, may be inhibited by solute drag more than other mechanisms such as RDRX. If the inhibited mechanism typically nucleates basal orientations common in wrought magnesium, inhibiting it could allow other RX mechanisms to nucleate the RE orientations. While there is significant experimental evidence showing the segregation of RE atoms to grain boundaries the resolution of these studies is too low to determine the extent of atomic segregation[95]. For example, are RE atoms evenly distributed over tens or hundreds of nm, do they exist in a mono-layer at the boundary or in small clusters. An understanding of the exact nature of atomic segregation is vital in accurately modelling the effects and could be vital in understanding the critical concentrations of each RE required for texture weakening.

In summary RE textures nucleate during recrystallisation and appear to form as a result of a combination of retarded DRX and an increase in non-basal slip. Both effects are likely to affect the dominant RX mechanism in magnesium in different ways. Retarded DRX by solute drag raises stored energy in the microstructure possibly increasing the activity of recovery processes in magnesium, with solute drag likely to retard some DRX mechanisms more than others which may promote the RX mechanism forming RE textures. Increasing non-basal slip meanwhile is also likely to affect recovery by promoting the formation of a subgrain structure such as that required for RDRX, which could lead to the nucleation of RE orientations. Fundamentally the mechanism of RE texture formation is still unknown as is the critical feature of RE atoms that cause this effect. Isolating this feature, eg atomic size, is vital in leading alloy design towards a class of magnesium alloys with RE textures but with the lowest possible concentrations of RE. In order to isolate this feature the mechanism by which RE textures form must be understood. The aim of this thesis is to understand the critical parameters in RE texture formation and define the mechanism by which it occurs.

1.11 Focus of the Thesis

Currently the recrystallisation mechanism leading to the formation of RE textures is very poorly understood. The focus of this thesis is developing a better understanding of this mechanism and in particular presenting with greater clarity the differences between

texture weakening in binary magnesium-RE alloys and tertiary magnesium-RE-Zn alloys. The binary alloys produce what is best described as a weakened deformation texture during recrystallisation while the ZEK alloys form a unique split of the basal texture in the TD after rolling and subsequent recrystallisation. Currently the relationship between the recrystallisation mechanism in each case is not understood and it is not known if the Zn additions lead to a completely different ‘RE effect’.

The critical concentration of RE required to activate texture weakening effects in binary alloys is also investigated, since this quantity is likely directly related to the mechanism of texture weakening. Hantzsche *et.al* [149] propose this concentration is a function of the solubility of each RE in magnesium, this hypothesis is tested by developing a range of magnesium-RE binary alloys with borderline critical concentrations of RE. These alloys are then hot rolled allowing the extent of the RE effects in these alloys to be quantified.

In this study static recrystallisation after cold rolling is used to examine the recrystallisation mechanism in both groups of alloys. The majority of studies to date have characterised SRX behaviour in partially dynamically recrystallised hot rolled material. The partial DRX makes it very difficult to characterise the recrystallisation mechanism as in many cases subsequent SRX is primarily the growth of DRX nuclei and grains. Observation of SRX after cold rolling decouples the effects of dynamic recrystallisation and allows the observation of nucleation and growth of RE orientations from the deformed material. Studying cold rolled material should also offer a good opportunity to quantify the extent of texture weakening possible in non-RE alloys after cold rolling. The similarity of the texture weakening effect in cold rolled RE and non-RE alloys can then be compared. Indeed, characterising the extent of texture weakening possible during cold rolling of non-RE alloys is critical because it is likely that the same mechanism exacerbates ‘RE texture weakening’ in cold rolled RE alloys.

Finally the segregation of RE atoms to grain boundaries is also believed to be critical in facilitating the RE effects, however to date only low resolution quantification of this effect is available. In this work high resolution TEM and EDX are used to quantify the extent of RE segregation to grain boundaries and characterise the morphology; are RE atoms present in clusters or in an evenly distributed mono-layer for example. Such experimental quantification is needed to allow validation of future modelling which although not the subject of this work is needed to determine the critical parameter required by RE atoms to form RE textures.

Chapter 2

Experimental Methods

2.1 Alloy Casting

All alloys were provided by Magnesium Electron USA, the commercial alloys AZ31 and ZEK100 were cast and rolled on an industrial scale. They were received as sheet 1.2 and 2.49mm thick respectively. A series of binary magnesium-RE alloys were also custom made for this study all received in the cast condition. Compositions are given in Figure 2.0 and Table 2.3 as measured by ICP-AES (Inductively Coupled Plasma-Atomic Emission Spectroscopy) which was carried out commercially by London & Scandinavian Metallurgical Co Limited. This technique measures compositions to an accuracy of 50ppm (5×10^{-3} at%). Semi-quantitative X-Ray Florescence (XRF) was also used to quantify the extent of impurities in the castings, which were found to be relatively low, Table 2.2.

2.2 Rolling

A series of rolling experiments were carried out on the as cast material at 400°C. In each case the cast alloy was solution heat treated at 550°C for 16hrs in an argon furnace followed by quenching prior to rolling. This temperature is very close to the solidus temperature of the alloys in question [7]. The alloys were sectioned into billets of 20x55x100mm and heated to rolling temperature for 20 minutes in a preheated furnace prior to rolling. Hot rolling trials were carried out at 400°C to a final strain of $\epsilon_T = -1.4$ in passes of $\epsilon_T = -0.2$ at a roll speed of 6 m/min on lab scale rolls; reductions are accurate to approximately +/- 0.1mm. The temperature was maintained between passes by a 5 minute reheat to the rolling temperature and the material was quenched within 5s of the final pass to preserve the deformed microstructure.

2.3 Alloy Compositions

A series of binary magnesium-RE alloys were commissioned in order to investigate the effects of RE concentration and changing RE element on wrought magnesium textures. The concentrations of RE as measured by ICP-OES are plotted in Figure 2.0 and listed in Table 2.3, compositions of each alloy are plotted relative to the solubility of the RE alloying element, as this is believed to be significant in determining the critical concentration of RE needed to activate RE effects. In all cases alloy compositions were targeted below the solubility limit of each RE in magnesium to avoid the precipitation of particles, however, especially in the highly insoluble systems, this was not always possible. Table 2.2 shows the compositions of some of the alloys as measured by XRF, illustrating the binary alloys contained very few contaminants.

Compositions were chosen based on the solubility of each RE in magnesium, Figure 2.1 a). In particular magnesium-Y and magnesium-La systems were investigated as they represent high and low solubility RE elements. A range of compositions about the solubility limit of Y and La in magnesium were chosen to investigate the dependence of RE effects on the solubility of RE element Figures 2.0 a) and c). Yb and Eu alloys were also investigated as both elements have large atomic size however, Yb has a high solubility in magnesium and Eu has a low solubility. These alloys give a measure of the influence solubility has on the critical concentration of RE. The remaining alloys Ce, Gd and Nd were chosen to provide a comparison with literature results, in particular the magnesium-Nd alloy was chosen to provide a comparison with ZEK100, a commercial Nd-Zn containing magnesium alloy. To evaluate the RE effects each RE alloy was hot rolled under conditions similar to those in the literature which produce RE texture weakening.

2.4 Optical Microscopy

Optical specimens were prepared using a standard mechanical grinding and polishing process, finished by polishing with water free fumed silica with a nominal particle size of $0.01\mu\text{m}$. Samples were etched using an Acetic-Picral acid etchant (5mL Acetic Acid, 6g Picric Acid, 10mL Water and 100 mL Ethanol) to reveal the microstructure. Images were taken using cross polarised light which colours grains by orientation, making them easier to differentiate.

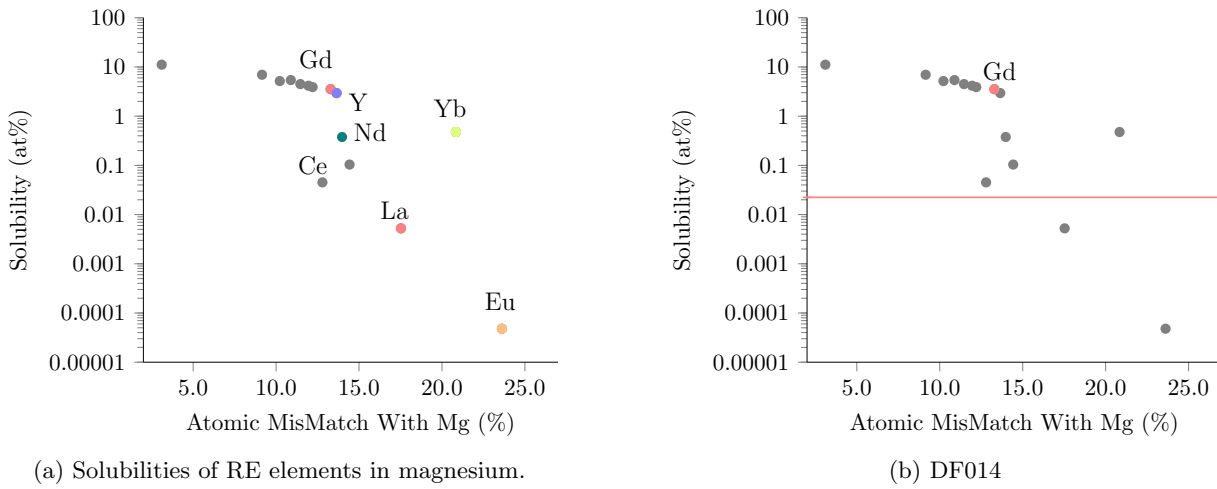
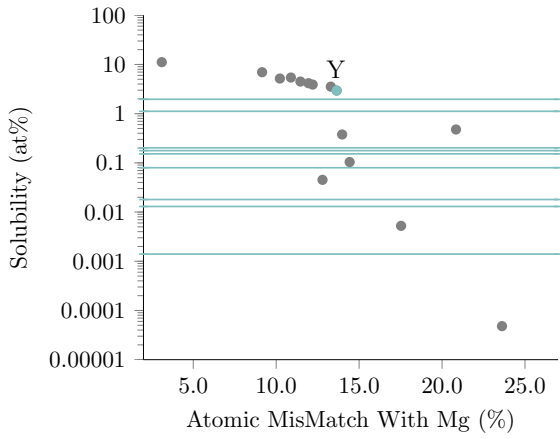


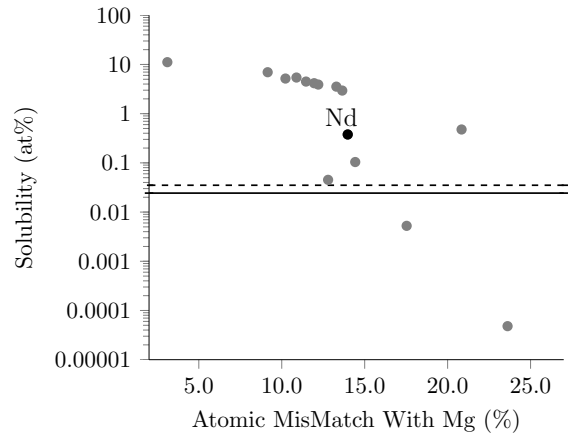
Figure 2.1: Figure showing a) the solubility of each RE element in magnesium [172] and b) the concentration of Gd in the DF014 alloy.

Table 2.1: Compositions of the range of binary magnesium-RE alloys measured using ICP testing.

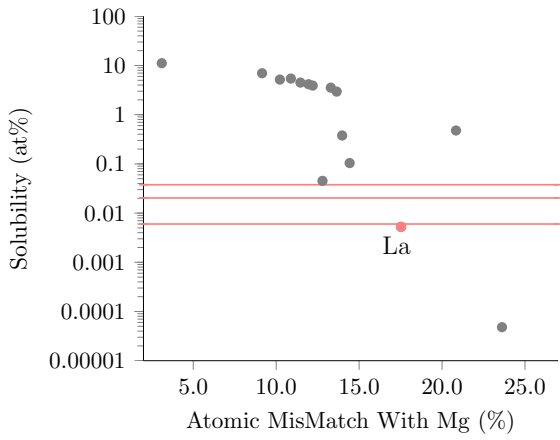
Code	Element	Concentration at%	Concentration wt%
DF02	Ce	0.0349	0.201
DF03	La	0.0050	0.030
DF04	La	0.0170	0.099
DF05	Yb	0.0210	0.149
DF06	Y	0.0120	0.045
DF07	Y	0.0090	0.033
DF08	Y	0.0010	0.005
DF09	Eu	0.0008	0.005
DF013	Nd	0.0243	0.144
DF014	Gd	0.0224	0.145
DF015	Ce	0.0009	0.005
DF016	La	0.0377	0.215
DF017	Y	0.0797	0.291
DF018	Y	0.2022	0.736
DF019	Y	0.1774	0.646
DF020	Y	0.1523	0.555
DF021	Y	1.9614	6.820
DF022	Y	1.1174	3.970
ZEK100	Nd	0.0351	0.208



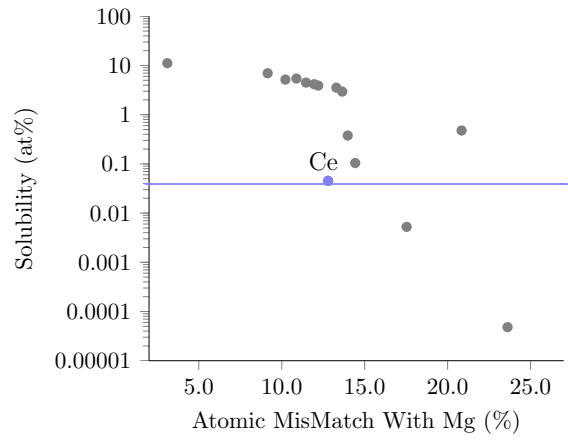
(c) DF06, 07, 08, 17, 18, 19, 20, 21, 22



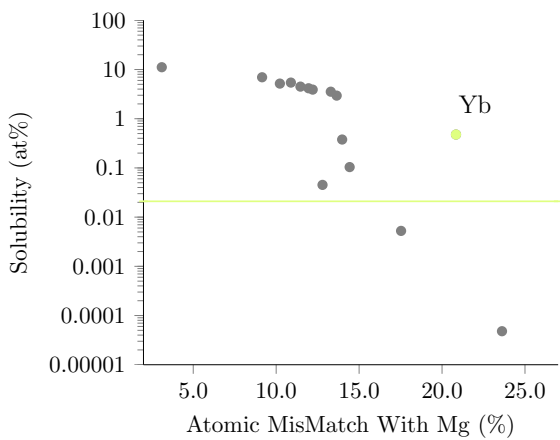
(d) DF13 and ZEK100 (Dashed)



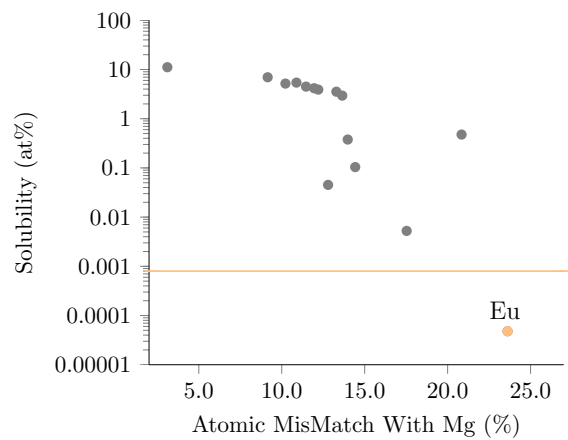
(e) DF03, 04, 16



(f) DF02



(g) DF05



(h) DF09

Figure 2.0: Figure showing the concentrations, in at%, of each binary magnesium-RE alloy in the study. The Nd concentration of the commercial ZEK100 alloy is also included. For reference the solubility of each RE in magnesium is included with the relevant element highlighted.

Table 2.2: Compositions of RE alloys in wt% as measured by XRF and Ni compositions of two alloys measured by ICP-OES.

Alloy	La	Y	Nd	Ce	S	K	Fe	Nb	Zr	Zn	Ni
DF002				0.27			0.01				
DF004	0.11				0.02	0.02	0.05				
DF021		6.22					0.01	0.08			
ZEK100			0.26						0.30	1.87	
DF20 (ICP)											20ppm
DF13 (ICP)											< 20ppm

2.5 Scanning Electron Microscopy (SEM)

Samples were prepared for scanning electron microscopy (SEM) as for optical microscopy. The primary SEM technique used in this work was electron backscatter diffraction (EBSD), for which specimens also received an additional electropolishing step in a solution of 175mL ethanol and 75mL of nitric acid at -25°C. Each specimen was electropolished in this solution at 12V for 5-10s, removing the surface layer of material, providing a smooth surface for analysis. For both imaging and EBSD three microscopes were used; FEI Sirion, Cam-Scan and FEI Magellan.

2.6 Electron Backscatter Diffraction (EBSD)

EBSD is an SEM technique used to identify the orientation of each point on a polycrystalline surface as the electron beam rasters over it. Automating the process allows thousands of points to be collected in a single map giving information on the microstructure of the material and defining the orientation of each point.

To acquire the map the specimen is tilted to 70° within the SEM chamber projecting an electron diffraction pattern onto an appropriately situated EBSD detector, Figure 2.1a). The diffraction pattern is produced as a result of inelastic scattering of electrons at the sample surface, which effectively creates a source of electrons with a range of wavelengths. Diffraction occurs when particular combinations of wavelength and plane satisfy the Bragg equation

$$n\lambda = 2d \sin\theta, \quad (2.1)$$

where n is an integer, λ is the wavelength of the incident electrons, d is the atomic spacing of planes hkl and θ is the angle of incidence between the beam and the plane. Where the Bragg equation is satisfied diffracting beams constructively interfere producing a Kikuchi band. Each type of plane produces a Kikuchi band with a different orientation, multiple planes diffracting at the same time produce a pattern which is characteristic

of the material crystal structure known as a Kikuchi pattern (Figure 2.1b)) consisting of a band for each diffracting atomic plane. The Kikuchi pattern allows the orientation of the crystal to be determined by matching the section of the pattern measured to a theoretical pattern for a particular orientation. This process is computer automated and occurs for each raster point producing a map composing thousands of orientations defining the material microstructure. EBSD data was acquired using the AZtecHKL software. Optimum SEM variables for EBSD change between specimen and machine however, typically an accelerating voltage of 20 kV, spot size of 4 and working distance of 10mm were used.

2.6.1 Processing EBSD Data

EBSD data has been processed using the HKL Channel5 software, the data can be presented in a variety of ways, here we primarily use three methods, colouring by inverse pole figures, kernel average misorientation (KAM) and band contrast;

Inverse Pole Figures: In this scheme each pixel is coloured based upon the orientation of the point as plotted on an inverse pole figure. Each vertex of the IPF is coloured red, green and blue as in Figure 2.2. In this work the rolling direction (RD) is chosen as the reference direction of the IPF unless otherwise stated. Maps with IPF colouring allow the orientation of each grain to be determined.

Kernel Average Misorientation: An alternative method of colouring pixels is to calculate the kernel average misorientation surrounding each one. In other words the misorientation of the central pixel with respect to each of the eight surrounding pixels in a 3×3 grid around the central pixel is calculated. The average of these eight misorientation angles gives the kernel average misorientation for the central point. The KAM value is plotted for each orientation in the map and colouring is based upon the magnitude of this value. KAM maps are useful for inferring the magnitude of stored energy at specific points in the microstructure, large misorientations are associated high dislocation densities and therefore high stored energies.

Band Contrast: Band contrast maps colour each pixel, typically in grey scale, based upon the magnitude of the average contrast between the Kikuchi bands and background. The band contrast is measured automatically during the acquisition process. Band contrast maps are useful for clearly identifying microstructural features, often appearing similar to optical micrographs of the material.

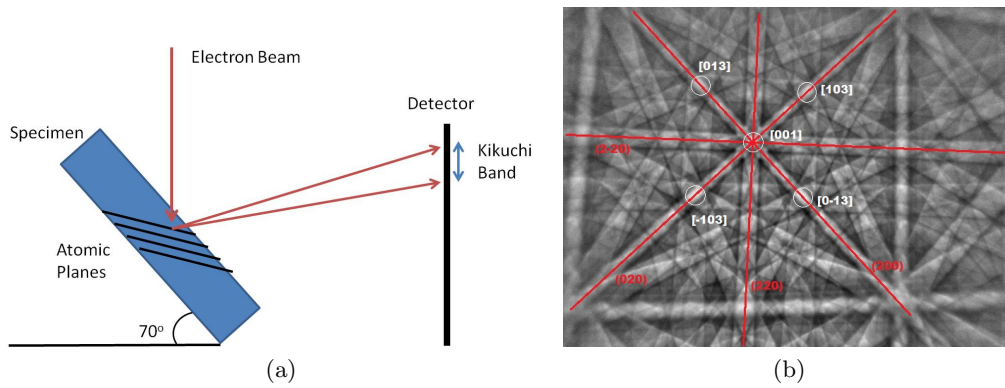


Figure 2.1: a) Schematic of specimen producing an Kikuchi patterns b) Figure showing an indexed Kikuchi diffraction pattern, the red lines indicate the fit of the measured pattern to a theoretical pattern[200].

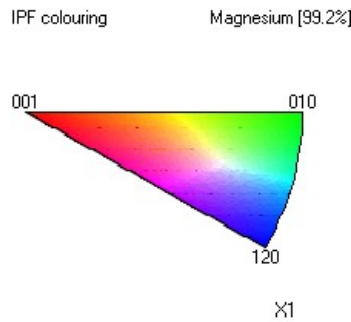


Figure 2.2: Inverse pole figure defining the colour of each orientation in an IPF coloured EBSD map.

In addition to these colour schemes, grain boundaries are plotted as black lines and defined by misorientations between grains of $> 10^\circ$. The characteristic twin boundaries are also highlighted in some band contrast maps; tension twins (red), compression twins (blue) and double twins in (green). The characteristic misorientation angles and about the $\langle 1\bar{2}10 \rangle$ axis for each twin system are given in Table 1.5. A tolerance of 5° about the axis and 10° about each characteristic misorientation is allowed. Both compression twinning systems have very similar characteristic misorientations, 56° and 54° , and cannot be reliably distinguished and both are indicated with a blue colour. Similarly, the double twinning systems have similar characteristic misorientations of 22° and 38° , so both of these systems are coloured green.

Finally pole figures of the EBSD data were plotted using the Channel5 software in which contouring was generated from each raw data point by applying a bell shaped curve with a half width of 20° and data clustering of 5° , $\{0001\}$ and $\{10\bar{1}0\}$ pole figures are presented.

2.7 Texture Measurement by X-Ray Diffraction

Macro-textures were measured by X-Ray diffraction using a Bruker D8 Discover diffractometer. Samples were ground and polished as for optical microscopy to remove the deformed surface layer prior to texture measurement. The $\{10\bar{1}0\}$, $\{0002\}$, $\{10\bar{1}1\}$ and $\{10\bar{1}2\}$ pole figures were measured, background corrections were made by measuring the background intensity either side of each reflecting peak and dynamically deducting the interpolated value from the peak intensity. Pole figures were combined to generate an orientation distribution function (ODF) using the MTEX texture analysis package [201] by a process known as pole figure inversion. There are a large number of pole figure inversion methods which approximate the ODF using a set of experimental pole figures. In MTEX the ODF is discretised by a linear combination of up to 100,000 radially symmetric bell shaped functions. Once the ODF has been approximated, fast Fourier techniques are applied to compute recalculated pole figures from the discretised ODF [201]. It is these recalculated pole figures that are presented in this work.

2.8 Transmission Electron Microscopy

Unlike scanning electron microscopy where the electron beam scans the surface of a specimen transmission electron microscopy (TEM) is a technique in which the electron beam is transmitted through the sample. In this work, scanning transmission electron microscopy (STEM) was used together with energy dispersive X-Ray (EDX) spectroscopy in the FEI Titan microscope. In STEM imaging, the instrument is set to focus a probe on surface of the specimen which can be rastered across the specimen surface in much the same way as in the SEM, although in STEM the beam is transmitted through the sample. A wide range of imaging can be carried out in this mode in this work the High Angle Annular Dark Field (HAADF) detector was mainly used. HAADF imaging detects electrons that have scattered through large angles as a result of a collision with an atomic nucleus (Rutherford forward scattering) with the scattering angle a function of the atomic number squared (Z^2) of the scattering nucleus.

STEM combined with EDX spectroscopy allows extremely high resolution chemical data to be extracted and correlated with HAADF images. EDX exploits the characteristic X-ray wavelengths emitted by atoms which are excited by the incident electron beam. These X-rays can be detected at each point producing a spectrum of energies. The presence of an element can be identified by the presence of its characteristic wavelengths in this spectrum and the concentration of each element relative to the others can be estimated by the intensity of each characteristic peak using the Cliff-Lorimer method. In this method

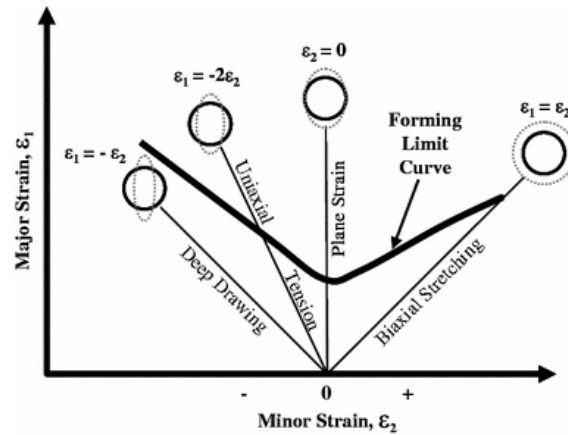


Figure 2.3: Schematic FLD with the principle strain states indicated.

the concentration of each element in the measured area is described as a function of the relative intensity of each characteristic peak weighted by a factor known as the Cliff-Lorimer factor (k). This factor is a function of a variety of factors including the absorption cross-section of each element and machine variables including accelerating voltage[202]. In this work EDX analysis was carried out using the Bruker QUANTAX software. EDX data was acquired using an accelerating voltage of 200kV, beam current of 500pA and a dwell time of $30\mu\text{s}$ was used on each raster point. Samples were prepared by mechanical grinding to $150\mu\text{m}$ followed by dimple grinding to $\approx 20\mu\text{m}$. The precision ion polishing system was then used for 20 hr at 4kV and an incident angle of 6° , to form a small hole in the centre of the specimen.

2.9 Generating a Forming Limit Diagram

The formability of sheet material can be measured using a forming limit diagram or FLD. FLDs are produced by deforming a series of samples to failure in a variety of different strain conditions, from biaxial tension to uniaxial compression, Figure 2.3. The strain to failure is measured in the sheet plane with the primary strain direction ϵ_1 parallel to the gauge length and the minor strain direction ϵ_2 parallel to the gauge width of the specimen, Figure 2.4a). There are a variety of forming limit tests available, in this work the Nakazima [203] test has been used with a hemispherical punch Figure 2.4a) and specimens with a curved gauge length Figure 2.4b).

FLDs were measured for ZEK100 with a sheet thickness of 2.5 mm and gauge length of 50mm. The strain state at failure is varied by changing the gauge width of the specimen, in the present case the gauge width of the specimen was varied from 4.5 mm to 120mm. A gauge width of 120mm represents biaxial tension. All experiments were carried out with the major strain axis ϵ_1 parallel to the TD. The die was lubricated using a thin disk of

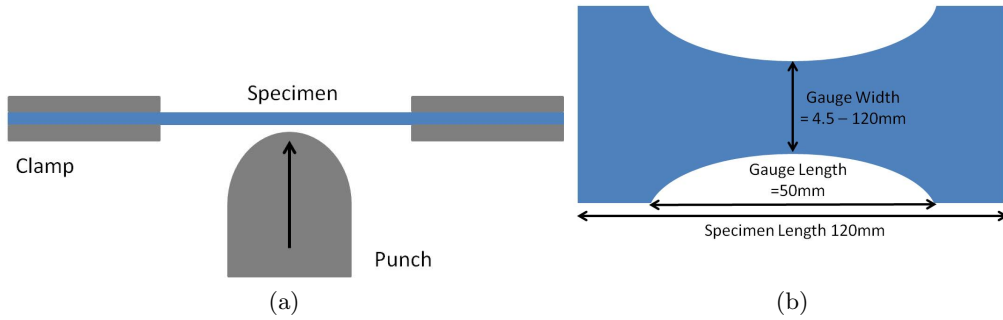


Figure 2.4: a) Schematic diagram of forming press with hemispherical punch. b) Schematic diagram of a Nakazima specimen.

PTFE and machine oil. Specimens were clamped with a force from 20-50 kN depending on specimen size and deformed with a ram speed of 10 mm s^{-1} .

The strains at failure were measured using a digital image correlation (DIC) system on an Erichsen forming press. In DIC the position of surface features on the specimen are tracked in a series of images taken throughout the deformation, the relative movements of these features can be used to generate a 3D strain map of the specimen surface. In this case, specimens were spray painted with thin layer of white primer and then ‘speckled’ with black paint, allowing accurate tracking of the surface shape at high resolution. The DaViz system used a pair of CCD cameras mounted above the forming press with an acquisition frequency of 2 Hz. The strains at failure were then measured using the digital image correlation technique.

2.9.1 Digital Image Correlation

Image correlation is a process of correlating features in two images (before and after) deformation. In this case the aim is to quantify how macroscopic strain is discretised during deformation. As discussed, the specimen is covered in speckle pattern which provides contrast in the image of the specimen surface. Various algorithms are available for carrying out the correlation process, here an algorithm developed by LaVision which uses fast Fourier transforms to compare and correlate subregions within each image was used. Subregions are selected to contain a number of features, which may be used to uniquely identify the region. The optimum size of a feature is 3×3 pixels and a subregion of 32×32 pixels [204]. The size of the subregion is a balance between being large enough to contain enough features to make it unique and small enough to preserve the assumption that strain within the subregion is negligible. In this study a subregion size of 32×32 and an overlap of 30% is used. The DaViz algorithm iteratively searches the after image for the

same subregion found in the before image, the subregion box is allowed to translate, rotate and deform to generate the best match in the after image. This allows the displacement between the two regions to be quantified between time steps t and $t + \delta t$, thus a displacement field for the entire sample at each time step can be calculated. A corresponding strain field can then be generated using the relation

$$\epsilon = \frac{du}{ds} \quad (2.2)$$

where u is the displacement vector from frame t to $t + \delta t$ and s is a spatial direction. The ϵ_1 and ϵ_2 values can then be extracted from the strain field in the image frame prior to failure of the test specimen.

In this study 3D DIC was used due to the 3D nature of the hemispherical punch. In 3D DIC two CCD cameras both of which have known positions in relation to the specimen surface are used. Similar correlation algorithms to 2D DIC are used to determine the surface height of the specimen at each time step by correlating subregions of the sample observed in each camera. Then regions of the specimen surface are correlated between time steps to generate a 3D displacement map of the surface from which a strain map can be generated as discussed above [205]. Full details of this method are given elsewhere [204–207].

Chapter 3

Results

3.1 Hot Rolling

Initially all experimental magnesium-RE alloys were hot rolled at 400°C and annealed for an hour according to the conditions described in Section 2.2. Under these conditions the RE effects should be active allowing a comparison of these effects between each alloy.

3.1.1 Magnesium-Y Alloys

Y has a high solubility in magnesium and as Figure 2.0 c) shows the Y alloys have spread of compositions from almost pure magnesium to the solubility limit of Y in magnesium. Representative microstructures and $\{0001\}$ pole figures of the as rolled and annealed magnesium-Y binary alloys are shown in Figure 3.1. After hot rolling all alloys showed a strong basal texture typical of magnesium, with basal planes parallel to the sheet ND. After full RX during a 1hr heat treatment at 400°C the more concentrated alloys (Y > 0.15 at%) showed significant texture weakening, with the most concentrated alloy 0.2022 at% Y showing the largest fall in texture intensity of 9 mrd. This texture weakening during annealing is characteristic of the RE texture weakening reported in the literature, Section 1.6.1. Alloys below the critical Y concentration (0.009 and 0.0797 at% Y) demonstrated only a slight texture weakening or strengthening during annealing. The most dilute alloy 0.009 at% Y presented basal textures much stronger than any other alloy primarily due to the significantly larger grain sizes in this material, Figure 3.1 a). Basal texture strength vs Y concentration of the alloys produced in this work against literature values is plotted in Figure 3.3, showing the behaviour of the present alloys is quite consistent with the literature. Representative $\{10\bar{1}0\}$ prismatic pole figures for the 0.0797 at%Y and 0.1523 at% Y alloys, which are below and above the critical RE concentration respectively, are

shown in Figure 3.2. In the as rolled condition, the prismatic textures are very weak ($\times 2$ mrd) showing only very slight peaks with $\langle 01\bar{1}0 \rangle$ parallel with the RD. After RX there is very little change in the texture of either alloy. RE texture weakening is clearly most significant in spreading $\{0001\}$ textures in magnesium alloys.

Most of the deformed microstructures are typical of magnesium showing heavily deformed material where shear bands are prevalent. The lowest concentration alloy (0.009 at% Y) has a quite different microstructure with large grain size and significant mechanical twins visible. Negligible alloying additions in this case are believed to lead to significant recrystallisation and grain growth during reheating processes between each rolling pass. Small RX grains visible in the low concentration alloys such as 0.0797 at% Y, may also have formed during reheating processes although it is not possible to distinguish such SRX grains from DRX grains formed (and deformed) in the final rolling pass. Low magnification images of shear banding in the highest and lowest concentration alloys are shown in Figure 3.4, demonstrating the significant difference in behaviour as a result of Y addition. In the low concentration 0.009 at% and 0.0797 at% Y alloys, small numbers of relatively large shear bands are observed while in the more concentrated 0.2022 at% Y alloy (showing RE effects) large numbers of smaller shear bands are visible. This more even distribution of smaller shear bands is a characteristic effect of RE additions as discussed in Section 1.7.1.

3.1.2 Magnesium-La Alloys

La alloys were chosen because La has a low solubility in magnesium (0.006 at%), as the RE effect is a solute based effect we are primarily interested in alloys with La concentrations below the solubility limit of La in magnesium. However, the La concentration of such alloys is so low that we were unable to produce such dilute alloys. As a result all La alloys have concentrations above the La solubility limit Figure 2.0 c). At such concentrations La precipitates are likely to form even in the most dilute alloy (0.005 at% La), depleting the matrix of solute La. As the RE effects are known to be solute based this may limit the effectiveness of La as a texture weakener. Figure 3.5 shows the basal $\{0001\}$ pole figures of the as rolled and annealed La alloys. As expected, all alloys show strong basal textures after rolling, these textures weaken by $\times 2 - 3$ mrd after full recrystallisation. Interestingly, in the more concentrated La alloys the texture weakens less than in the most dilute alloy, this could be due to a lower matrix La concentration as a result of increased precipitation in this alloy. Figure 3.6 shows the prismatic pole figures for two of the La alloys after hot rolling and annealing. Like the Y alloys the prismatic texture is not greatly affected during annealing, showing a negligible fall in texture strength.

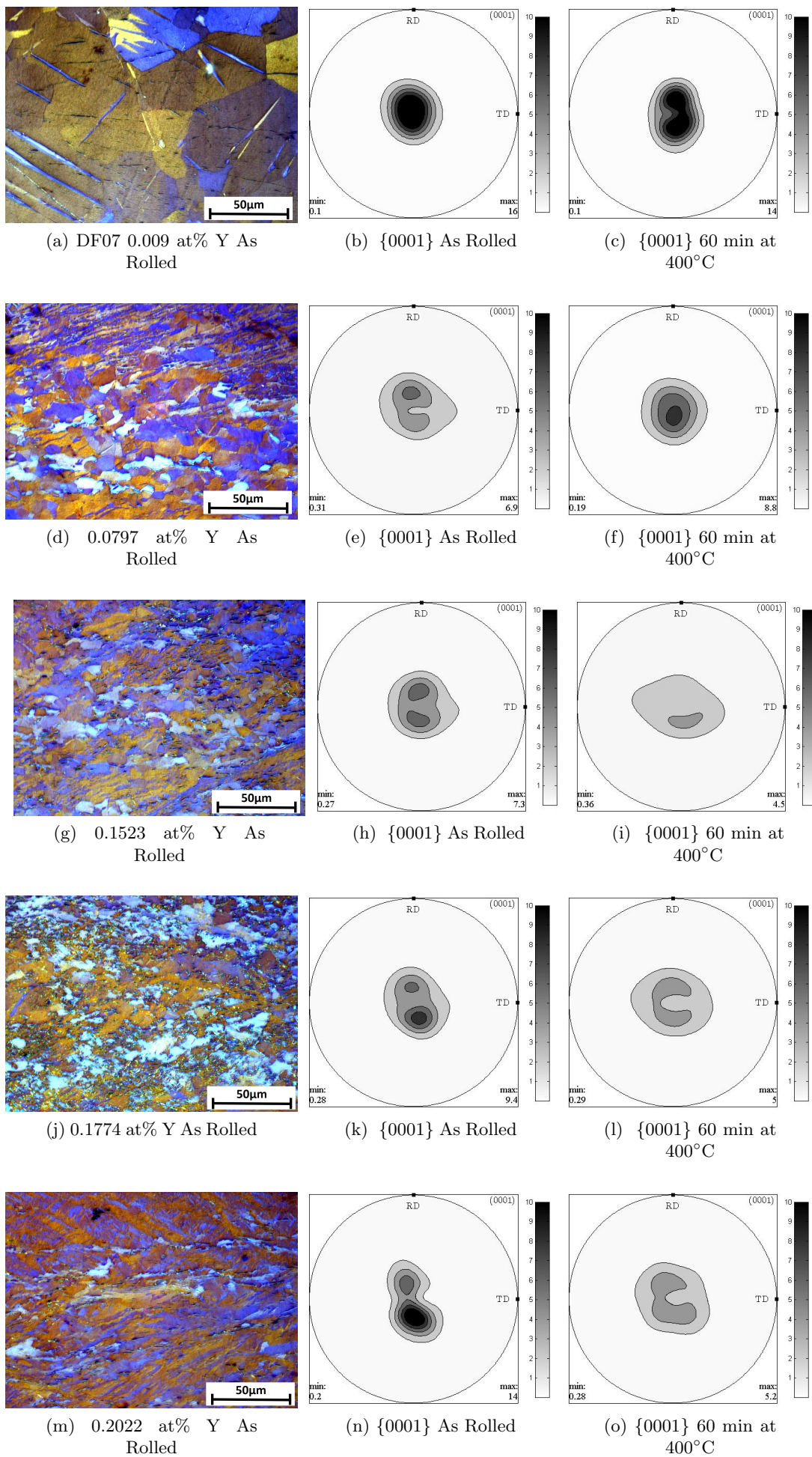


Figure 3.1: Microstructures of Y alloys after rolling at 400°C in 7 passes pf $\epsilon_T \approx 20\%$

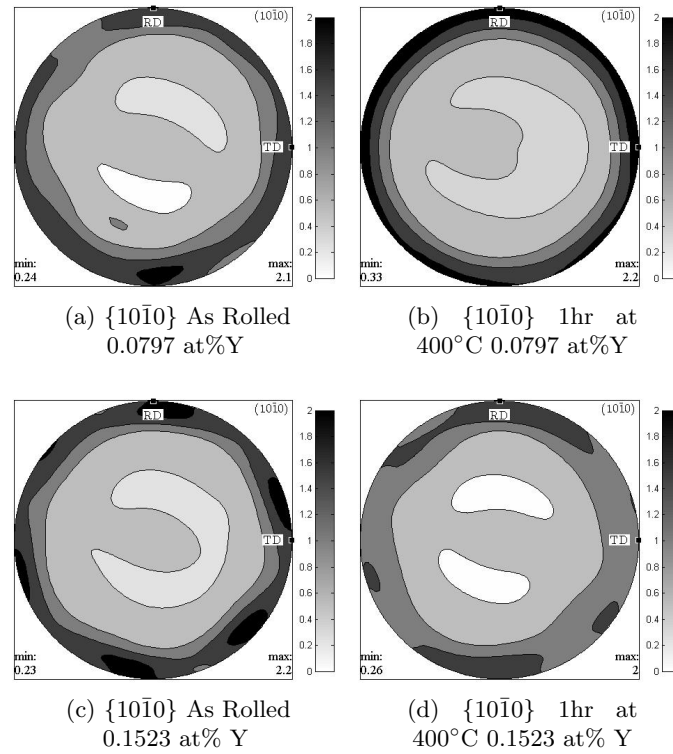


Figure 3.2: $\{10\bar{1}0\}$ pole figures for the 0.0797 at% Y (below critical concentration) and 0.1523 at% Y (above critical concentration) alloys in as hot rolled and annealed conditions. The 0.1523 at% Y pole figures are representative of the other binary Y alloys showing the RE effect.

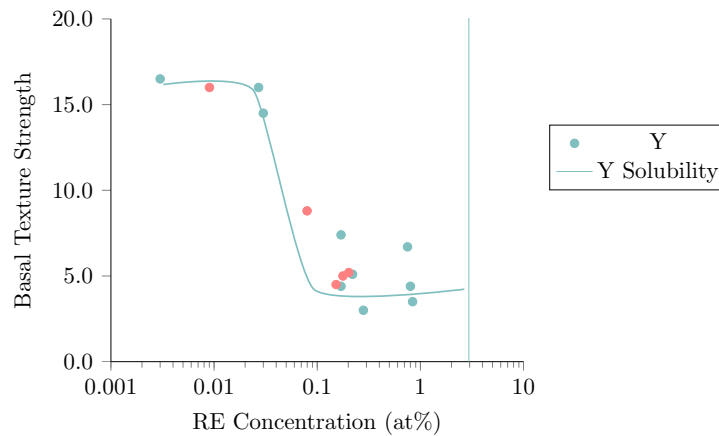


Figure 3.3: Comparison between the annealed basal texture intensity of the Y alloys (red) with literature data (green) from Hantzsche *et.al* [149].

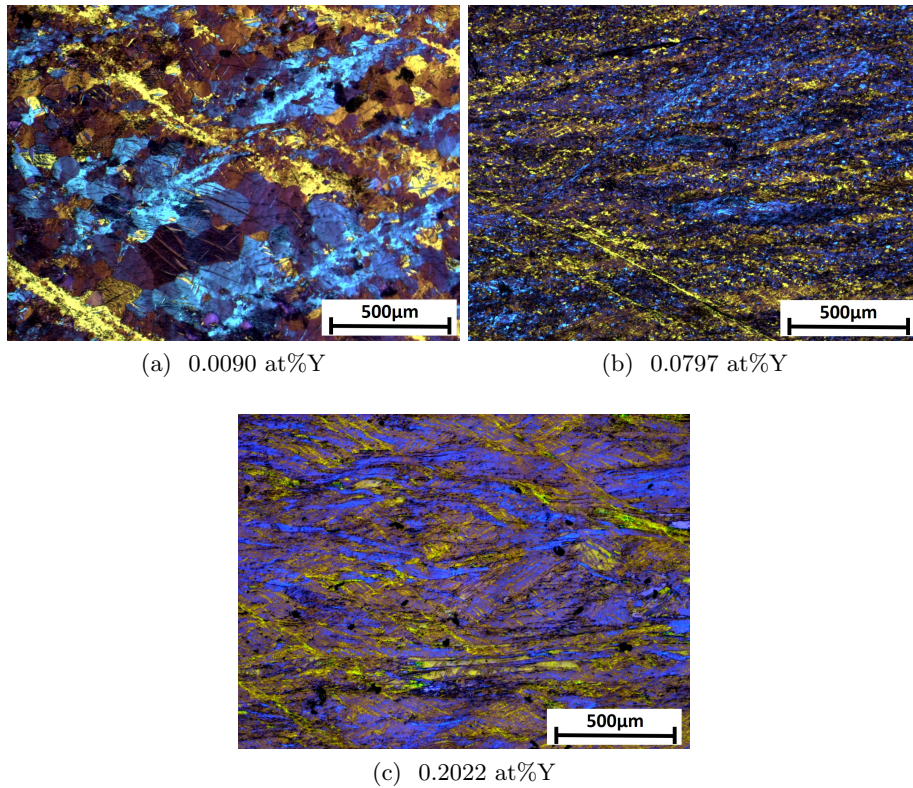


Figure 3.4: Low magnification images of 0.009 at% and 0.0797 at% Y (below critical concentration) and 0.2022 at% Y (above critical concentration) alloys after rolling at 400°C and quenching. Fewer larger shear bands are visible in the more dilute alloys while a more even distribution of finer shear bands is present in the more concentrated alloy.

Microstructures of the alloys, Figure 3.5a,d,g), are very similar showing high levels of deformation and prominent mechanical twinning. When viewed at lower magnification, Figure 3.7, the microstructures also appear similar with small numbers of intense shear bands visible. These microstructures are in contrast to the high concentration Y alloys, where a large number of fine shear bands are visible in the microstructure, Figure 3.4b). The La alloy microstructures are more similar to the dilute Y alloys (below critical concentration) where shear bands were larger and fewer in number.

3.1.3 Magnesium Ce, Yb, Nd and Eu Alloys

For each remaining RE element of interest a single alloy was produced with a target composition close to the estimated critical concentration of RE. The microstructures and basal pole figures of the as rolled and annealed material are presented in Figure 3.8. Recrystallised grain size is also given because a significant variation in grain size has an impact on

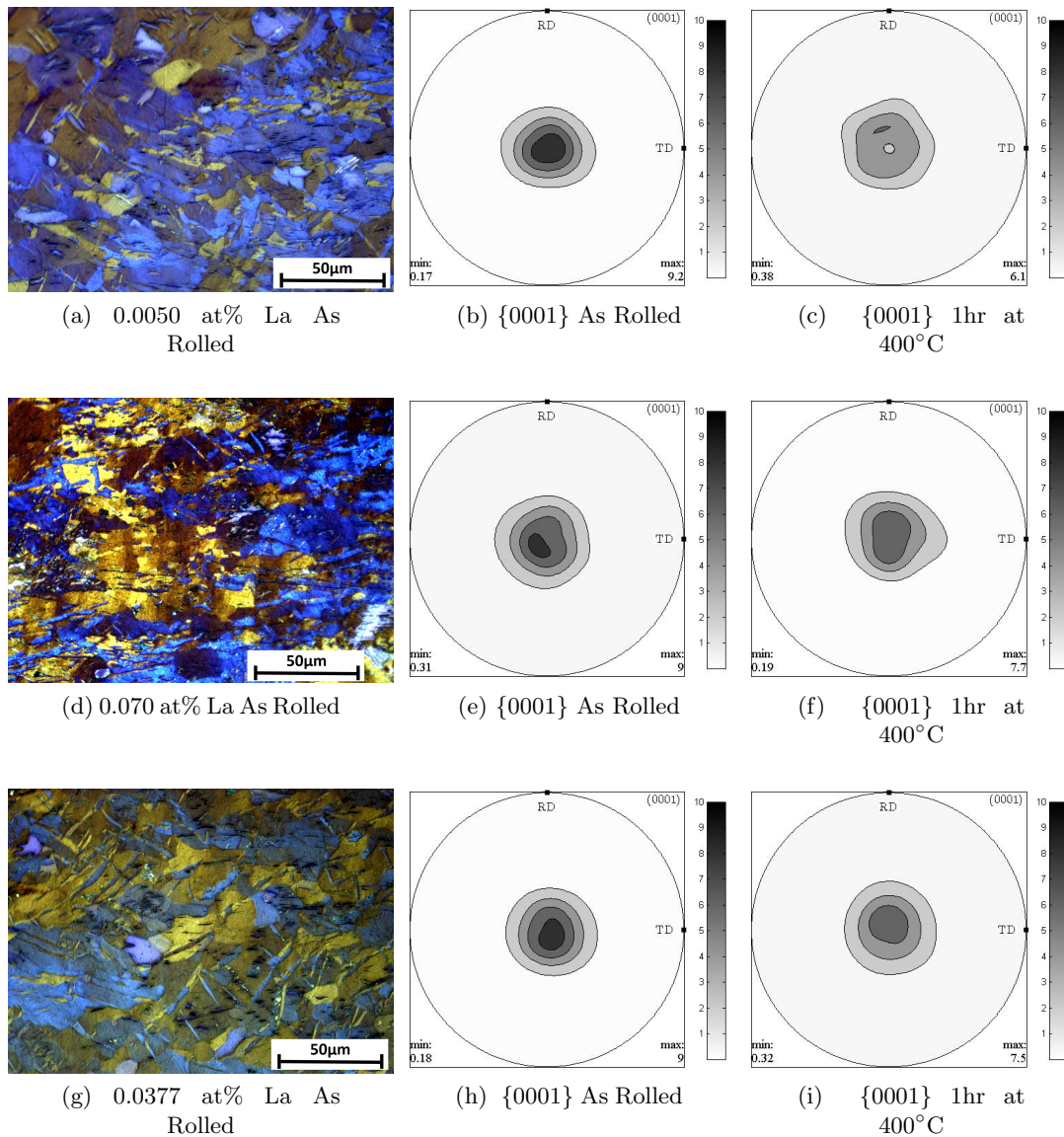


Figure 3.5: Microstructures and $\{0001\}$ pole figure of the La alloys after rolling and annealing for 1hr at 400°C

texture intensity, larger grains strengthening texture. $\{10\bar{1}0\}$ prismatic textures are omitted for brevity, however in each case a similar behaviour to the Y and La alloys is observed.

Ce

The 0.0349 at% Ce alloy has a composition just below the solid solubility of Ce in magnesium at 500°C, meaning some Ce precipitates are likely after rolling at 400°C. The as rolled microstructure and basal pole figures in as rolled and annealed condition are shown in Figure 3.8 a-c). The as rolled condition is highly deformed with a strong basal texture strength of $\times 12$ mrd with no evidence of dynamic recrystallisation during rolling.

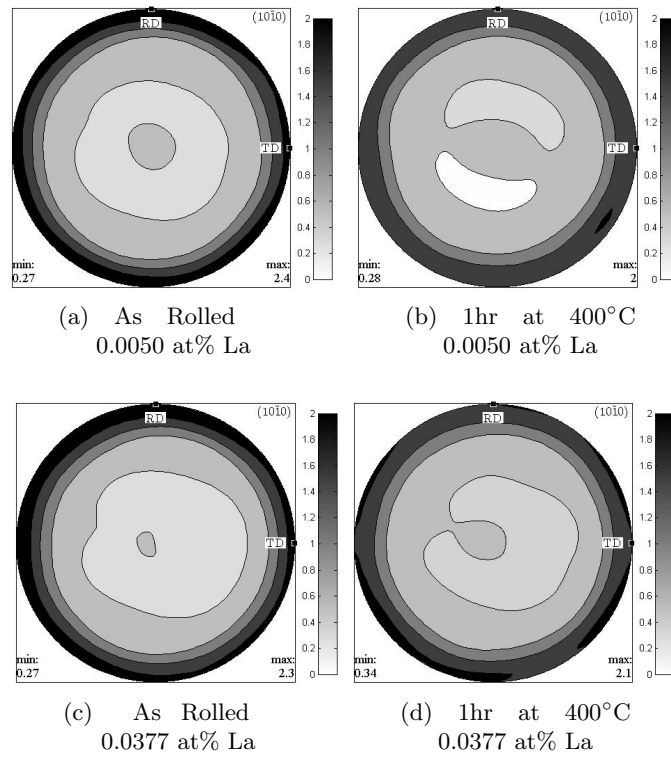


Figure 3.6: Figure showing the $\{10\bar{1}0\}$ pole figures for the 0.0050 and 0.0349 at% La alloys in the as hot rolled condition and after annealing for 1hr at 400°C.

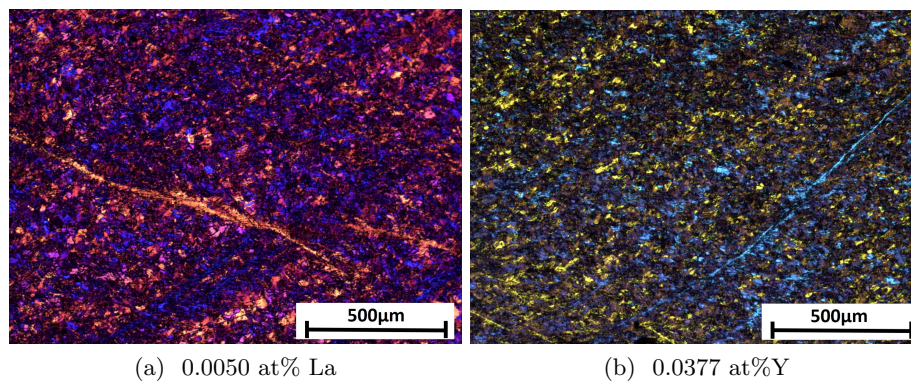


Figure 3.7: Low magnification images of 0.0050 at% La and 0.0377 at% La alloys after rolling at 400°C and quenching.

After annealing this basal texture strength falls to $\times 9$ mrd, this texture weakening is significantly less than that in the Y alloys displaying RE texture weakening. Figure 3.9 plots the annealed texture strength of the 0.0349 at% Ce alloy against literature values, showing that this alloy is at the lower end of the Ce concentration range that would be expected to produce RE texture effects. While the texture does weaken during RX in this alloy, the recrystallised texture strength is significantly higher than that of similar Ce alloys showing the RE effect.

Yb and Eu

Yb and Eu are both elements with a large atomic size, however they have very different solubilities in magnesium. Yb has a high solubility while Eu has a very low solubility, Figure 2.0 e-f) shows the Yb alloy has a Yb concentration well below the solubility limit while the Eu alloy has a composition above the solubility limit. In both cases, the absolute concentrations of Yb and Eu (0.0210 and 0.0008 at% respectively) are very low. Figure 3.8 d-i) shows the as rolled microstructure, basal texture and the annealed basal texture of the rolled alloys. Both alloys display typical strong basal textures in the as rolled condition which weaken during recrystallisation. Yb basal texture intensity halves during DRX while Eu only slightly reduces by 4 mrd. Very strong basal textures in the Eu alloy are at least partly due to the large grain size, which is $97\mu\text{m}$ in the recrystallised condition in comparison to $48\mu\text{m}$ in the Yb alloy. Deformation microstructures between the materials are also very different with the Eu alloy producing a small number of very large shear bands, while the Yb alloy produces a more homogeneously deformed microstructure with extensive deformation twinning.

Nd

The Nd alloy was chosen for comparison with the commercial ZEK100 alloy. Nd has a relatively high solubility in magnesium (≈ 0.4 at% Nd), this alloy has a concentration of 0.0243 at% Nd, well below the solubility limit (Figure 1.6.1). Figure 3.8 k,l) shows the Nd alloy forms a normal basal texture in the as rolled condition, which falls only marginally by 1 mrd during recrystallisation, and develops a slight spreading of the texture in the TD. The microstructure of this material is very deformed with deformation heterogeneously distributed into coarse shear bands and heavily deformed grains. Figure 3.10 plots the composition and recrystallised texture intensity of this alloy against the data of Hantzsche *et.al* showing that this alloy is at the low end of compositions which might be expected to produce RE effects. The recrystallised texture strength of this alloy is significantly higher (7.1 mrd) than that of the other alloys demonstrating the RE texture effect (≈ 4.5 mrd) and is below the critical concentration Hantzsche *et.al* consider required to activate the

RE effect, > 0.041 at% Nd [177].

Gd

Gd has a very similar solubility in magnesium to Y and this dilute magnesium 0.0224 at% Gd alloy should behave similarly to the 0.0797 at% Y alloy previously reported in Figure 3.1 d-f) which showed a texture strengthening during recrystallisation. This is not found in the Gd case where the recrystallised texture weakens slightly during recrystallisation (by 5 mrd), although the overall intensity remains high (10 mrd), Figure 3.8 n,o). There are also significant microstructural differences between the two alloys, with the Gd alloy showing much less evidence of recrystallisation in the as rolled condition, all grains appear heavily deformed and significant twinning and shear banding are visible.

3.1.4 Commercial Alloys ZEK100 and AZ31

Commercial magnesium alloys were also studied in this work, ZEK100 (0.0351 at% Nd, 0.695 at% Zn, 0.08 at% Zr) and AZ31 (2.705 at% Al and 0.372 at% Zn). The Nd concentrations of ZEK100 and the 0.0243 at% Nd binary alloy are plotted on Figure 2.0 d) showing that both alloys have a similar Nd content. The as received material was hot rolled with the microstructure, $\{0001\}$ and $\{10\bar{1}0\}$ pole figures shown in Figure 3.11a-c). In the as received condition, the material is almost fully recrystallised and the $\{0001\}$ pole figure shows a weak texture of 2.2 mrd expected of a RE alloy. The texture morphology is very different to the binary 0.0243 at% Nd alloy after rolling, Figure 3.8. In ZEK100 the basal pole is split into two lobes tilted towards the TD, typical of magnesium zinc-RE alloys as discussed in Section 1.6.1. The prismatic $\{10\bar{1}0\}$ pole figure has an even weaker texture than the basal pole figure with the prismatic poles tilted out of the RD-TD plane. Again this is in contrast to the binary Nd alloy which has the normal prismatic texture of magnesium alloys with prismatic poles evenly distributed perpendicular to the ND, within the RD-TD plane (Figure 3.11 f).

AZ31 is a typical non-RE alloy included for comparison with the RE containing alloys described above. It was received as rolled sheet with recrystallised microstructure and typical magnesium basal texture, Figure 3.11 d-f).

3.1.5 Summary

In summary all the alloys investigated produced strong basal textures typical of magnesium during rolling and in the majority of cases these textures weakened during subsequent recrystallisation. However, the magnitude of texture weakening relative to the as rolled

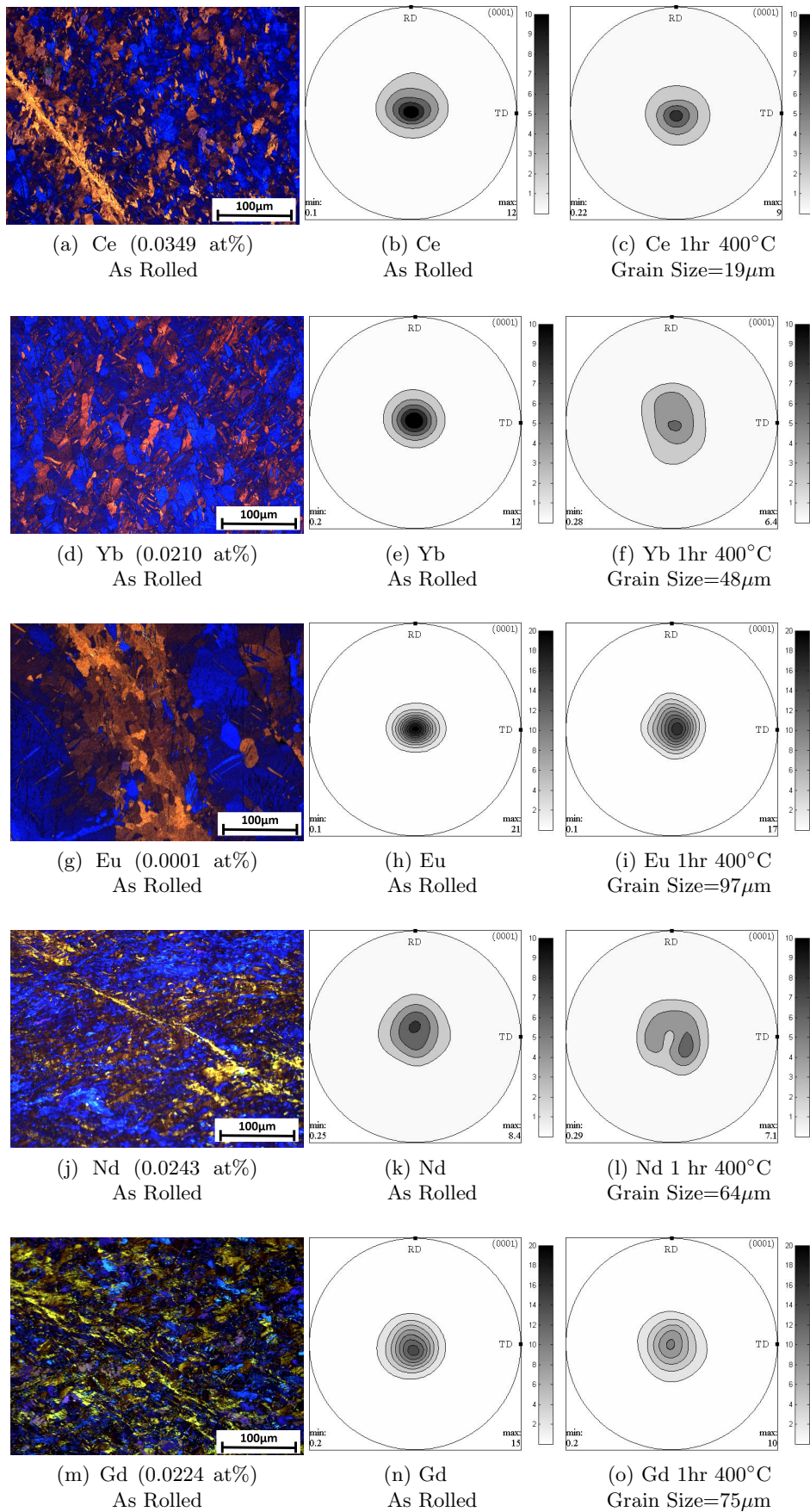


Figure 3.8: Microstructures of Ce, Yb, Eu, Nd and Gd alloys after rolling at 400°C. The $\{0001\}$ pole figures show the texture of the as rolled material in the as rolled condition b),e),h) and after annealing at 400°C for 1hr leading to full recrystallisation c), f) and i). The grain sizes as measured by the linear intercept method are given for the recrystallised material.

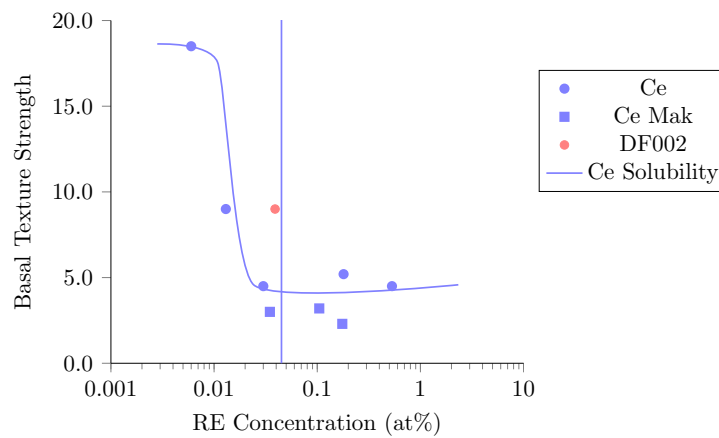


Figure 3.9: Figure plotting Ce concentration against peak basal texture strength after rolling and full recrystallisation, data from Hantzsche *et.al* (blue) circles [149], Mackenzie *et.al* squares [138], together with the composition of our alloy (red). The solubility of Ce in magnesium is also displayed as a vertical blue line [172].

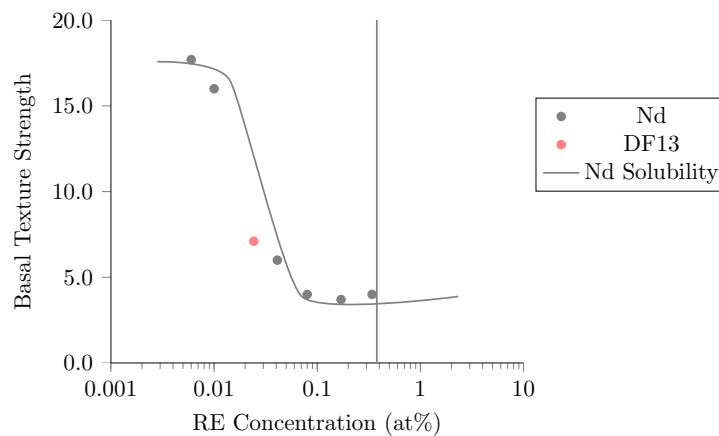


Figure 3.10: Figure plotting Nd concentration against peak basal texture strength after rolling and full recrystallisation, data from Hantzsche *et.al* black [149], together with the composition of our alloy 0.0243 at% Nd (DF013), red. The solubility of Nd in magnesium is also displayed as a vertical red line [172].

texture varies considerably and in many cases it is difficult to determine if the RE effects are active. In the following some of these alloys are statically recrystallised after cold rolling which decouples dynamic effects and allows recrystallisation to be observed during a static annealing process. In particular the extent of texture weakening in each alloy can be quantified.

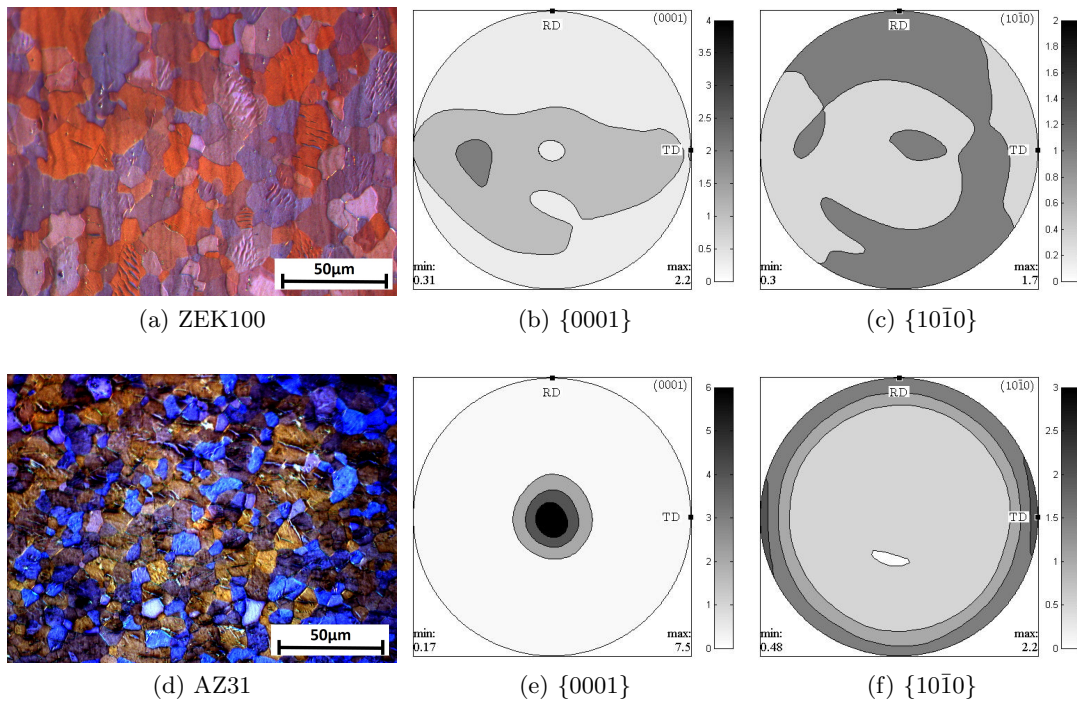


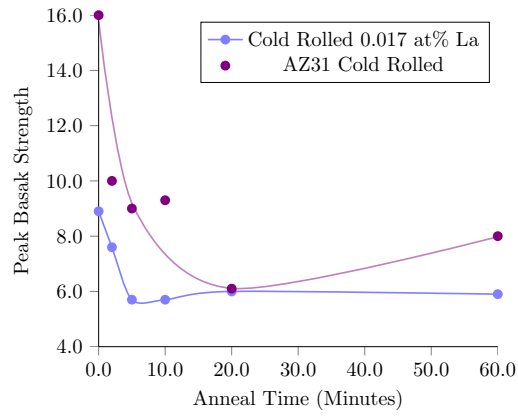
Figure 3.11: Figure showing the microstructure and the $\{0001\}$ and $\{10\bar{1}0\}$ pole figures of the as received ZEK100(a, b, c) and AZ31 (d, e, f). The pole figures have been measured by XRD.

3.2 Static Recrystallisation of Magnesium Sheet

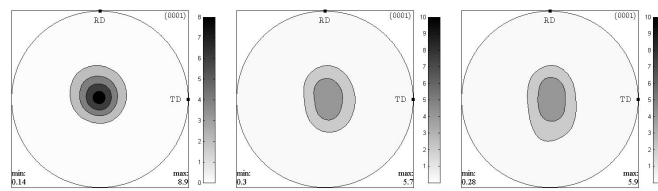
3.2.1 Cold Rolling of AZ31 and Dilute Magnesium-La Alloys

In the as hot rolled condition all of the alloys presented deformed microstructures, with varying amounts of DRX or SRX between rolling passes. In some of the more dilute alloys the texture weakening during SRX is likely to be similar to that observed in the non-RE alloys where static recrystallisation of deformed grains occurs. Cold rolling prevents DRX during deformation and so, during subsequent annealing, recrystallisation is entirely static. The AZ31 and 0.017 at% La alloys were chosen for this experiment as examples of a non-RE alloy and a dilute RE alloy where texture weakening after hot rolling was minimal. AZ31 and the La alloy were cold rolled according to the schedule in Table 3.1. The strain per pass in AZ31 was higher than in the La alloy as the AZ31 sheet was thinner and the minimum reduction possible per pass was $\approx 0.1\text{mm}$. The AZ31 was also rolled to a much higher total strain than the La alloy. After cold rolling static recrystallisation occurred during annealing at 400°C , during which changes in texture and microstructure were monitored.

The change in basal texture intensity with annealing time is plotted in Figure 3.12a), with pole figures presented in Figure 3.12b-m). After cold rolling all alloys presented



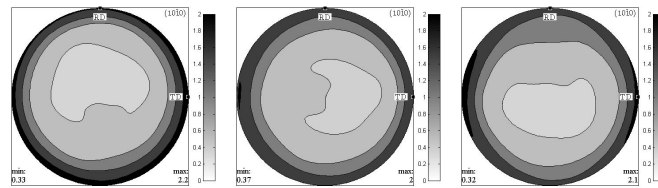
(a)



(b) La Cold Rolled As Rolled

(c) La Cold Rolled 5 min Anneal

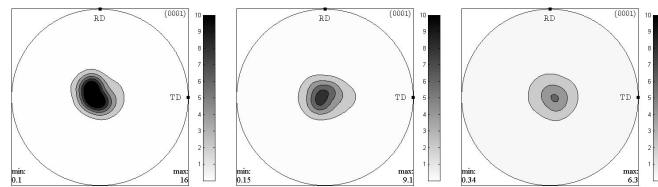
(d) La Cold Rolled 20 min Anneal



(e) La Cold Rolled As Rolled

(f) La Cold Rolled 5 min Anneal

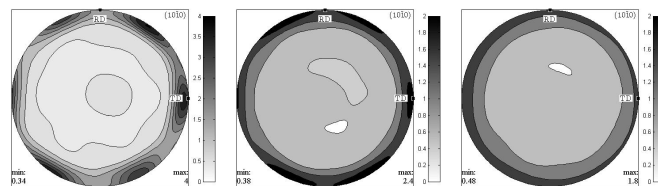
(g) La Cold Rolled 20 min Anneal



(h) AZ31 Cold Rolled As Rolled

(i) La Cold Rolled 5 min Anneal

(j) La Cold Rolled 20 min Anneal



(k) AZ31 Cold Rolled As Rolled

(l) La Cold Rolled 5 min Anneal

(m) La Cold Rolled 20 min Anneal

Figure 3.12: a) Plot of the basal texture strength Vs annealing time at 400°C. For cold rolled magnesium-0.020at% La, 0.08 at% Y and AZ31. Curves fitted to guide the eye. b-m) textures of La and AZ31 in the as cold rolled condition together with annealed textures after 5 and 20 minutes annealing.

Table 3.1: Cold rolling schedule for AZ31 and magnesium 0.0170 at% La alloy. Prior to cold rolling the AZ31 and hot rolled La alloy were annealed for 1hr at 400°C to fully recrystallise.

Pass	La True Strain	La t (mm)	AZ31 True Strain	AZ31 t (mm)
0	-0.02	4.90	-0.04	2.65
1	-0.03	4.81	-0.08	2.55
2	-0.04	4.76	-0.12	2.45
3	-0.07	4.69	-0.16	2.35
4	-0.09	4.57	-0.21	2.25
5	-0.12	4.46	-0.26	2.15
6	-0.15	4.34	-0.31	2.05
7	-0.18	4.22	-0.36	1.95
8	-0.20	4.11	-0.41	1.85
9	-0.23	4.00		
10	-0.26	3.89		

strong textures typical of the hot rolled conditions discussed in Section 3.1, these basal textures weaken by approximately half during annealing in both. The minimum in basal texture intensity corresponds to the full recrystallisation of the material, observed in optical micrographs. AZ31 has an as rolled texture intensity twice that of the 0.017 at% La alloy, most probably due to the increased strain the AZ31 underwent during cold rolling, Table 3.1. This may also be partly be responsible for the presence of $\{0001\}\langle 11\bar{2}0\rangle$ texture component in the as cold rolled texture, Figure 3.12k). During recrystallisation this component spreads completely disappearing after 20 minutes annealing where the prismatic poles become evenly distributed perpendicular to the ND.

3.2.2 Cold Rolling of Magnesium-Y Alloys

Similar cold rolling experiments were carried out on some of the concentrated magnesium-Y alloy systems which were cold rolled after hot rolling and annealing for 1hr at 400°C as described in Section 3.1.1. Three compositions were selected for cold rolling: 0.08 at% Y which is below the critical concentration of Y required for texture weakening, 0.15 at% Y and 0.18 at% Y which are both above the critical concentration. These alloys were cold rolled according to the schedule in Table 3.2 and annealed for 1hr at 400°C causing full recrystallisation.

$\{0001\}$ and $\{10\bar{1}0\}$ pole figures for the as rolled and recrystallised material are shown in Figure 3.13. The as cold rolled textures of all three alloys are very similar showing a basal texture split slightly in the RD with an intensity ≈ 6 mrd. After one hour at 400°C all alloys had fully recrystallised and the 0.08 at% Y alloy showed a slight strengthening of the basal texture intensity and a move back to a single peak in the basal texture. In

Table 3.2: Cold rolling schedule for the magnesium-Y binary alloy systems.

Pass	True Strain		
	0.08 at% Y	0.15 at% Y	0.18 at% Y
0	-0.02	-0.03	-0.03
1	-0.04	-0.04	-0.04
2	-0.05	-0.06	-0.06
3	-0.07	-0.08	-0.08
4	-0.09	-0.10	-0.09
5	-0.11	-0.12	-0.12
6	-0.14	-0.14	-0.14
7	-0.16	-0.17	-0.17
8	-0.18	-0.19	-0.19
9	-0.21	-0.22	-0.21
10	-0.23	-0.24	-0.24
11	-0.26	-0.26	-0.26
12	-0.28	-0.29	-0.29
13	-0.32	-0.32	-0.32
14	-0.34	-0.34	-0.34
15	-0.38	-0.37	-0.38
16	-0.41	-0.41	-0.41
17	-0.44	-0.44	-0.44

contrast both alloys with Y concentration above the critical concentration showed a fall in texture intensity by approximately half and a distinct spreading of the basal texture about the ND.

The prismatic $\{10\bar{1}0\}$ textures of all the as rolled materials were very similar to hot rolled magnesium with prismatic poles evenly distributed perpendicular to the ND. After recrystallisation the 0.08 at% Y alloy forms the $\{10\bar{1}0\}\langle 10\bar{1}0\rangle$ texture component with a slight strengthening in intensity. The prismatic texture in the more concentrated alloys remains diffuse, weakening slightly during recrystallisation.

Clearly there is a difference in the recrystallisation behaviour of the Y alloys above and below the critical concentration, this is observed by comparing the partially recrystallised microstructure in cold rolled Y alloys above and below this concentration. Figures 3.14 a,b) show EBSD maps of two such alloys after annealing for 4 minutes at 350°C after cold rolling, the 0.08 at% Y alloy is $\approx 36\%$ recrystallised while the 0.15at% Y alloy is $\approx 43\%$ recrystallised. Figures 3.14 c,d) plot the kernel average misorientation between neighbouring points within a grain for the same maps, clearly identifying deformed (blue) and recrystallised (white) grains. In the dilute 0.08 at% Y alloy the number of recrystallised grains is smaller and the recrystallised grain size larger than in the more concentrated 0.15 at% Y alloy. The deformed grains in the more concentrated alloy contain more stored energy than the dilute alloy as indicated by the darker blue colouring in the KAM map

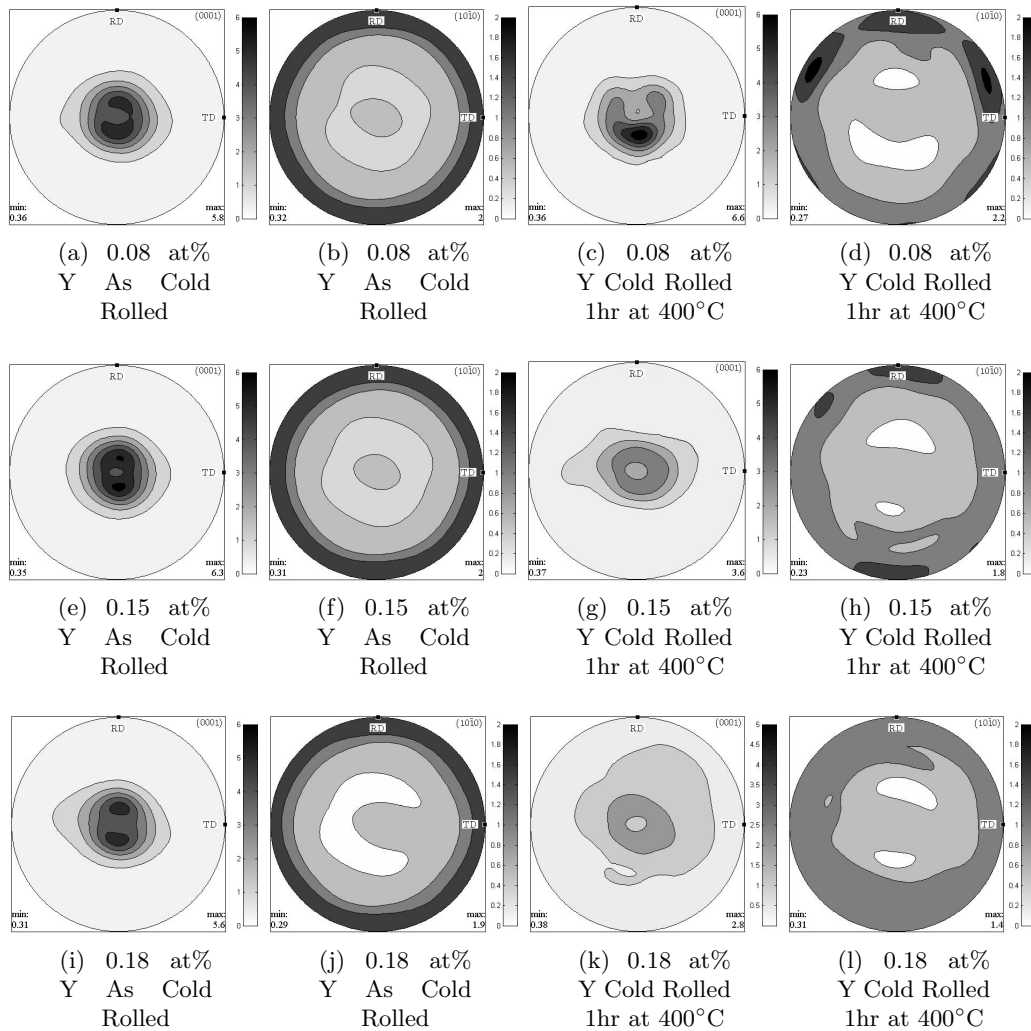


Figure 3.13: Textures of magnesium-Y alloys in the as cold rolled and recrystallised conditions. $\{0001\}$ and $\{10\bar{1}0\}$ pole figures are shown of the 0.08, 0.15 and 0.18 at% Y alloys.

showing larger average misorientation between neighbouring points. High stored energy in RE alloys is also reported by Stanford *et.al* [179] when comparing a magnesium-Gd alloy to AZ31. In the current study we see the RE texture weakening only occurs once Y concentration reaches a critical value and this appears to be associated with an increase in stored energy after partial SRX. As both alloys underwent identical cold deformation with minimal recovery or DRX, it is assumed that the stored energy in the as cold rolled material is similar in both alloys and that differences in stored energy after SRX are due to the distribution of this stored energy in the original deformed microstructure and not simply the concentrated alloy having a higher initial stored energy. In the concentrated alloy, deformation is more homogeneous with strain accommodated equally throughout the microstructure, while in the dilute alloy it is expected that strain is concentrated in

localised regions, which have subsequently recrystallised. There is a precedent in the literature for more even strain distribution in RE alloys with Sandlöbes *et.al.* observing a far more uniform strain distribution in a magnesium 0.838 at% Y alloy in comparison to pure magnesium Figure 1.36 [94]. Regions of concentrated strain in the dilute alloy are hidden from the EBSD map in Figure 3.14 as these areas are likely to recrystallise first during the 4 minute heat treatment. As a result the dilute alloy retains less stored energy after the 4 minute anneal than the concentrated alloy because recrystallised grains have quickly consumed the regions of locally high stored energy leaving only comparatively low energy in surrounding deformed grains. In contrast nucleation of recrystallised grains appears to be much more widespread in the concentrated alloy, due to more evenly distributed stored energy, so while a similar fraction of the material has recrystallised there is a larger number of smaller recrystallised grains in this material.

The differences in deformation behaviour between the two alloys are further emphasised in Figure 3.14 e,f) which shows twin boundaries present in both materials. The concentrated alloy clearly contains a larger number of compression and double twins in comparison to the dilute alloy, in which primarily tension twins are found. Similarly high levels of compression and double twinning in the magnesium-Y system, in comparison to pure magnesium, have also been reported by Sandlöbes *et.al.*[94]. However, the present study shows the change in twin activity, and stored energy, are not simply due to Y addition but a critical concentration of Y is required to change deformation behaviour and this appears to be closely linked to the activation of RE texture weakening. In addition to changes in the twinning behaviour intragranular misorientation axis (IGMA) analysis of deformed grains shows a difference in the distribution of geometrically necessary dislocations (GND) between the two materials, Figure 3.15. The concentrated Y alloy shows a distinct $\{0001\}$ peak in its misorientation axis distribution (Figure 3.15 f)) not present in that of the dilute alloy (Figure 3.15 e)). An $\{0001\}$ peak is characteristic of prismatic slip (see Table 1.4 for characteristic IGMA axes), suggesting prismatic slip is more active in the concentrated Y alloy, similar observations have been made in other RE alloys [95, 134, 160, 176]. Figure 3.16 shows IGMA analysis for a number of individual grains of various orientations the $\{0001\}$ peak is not exclusively observed in grains of a particular orientation. In particular grains A and C have similar basal orientations however, the $\{0001\}$ peak is only present in the C grain, suggesting the factor controlling prismatic GND population is more subtle than grain orientation.

It is also important to determine the extent of changes to the recrystallisation mechanism in magnesium-Y alloys above and below the critical concentration. This is may be significant for formation of RE textures if the SRX mechanism is found to be different in the concentrated alloy, nucleating RE orientations. Figure 3.17 highlights recrystallising regions in the concentrated alloy, in which widespread strain induced grain boundary

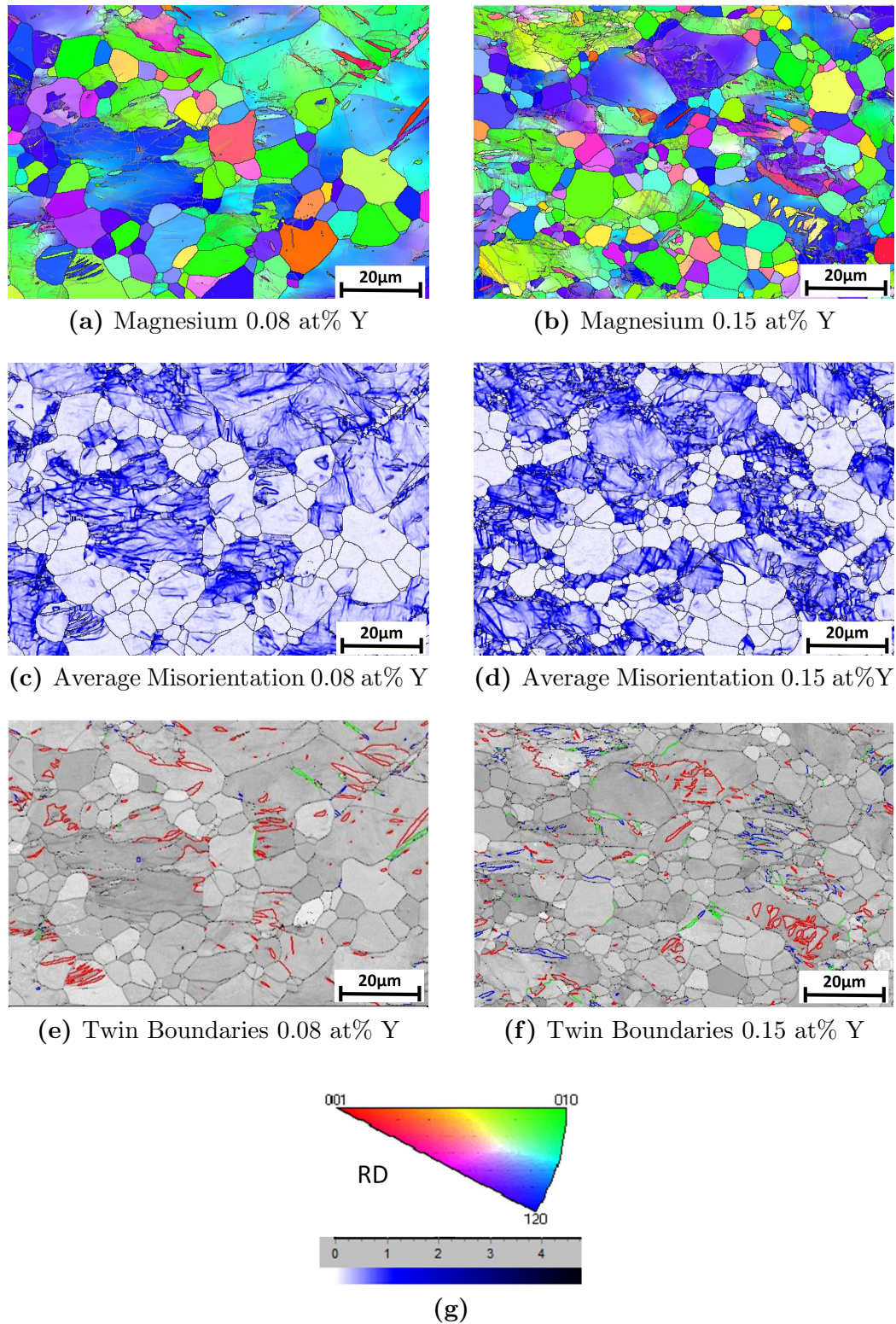


Figure 3.14: Figure showing EBSD maps for magnesium 0.08 at% Y and 0.15 at% Y alloys cold rolled and annealed for 4 minutes at 350°C. a,b) IPF maps relative to sheet rolling direction, c,d) kernel average misorientation maps, e,f) twin boundary maps for tension (red), compression (blue) and double twins (green), g) IPF colour scheme and misorientation colouring.

migration is observed, Section 1.5.2.1. Both highlighted regions show a recrystallising grain, which appears white in KAM maps due to low local misorientation, growing into a neighbouring deformed grain. The recrystallising grain occurs at a bulge in the prior grain boundary and is bounded by a low angle boundary with the parent grain (blue line) and a high angle boundary with the neighbouring grain. As expected the recrystallising SIBM grain has a very similar orientation to the parent grain. This recrystallisation mechanism is commonly reported in magnesium alloys and its activity is not necessarily associated with RE textures, as many magnesium alloys recrystallise by SIBM and show no texture weakening. This point is underlined in Figure 3.18 where SIBM is also found to be active in the dilute Y alloy which does not show texture weakening after full recrystallisation (Figure 3.13 c)). While SIBM is not necessarily the only SRX mechanism operational it is difficult to identify a characteristic RE SRX mechanism from these maps that could cause weak recrystallisation textures in the RE alloy. The deformation and recrystallisation textures of both alloys are presented in Figure 3.19, showing the recrystallised grains in both alloys have comparable orientation distributions, which appear to be broadly similar to the deformed parent grains. Although even if a different SRX mechanism were operational in the concentrated Y alloy it would be difficult to detect in this way as it must nucleate grains with a slightly weaker basal texture than in the dilute Y alloy and not completely new texture component, which would be much easier to detect.

In summary, cold rolling and recrystallisation of magnesium-Y alloys produces weak basal textures where Y concentration is above the critical limit and strong basal textures below the critical limit. As both materials produce basal textures it is difficult to isolate the ‘RE’ grains in the microstructure during recrystallisation and recrystallised grains in both alloys appear to nucleate by similar mechanisms, SIBM in particular is found to be active in both alloys. The primary differences between the concentrated alloy and the dilute alloy are a finer recrystallised grain size and more homogeneous strain distribution in the concentrated alloy. These effects are commensurate with an increased number of contraction and double twins in the concentrated alloy together with an increase in prismatic GND’s. In Section 5.1 we discuss how these effects could lead to weaker texture forming in the concentrated alloy.

3.2.3 ZEK100

To compare the recrystallisation mechanism between binary and tertiary magnesium-RE alloys the commercially hot rolled ZEK100 was cold rolled under a variety of schedules. Unlike the binary magnesium-RE alloys which display a weak basal texture on recrystallisation ZEK100 produces a characteristic split basal texture in the TD, Figure 3.11. This unique RE texture makes it easier to distinguish whether RE effects are active during

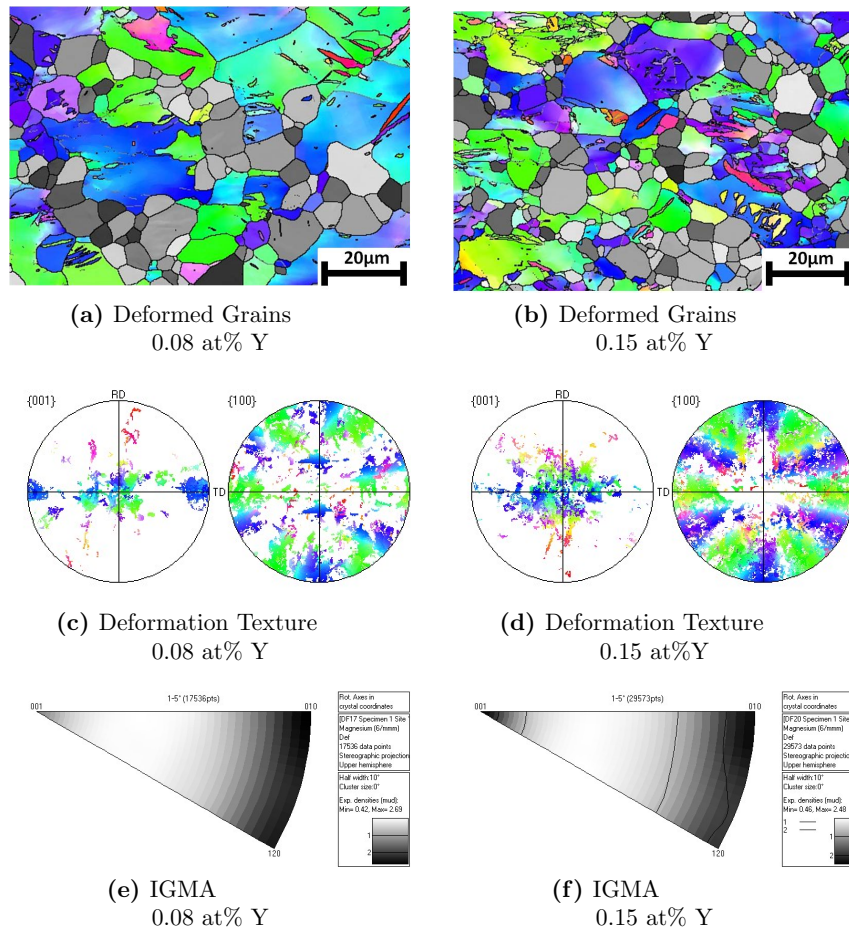


Figure 3.15: IGMA analysis between deformed grains in magnesium 0.08 and 0.15 at% Y alloys. a,b) plots deformed grains on EBSD map. c,d) Plots the orientations of deformed grains. e,f) inverse pole figures showing the misorientation axes between neighbouring points.

cold rolling and static recrystallisation because if RE effects are active the TD split basal texture will reform from a basal deformation texture during recrystallisation. Three cold rolling trials were carried out shown schematically in Figure 3.20. In Path 1, straight cold rolling (SCR), the cold rolling direction (RD_{CR}) is parallel with the hot rolling direction (RD_{HR}) of the commercially hot rolled ZEK100 sheet. In path 2, Transverse cold rolling (TCR), RD_{CR} is perpendicular to RD_{HR} and finally in path 3 or equal cold rolling (ECR) the sheet was rotated between rolling passes to provide equal strain both parallel to the RD_{HR} and perpendicular to the RD_{HR} . In ECR difficulty in controlling the thickness reduction per pass resulted in each orientation receiving a different number of passes but the final strain in each orientation is almost equivalent. These distinct rolling paths will allow the influence of deformation and deformation texture on the RE texture formation to be determined.

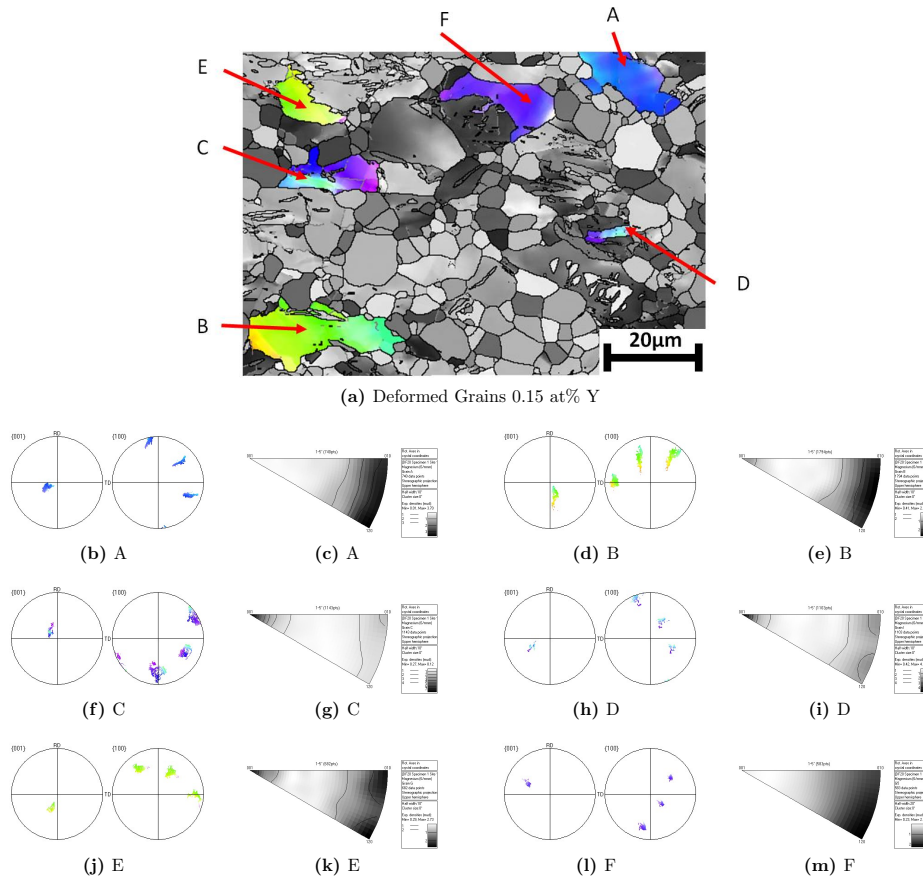


Figure 3.16: IGMA analysis of individual deformed grains in 0.15 at% Y alloys. Showing a) each grain on EBSD map, the orientation of that grain and the orientation of the misorientation axes on an inverse pole figure.

3.2.3.1 Straight Cold Rolling (SCR)

In SCR the RD_{CR} is parallel to the RD_{HR} , $\{0001\}$ pole figures of the cold rolled and recrystallised ZEK100 are given in Figure 3.21 a). After cold rolling, the basal texture strengthens and the TD split basal texture moves back towards the sheet ND, forming a strong basal texture with a slight split towards the RD typical of magnesium sheet. Although a spread of basal orientations towards the TD is preserved in the deformation texture little remains of the characteristic TD oriented lobes of the initial sheet material. The cold rolled material was then annealed for 1hr at 400°C leading to full recrystallisation, during which the TD split in the basal texture re-forms indicating that the RE texture weakening is active, since a typical non-RE recrystallisation mechanism would be expected to produce a slightly weaker deformation texture but no significant TD split, as Figure 3.21 b) shows in the case of AZ31. In AZ31, the strong basal texture created

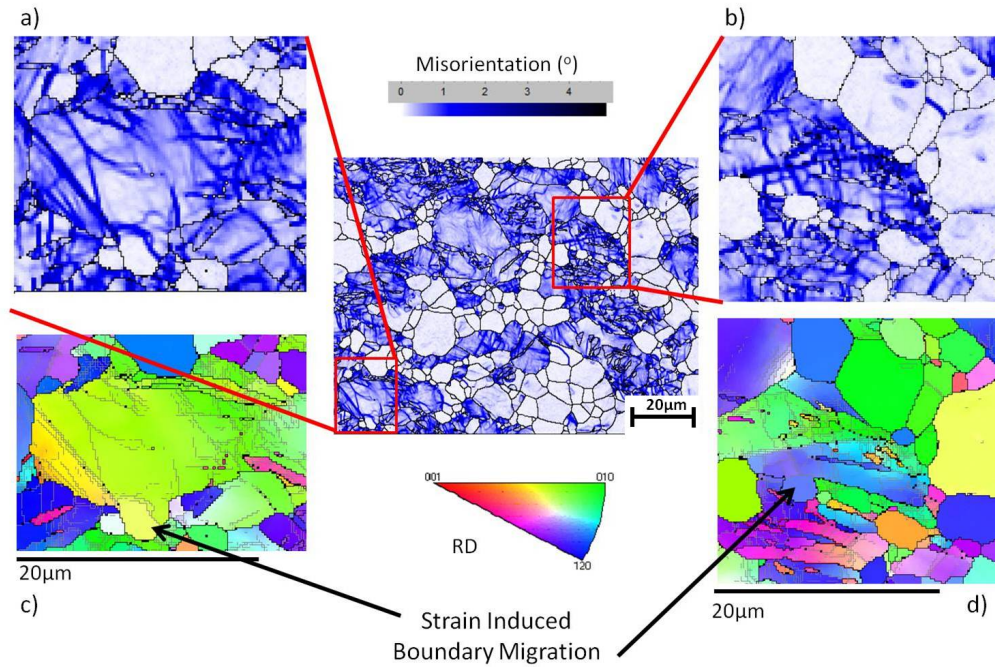


Figure 3.17: High magnification images of magnesium 0.15 at% Y cold rolled and annealed for 4 minutes at 350°C. a,b) kernel average misorientation maps and c,d) IPF colour maps relative to RD for the indicated regions. Black boundaries $> 10^\circ$, grey boundaries $> 1^\circ$.

during cold rolling is only weakened during recrystallisation with no change in texture morphology.

3.2.3.2 Transverse Cold Rolling (TCR)

Figure 3.22 shows the deformation and recrystallisation textures of ZEK100 during transverse cold rolling where the RD_{CR} is perpendicular to the RD_{HR} . The deformation texture of transverse cold rolled material is very similar to the straight cold rolled case, with the misorientation of the TD_{HR} split falling from $\approx 30^\circ$ to $\approx 10^\circ$ from the ND and remaining in the TD_{HR} direction, Figure 3.22d). During recrystallisation the RE texture re-forms with the TD_{CR} split in the RE recrystallisation texture rotated by 90° in comparison to the original TD_{HR} orientation of the RE texture in the hot rolled material. In other words after transverse cold rolling the TD split of the recrystallisation texture forms in the cold rolling TD (TD_{CR}) despite this being perpendicular to the hot rolling TD of the original hot rolling process. Figure 3.22 also gives the $\{10\bar{1}0\}$ pole figures for this process which show the expected formation of a typical basal texture after cold rolling and the reforming of the RE texture in recrystallised material with a 90° rotation about the sheet ND. The RE texture formation in ZEK alloys is clearly associated with recrystallisation as Figure 3.22a) plots the basal texture intensity against annealing time, showing that a

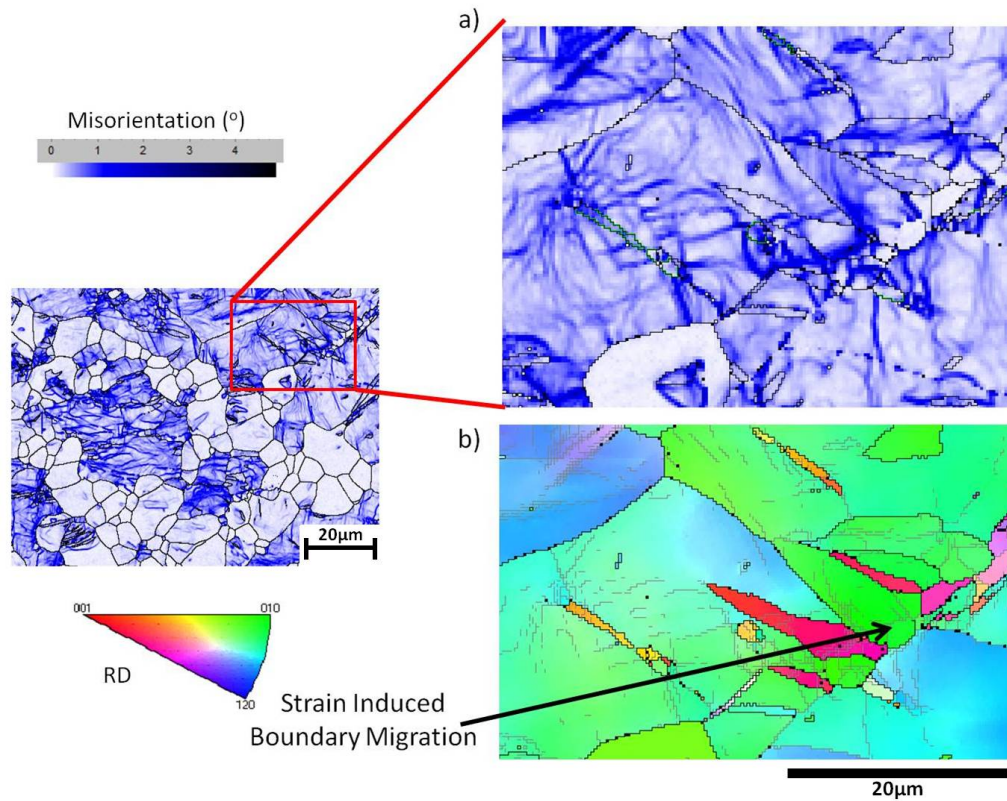


Figure 3.18: High magnification images of magnesium 0.08 at% Y cold rolled and annealed for 4 minutes at 350°C. a) kernel average misorientation maps and b) IPF colour maps relative to RD for the indicated regions. Black boundaries > 10°, grey boundaries > 1°.

minimum in texture intensity had been reached after only two minutes at 400°C, which coincides with full recrystallisation of the material, Figure 3.23b).

Table 3.3: Rolling schedule for the transverse cold rolled (TCR) and straight cold rolled (SCR) ZEK100, showing cumulative true strain over nine passes.

Pass	TCR	SCR
0	0.00	0.00
1	-0.03	-0.04
2	-0.06	-0.07
3	-0.09	-0.11
4	-0.14	-0.16
5	-0.18	-0.22
6	-0.22	-0.29
7	-0.27	-0.35
8	-0.32	-0.41
9	-0.37	-0.46

In order to observe the nucleation and growth of this TD split in the basal texture after transverse cold rolling EBSD was used to analyse the material in as rolled and partially

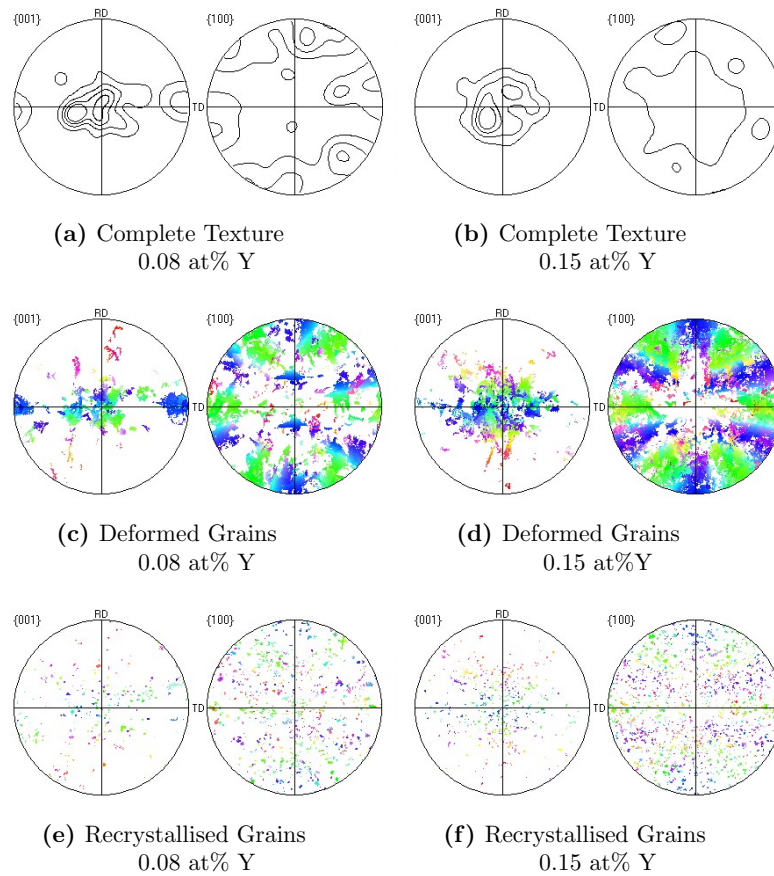


Figure 3.19: $\{0001\}$ and $\{10\bar{1}0\}$ pole figures for the cold rolled and partially recrystallised magnesium 0.08 and 0.15 at% Y alloys. a.) Complete textures, c,d) deformed grains only ($> 1^\circ$ average internal misorientation) and e,f) recrystallised grains only ($< 1^\circ$ average internal misorientation).

recrystallised states. Figure 3.24 shows TCR ZEK100 in a) the as rolled condition, b-d) partially recrystallised conditions after annealing for up to five minutes at 350°C . The annealing temperature of 350°C was used to slow SRX, allowing the material to be observed in different microstructural conditions. Macro texture analysis, omitted for brevity, shows the same recrystallisation textures form during annealing at 350°C and 400°C and so it is reasonable to assume the same mechanism is responsible. Figure 3.24 a) shows the deformed microstructure of the TCR material, basal textures in IPF colouring relative to RD_{CR} are indicated by green/blue grains. As expected, the majority of deformed grains have a basal orientation. Black points indicate sections of the map that could not be indexed most likely due to the high levels of deformation in these regions. These black regions appear to be arranged in bands aligned approximately 30° to the RD_{CR} , which are identified as shear bands. As the material is annealed, Figures b) and c) show recrystallisation is concentrated in these shear bands nucleating a large number

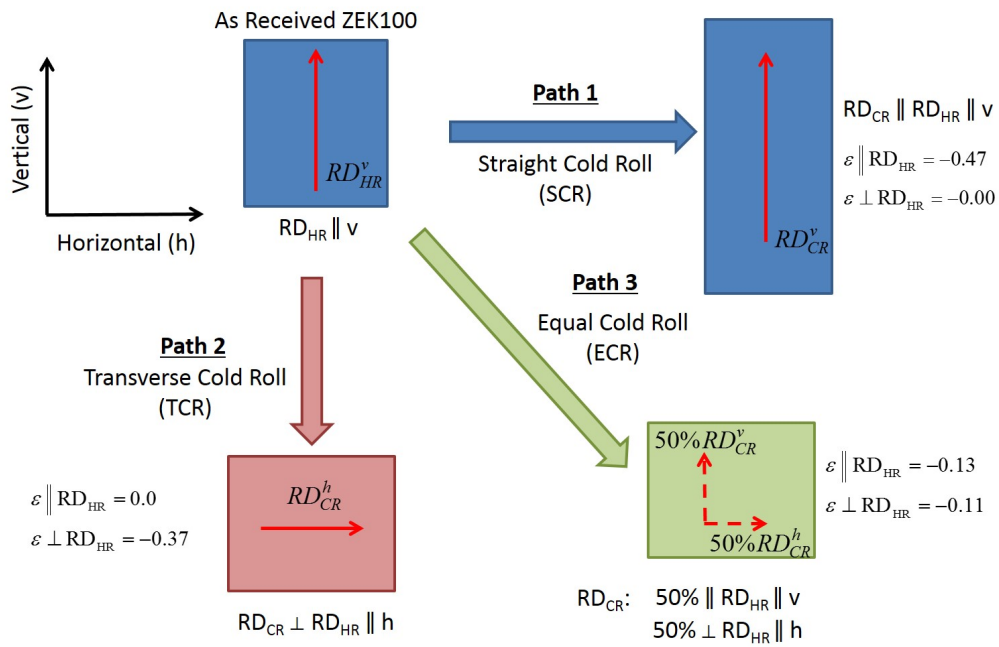


Figure 3.20: Schematic diagram showing the three paths used when cold rolling ZEK100. RD_{HR}^v indicates the hot rolled direction of the as received material is parallel with the vertical direction in frame of reference used on this page. Three rolling pathways are then defined with associated true strains in each cold rolling direction, these are: Straight cold rolled where the cold RD is parallel to the original hot RD, transverse cold rolled where the cold rolled RD is perpendicular to the hot RD and equal cold rolled where the sheet was cold rolled equally parallel and perpendicular to the original hot RD.

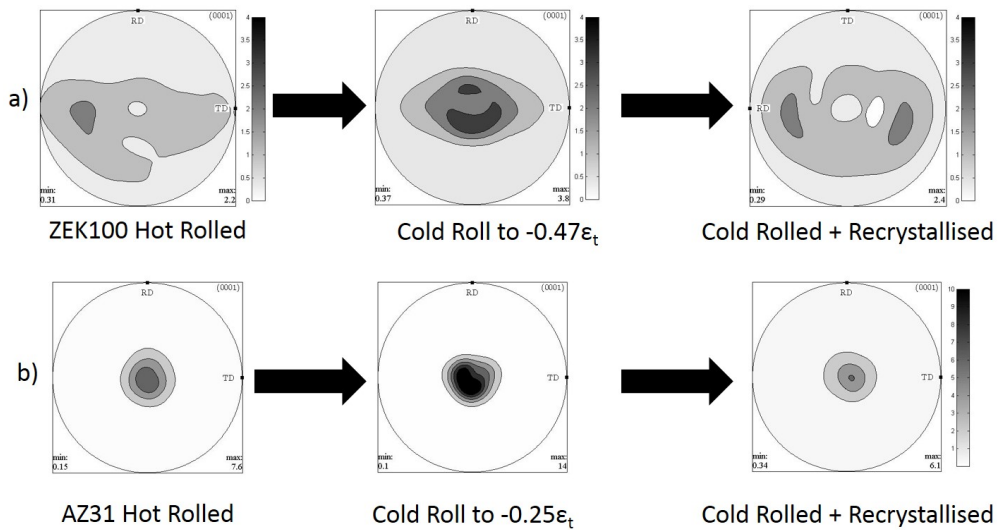


Figure 3.21: $\{0001\}$ pole figures showing the texture development of a) ZEK100 and b) AZ31 after a hot rolled sheet is straight cold rolled and fully recrystallised at 400°C . After SCR both alloys form strong basal textures but the RE texture only forms after full recrystallisation in the RE alloy.

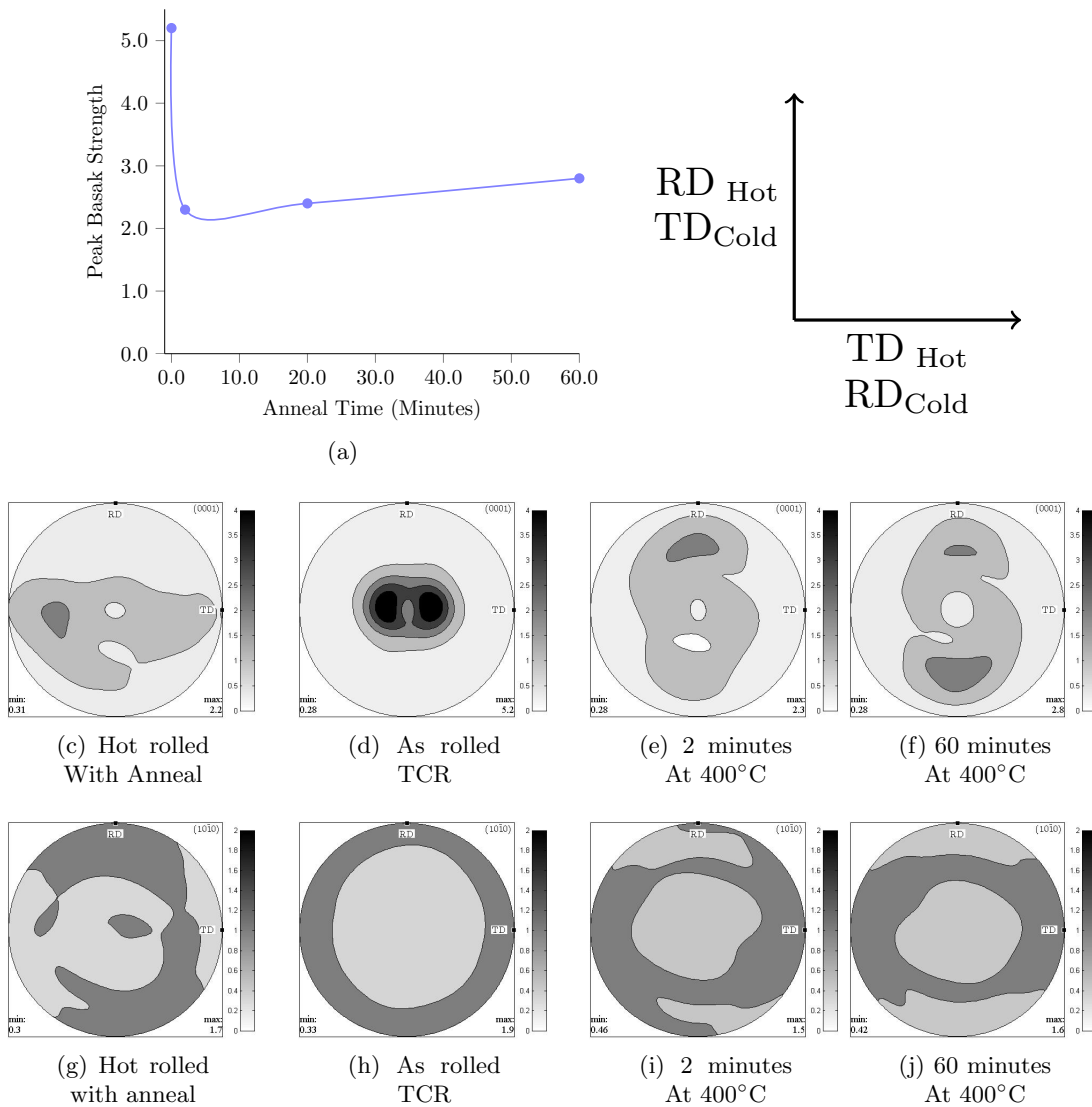


Figure 3.22: Figure a) shows a plot of the peak basal strength Vs annealing time of ZEK100 transverse cold cross rolled to $\epsilon_T = -0.45$ followed by annealing at 400°C. c-j) Present the {0001} and {10 $\bar{1}$ 0} pole figures for the TCR material before cold rolling, in the as cold rolled state and after annealing for 2 minutes and 60 minutes.

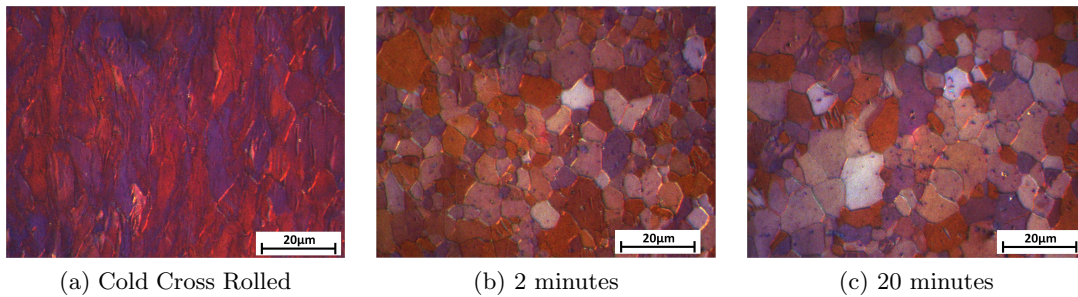


Figure 3.23: Optical micrographs of ZEK100 after a) transverse cold cross rolling and annealing at 400°C for b) 2 and c) 20 minutes.

of small grains. There are very few black regions in these maps as these heavily deformed regions have been consumed by the recrystallising grains. After five minutes of SRX, d), many of the recrystallised grains have grown significantly in size and begun to consume the surrounding microstructure, there are very few un-indexed points in this map.

The textures of deformed and recrystallised grains are presented in Figure 3.25 together with the position of the grains on the EBSD map. Recrystallised grains are defined as having average internal misorientations of less than 1° . At each stage of the heat treatment the deformed grains present a strong basal texture, however the recrystallising grains show a transition from a split basal texture towards the RD_{CR} , after one and two minutes annealing, to a split basal texture towards the TD_{CR} after five minutes annealing. The RD indicated in the figures is the RD_{CR} orientation and so Figure 3.25 a) shows the smallest detected regions in as rolled shear bands have orientations split in the RD_{CR} , the same RD_{CR} split is also found in the earliest recrystallised grains after one and two minutes annealing in Figures 3.25 b) and c). After five minutes of annealing however, many of these small recrystallising grains have been replaced with a relatively small number of very large recrystallising grains which have orientations split in the TD_{CR} . Clearly as recrystallisation continues, these TD_{CR} orientations come to dominate leading to the RE texture forming in the TD_{CR} as shown in Figure 3.22.

The split basal texture in the TD_{CR} is the RE texture component and to determine how grains with this orientation come to dominate the recrystallised material the recrystallised grains are partitioned by size; Small grains less than $1\mu\text{m}$ and large grains greater than $1\mu\text{m}$. It is thus possible to detect the growth of the TD_{CR} texture component earlier in the annealing process. Figure 3.26 breaks down the RX grains by size showing that even after one minute at 350°C the largest RX grains are spread in the TD_{CR} . Likewise the smallest grains retain a slight split in the RD_{CR} after annealing for five minutes showing that while both RD and TD grains nucleate during recrystallisation the TD grains have an advantage which leads to the eventual domination of the texture. Although these maps represent relatively small areas ($100\times 70\mu\text{m}$) the same behaviour is observed in larger maps which are omitted for brevity.

The dominance of the RD_{CR} texture component in the early stages of recrystallisation appears to be at least partly due to the deformation texture of the material within the shear banded regions, which recrystallises first. In the deformed areas of the shear bands which can be indexed the RD_{CR} split texture component is found, Figure 3.25 a). The link between these RD_{CR} orientations in shear bands and the initial recrystallising grains is further explored in Figure 3.27, which shows a high resolution EBSD map (step size $0.01\mu\text{m}$) of an enlarged region of the TCR material annealed for one minute at 350°C . The shear banded regions contain a mixture of deformed ‘grains’ with average misorientations

greater than 1° and recrystallising grains with average misorientations less than 1° . The exact recrystallisation mechanism is very hard to identify, however at this small scale there does not appear to be a significant difference between the orientations of the deformed grains in the shear band and the recrystallising grains which both have orientations split in the RD_{CR} . Of course the shear banded regions which are not indexed in the as rolled material are most likely to nucleate recrystallisation first and may contain unseen TD_{CR} components. However, after one minute of recrystallisation these regions which are not indexed have nearly disappeared and the high resolution map shows no significant preference for TD_{CR} recrystallised grains in this small area. However, maps over larger areas do show the TD_{CR} component present preferentially in larger recrystallising grains after one minute at 350°C , Figure 3.26 b).

The RD_{CR} split detected in deformed grains within shear bands has previously been reported in magnesium [99, 101]. In these cases it has been attributed to the activity of basal slip within the shear band orienting basal planes parallel to the shear band plane with a misorientation of $\approx 30^\circ$ to the RD. A schematic diagram of this type of shear banding (red) is shown in Figure 3.28. Similarly shear bands misorientated towards the TD_{CR} , green in Figure 3.28 have been proposed to nucleate the TD_{CR} texture split, as deformed grains in these bands would, in theory, have the same TD_{CR} misorientation as the recrystallised texture if basal slip were dominant. The EBSD maps considered to this point, such as Figure 3.25 a), have contained the ND- RD_{CR} plane which is most likely to contain the RD_{CR} oriented (red) shear bands as shown in Figure 3.28. Sectioning the ND- TD_{CR} plane may reveal more of the TD_{CR} (green) shear bands and thus the deformed grains from which the split TD_{CR} could nucleate. A comparison between ND- RD_{CR} and ND- TD_{CR} cross-sections in TCR material annealed for five minutes is shown in Figure 3.29. In these partially recrystallised materials the shear bands have mostly recrystallised and are now identified by bands of recrystallising grains. The texture of the recrystallising grains are also plotted in this figure showing that, if anything, the recrystallising grains have a more strong basal orientation in the ND- TD_{CR} section and there is no obvious preference for the TD_{CR} orientations nucleating in this plane. Overall, shear banding of the kind described by the green lines in Figure 3.28 does not appear prominent in the ND- TD_{CR} orientation in ZEK100 and the behaviour of recrystallised grains appears very similar to that previously reported in the ND- RD_{CR} plane. The RE texture components cannot simply be explained by the orientation of shear bands in this case.

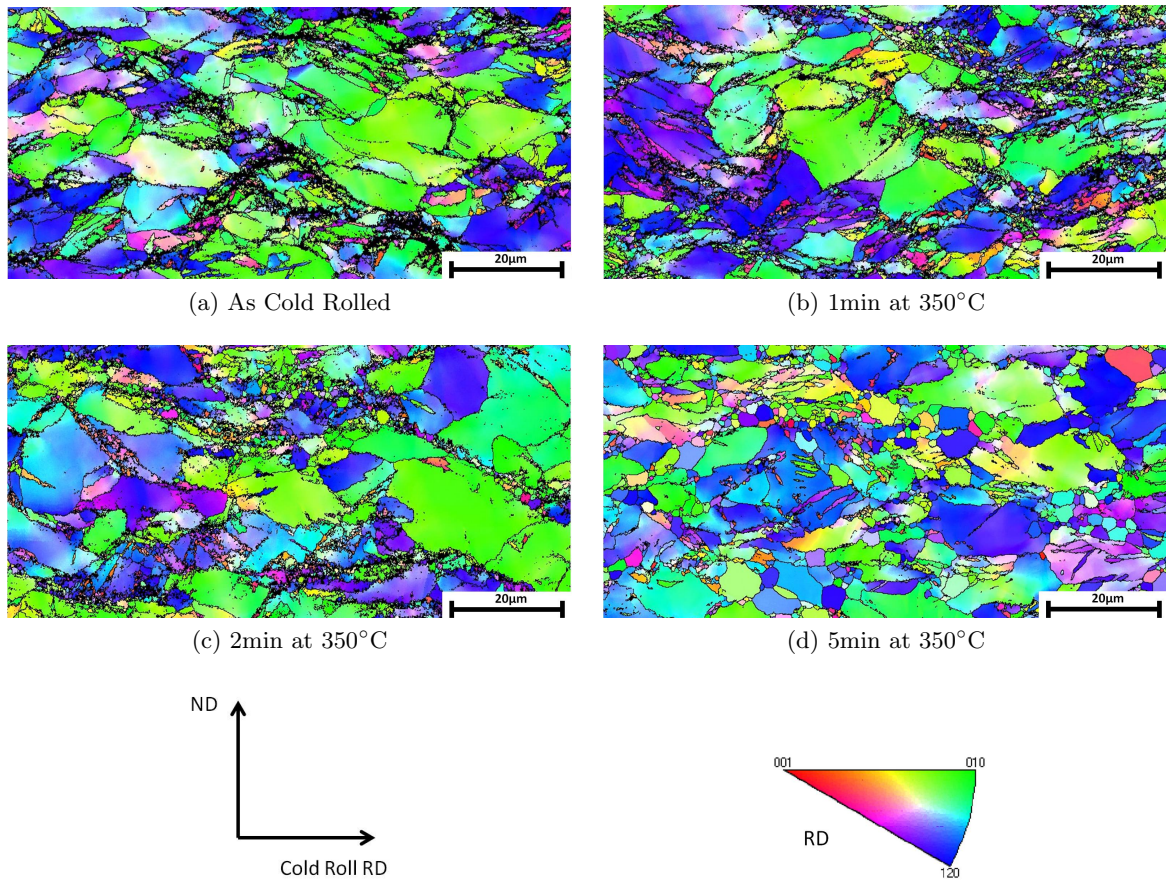


Figure 3.24: EBSD maps of the transverse cold rolled ZEK100 in a) the as rolled condition, b) annealed for one minute, c) two minutes and d) five minutes at 350°C. The maps are in IPF colouring relative to the cold rolling RD.

3.2.3.3 Equal Cold Rolling (ECR)

During equal cold rolling, the commercially hot rolled ZEK100 sheet was cold rolled such that equal strain was imparted with the RD_{CR} parallel to and perpendicular to the RD of the original hot rolled sheet. Difficulty in controlling the reduction per pass by less than 0.1mm meant that it was not possible to achieve equal strain in both directions with an equal number of passes. As a result the strain in each direction was equalised by rolling with 8 passes parallel to the RD_{HR} and 3 passes perpendicular to the RD_{HR} , as shown in Table 3.4.

The textures of the as rolled and recrystallised equal cold rolled material are presented in Figure 3.31. The as cold rolled texture (Figure 3.31 a,c)) is similar to that after TCR, showing a strengthened basal texture in which the misorientation of the TD_{HR} split about the ND is reduced from 30° to around 20°. The wider misorientation about the ND after cold rolling in comparison to SCR and TCR is probably due to the low total strain of $\epsilon_t = -0.24$ imparted during the rolling process; unfortunately the material failed during

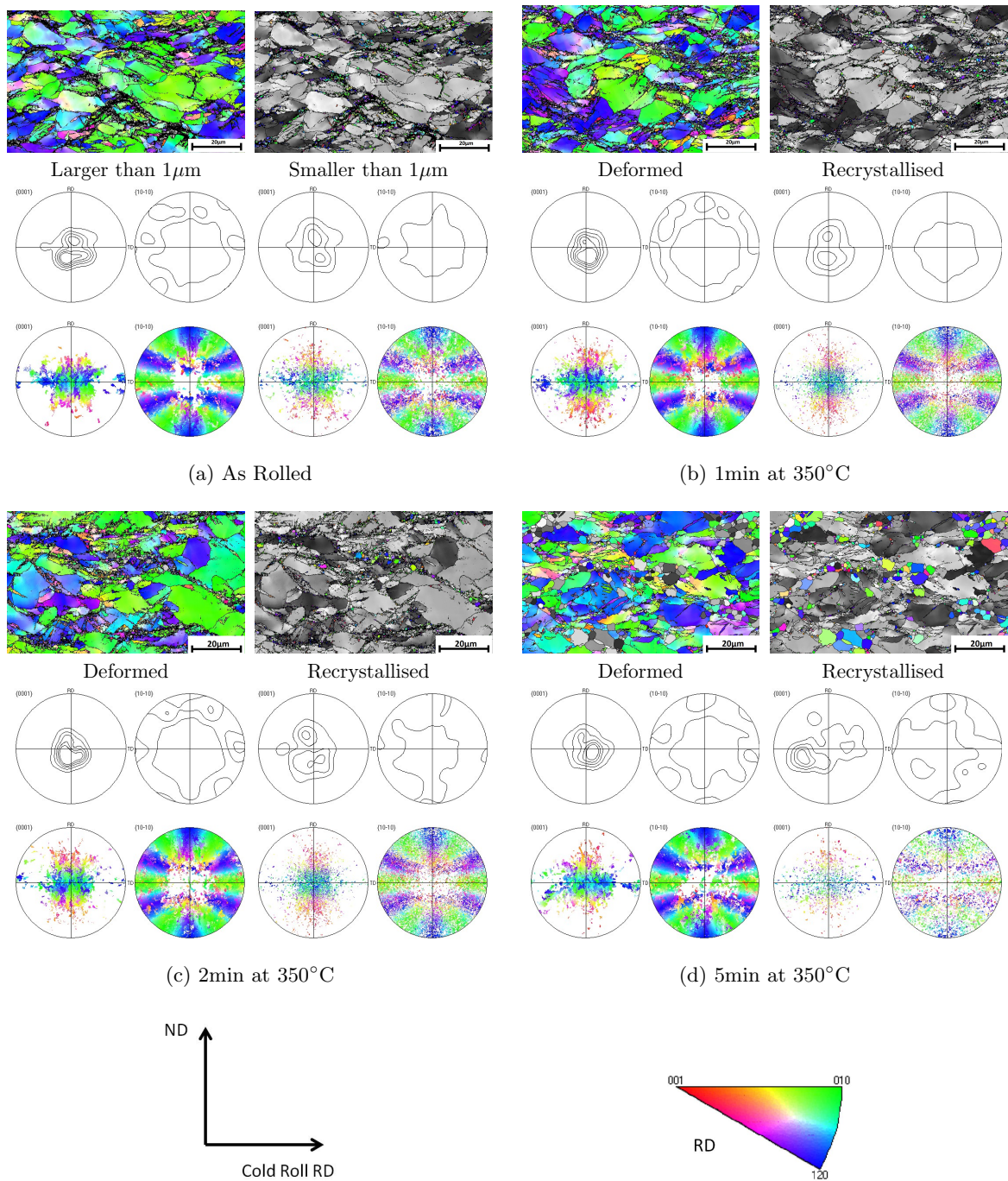


Figure 3.25: EBSD maps separated into regions of deformed and RXed grains based on average misorientations of greater than 1° defining deformed grains. In the as rolled case as no grains are RXed we plot grains less than $1\mu\text{m}$ in size. The orientation and IPF colouring of the EBSD map are also included for convenience.

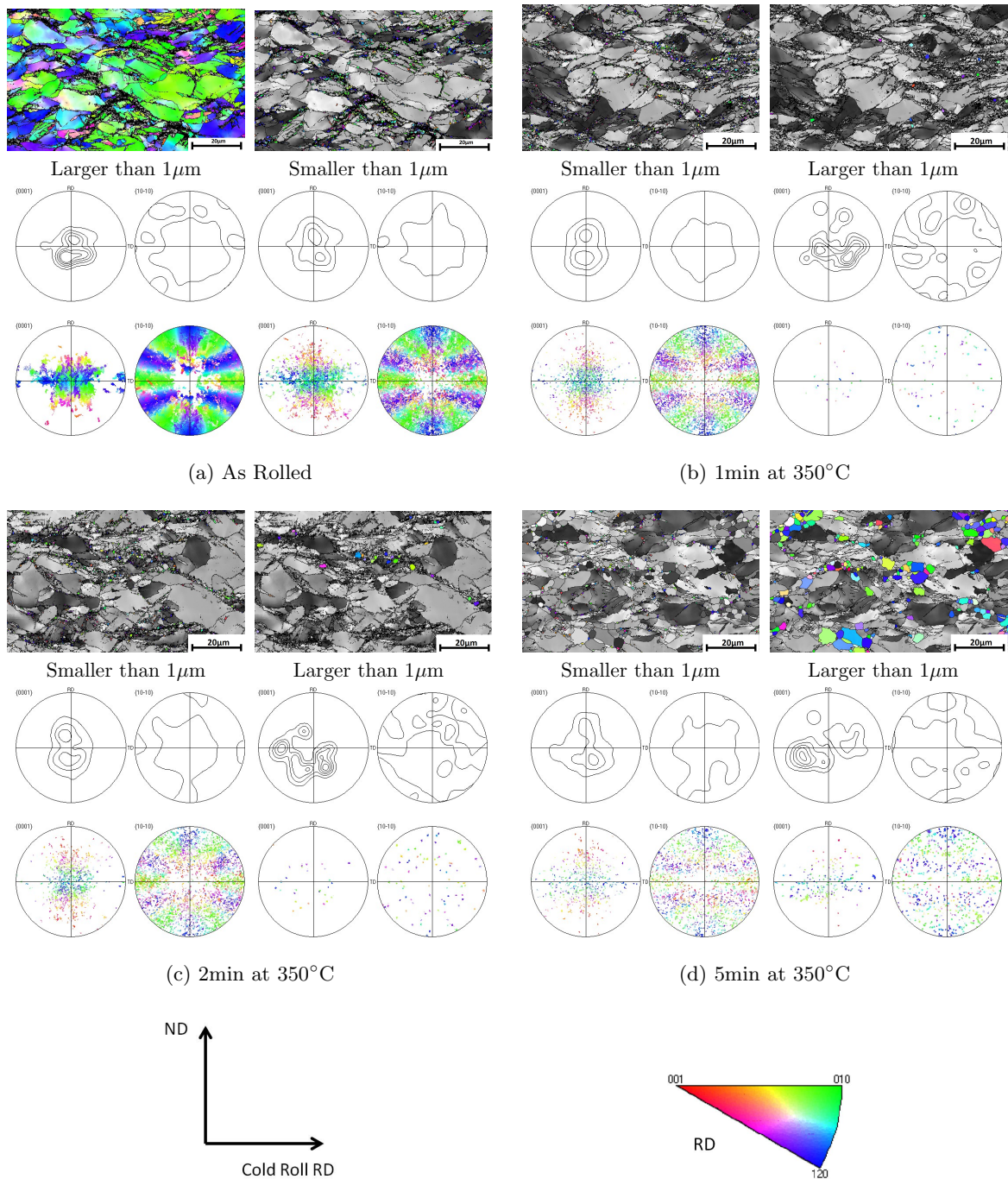


Figure 3.26: Separating the RX grains (grains with less than 1° misorientation) into small and large sizes, greater than or smaller than $1\mu\text{m}$.

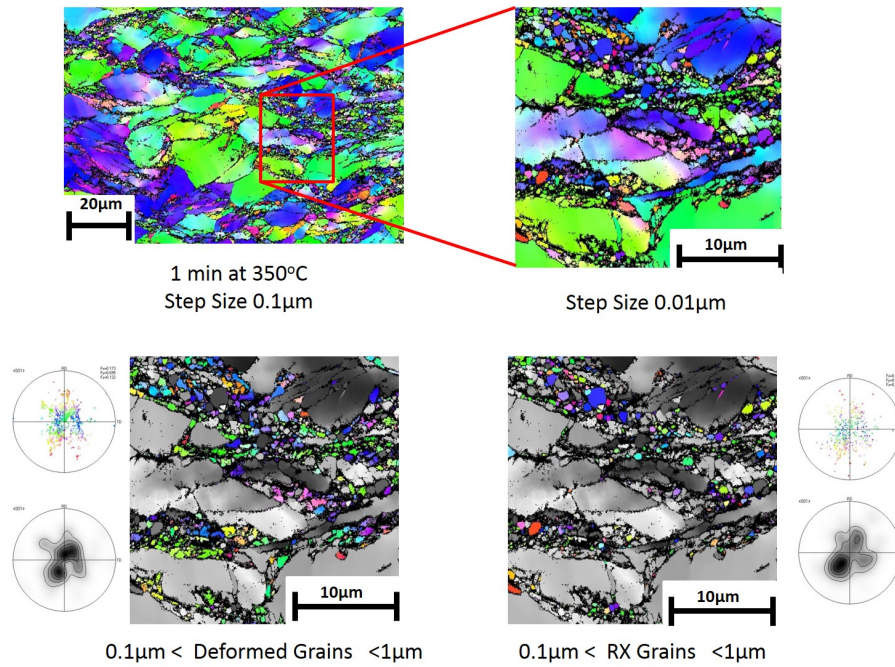


Figure 3.27: Figure showing a high resolution EBSD map with a step size of $0.01\mu\text{m}$ of a small area of the TCR ZEK100 annealed for 1 min at 350°C . The high resolution map has been broken down to show the positions and orientations of deformed and recrystallised grains with sizes between $0.1\mu\text{m}$ and $1\mu\text{m}$.

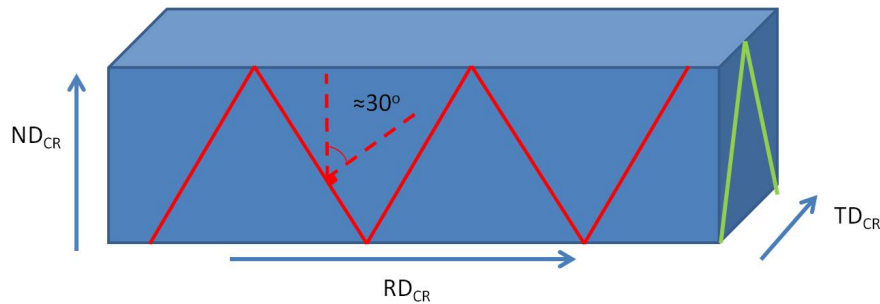


Figure 3.28: Schematic diagram of rolled billet showing shear bands intersecting ND_{CR} - RD_{CR} (red) and ND_{CR} - TD_{CR} (green) planes.

ECR before the higher total strains of $\epsilon_t = -0.45$ achieved in the other cold rolling processes could be reached. As the largest strain during rolling was imparted with RD_{CR} parallel to the RD_{HR} in the following we consider TD_{HR} parallel to TD_{CR} after ECR. Upon recrystallisation, after 1hr at 400°C , the basal texture weakened slightly to 3.6 mrd and spread slightly in the TD_{CR} , Figure 3.31 b,d). Significantly, this texture is different to the RE recrystallisation textures previously reported; the lobes which typically form about the TD_{CR} are much less distinct and have a lower misorientation with respect to the sheet ND in comparison to the previously reported cases. The basal texture intensity of the TD_{CR} lobes is also slightly higher.

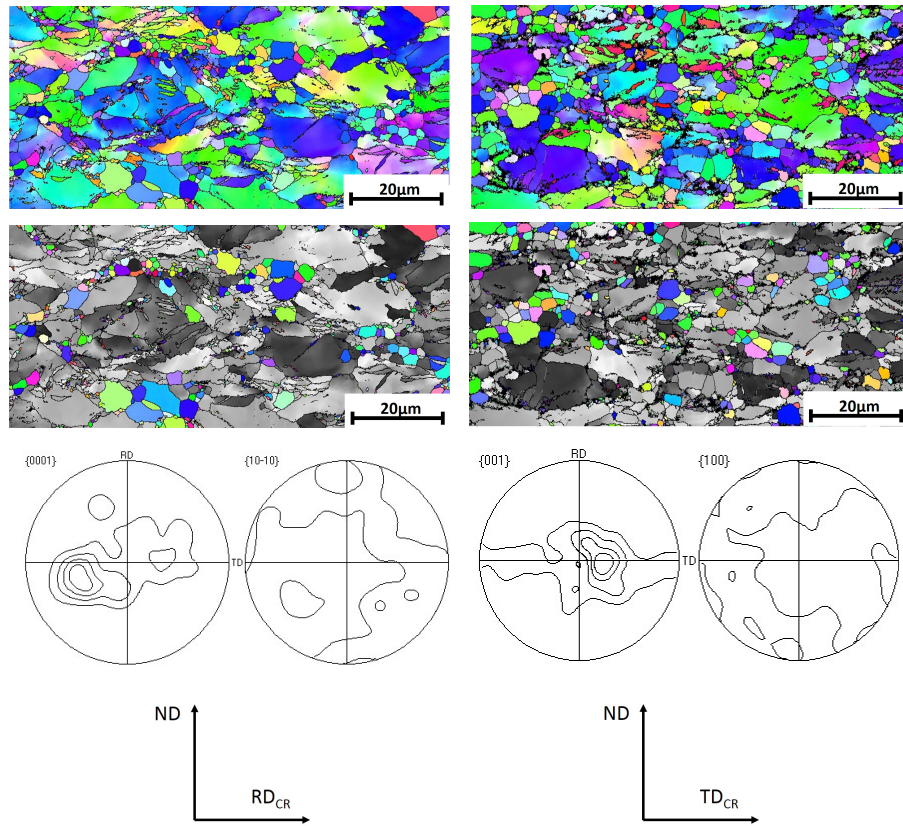
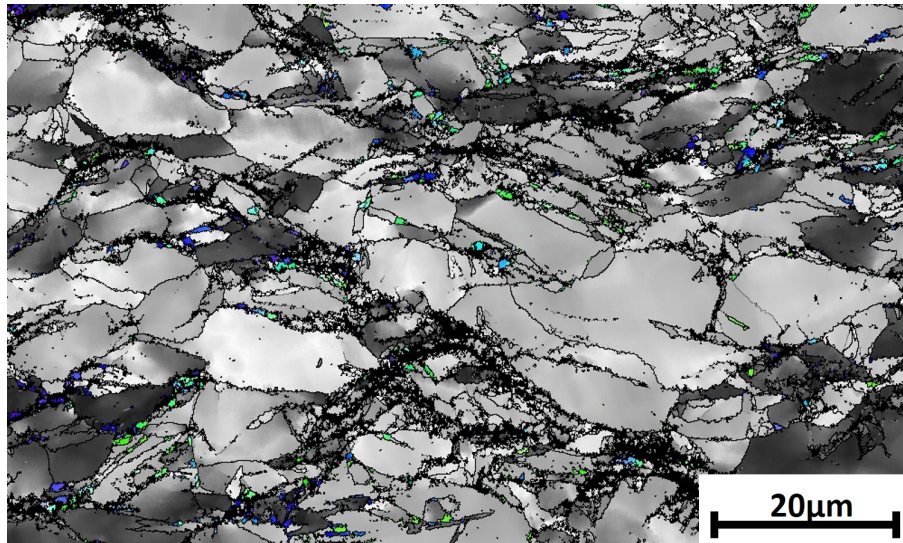


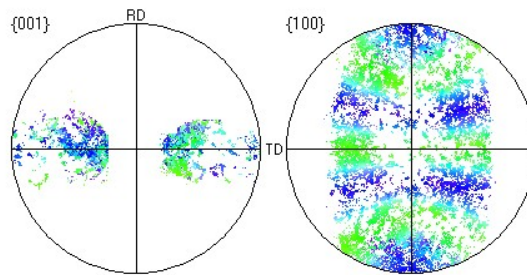
Figure 3.29: Figure comparing the overall microstructure and recrystallised grains in the ND- RD_{CR} and ND- TD_{CR} cross sections of the transverse cold rolled ZEK100 after annealing for five minutes at 350°C.

Table 3.4: Cold rolling schedule for the equal cold rolled ZEK100, all strains true.

Passes	$RD_{CR} \parallel RD_{HR}$	$RD_{CR} \perp RD_{HR}$	ϵ_{Total}
	ϵ	ϵ	
1	0.004		0.004
2		-0.023	-0.027
3	-0.011		-0.038
4		-0.032	-0.070
5	-0.015		-0.085
6	-0.027		-0.112
7	-0.029		-0.141
8	-0.018		-0.159
9		-0.052	-0.211
10	-0.008		-0.218
11	-0.026		-0.245
Total	-0.14	-0.11	



(a)



(b)

Figure 3.30: a) EBSD map of as transverse cold rolled ZEK100 with the TD_{CR} orientations highlighted. b) pole indicated the TD orientations selected.

Table 3.4 shows that overall a slightly larger strain was imparted during cold rolling parallel to the RD_{HR} and so the same recrystallisation mechanism as that observed during SCR would be expected to produce a RE texture split in the TD_{HR} (equivalent to TD_{CR}). Although the recrystallised texture after ECR is split in this direction, critically the TD_{CR} lobes formed in recrystallised ECR material have a higher intensity and lower misorientation from the ND than that observed after either SCR or TCR. Texture weakening during annealing after ECR is therefore much more comparable to that observed in the binary alloys discussed above, Section 3.2.2, in which the recrystallised texture was simply a weakened deformation texture.

The cause of the change in recrystallisation behaviour after ECR must be a result of the deformed microstructure generated during cold rolling, which is observed in the EBSD maps presented in Figure 3.32. The ECR material has a larger grain size and fewer shear banded regions than the TCR material. Both of these observations are a result of the lower total strains achieved under the ECR. Lower strains mean the grains are compressed less in the ND, resulting in less grain elongation in Figure 3.32 b) and a lower likelihood of

shear bands developing. However, failure of the material in other ECR experiments always occurred at strains below $\epsilon = -0.3$ and, since shear band formation is strongly associated with incompatibility stresses which are largest at strains close to failure ($\epsilon = -0.24$ in this ECR experiment), one might expect a larger number of shear bands in the ECR material. Another key difference between the materials is the twinning behaviour; Figure 3.32 b) shows regions of unusual twinning (in the lower half of the figure) where a number of grains have heavily twinned in various directions. Identification of these twins based on characteristic misorientations is not possible, due to the deformation of both twin and matrix occurring after rotating between each pass. However, qualitatively note that many of the twins are quite wide, a typical characteristic of tension twins. Regardless of twin type, similar regions of intersecting wide twins are not observed after TCR, where more typical twinning behaviour including a mix of tension compression and double twinning is found. In addition to the observed microstructural features a intragranular misorientation analysis (IGMA) investigation was performed on a number of deformed grains of different orientations in both materials. IGMA analysis is often useful in identifying the dominant type of geometrically necessary dislocation required to account for rotations in each grain. Unfortunately however, in the grains analysed little preference for particular GND systems could be found, in either material with intensities less than 2 mrd in both cases. Overall while dislocation activity is expected to be very different between ECR and TCR deformed structures, no strong evidence of this in IGMA analysis was found.

In summary, after equal cold rolling, where strain was equally distributed between rolling parallel to and perpendicular to the RD_{HR} , a change in recrystallisation behaviour was observed in comparison to SCR and TCR, despite a similar deformation texture forming during ECR. Unlike in SCR and TCR where recrystallisation led to a distinct $\approx 30^\circ$ split towards the TD_{CR} , recrystallisation in ECR simply produced a weakened deformation texture. The origins of this change must be in the deformed microstructure in the form of different microstructural features or dislocation activity. IGMA analysis between as rolled TCR and ECR material failed to identify a significant difference in GND activity between the materials, although given the small number of grains observed this is inconclusive. However, significant differences in the twinning and shear banding behaviour were observed; shear banding was much less prevalent in ECR in comparison to TCR and although this is partly a result of lower applied strains in ECR it may also be due to a lower propensity for shear banding in ECR process, because the material was deformed very close to the failure without significant shear banding. Twinning in the ECR material was also very different to TCR, with a large number of densely packed twins intersecting at unusual angles found after ECR. These twins were qualitatively identified as tension twins due to their large width. The contribution of each feature to the change in ECR recrystallisation texture is not obvious and will be discussed in Section 5.2.2.

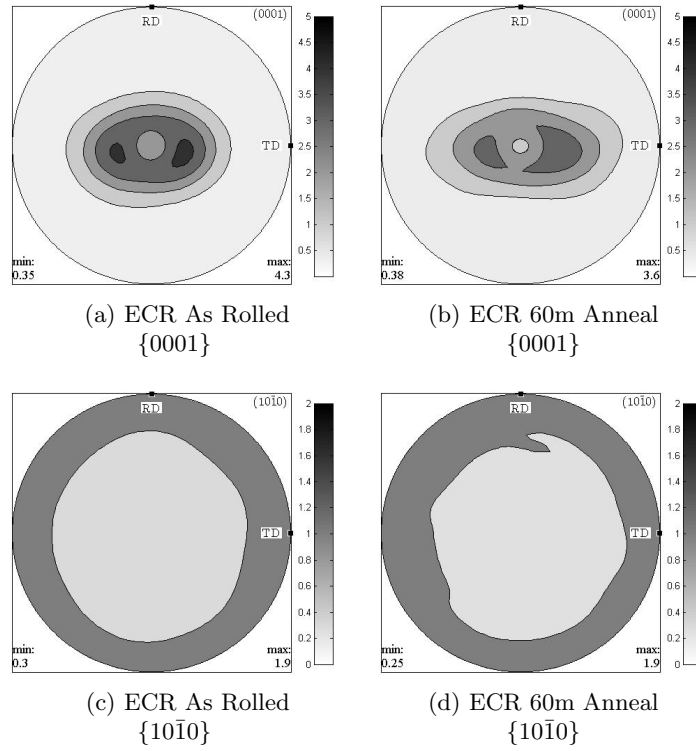


Figure 3.31: ZEK100 Equal Cold Rolled in both directions ($\epsilon_T = -0.13$ RD and $\epsilon_t = -0.11$) in the TD. RD and TD refer to the original hot rolling orientations.

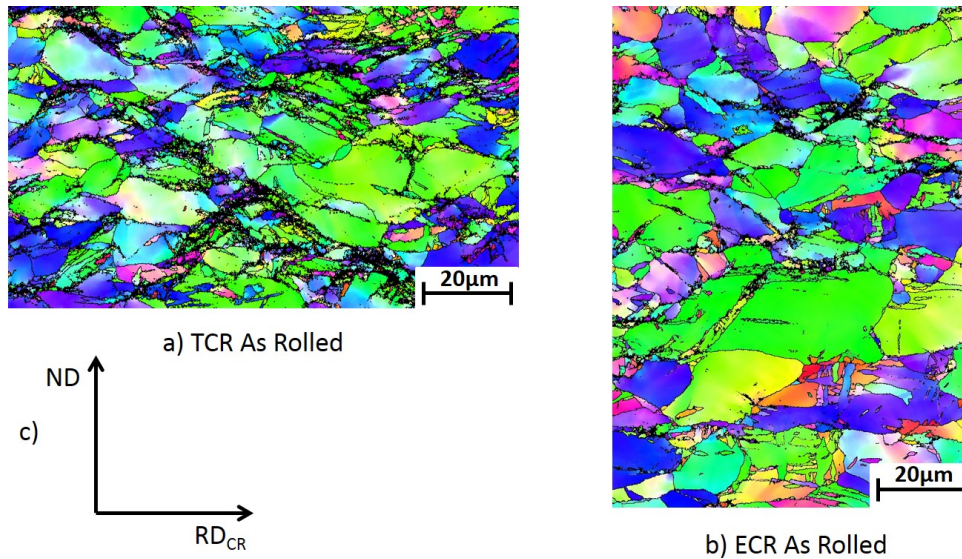


Figure 3.32: a) ZEK in the as rolled condition after TCR to $\epsilon = -0.37$ and b) ZEK100 in the as rolled condition after ECR to $\epsilon = -0.24$. c) Indicates the orientation of the figure note that due to the 90° rotations in b) RD_{CR} also corresponds to TD_{CR} in 50% of passes. IPF relative to RD_{CR} .

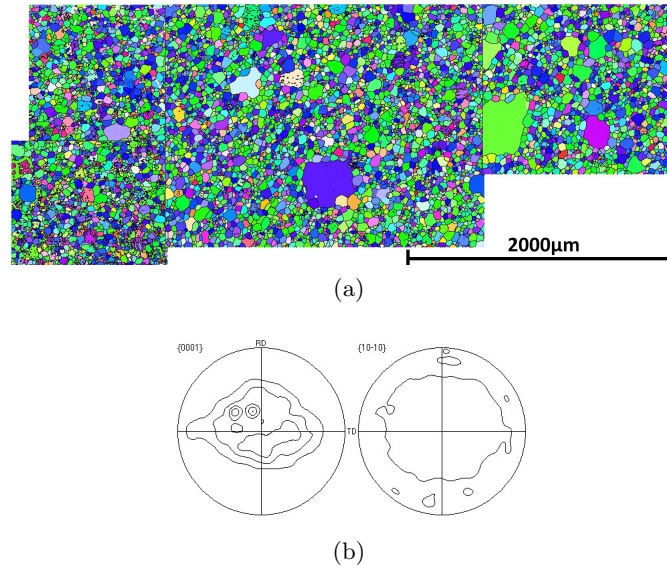


Figure 3.33: a) Composite EBSD map of ZEK100 annealed for 30 days at 400°C, b) texture of the complete map, contours 1,2,3,4 mrd and IPF colouring relative to RD.

3.3 Grain Growth in ZEK100

RE textures form during recrystallisation but how stable are they during grain growth or secondary recrystallisation? To investigate this, a specimen of hot rolled ZEK100 was annealed for 30 days at 400°C in an inert Ar atmosphere. The subsequent textures and grain size distribution were investigated using EBSD, Figure 3.33. This data is a composite map of several smaller maps over a very large area (scale bar 2000µm), several abnormally grown grains are observed with sizes up to 400µm against an mean grain size of 28µm. The texture of the complete map, Figure 3.33 b), shows a spreading of the poles in the TD however, the unique split of the basal texture into two TD lobes as observed prior to annealing (Figure 3.11b)) is not found.

To identify the source of the re-emerging basal texture component, the texture of the composite map has been plotted as a function of grain size over four intervals in Figure 3.34. The intervals are based on the mean (28µm) and standard deviation (SD=18µm) of the data which are plotted in the grain size distribution of Figure 3.34 a). The textures and locations of grains with sizes less than one SD below the mean, one SD below the mean, one SD above the mean and greater than one SD above the mean but less than 100µm (which are considered to be abnormally grown) are plotted. While none of the size ranges plotted show the TD lobes of the original material there does appear to be some preference for larger grains to have a more basal texture with grains in the 28-46µm range having a high intensity basal band not observed in the smaller 10-28µm range. However, the link between large grain size and basal orientation is quite weak and it is

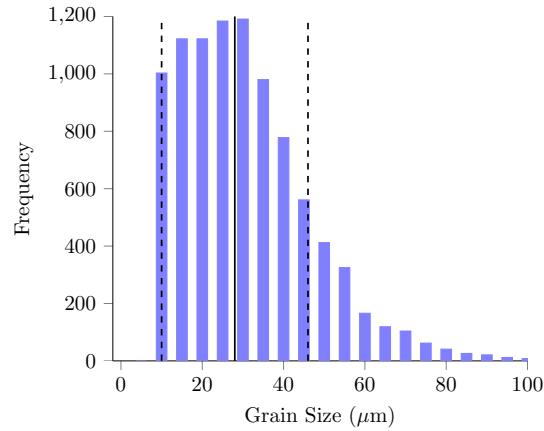
worth noting that amongst the abnormally grown grains, Figure 3.34 j,k) the textures are not exclusively basal.

A similar analysis has been carried out on fully recrystallised ZEK100 after annealing for one hour at 400°C, Figure 3.35. In this case the grains were separated into two groups, small and large, about the mean grain size of $\approx 6\mu\text{m}$. Figure 3.35 c,d) shows the split basal texture in the TD is contained in the larger grains which dominate the microstructure post recrystallisation. However, smaller grains remain and these contain a more basal texture component, Figure 3.35 e,f). This basal component appears very similar to the dominant texture component after 30days annealing Figure 3.33 b). These more basally oriented grains must have a growth advantage allowing them to grow more quickly than grains with the split TD texture component during grain growth.

3.4 Formability of ZEK100 Sheet

The cold formability of the commercial ZEK100 alloy has also been measured using the Nakazima strip test and digital image correlation system described in Section 2.9. The forming limit curve (FLC) was measured in ZEK100 after annealing as received material for 1hr at 400°C post hot rolling. The strain at failure was measured two images prior to specimen failure at a point in the centre of the sample by the method in Section 2.9. The room temperature FLC produced is plotted in Figure 3.36 together with that of AZ31 and aluminium 6016 for comparison. The RE alloy demonstrates significantly higher formability under all strain states, with the lowest minimum major forming strain rising by $\epsilon = 0.14$ in comparison to AZ31. The high formability of ZEK100 has also been reported by other authors[111, 117]. Note that minimum of the ZEK100 FLC lies at a minor strain of 0.1, this is unusual as classically this lies at $\epsilon_{\text{minor}} = 0$. Although not the subject of this research this is believed to be a fundamental effect in the Nakazima forming test, which is only observed here because of the improved accuracy available with the DIC technique. A similar shift has been observed other materials including aluminium alloys and it is not accounted for by the usual methods for correcting the data for non-linear strain paths measured during the deformation[111].

The significantly weaker texture of ZEK100 in comparison to AZ31 is thought to be the primary cause of improved formability although, as discussed in Section 1.8 increased non-basal slip and a change in the nature and distribution of shear banding are also likely to be contributory factors. Significantly, the rare earth additions raise the formability of magnesium to a similar level as aluminium 6016. This is extremely promising considering the aim of RE additions in magnesium is to achieve room temperature formability good enough to challenge competing aluminium materials.



(a) Grain size distribution with mean (solid line), one standard deviation (SD) above and below mean (dashed lines) indicated.

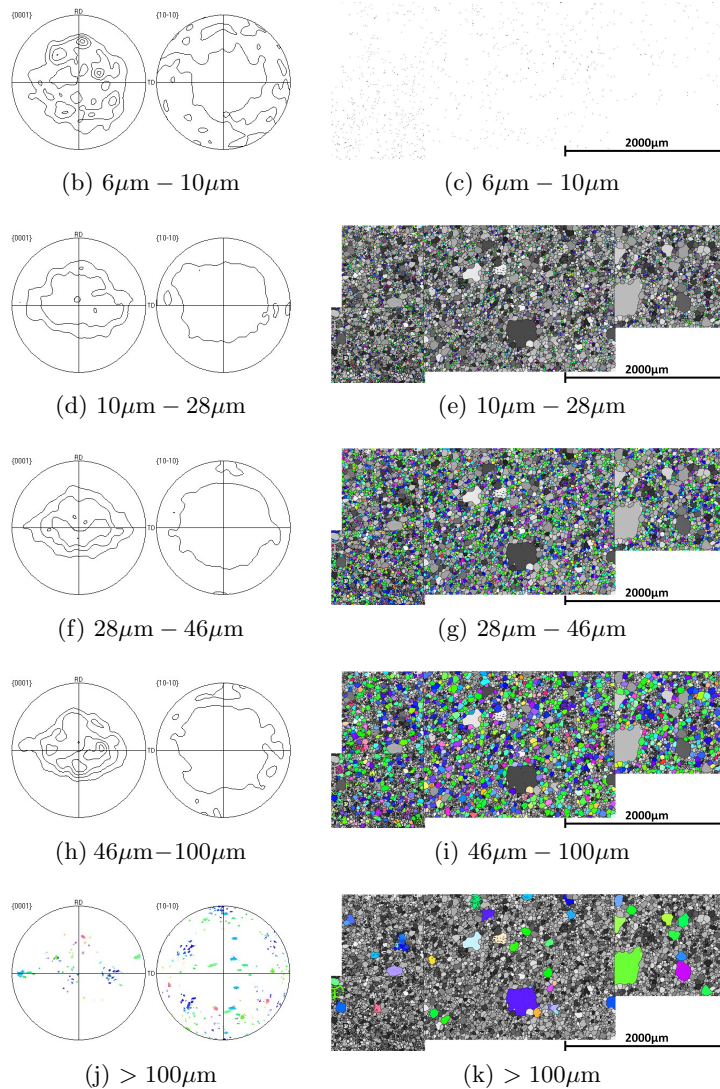


Figure 3.34: a) grain size distribution of a composite EBSD map for ZEK100 annealed for 30 days at 400°C. Textures and EBSD maps for various grain size ranges are also presented. 6-10 μm grains are less than one SD away from the mean, 10-28 μm grains are one SD below mean, 28-46 μm grains one SD above the mean, 46-100 μm grains greater than one SD above mean excluding abnormally grown grains. Finally > 100 μm grains are considered abnormally grown.

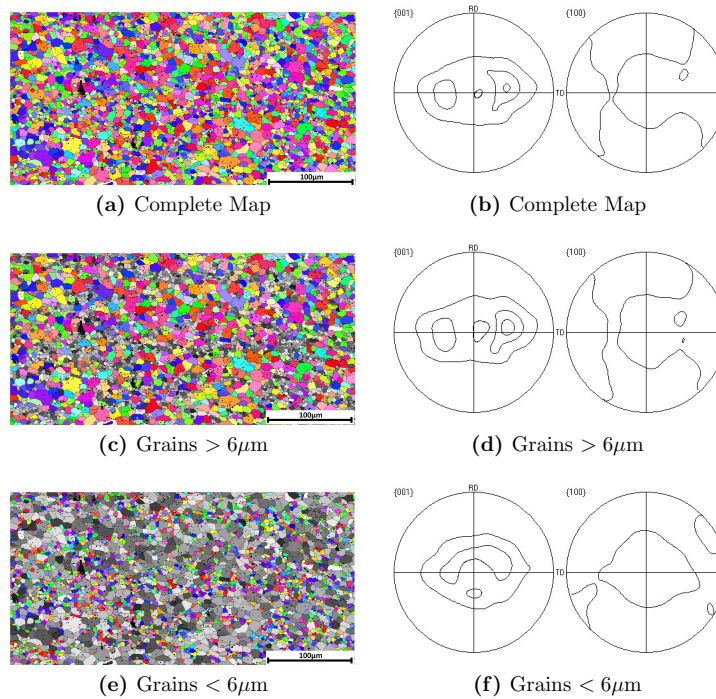


Figure 3.35: EBSD map of as received ZEK100 in the fully recrystallised condition. a,b) IPF coloured map and pole figures for the complete map. c,d) map and pole figure for grains larger than $6\mu\text{m}$ and e,f) map and pole figure for grains smaller than $6\mu\text{m}$.

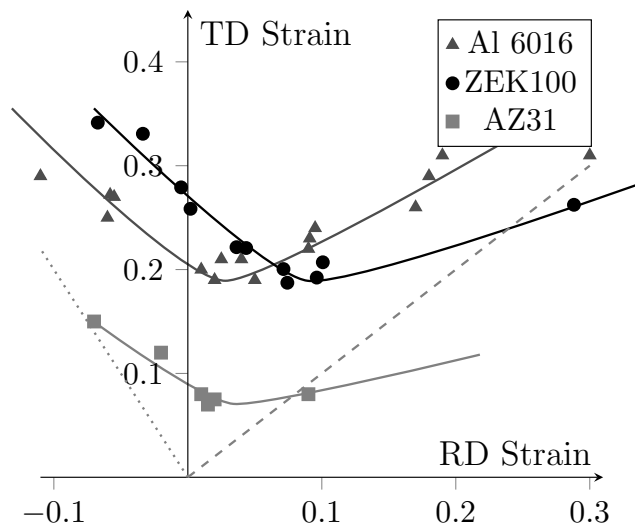


Figure 3.36: Forming limit diagram of ZEK100, aluminium 6016[110] and magnesium AZ31[111] are plotted for comparison, curves are added to guide the eye. Uniaxial tension is indicated by the dotted line and biaxial tension by the dashed line.

3.5 Segregation of Rare Earth Atoms

Segregation of RE atoms to grain boundaries is thought to be one of the most important factors in activating texture weakening in RE alloys, as discussed in Section 1.9. In the following we use EDX mapping with high resolution TEM imaging to observe the segregation of RE atoms to grain boundaries in the 0.1523 at% Y alloy, Y is a highly soluble RE element which clearly demonstrated RE texture weakening effects, Figure 3.1. We compare this to Nd segregation in the magnesium-0.0243 at% Nd alloy. Nd has a low solubility in magnesium and this alloy is only thought to have a borderline RE concentration for activating texture weakening, having only produced a slight texture weakening during hot rolling, Figure 3.5. Both alloys are imaged following hot rolling at 400°C and annealing for 1hr at 400°C followed by quenching. This heat treatment should reproduce the segregation conditions which produce RE textures in hot and cold rolled material.

3.5.1 Grain Boundaries

The segregation of solute elements to grain boundaries in the 0.1523 at% Y alloy is clearly shown in the HAADF images presented in Figure 3.37. In this form of imaging areas of white contrast correspond to atoms with a high atomic number which clearly segregate to grain boundaries, identifiable by the change in direction of lattice fringes at the boundary. EDX of these grain boundary regions is shown in Figure 3.38 where Y is found to strongly segregate to the two different grain boundaries examined. Figures 3.38 e) and f) contain plots of the variation in Y concentration across each grain boundary. For each of the 2 analysed boundaries multiple EDX maps were taken at different positions along the boundary and are plotted as a different curve in each graph giving an indication of the variability of segregation across the same boundary. Quantified EDX data should be considered with extreme caution as it is sensitive to large number of variables especially number of counts, specimen thickness, size of area considered to name but a few. However, the present results suggest in the 0.1523 at% Y alloy the peak concentration of Y at grain boundaries is between 1.2 and 1.5 at% varying along the boundary with a full width half maximum of 2–4nm. The peak in Y concentration is similar to the peak segregation of 1.3 at% Y observed by Hadorn *et.al*[95] in a 0.28 at% Y alloy, in a much lower resolution SEM study. In a similar study Stanford *et.al* find segregation of Gd (with similar solubility to Y) of up to 1.5 at% at grain boundaries in a 0.23 at% Gd alloy[194]. The present results show for the first time the strength of the segregation to grain boundaries with Y distributed less than 5nm either side of the boundary, limited resolution in previous studies indicated a segregation of less than 300nm. A higher resolution EDX mapping of

one boundary is shown in Figure 3.39, where the Y atoms are clearly shown to form small clusters on the grain boundary less than 2nm in size. The strength of the Y segregation shown here is a strong indicator that the segregation of RE elements to grain boundaries is required for RE texture weakening.

The same segregation of Nd to grain boundaries was not observed in the magnesium-0.0243 at% Nd alloy, where most of the Nd content was present in the form of a fine distribution of particles. Although the RE concentration in the Nd alloy is almost an order of magnitude lower than in the Y alloy we would still expect to detect the presence of Nd on grain boundaries if it had strongly segregated there. Instead, the Nd atoms were found within particles in the matrix.

3.5.2 Precipitates

Precipitates were observed in both alloys, examples of those found in the 0.15 at%Y alloy are presented in Figure 3.40 and the magnesium-0.0243 at% Nd alloy in Figures 3.41, 3.42 and 3.43. In the 0.15 at%Y alloy Y was found to precipitate in particles approximately 20nm in size composed primarily of Y, O and Fe. Trace amounts of Fe were detected by XRF analysis as impurities in the casting see Table 2.2 however, this technique is not sensitive to O additions. The oxygen detected in Figure 3.40 c) is homogeneously distributed suggesting at least some of the O detected is due to contamination of the sample, possibly oxidation in atmosphere prior to loading the TEM. High O levels are reported in some particles, such as Figure 3.40 e), where 20 at% O is reported. This may suggest some O contamination during the casting process allowing O containing precipitates to form. A significant Fe and Y content is also observed in this particular precipitate Figure 3.40 g-i). In any case as well as segregation to grain boundaries Y is also found in precipitates both largely alone, as in Figure 3.40 a) and with impurities as in Figure 3.40 e).

Precipitates in the Nd alloy were found to have various compositions including Fe, O and Nd constituents as shown in Figures 3.41, 3.42 and 3.43. These particles were primarily found in the matrix and although some were observed on grain boundaries but the overall volume fraction is expected to be too low to contribute significantly to pinning effects. The majority of Nd additions were located within such particles in spite of the magnesium-Nd phase diagram indicating that Nd additions should be present in solid solution at concentrations lower than 0.4 at% [7]. The particles shown in Figures 3.41 and 3.42 have Nd atoms strongly segregated to Fe and O containing particles. These particles are relatively large > 100nm with Nd concentrations estimated to be 6 and 12 at% respectively. These are remarkably high Nd concentrations considering the low Nd concentration of 0.0243

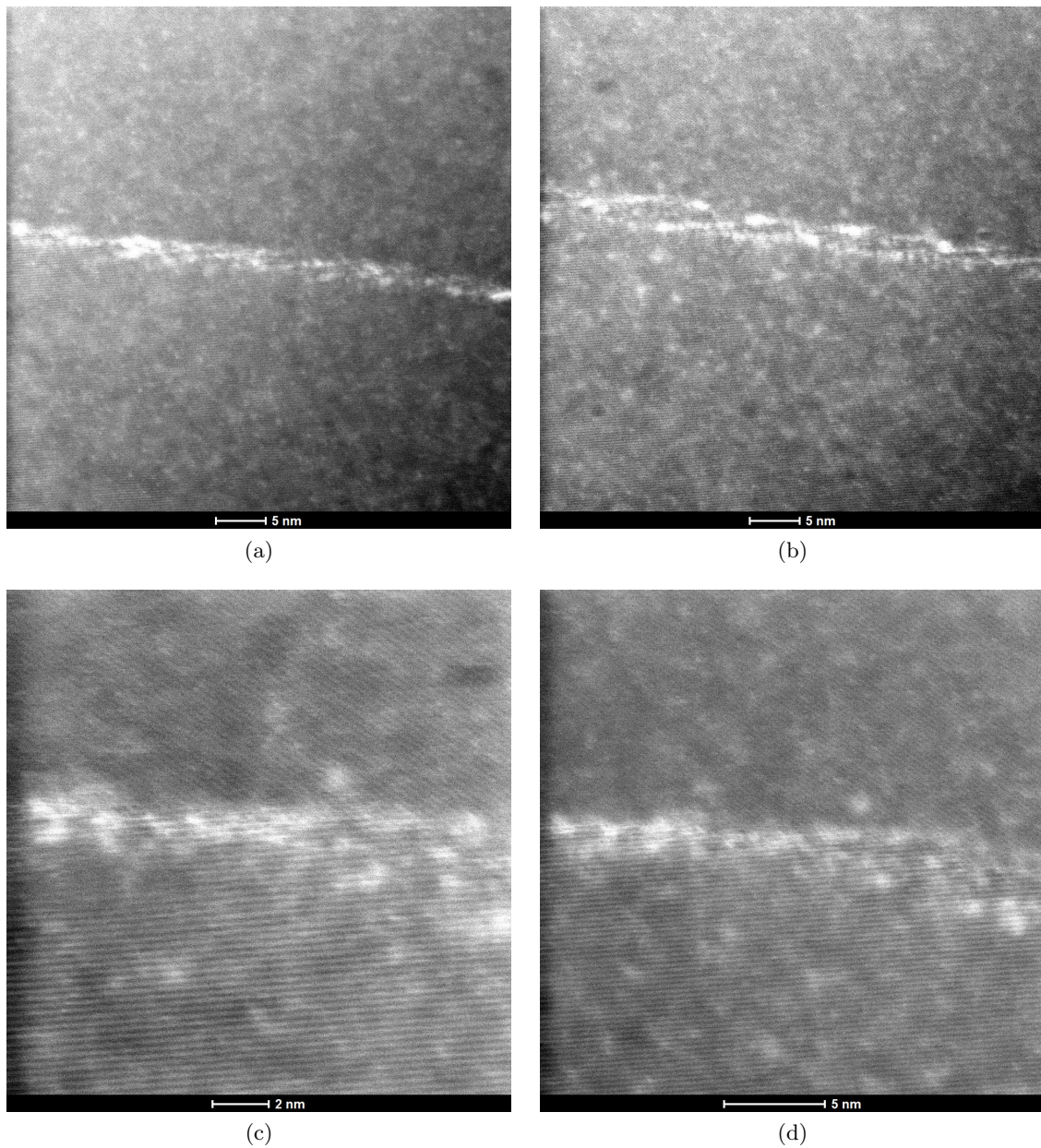


Figure 3.37: HAADF images showing the segregation of Y to grain boundaries in magnesium-0.15 at%Y after cold rolling and annealing for one hour at 400°C. Two grain boundaries were observed; a,c) grain boundary one and b,d) grain boundary 2, at low and high mag respectively.

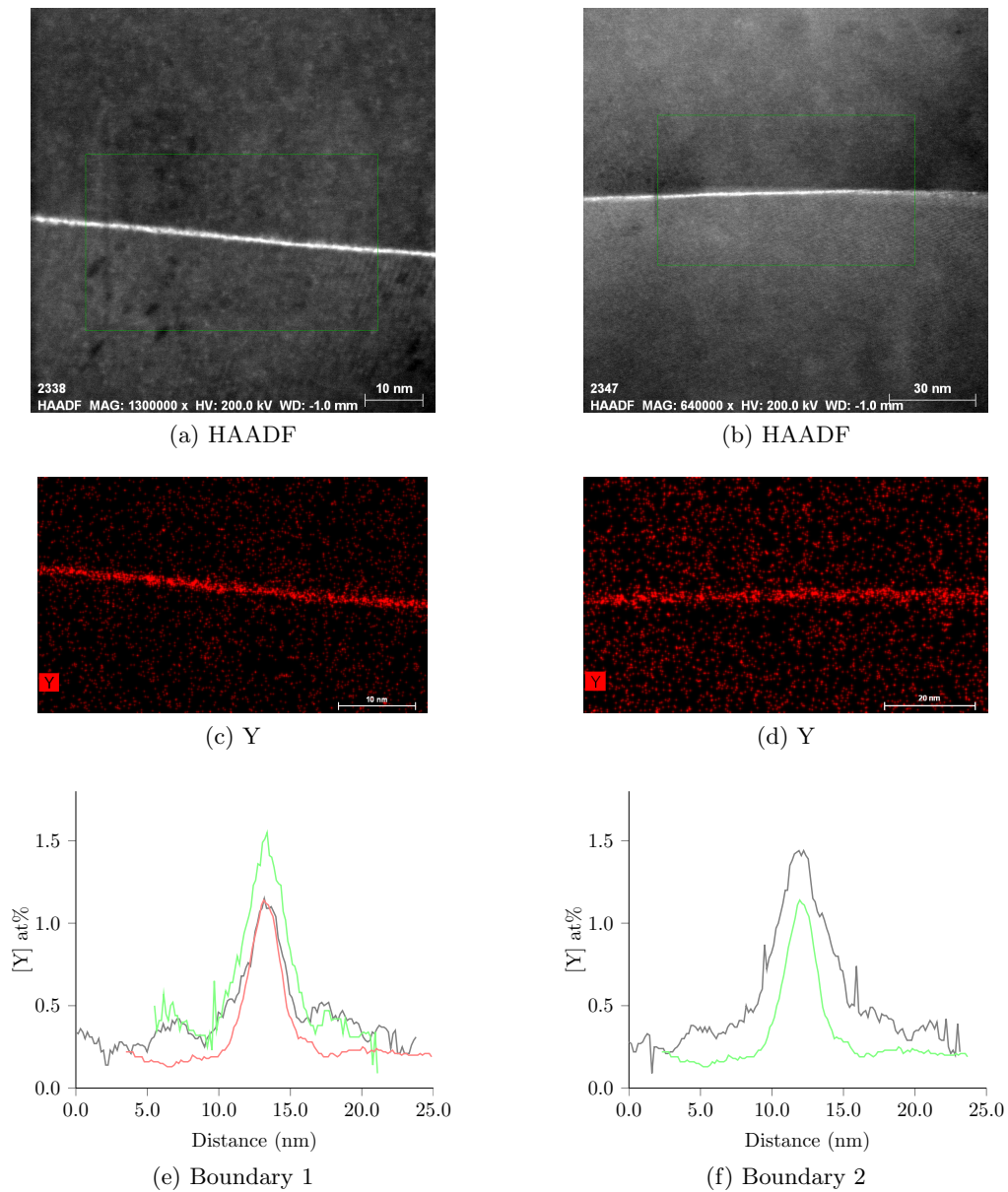


Figure 3.38: EDX map showing the segregation of Y across two different grain boundaries, in magnesium-0.15 at%Y after cold rolling and annealing for one hour at 400°C. Mapped regions are indicated by green box in HAADF images a,b). e,f) plot the concentration of Y across the two different grain boundaries analysed. Each curve within each plot is from a different area of the same boundary.

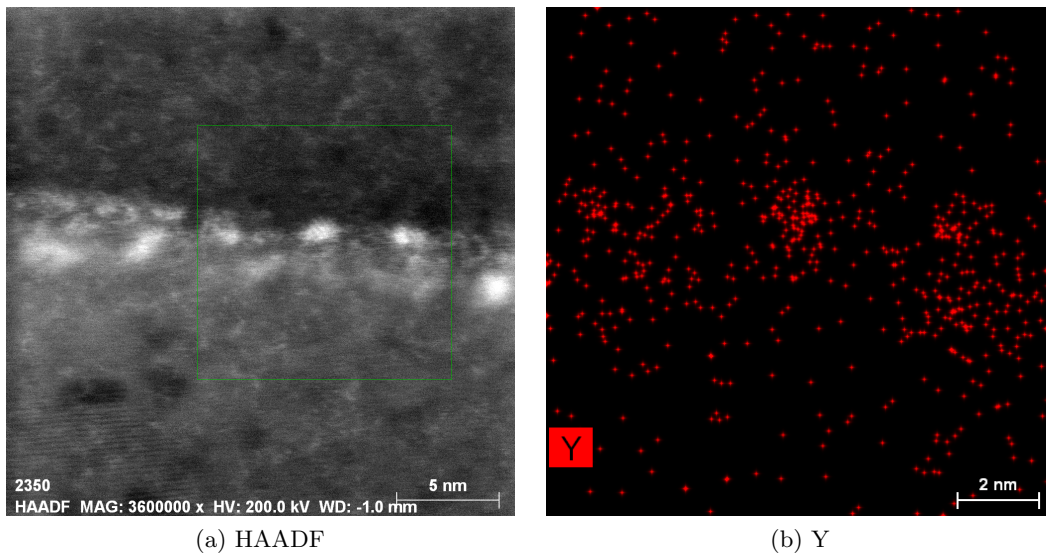


Figure 3.39: High resolution EDX map showing segregation of Y to grain boundaries in magnesium-0.15 at%Y after cold rolling and annealing for one hour at 400°C. Mapped region is indicated by green box in HAADF image a).

at% in this alloy. Even after allowing for errors in EDX quantification it seems that the majority of Nd in this alloy is present in precipitates. Figure 3.43 shows that while most of the observed Nd precipitates contained Fe or O impurities, some Nd was present in primarily Nd containing particles.

As Nd is expected to be in solution at these concentrations the present results suggest either low level impurities such as Fe and O significantly change the solubility of Nd or the magnesium-Nd phase diagram is not accurate at these low concentrations. This could be a critical factor in understanding the critical RE concentration for texture weakening because the RE effects are thought to be primarily solute based. In the Nd alloy little solute Nd was found, no RE texture weakening was observed, emphasising the importance of understanding the solubility of each RE particularly in the presence of impurities and other alloying additions.

In summary RE additions in the 0.15 at%Y alloy, which demonstrated RE texture weakening, were found to strongly segregate to grain boundaries. While no segregation of Nd atoms was observed in the 0.0243 at% Nd alloy, which did not display RE effects. In this alloy the majority of Nd was found to precipitate with impurities. This supports the assertion that segregation of solute RE elements to grain boundaries is critical in activating the RE effects, this is explored in Section 5.3.

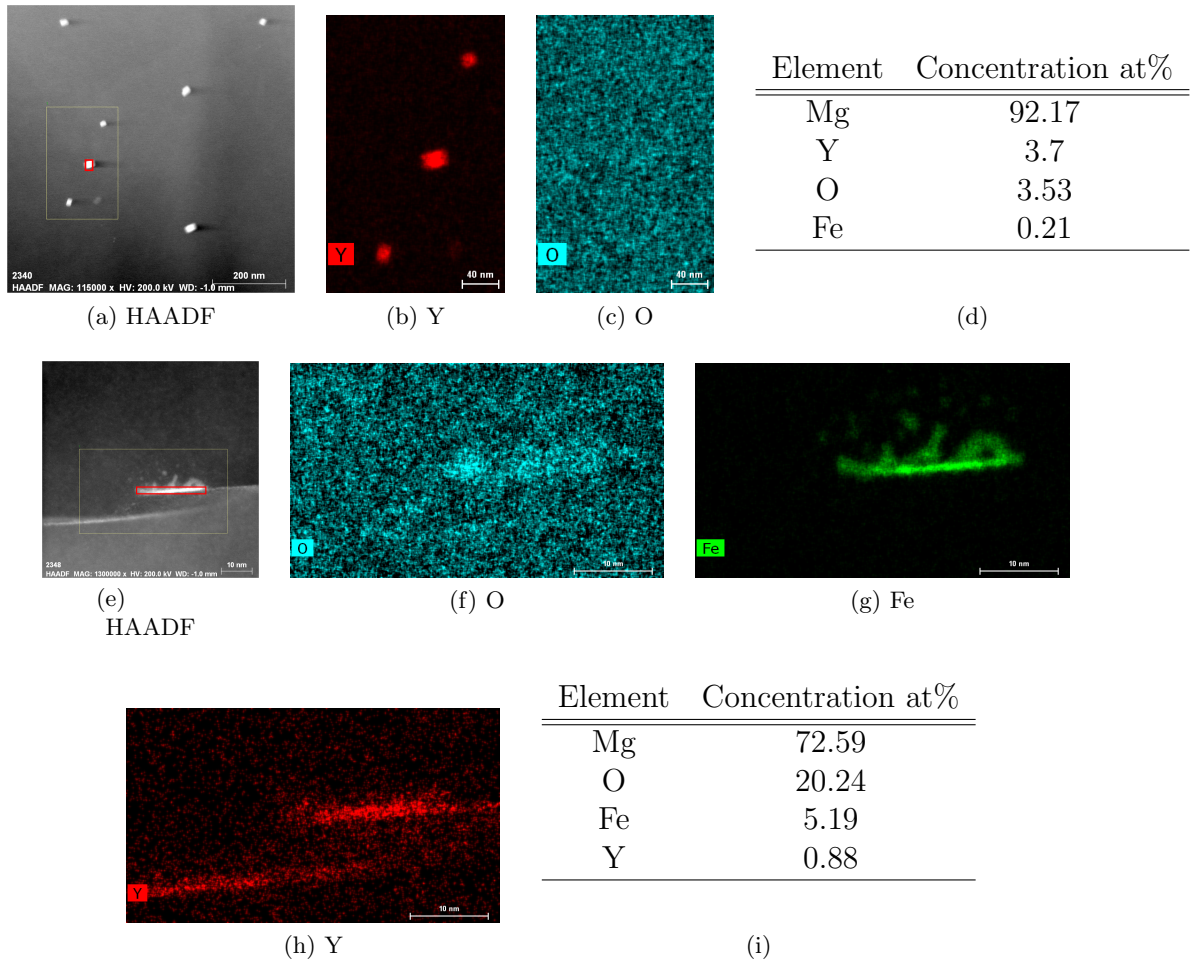
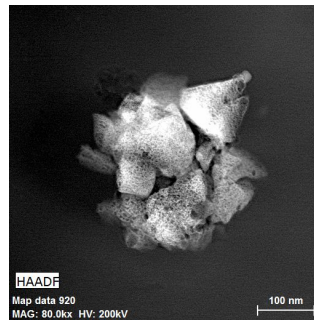


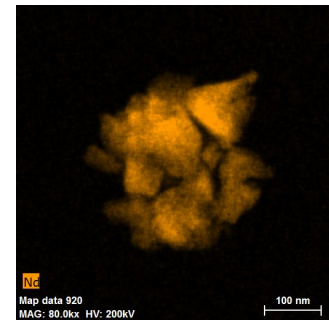
Figure 3.40: High resolution EDX maps showing composition of particles found in magnesium-0.15 at%Y after cold rolling and annealing for one hour at 400°C. Mapped region is indicated by green box in HAADF images a) and e). The regions analysed to give indicated compositions are shown by red boxes in a) and e)

Element	Concentration at%
Mg	63.63
Nd	5.97
O	28.33
Fe	0.16

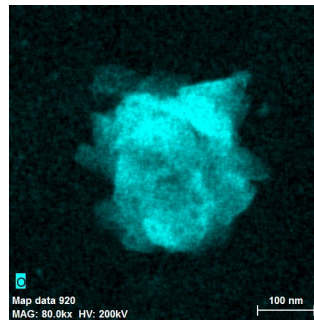
(a)



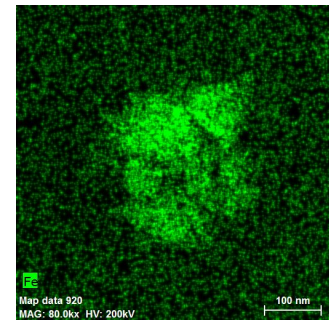
(b) HAADF



(c) Nd



(d) O

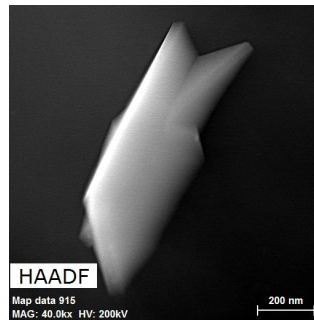


(e) Fe

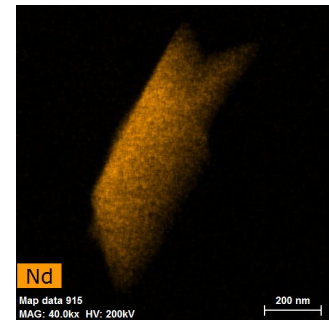
Figure 3.41: High resolution EDX map showing composition of particles found in magnesium-0.0243 at% Nd alloy after cold rolling and annealing for one hour at 400°C. Mapped region is indicated by green box in HAADF image a).

Element	Concentration at%
Mg	81.71
Nd	12.16
Fe	2.57
O	1.54

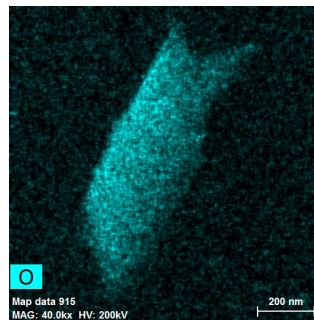
(a)



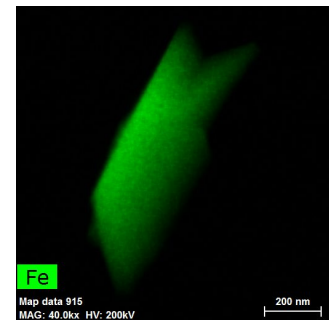
(b) HAADF



(c) Nd

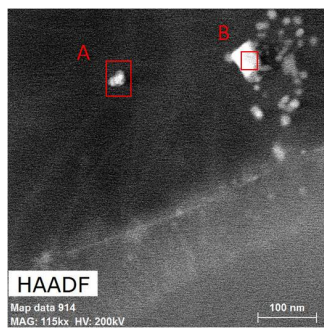


(d) O

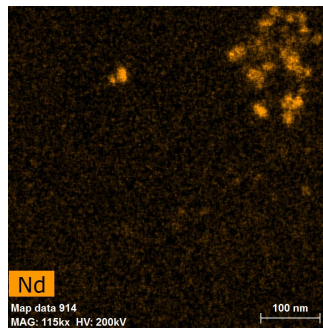


(e) Fe

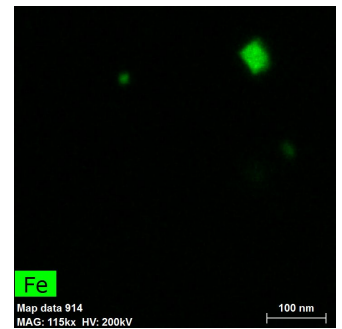
Figure 3.42: High resolution EDX map showing composition of particles found in magnesium-0.0243 at% Nd alloy after cold rolling and annealing for one hour at 400°C. Mapped region is indicated by green box in HAADF image a).



(a) HAADF



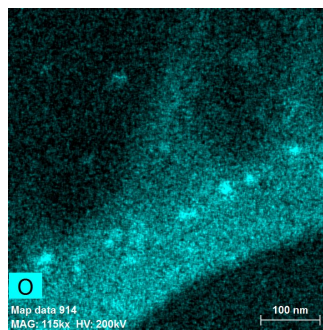
(b) Nd



(c) Fe

Element	Concentration at%
Mg	95.99
Fe	1.46
Nd	0.51
O	1.49

(d) Particle A



(e) O

Element	Concentration at%
Mg	89.16
Fe	9.02
Nd	0.31
O	0.97

(f) Particle B

Figure 3.43: High resolution EDX map showing composition of particles found in magnesium-0.0243 at% Nd alloy after cold rolling and annealing for one hour at 400°C.

Mapped region is indicated by green box in HAADF image a).

Chapter 4

Modelling Cold Rolling

4.1 Crystal Plasticity Modelling

4.1.1 Constitutive Model

Crystal plasticity modelling is used to predict the deformation behaviour and texture evolution in a polycrystalline material from the constitutive behaviour at the single crystal level. In each model, this relationship is controlled by constitutive laws which define material behaviour by linking strain rate and stress to a variety of material parameters such as dislocation density, critical resolved shear stress and texture[208]. Constitutive equations generally consist of a state equation of the form

$$\sigma = f(\dot{\epsilon}, X_i). \quad (4.1)$$

This links stress (σ) to strain rate ($\dot{\epsilon}$) and all the other state variables included in the model (X_i). The state equation is associated with a variety of evolution equations which define how each state variable evolves as a function of the other variables;

$$\dot{X}_i = f(\dot{\epsilon}, X_j). \quad (4.2)$$

In principle there are two types of constitutive model; phenomenological models and physics based models. Phenomenological models are more empirical and are not necessarily based on the real physics of the situation, unlike physics based models which are in principle true reflections of the material physics. In crystal plasticity modelling the most common phenomenological constitutive law defines the critical resolved shear stress (τ_0) as the state variable controlling dislocation slip (and therefore plastic strain) on each slip system [209]. In this regime, slip occurs on a given system once the resolved

shear stress exceeds τ_0 . An equivalent physics based constitutive law for dislocation slip uses dislocation density as a key state variable. The choice of constitutive equation is a balance between the computational cost and the level of detail needed from the model. Currently the phenomenological model described above is frequently used as τ_0 can be experimentally measured relatively easily from single crystal investigations, unlike dislocation density which is far more difficult to quantify experimentally (especially on the macro-scale). A state equation is then used to link the strain rate to the applied stress in each grain [210], this may take various forms however, models differ more significantly in how these state equations for each grain combine to meet macroscopic boundary conditions. The approaches can broadly be considered as either mean field or full field [211]. Full field approaches treat grain-grain interactions explicitly, with the strain rate in each grain a function of how hard or soft the surrounding grains are. In contrast, a mean field model treats grain-grain interactions in an average way, with each grain subject to the same average response from the matrix. In principle, full field approaches offer the highest accuracy as explicitly modelling grain-grain interactions may reproduce complex structural inhomogeneity with more precision than the average approach of mean field methods. However, full field approaches are significantly more computationally expensive than the relatively simple mean field approach. In the following we review some leading full and mean field models and discuss their application to crystal plasticity in h.c.p systems.

4.1.2 Mean Field Models

Mean field models come with a significant reduction in computational cost over full field models as each grain experiences an average interaction with all other grains, meaning explicit grain grain interactions do not need to be calculated. The process of spreading the macroscopic boundary conditions across all grains to produce this average interaction term is known as homogenisation. There are various homogenisation schemes available, all of which ensure that the macro-level boundary conditions are met while allowing each individual grain to deform differently (to a greater or lesser extent) based on its internal state functions. Homogenisation schemes are bounded by two models; the upper bound of the Taylor (full constraints) model and the lower bound of the Sachs model. The Taylor model represents the stiffest interaction between grain and matrix where each grain is confined to experience the macroscopic strain applied [212]. In this way strain is accommodated homogeneously throughout each grain in the material meeting the boundary conditions. The lower bound Sachs scheme enforces each grain to experience an equivalent material stress behaving as if it were an unconstrained single crystal, allowing an inhomogeneous strain distribution in the material. Neither case is appropriate for

anisotropic h.c.p materials, where grains with a soft orientation for slip would be expected to deform more than grains with a hard orientation. The Taylor model enforces both hard and soft grains to accommodate equivalent strain. While in the Sachs model soft grains are allowed to deform too much as they are not constrained by hard oriented grains in the matrix[213]. There are a range of intermediate solutions available, most commonly the Tangent and Secant approximations are applied, they are defined fully in [213, 214]. In both cases the interaction is defined by the macroscopic stress and strain rate applied to the system, with the secant model a linear function defined by the origin and macroscopic stress and strain rate[213, 215]. The Tangent response is a linear tangent of the macroscopic stress strain rate function defined by a first order Taylor expansion at the given macroscopic stress and strain rate[210, 213, 216]. Other first order approximations include the Affine which [217] expands on the secant approach making it softer[217]. Various other second order homogenisation schemes are available which try to retain the computational cost of the mean field approach while increasing the accuracy of simulations[213, 214, 218].

Comparison of the effectiveness of the linear first order homogenisation schemes described above in h.c.p materials have been carried out by various authors [26, 213, 219] showing as expected the Tangent and Secant approaches represent compliant and stiff matrix interactions respectively[26]. A full comparison of the predictive capabilities of each of these first order homogenisation functions suggests the Affine approximation is the best homogenisation scheme for magnesium AZ31[26]. The study shows that while all of the above schemes may be fitted to experimental RD tension and RD compression flow stress curves, the predictions made by these fitted models vary in accuracy. The Tangent interaction significantly underestimates flow stress of ND compression, due to overestimation of basal slip at low strains. Similarly the Secant model poorly predicts Lankford coefficients, both of which are well predicted by the Affine model.

Once chosen, the constitutive equations and homogenisation scheme must be combined to form the overall model. In the present work we focus on the Visco-Plastic-Self-Consistent (VPSC) method has been used, developed by Molinari et al. [216] and extended to anisotropic materials by Lebensohn and Tomé [210, 220]. The Los Alamos VPSC model has been successfully used to model crystal plasticity in a variety of cubic and h.c.p systems [25, 25, 26]. Using the Eshelby inclusion formalism [221] each grain is modelled as an ellipsoid inclusion within a homogeneous effective medium (HEM). The HEM effectively simulates the macroscopic stresses and strains and grain-grain interactions using the chosen homogenisation scheme. Without considering the detailed mechanics of this model, which are discussed at length elsewhere, the method used to incorporate mechanical twinning and work hardening in the Los Alamos VPSC model are summarised below.

Work hardening on each slip system s is normally simulated using a Voce type hardening law [222];

$$\hat{\tau}^s = \tau_0^s + (\tau_1^s + h_1^s \gamma_{\text{acc}}) \left(1 - \exp \left(-\frac{h_0^s}{\tau_1^s} \gamma_{\text{acc}} \right) \right) \quad (4.3)$$

where τ^s is the CRSS required to activate the slip system s . τ , h and γ_{acc} represent CRSS's, hardening rates and accumulated shear strain respectively with subscript 0 indicating initial values and 1 indicating the asymptotic values.

Twinning is a critical deformation mode in h.c.p materials and causes a significant amount of anisotropy in mechanical properties. It differs from slip in two ways; shear only occurs in one direction and a fixed and well defined amount of shear forms only once a twin has formed and so is not continuous like slip. This causes a number of problems in modelling twinning, in deciding which grains should twin and also dealing with the interaction of twinned region with the matrix, as a twin has such a high misorientation with respect to the parent grain it effectively acts like a new grain. An increasing number of grains during a computation limits efficiency with simulations often becoming too large to run[210]. There are various approaches to dealing with twinning in crystal plasticity modelling[84, 223]. In the Los Alamos VPSC model the Predominant Twin Reorientation (PTR) scheme is usually applied[84]. In this scheme, twinning is modelled essentially as slip which only occurs in one direction with a representative CRSS required to activate it. At each time step the volume fraction of twinned material in each grain is calculated and summed over all grains giving a 'real' volume fraction of twinning over each twin system for the simulation (F_R). A threshold value (F_T) for twin reorientation is defined based on the 'real' twin volume fraction at that point in the simulation and the fraction of twinned grains that have been reoriented (F_E);

$$F_T = 0.25 + 0.25 \frac{F_E}{F_R}. \quad (4.4)$$

At each time step if the twin volume fraction within an individual grain exceeds this threshold value the entire grain is reoriented. In this way twinning predominantly occurs in grains with the highest twinning activity and, because the threshold twin fraction is related to the total fraction of twinned grains, this threshold grows during the simulation. The constants used in Equation 4.4 may be adjusted to fit the model to observations [84].

The VPSC model with the PTR twinning scheme has been widely used to model the behaviour of hexagonal materials with significant successes. In particular, tension-compression yield anisotropy in magnesium sheet has been captured [26, 82, 83] together with Lankford coefficients [25, 82, 118, 210] and the full yield locus of a zirconium system [210]. VPSC has also been combined with a suitable failure criterion (Marciniak-Kuczynski method) to predict the forming limit diagram of magnesium sheet[118]. An extension of the VPSC

model to include elastic behaviour, the Elastic Plastic Self Consistent (EPSC) model, summarised in [224], has also been developed, applied to magnesium and validated using neutron diffraction, where the flow curves and internal strain development were successfully simulated [225, 226].

In the above cases the CRSS's, and hardening parameters of each slip system have been tuned to accurately reproduce the macroscopic material behaviour such as flow stress curves and Lankford coefficients. After fitting, other material parameters such as a slip and twinning mode activity, deformation textures and hardening behaviour can be predicted for any number of conditions. However, the accuracy of these predictions are strongly sensitive to the quality of experimental fitting, as experimentally determined CRSS's from single crystal experiments are not generally applicable to polycrystalline material [25–27, 43, 44, 64, 227] and as a result fitted variables change widely from study to study and alloy to alloy. Model predictions are therefore only likely to be accurate for material and deformations similar to those used to fit the model initially.

The model is also intrinsically limited in its reproduction of micro scale parameters such as recovery and grain size both of which are accounted for in an average way within the Voce hardening law (Equation 4.3). While the model has been extended in various ways to account for other temperature dependent behaviours, such as dynamic recrystallisation, the mean field approach is only able to reproduce these behaviours in an average way such that the physics of many micro scale events such as twinning, work hardening and recrystallisation is inevitably lost. These effects are quantified explicitly in full field models.

4.1.3 Full Field Models

In order to explicitly deal with grain-grain interactions a full field model is required. The most commonly applied full field model utilises the finite element (FE) method. In this methodology the material microstructure is discretised into a finite number of representative volume elements (RVEs), the scale of the RVEs ranges from one element per grain [44] to hundreds of elements per grain [228] depending on the purpose of the model. FE modelling essentially solves equations balancing forces and displacements within each element, summing these solutions together meets a given set of macroscopic boundary conditions. Finite element crystal plasticity modelling (CPFEM) is the application of the FE methodology to simulate crystal plasticity, introduced by Peirce *et.al* [229] and reviewed in detail by Roters *et.al* [209]. In principle CPFEM models may apply the same constitutive and twinning models as discussed for mean field approaches, solving them using the FE approach.

CPFEM has had considerable success in modelling deformation in h.c.p materials including magnesium [230–234]. The technique has been successfully used to simulate macro scale forming and deformation processes including flow stress curves and Lankford values under various deformation conditions, reproducing yield stress anisotropies in magnesium similarly to mean field models [235–237]. Unlike mean field models, CPFEM models can be extended to simulate deformation on the microstructural level [228, 238, 239]. It can even be applied to specific microstructures, which can be measured using EBSD and the results of simulations can then be directly compared to experimental deformation of the same microstructure to validate the model [238, 240]. Grain level strains simulated by CPFEM can also be validated using neutron diffraction data to probe intra granular strains [239].

While CPFEM has been used with significant success to model h.c.p systems on a variety of scales such accuracy comes with significant computational costs. So while in principle a full field model may explicitly model each grain in the microstructure in practice this is not possible when simulating deformation of large parts[209, 228]. In such cases some kind of homogenisation scheme is required, where each element may represent anything from one to hundreds of grains[209].

4.1.4 Summary

In summary, while significant advances in crystal plasticity modelling have been made in recent years all modelling approaches face a trade off between computational cost and accuracy. Full field approaches such as CPFEM offer the best prospects for reproducing a full range of material effects from intergranular stresses to twinning however at significant computational cost. At the other end of the spectrum, mean field models are able to simulate a wide range of macroscopic properties at relatively low computational cost. However, these models are unable to explicitly account for microstructural effects such as grain morphology and work hardening which must be approximated through a homogenisation scheme.

4.2 Model Parameters

In the following the mean field VPSC crystal plasticity model is used to simulate the rolling of magnesium and estimate the impact changes in the activity of each deformation mode has upon the deformation texture of the material. The minimum parameter approach to crystal plasticity modelling proposed by Hutchinson, Jain and Barnett [45] has been adopted, this approach has successfully simulated changing r values during a tensile test

of AZ31 magnesium sheet. In this approach the many variables of the VPSC model are minimised by approximating the same work hardening for each slip system described by h_0 , τ_1 and a microstructure constant. The authors argue this approximation is justified as each slip system intersects the same matrix and so hardening of one system is also likely to harden the others. With these approximations the Voce hardening law Equation 4.3 becomes;

$$\hat{\tau}^s = \tau_0^s + \tau_1 \left(1 - \exp\left(-\frac{h_0}{\tau_1} \gamma_{acc}\right) \right), \quad (4.5)$$

where h_0 and τ_1 are no longer dependent on which slip system s is operational. As latent hardening and self hardening are excluded in this model the components of the hardening matrix are set to unity, such that each deformation mode experiences the same hardening. The authors use the same approximation on twinning systems for simplicity although the argument for hardening of twinning systems is more complex than that for slip system hardening.

As a benchmark the variables optimised for AZ31 by Hutchinson *et.al* are used, these are given in Table 4.1. The τ_0 for each slip system are an average of experimentally measured values from single crystals [27]. Tension twinning has been added to the model a fundamental CRSS of 7 MPa is used based on the work of Chapuis and Driver [28], from which Hutchinson *et.al* estimate the CRSS of compression twinning. Identical adjustable parameters as Hutchinson *et.al* are also used for the hardening and microstructure constants.

Table 4.1: Parameters used in the VPSC model, based on the minimum parameters approach by Hutchinson *et.al*[45]

Parameter	Value
CRSS Basal $\langle a \rangle$	1 MPa
CRSS Prism $\langle a \rangle$	46 MPa
CRSS Pyram $\langle c + a \rangle$	65 MPa
CRSS Compression Twin	85 MPa
CRSS Tension Twin	7 MPa
Shear Compression Twin	0.14
Shear Tension Twin	0.13
Microstructure Constant	35 MPa
h_0	1500 MPa
τ_1	70 MPa

4.3 Benchmark Magnesium Rolling

Rolling was simulated by plane strain compression of 500 random orientations simulating a random texture, Figure 4.1 c,g). The simulation was carried out in increments of 0.001

strain up to a maximum $\epsilon_{\text{total}} = 2.0$, the model does not include DRX effects and so it is effectively a cold rolling simulation. Results of the benchmark simulation are presented in Figure 4.1. These conditions produce a flow stress curve with a reasonable yield point for magnesium of $\approx 150\text{MPa}$, however the flow stress curve does not pass through the origin or fail during the present simulation. These anomalies are because the VPSC model does not simulate elastic effects or failure of the material. As the impact of changing CRSS values on texture is of primary interest elastic effects are overlooked and it is simply noted that material failure is likely to occur significantly before $\epsilon_{\text{total}} = 2.0$, at around $\epsilon_{\text{total}} = 0.5$ during cold rolling of ZEK100, Section 3.2.3. Figure 4.1 also shows a plot of the activity of each slip system as a function of strain. Activity is defined as the fraction of strain accommodated by each slip system at each strain increment;

$$\text{Activity}^s = \frac{\epsilon_{\text{step}}^s}{\sum^s \epsilon_{\text{step}}^s} \quad (4.6)$$

where s is the deformation mode and ϵ_{step} is the strain advanced during each simulation step. In the benchmark simulation basal slip is found to be the dominant deformation mode followed by pyramidal and prismatic slip, the activity of these latter deformation modes quickly drops off during the deformation as grain orientations harden during straining. Tension twinning is very active up to $\epsilon = 0.1$ however again this mode quickly becomes in-active once favourable twinning orientations are exhausted. Contraction twinning is not predicted to be active during this deformation.

Finally basal and prismatic pole figures are presented for strains of 0.2, 0.5 and 2.0. After 0.2 strain tension twinning and basal slip have formed a TD band of orientations which gradually forms two lobes in the RD after 0.5 strain. The intensity of these lobes increases after 2.0 strain, however in reality the material would probably fail long before $\epsilon = 2.0$, especially during cold rolling. The formation of the RD split in the basal texture has been observed experimentally (Figure 1.32 a)) and in VPSC simulations where the split is attributed to the activity of the pyramidal slip system [83]. These modelling conditions reasonably reproduce experimental flow stress curves and textures as well as previous VPSC simulations and so they will be used as a benchmark for further investigations.

4.4 Contribution of Each Slip System to Deformation Texture

The deformation texture of each simulation is a function of the activity of each slip system, in this experiment each deformation mode is individually deactivated and the effect on deformation texture is observed. Note that these are not necessarily physically probable

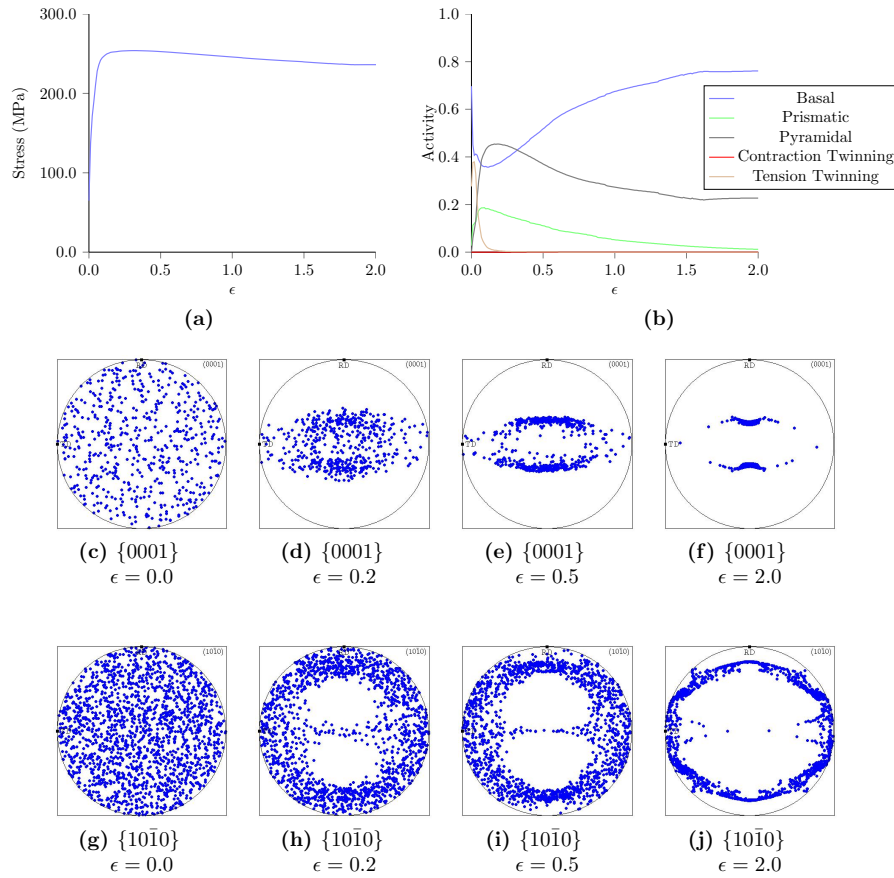


Figure 4.1: Figure showing a) flow stress curve, b) slip system activities and c-j) deformation textures after 0.0, 0.2, 0.5 and 2.0 true strain after the benchmark simulations.

scenarios and are merely intended to give an idea of the effect of each system.

Basal Slip Figure 4.2 a-c) shows deactivating basal slip forces pyramidal slip to become the dominant deformation mode. After 0.5 strain this leads to a more diffuse basal texture in comparison to the benchmark tests, however the split basal texture in the RD remains and the increased pyramidal activity appears to increase the misorientation of this split relative to the normal direction.

Prismatic Slip Absence of prismatic slip increases the activity of pyramidal slip during the deformation which appears to intensify the split basal texture in the RD, Figure 4.2d-f). There are also fewer orientations spread between the ND-TD when prismatic slip is deactivated

Pyramidal Slip As previously noted pyramidal slip is thought to control the ND-RD

split basal texture in VPSC simulations, as a result deactivation of pyramidal slip leads to a strong basal texture typical of magnesium alloys, Figure 4.2g-i). Without pyramidal slip basal and prismatic slip are the dominant deformation modes aligning basal planes parallel to the sheet plane. Figure 4.2g) shows an instability in the simulation at $\epsilon = 1.0$, however this does not affect the deformation textures presented at $\epsilon = 0.5$. We note also that the absence of pyramidal slip has led to the peaks in the prismatic pole figure, Figure 4.2i) characteristic of the $\{0001\}\langle 11\bar{2}0 \rangle$ texture component. This is not observed in any other simulation.

Twinning The deactivation of contraction and tension twinning are considered independently, Figure 4.2 j-o). As compression twinning was not active during the benchmark test no change is observed in simulation results when this mode is deliberately deactivated. Deactivating tension twinning increases the activity of prismatic slip and contraction twinning in the early stages of the deformation, pyramidal slip activity also reduces. This combination of increased contraction twinning and reduced pyramidal slip appears to create a wider spread of orientations in the TD, although the RD texture split is still dominant.

In summary the activity of pyramidal slip is predicted to be the most important parameter in determining the deformation texture morphology. High pyramidal activity increases the split of the basal texture in the RD while deactivation of this deformation mode removes the split entirely. The relative activity of the twinning modes also appears important in controlling the spread of orientations in the TD, with increased contraction twinning increasing the TD spread. None of the above conditions produce the a basal texture split in the TD as observed in recrystallised ZEK100, however a small number of orientations spread in the TD (possibly by increased contraction twinning) may nucleate the TD split during recrystallisation.

4.4.1 Changing Deformation Mode Activities

The effect of changing the CRSS of each slip system, rather than deactivating each system entirely, is studied in the following. In particular the effects of increasing non-basal prismatic and pyramidal slip together with increased contraction twinning on deformation textures are of interest, as both these effects are associated with RE addition. Increased non basal slip may thus help to explain the formation of RE textures if it leads to non-basal orientation in the microstructure which could subsequently nucleate RE textures, such as the TD split basal texture of ZEK100 or the weak basal texture of the binary magnesium-rare earth alloys.

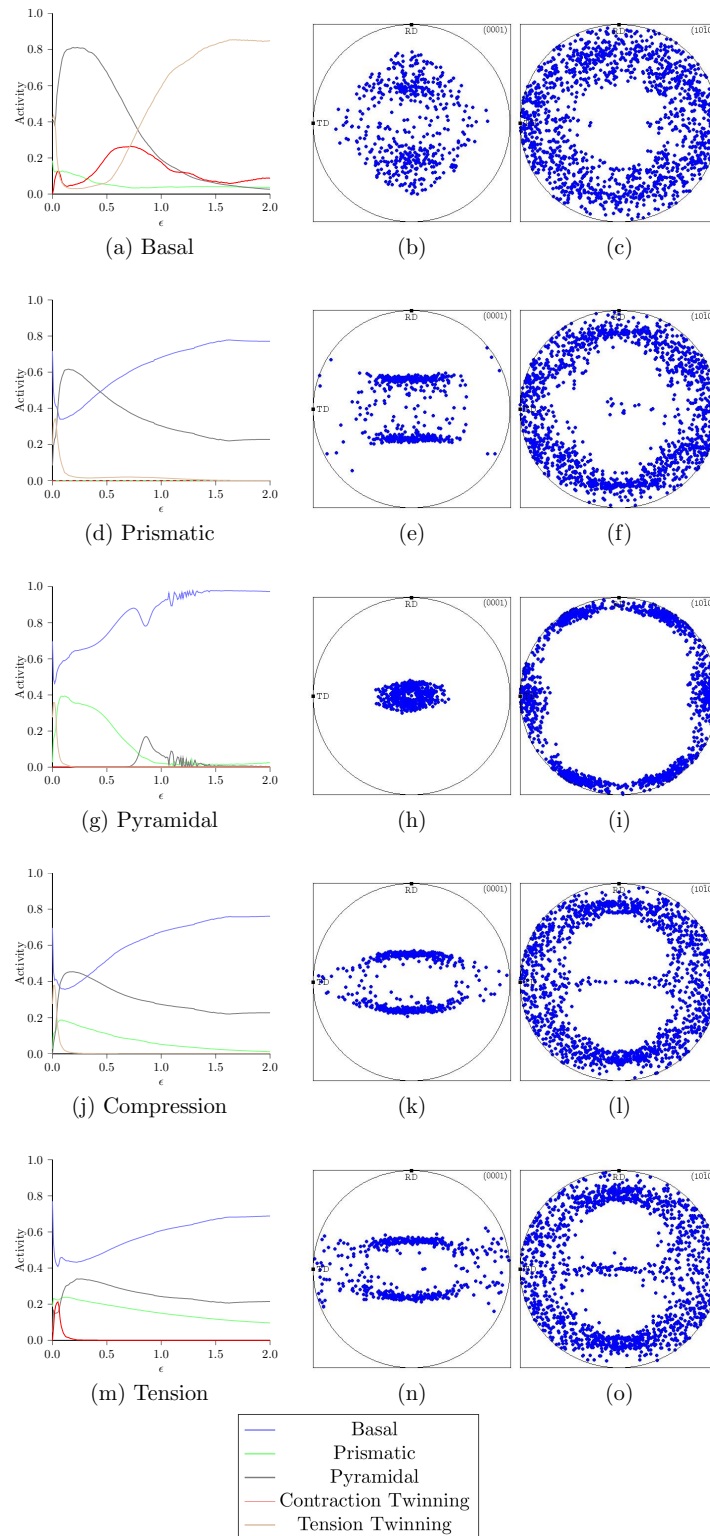


Figure 4.2: Figure showing the effect of individually deactivating each deformation mode during plane strain compression. Slip system activities are shown to $\epsilon = 2.0$ and deformation textures are reported at $\epsilon = 0.5$.

4.4.1.1 Increasing Non-Basal Slip

Pyramidal slip has been identified as very influential on the deformation texture morphology during rolling. Figure 4.3 shows the predicted effect of reducing the CRSS of pyramidal slip from 65MPa to 10MPa on slip system activities and deformation textures. Reducing the CRSS increases the peak activity of pyramidal slip from 0.45 to 0.7, Figure 4.3a). This leads to the dominance of pyramidal slip during the deformation, Figure 4.3g), and a split basal texture in the RD Figure 4.3d). The misorientation of this RD split with respect to the ND falls as pyramidal slip activity increases, which is consistent with the literature. This texture morphology is similar to the case where prismatic slip was deactivated, Figure 4.2e), as deactivation of prismatic slip had a similar effect promoting pyramidal slip activity.

Figure 4.4 shows the effect of reducing the prismatic CRSS from 46MPa to 10MPa. This had a negligible effect on the deformation texture, Figure 4.4d), which shows a slightly increased spread of orientations in the TD, however the RD split remains dominant.

Finally increasing the CRSS of basal slip relative to all other deformation modes was investigated by increasing it from 1MPa to 100MPa. This should give an indication of the effect on the texture if all other deformation modes become relatively softer in comparison to basal slip. The results are shown in Figure 4.5, in which raising the basal CRSS to 100MPa reduces the minimum activity of the system from 0.4 to 0.05, making pyramidal slip the dominant deformation mode. In this case the RD texture split is prominent although more diffuse than in the benchmark case, a slight spread of orientations in the TD remains.

In summary the reduced CRSS of pyramidal slip expected in RE alloys, is predicted to increase the RD-ND misorientation of the split basal texture, while reduced prismatic CRSS does not appear to have a significant effect on the texture morphology. In both cases the increased spread of orientations about the ND observed in recrystallised RE textures, is not predicted. On the other hand raising the CRSS of basal slip, and thereby effectively softening all other systems, does seem to produce a more diffuse spread of orientations around the RD split after $\epsilon = 0.5$.

4.4.1.2 Effect of Twin Activity

Rare earth alloys are frequently reported to show significantly different twinning activity to that typically expected in magnesium. In particular contraction twinning is often reported to be more active in RE systems. This effect is simulated in Figure 4.6 by reducing the compression twinning CRSS from 85 to 10 MPa which increases compression

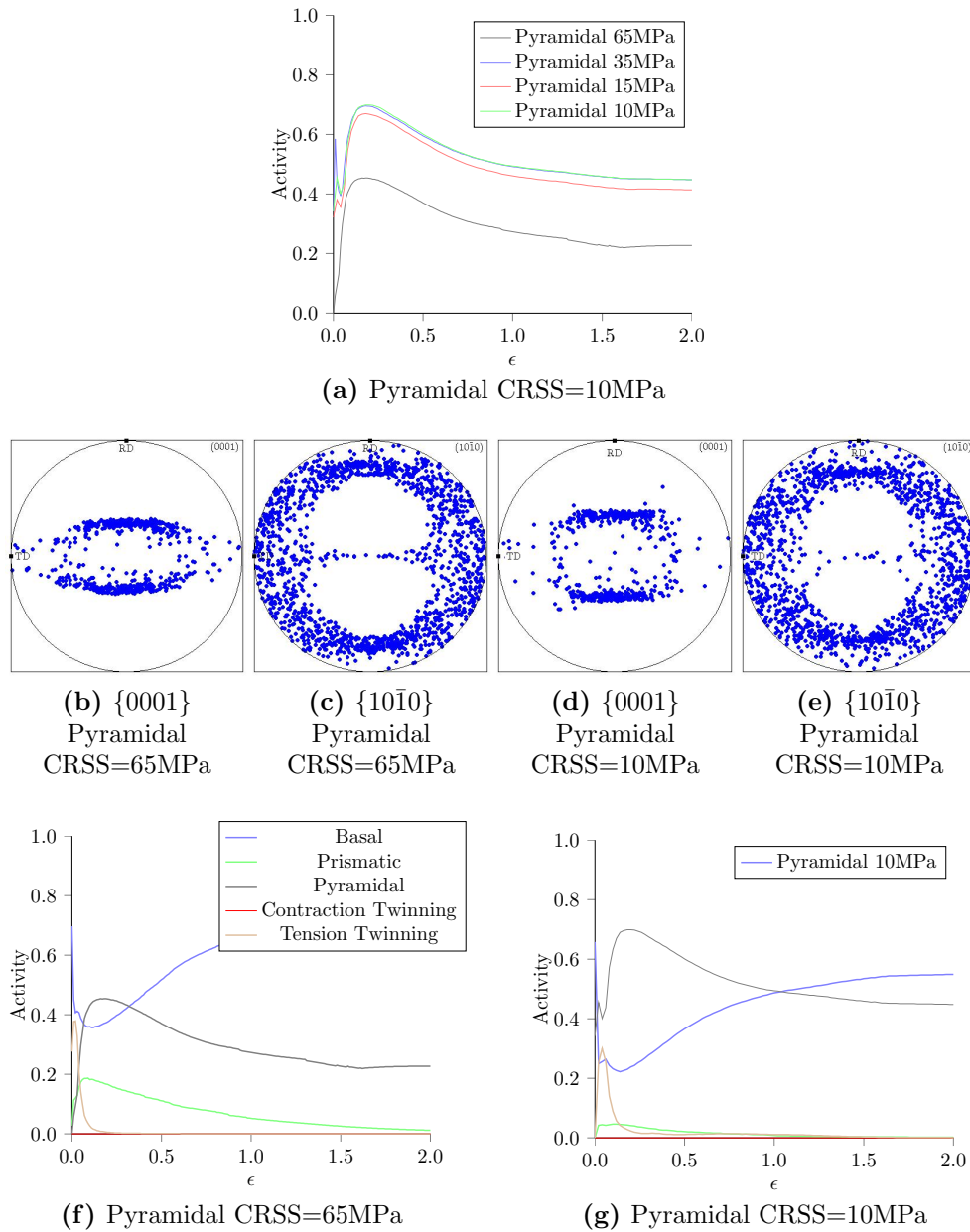


Figure 4.3: Effect of changing CRSS of pyramidal slip during plane strain compression on a) the activity of pyramidal slip, b-e) $\{0001\}$ and $\{10\bar{1}0\}$ pole figures measured at $\epsilon = 0.5$ and f,g) activities of each slip system during plane strain compression, where the CRSS values of pyramidal slip are set at 65MPa and 10MPa.

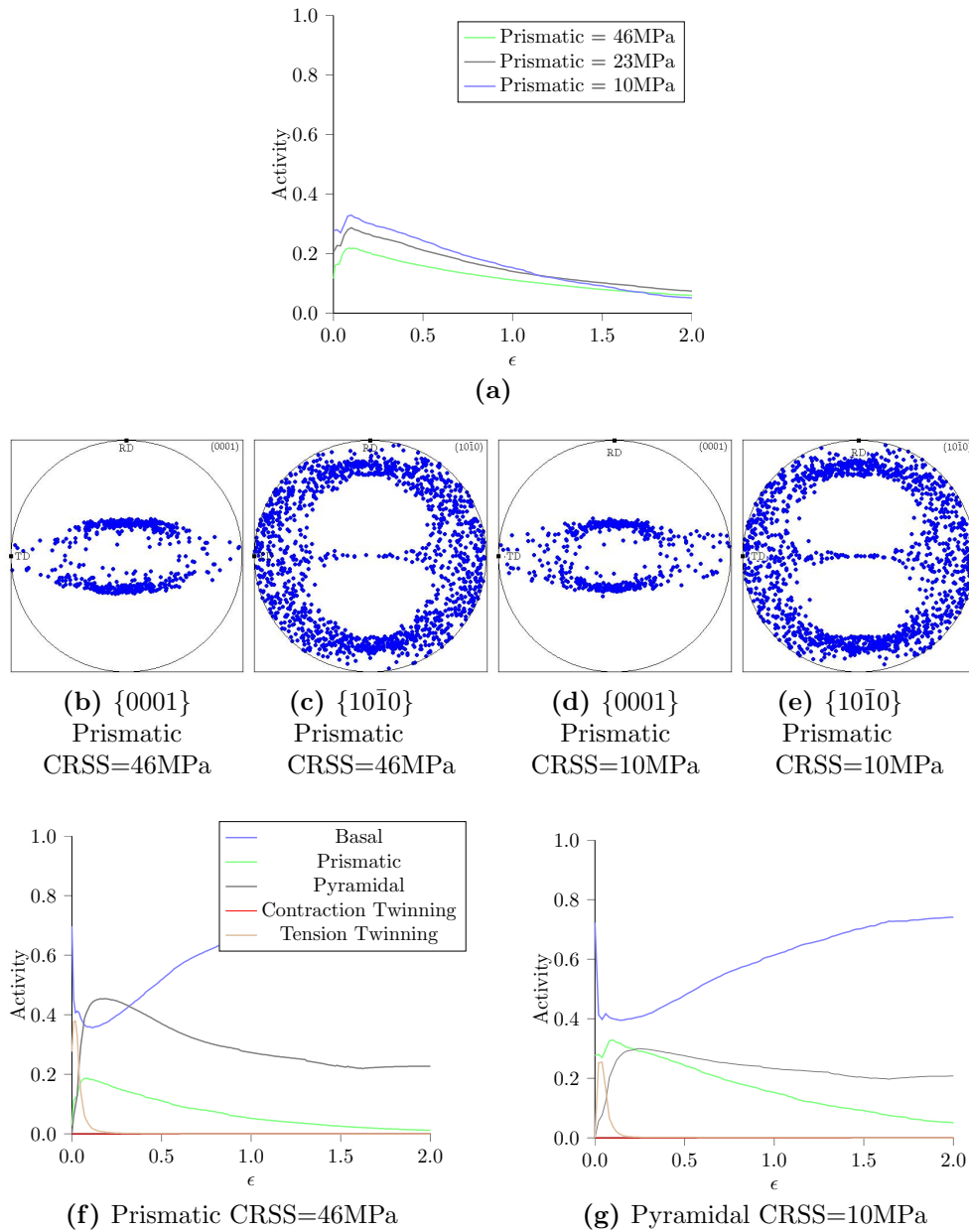


Figure 4.4: a) Effect of changing CRSS on the activity of prismatic slip during plane strain compression. b) and c) $\{0001\}$ pole figures showing the effect of prismatic slip on the deformation texture of a randomly textured material during plane strain compression. d) and e) activities of each slip system during plane strain compression with different prismatic slip CRSS's.

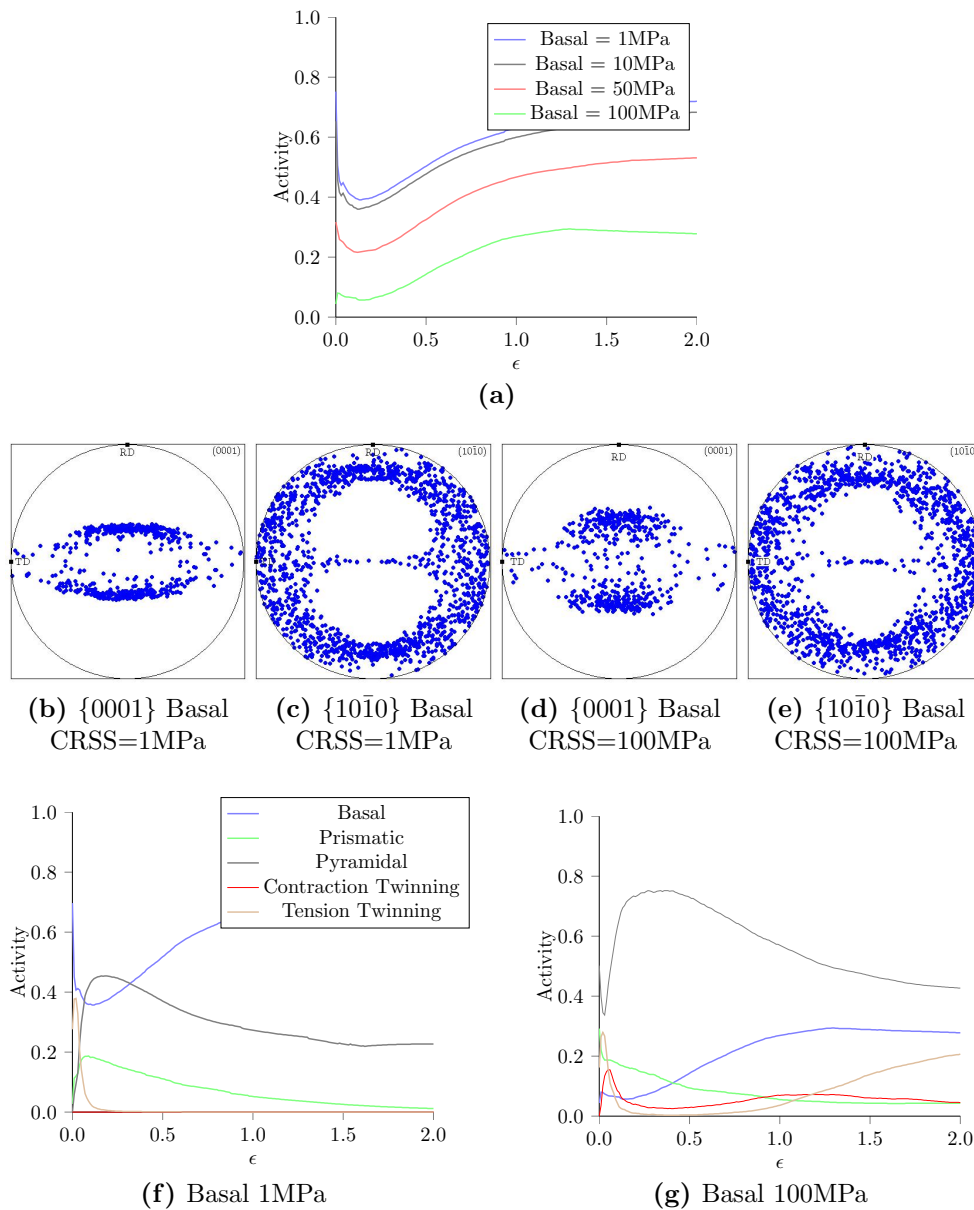


Figure 4.5: a) Effect of changing CRSS on the activity of basal slip during plane strain compression. b) and c) $\{0001\}$ pole figures showing the effect of basal slip on the deformation texture of a randomly textured material during plane strain compression. d) and e) activities of each slip system during plane strain compression with different basal slip CRSS's.

twinning activity to a maximum of 0.56. Increased compression twinning activity reduces the contribution of basal and prismatic slip to the deformation textures at strains of 0.5 and completely deactivates tension twinning, leaving pyramidal slip to become the dominant deformation mode. As in previous examples increased pyramidal slip leads to a discretisation of the RD split in the basal texture (Figure 4.6 d). Of particular note is that there is no observable TD split in the basal pole figure, which is observed in the recrystallisation textures of ZEK100.

The ratio of contraction to tension twins in the microstructure is also increased by raising the CRSS of tension twinning which indirectly increases the activity of contraction twins. Figure 4.7 illustrates where tension twinning is inactive (when the CRSS is 160MPa) compression twin and pyramidal slip both increase in activity. These increased activities lead to slightly greater TD spreading of basal orientations (Figure 4.7d) in the deformed textures at 0.5 strain.

4.5 Simulating Cold Rolling of ZEK100

The VPSC model can also be used to simulate the cold rolling of ZEK100 and predict the relative activities of each deformation mode under the different rolling schedules. The simulations should give an estimate of the activity of each deformation mode during cold rolling. Dislocation density is thought to be very significant in the 'RE' recrystallisation mechanism and so changes in the activity of each slip system during deformation may be expected to correlate with the different recrystallised textures produced after straight cold rolling (SCR), transverse cold rolling (TCR) and equal cold rolling (ECR).

4.5.1 Straight Cold Rolling

To simulate cold rolling of ZEK100 the experimentally measured hot rolled ZEK100 texture was used with the VPSC model by selecting 500 random points from a bulk texture measurement of the material. The input texture used is presented in Figure 4.8 a,b) and experimentally measured texture of as received material in Figure 4.8 i,j). As a starting point the input parameters used in the benchmark analysis above were used (where pyramidal slip has a CRSS of 63MPa), simulated textures and activities for plane strain compression to -0.47 strain are shown in Figure 4.8 c,d and g). For comparison the experimental textures of ZEK100 cold rolled to -0.47 strain are shown in Figure 4.8 k,l). The simulated textures are very similar to previous simulations with a split basal texture in the RD which does not resemble the experimentally measured texture. However, by increasing the CRSS of pyramidal slip to 160MPa the simulation produces a deformation

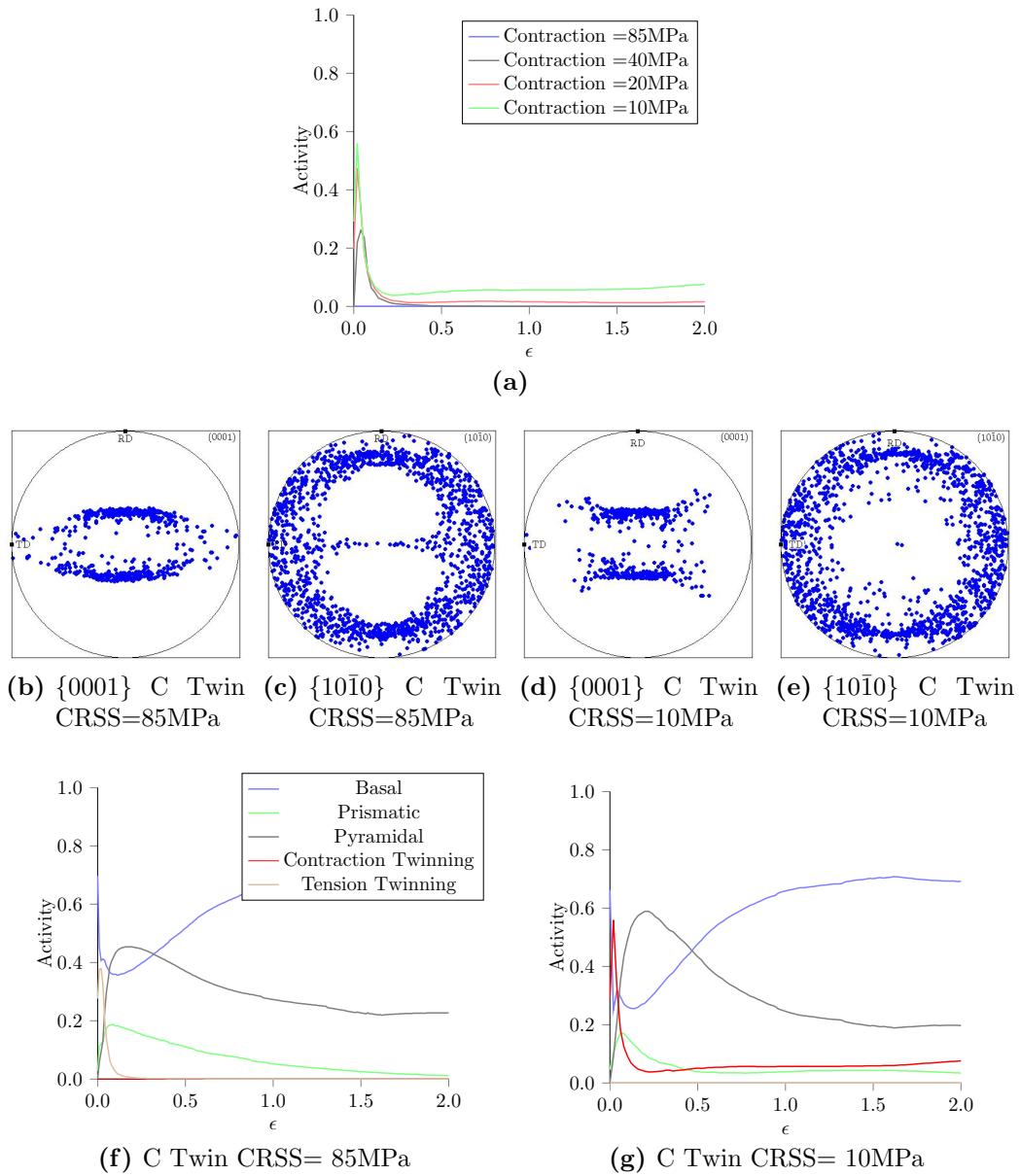


Figure 4.6: a) Effect of changing CRSS on the activity of contraction twinning during plane strain compression. b) and c) $\{0001\}$ pole figures showing the effect of contraction twinning on the deformation texture of a randomly textured material during plane strain compression. d) and e) activities of each slip system during plane strain compression with different contraction twinning CRSS's.

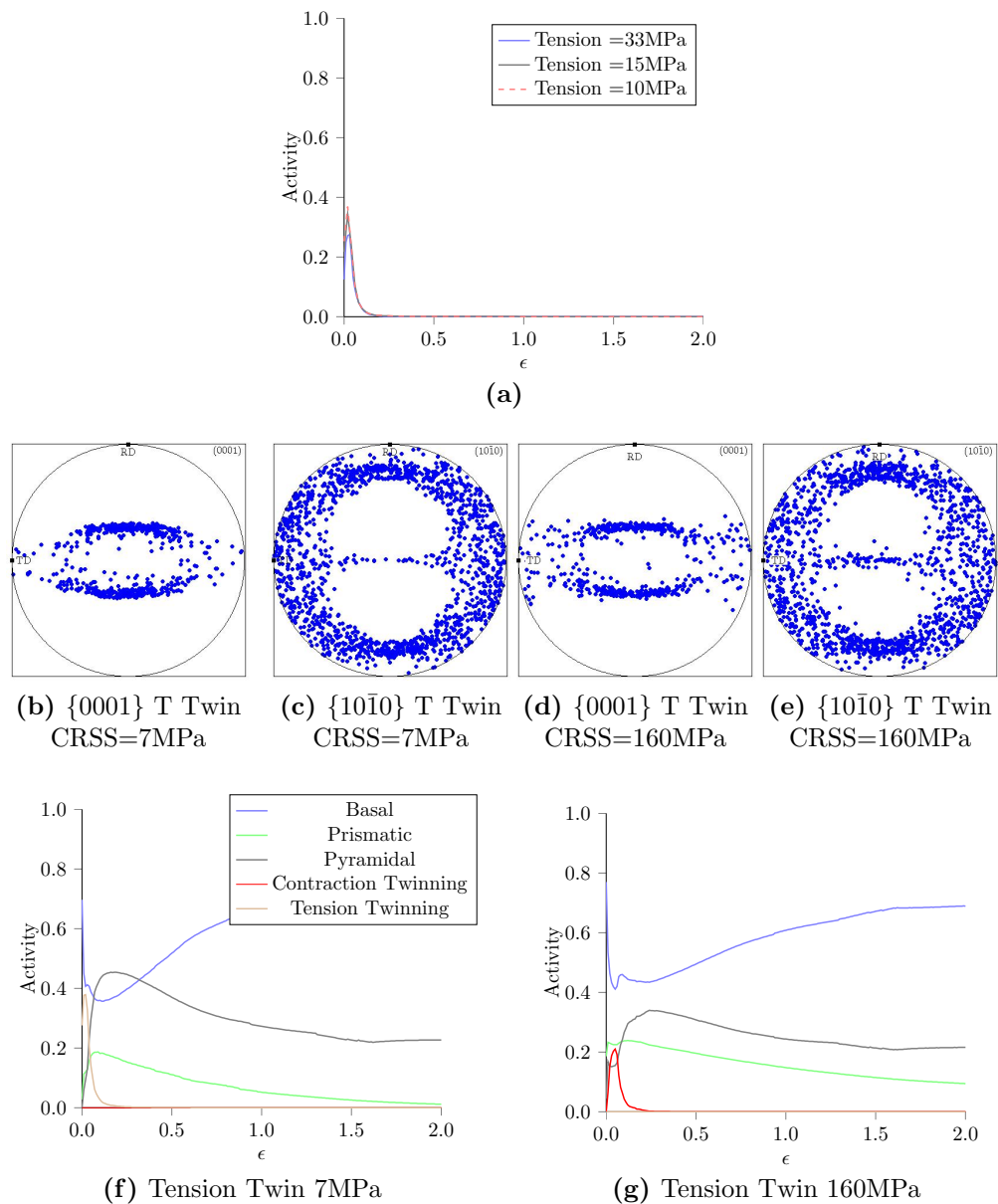


Figure 4.7: a) Effect of changing CRSS on the activity of tension twinning during plane strain compression. b) and c) $\{0001\}$ pole figures showing the effect of tension twinning on the deformation texture of a randomly textured material during plane strain compression. d) and e) activities of each slip system during plane strain compression with different tension twinning CRSS's.

Table 4.2: Table showing the total percentage of strain accommodated by each deformation mode during SCR, TCR and ECR simulations.

Schedule	Pyram CRSS MPa	Strain	Basal %	Pris %	Pyram %	Compression %	Tension %
SCR	65	-0.47	36.4	25.1	35.5	0	3.3
SCR	160	-0.47	46.4	45.2	5.9	0	2.6
TCR	160	-0.37	68	12.6	14.1	0	5.7
ECR	160	-0.25	59.8	22.6	9.7	0	8.2

texture (Figure 4.8 e,f)) similar to the experimentally measured one (Figure 4.8 k,l). The percentage of strain accommodated by each deformation in both simulations is presented in Table 4.2 and Figure 4.9, showing that the rise in pyramidal CRSS is associated with 20% increase in prismatic slip and a 10% increase in basal slip, meaning that strain during rolling is accommodated equally between the basal and prismatic systems. As the predicted deformation texture with a high pyramidal CRSS of 160 MPa is most similar to the experimentally measured texture, it is proposed the higher CRSS for pyramidal slip is more representative of the deformation occurring in the material and resultantly we use this value in the following simulations.

4.5.2 Transverse Cold Rolling

TCR of the as received ZEK100 was also simulated with the pyramidal CRSS set to 160MPa, the predicted deformation texture after -0.37 strain is shown in Figure 4.10 a,b). Comparison with Figure 4.10 e,f) shows the simulated texture is quite similar to the texture measured experimentally after TCR to -0.37 strain. The activities of the deformation modes during this simulation are presented in Figure 4.9 and Table 4.2, where basal slip is the dominant deformation mode with a significantly high activity of tension twinning in the early stages of the deformation. In comparison to SCR the activity of basal and pyramidal slip are 20% and 10% higher respectively in TCR, while the activity of prismatic slip falls by 30%.

4.5.3 Equal Cold Rolling

ECR was an attempt to impart the same levels of strain during rolling in directions perpendicular and parallel to the original hot RD (RD_{HR}). This was achieved by rotating the specimen by 90° alternately after each rolling pass. In practice it was not possible to impart the same strain during each pass and so we dynamically adjusted the rolling schedule to equalise the strain, leading to an unequal number of passes in each direction see Table 3.4. The VPSC model has been used to directly reproduce the experimental

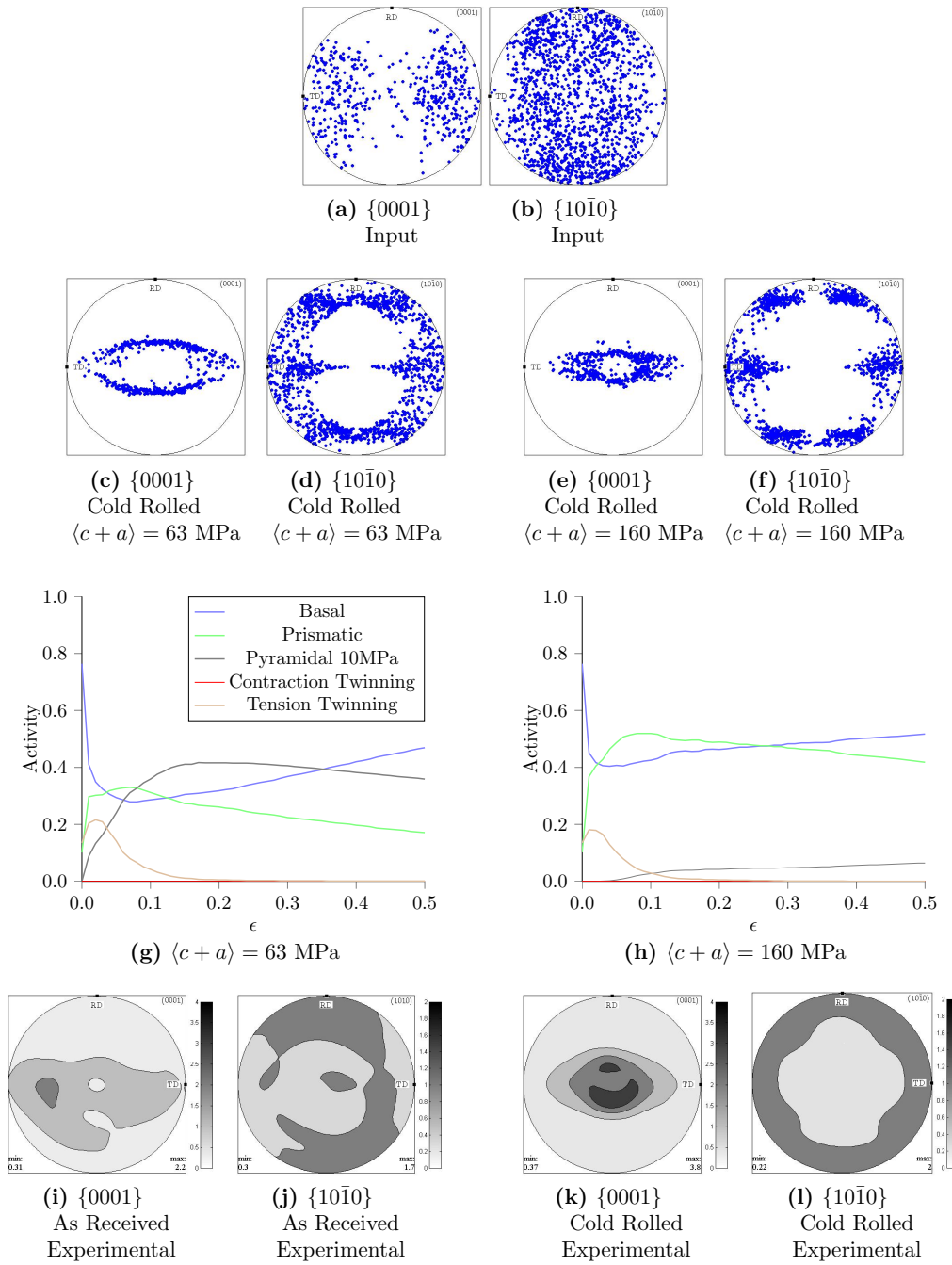


Figure 4.8: a,b) Input texture for the VPSC cold rolling simulations. c,d) Predicted texture after straight cold rolling to -0.47 strain with the benchmark CRSS for pyramidal slip of 63MPa. e,f) Predicted texture for straight cold rolling where the CRSS for pyramidal slip is 160 MPa. g,h) Slip system activities for simulations with the CRSS for pyramidal slip 63 MPa and 160 MPa respectively. i,j) experimental as received hot rolled ZEK100 texture and k,l) experimental as cold rolled texture.

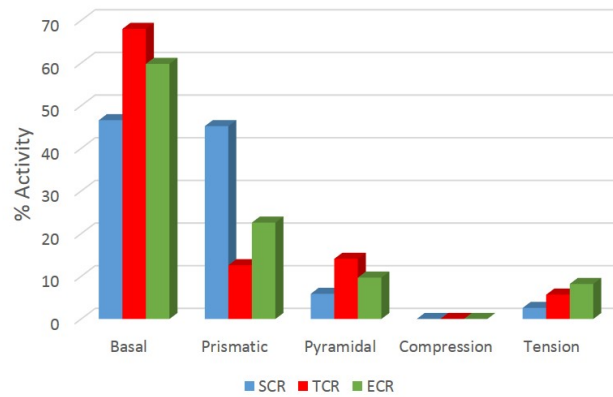


Figure 4.9: Percentage Activities of each deformation mode during SCR, TCR and ECR as predicted by the VPSC model.

rolling schedule in Table 3.4, where 6 rotations were required. The CRSS of pyramidal slip was maintained at 160MPa in these simulations.

The simulated ECR texture is presented in Figure 4.10 c,d) together with the experimentally measured ECR texture in g,h) for comparison. The simulated texture appears to show a good correlation with the experimental one, reproducing the diffuse spread of the basal texture in the TD, however the model suggests peaks in the prismatic pole figure with $\langle 11\bar{2}0 \rangle$ directions parallel to the RD, which are not experimentally observed. Deformation mode activities are plotted in Figure 4.10 j) with rotations of the material highlighted by vertical dashed lines, the percentage strain accommodated by each deformation mode is given in Table 4.2 and Figure 4.9.

The most significant effect of rotating the material between passes appears to be on the activity of prismatic slip; when rolled parallel to RD_{HR} prismatic slip activity is high, however when rotated such that the RD is perpendicular to RD_{HR} prismatic slip activity is suppressed, Figure 4.10 j). Where prismatic slip is suppressed basal slip accommodates the majority of the strain causing a corresponding complimentary increase in basal slip activity. This results in the relative activities of prismatic and basal slip in ECR falling between upper and lower boundaries of the other two rolling processes. In comparison to TCR prismatic slip activity has increased by 10% in ECR while basal slip activity falls by approximately 10% as shown in Table 4.2. The proportion of strain accommodated by each deformation mode as a function of rolling direction in ECR is shown in Table 4.3. In ECR 22.6% of the total deformation mode activity is due to prismatic slip and Table 4.10 shows of that 19.5% occurred during rolling parallel to the RD_{HR} while only 3.1 % occurred during rolling perpendicular to the RD_{HR} . This could be significant in RE texture formation as the ECR material does not produce the same TD split in the recrystallised texture as the SCR or TCR material. The dislocation content has been

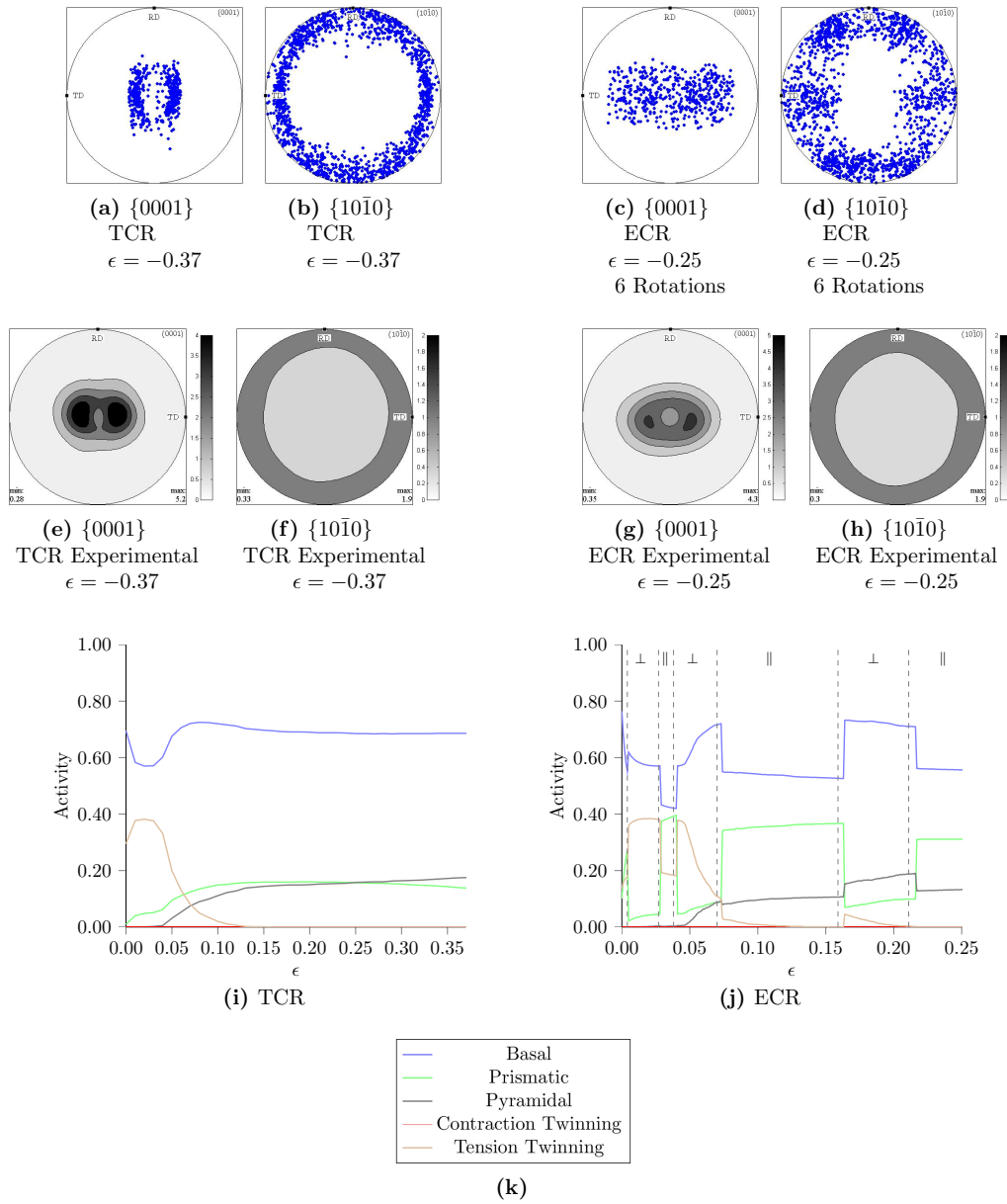


Figure 4.10: Simulation of transverse cold rolling to $\epsilon = -0.37$ and equal cold rolling to $\epsilon = -0.25$, 0.14 strain with $RD_{CR} \parallel RD_{HR}$ and 0.11 strain with $RD_{CR} \perp RD_{HR}$, pyramidal CRSS set to 160 MPa in both cases. a,b) Predicted TCR texture after 0.37 strain and c,d) predicted ECR texture after experimental rolling schedule to $\epsilon = -0.25$. e,f) and g,h) experimental TCR and ECR textures respectively. i,j) Predicted slip system activities during TCR and ECR rolling processes.

cited as a key factor in determining the recrystallisation mechanism and is discussed in Section 1.8.1.

Table 4.3: Table showing the total percentage of strain accommodated by each deformation mode during ECR simulations to $\epsilon = -0.25$ when the cold rolled RD was parallel and perpendicular to the RD_{HR} respectively.

Cold RD MPa	Strain	Basal %	Prismatic %	Pyramidal %	Compression %	Tension %
$\parallel RD_{HR}$	-0.13	30.5	19.5	5.4	0	1.4
$\perp RD_{HR}$	-0.11	29.4	3.1	4.3	0	6.8

4.6 Summary

VPSC modelling as been used to simulate the cold rolling behaviour of magnesium alloys. The approach and parameters of Hutchinson *et.al* produce acceptable flow stress curves and deformation textures in which the deformation texture forms a characteristic split of the basal planes in the RD typical of many magnesium alloys. Pyramidal slip is found to be most significant in forming this RD split, as where pyramidal slip is inactive equivalent rolling simulations produce a strong basal texture with basal planes parallel to the sheet plane. Deactivation of the remaining deformation modes did not cause significant changes to the predicted deformation texture and where changes were observed we suspect them to be related indirectly to a change in pyramidal slip activity. The influence of pyramidal slip predicted by the model was directly observed by reducing its CRSS which increased the misorientation of the RD split with respect to the ND as pyramidal slip activity rose. In contrast reducing the CRSS of other non-basal systems, including prismatic slip had relatively little impact on the deformation texture.

The model has been used to predict if changes in deformation mode activities might be expected to nucleate orientations from which the RE texture components could grow, such as the weak basal texture in binary alloys or TD split of the ZEK alloys. Overall there is little evidence of such orientations becoming more common, with the exception of hardening basal slip, which appears to promote a more diffuse spread of the RD texture split, and reducing the activity of tension twins which slightly increased the number of orientations spread in the TD. In both cases the evidence is not clear cut and the generation of these RE orientations is though to be more complex than this model can simulate. In particular the role of shear bands, not accounted for in the VPSC model may be critical in the nucleation of these orientations.

The VPSC model was extended to model the cold rolling experiments of ZEK100 by SCR, TCR and ECR. In order to accurately reproduce experimental deformation textures the CRSS of pyramidal slip was increased to 160 MPa producing simulated textures in good agreement with experiment. The dominant deformation systems are thus predicted to be basal and prismatic slip, SCR with the RD parallel to the RD_{HR} producing a 50:50

split between basal and prismatic slip. While TCR with the RD perpendicular to RD_{HR} favours primarily basal slip. Both of these materials recrystallise with a split in basal texture in the cold rolled TD. In comparison after ECR ZEK100 recrystallises with only a weakened deformation texture. The VPSC model predicts that in ECR the overall activity of each deformation modes lies between upper and lower limits defined by SCR and TCR in each case. The model also predicts that the majority of prismatic slip occurs during rolling parallel to the hot RD, as might be expected given the previous results. The potential impact of the differing slip system activities on recrystallisation textures will be discussed in Chapter 5.

Chapter 5

Discussion

5.1 Rare Earth Textures In Binary Magnesium-Rare Earth Alloys

In Section 3.1 the deformation and recrystallisation textures of a variety of magnesium-RE alloys after hot rolling and subsequent static recrystallisation were presented. All alloys produced deformation textures typical of magnesium in which basal planes are aligned parallel to the sheet plane, however during static recrystallisation a range of behaviours were observed; in some alloys recrystallisation strengthens basal textures while in others it weakens them, to varying extents. In the following these texture weakening effects are explored.

5.1.1 Activation of RE Effects

Most of the magnesium-RE binary alloy systems examined showed texture weakening during recrystallisation with the intensity of the fully recrystallised texture varying strongly from alloy to alloy. This poses the question in which alloy systems are the ‘rare earth effects’ active? To answer to this question the magnesium-Y alloy systems with concentrations ranging from almost pure magnesium up to the solid solubility of Y in magnesium were considered. In these alloys there was a clear transition between RE and non-RE recrystallisation textures once the Y concentration exceeded 0.1523 at%Y, after both hot (Figure 3.1) and cold (Figure 3.13) rolling. The RE textures produced are best described as weak basal textures characterised by an increased spreading of the basal poles about the ND and the prismatic poles evenly distributed normal to the ND. The intensity of

the recrystallised textures were quite insensitive to Y concentration once the critical concentration had been exceeded, with 0.2022 at% Y having a basal texture intensity of 5.2 mrd in comparison to 4.5 in the 0.1523 at% Y alloy.

Rare earth effects are much more difficult to isolate in the other binary alloys where the same range of RE concentrations was not available. If the critical RE concentration is linked to the solubility of each RE element then in theory the RE effects should be potent in the Ce, La and Eu containing alloys, which have high rare earth concentrations relative to solid solubility of each element in magnesium. While these alloys do show a texture weakening of 3-4 mrd during recrystallisation the intensity of the recrystallised texture is much higher than that of the Y alloys after the same treatment; 9 mrd in the Ce alloy, 6-7.5 mrd in the La alloys and 17 mrd in the Eu alloy, compared to 5 mrd in the Y alloys. These strong textures are not typical of RE alloys and suggest texture weakening during recrystallisation is not enough to identify the RE effects. Figure 1.30 plots the basal texture intensity against RE concentration for a number of magnesium-RE binary alloy systems from the literature showing recrystallised textures appear to have intensities ranging from 2-6 mrd after rolling and annealing in all cases. It is thus proposed that both texture weakening during recrystallisation and a weak final texture intensity (probably within the 2-6 mrd range) is required to conclude RE effects are active. On this basis the RE effects are active in the most dilute 0.005 at% La alloy but not in the more concentrated La alloys, Ce or Eu systems, as the final texture in these alloys remains high compared to what might be expected for a RE texture. A complicating factor in these systems is the presence of second phase particles which precipitate because the concentrations of RE in these alloys is above the solubility limit of Eu, Ce and La in magnesium. Precipitation of particles may deplete the matrix of RE possibly reducing it below the critical concentration required for RE effects. This may explain why increasing the La concentration above 0.005 at% actually increases the recrystallised texture intensity effectively deactivating the RE effects. A further complication in the Eu system is the large grain size which is approximately $97\mu\text{m}$ in the recrystallised condition. Such a large grain size is likely to contribute to increased texture intensity in this material as fewer grains are sampled during texture measurement. We note that this effect also most likely contributes to the high intensity of textures in other very dilute alloys such as 0.009 at% Y, in these dilute alloys grain growth is not restricted by alloying additions and so lean alloys generally have large grain sizes and thus strong textures as a result of intermediate heat treatments between rolling passes. This probably means the transition between non-RE and RE texture is not as prominent as suggested in Figure 1.30 because alloys below the critical concentration probably have much larger grain sizes than those above the critical concentration in most cases.

The remaining alloys based upon the Gd, Nd and Yb systems all produce texture weakening during recrystallisation however only the 0.0210 at% Yb system produces a recrystallised texture with an intensity low enough to be considered a RE alloy. In this case the final texture intensity is 6.4 mrd which considering the relatively large grain size of $48\mu\text{m}$ allows us to consider it a RE alloy. The Nd and Gd alloys are both borderline RE materials in terms of their concentrations, which are fractionally above the critical concentration thought to be required for RE effects Figure 1.30. In both cases however strong recrystallised textures and minimal texture weakening in the case of the Nd alloy prevent us from considering the RE effects to be active.

5.1.2 Texture Weakening in Binary Alloy Systems

Although ‘RE’ texture weakening is proposed to be active in only a small number of the binary RE alloy systems studied, the texture weakens during static recrystallisation in almost all cases, even in non-RE alloys. This is particularly true after cold rolling where Figure 3.12 shows that even AZ31 (a non-RE alloy) displays significant texture weakening during SRX. This is unusual in the magnesium alloys which normally display a strengthening of the basal texture during recrystallisation and grain growth, see Section 1.5.4.1. In both RE and non-RE alloys the final recrystallised texture morphology is simply a weak basal texture, no unique RE texture components form, even in the Y alloys, raising the question ‘how different is the texture weakening between RE and non-RE alloys?’ One factor which does appear to be significant in both alloy types is the deformation prior to recrystallisation, with cold rolling producing weaker recrystallised textures than hot rolling in both RE and non-RE alloys. The binary magnesium-Y alloys provide an interesting comparison between the non-RE and RE recrystallisation mechanisms, Figure 3.13 compares SRX after cold rolling and partial recrystallisation in the 0.0797 at% Y (non-RE) and 0.1523 at% Y (RE) alloys. It was concluded there is no obvious difference in the SRX mechanism or the orientation distributions of the SRX grains in the material above or below the critical concentration. The lack of a significant difference in SRX grain orientations between the two alloys is perhaps unsurprising as both RE and non-RE alloys recrystallise to produce a weak basal texture, requiring similar orientations, the real question is why does the texture weakening go so much further in the RE alloy? The answer may lie in the observation that more stored energy remained after partial SRX in the RE alloy in comparison to the non-RE alloy, Figure 3.13. This suggests that in the as rolled microstructure the stored energy is more homogeneously distributed in the RE alloy, which may be associated with an increase in non-basal slip, such as the increase in prismatic GND’s detected in IGMA analysis, Figure 3.15. As discussed in Section 4.4 a small increase in the activity of prismatic slip or pyramidal slip is unlikely to significantly

change the deformation texture (Figure 4.4), which is consistent with experimental observation. The transition from inhomogeneous deformation to homogeneous deformation can be seen in Figure 3.4, where the 0.0202 at% Y alloy demonstrated evenly distributed shear banding after hot rolling in contrast to the dilute 0.009 and 0.0797 at%Y non-RE alloys where few intense shear bands are observed. Recrystallisation of the homogeneously deformed microstructure in the RE alloy leads to a larger number of smaller recrystallised grains. Once the material fully recrystallises these smaller SRX grains are found to retain a much weaker SRX texture than the larger SRX grains in the non-RE material.

An explanation for this effect can be found if an assumption is made that the probability of typical magnesium SRX mechanisms, such as SIBM, nucleating weak basal orientations is proportional to the intensity of deformation in the recrystallising region. In some ways this is justified as regions of high strain concentrations are likely to generate large incompatibility stresses and some suggest such stresses could be as much as five times the applied stress [42]. These high stresses are likely to cause unusual slip activity in these isolated areas which in turn develop off-basal orientations as a result. So while overall strong basal textures are produced, in highly localised regions, including grain boundaries and shear bands, slightly off-basal orientations are likely to form in order to accommodate incompatibility strains. A proposed mechanism for this effect causing texture weakening is presented in Figure 5.1 which shows SRX in the cold rolled non-RE and RE alloys. a) and d) show the deformed microstructure in which strain is concentrated into small areas (large shear bands) in the non-RE alloy while in the RE alloy strain is more homogeneously distributed across the microstructure (small evenly distributed shear bands). b) and e) show the start of SRX in which basal (blue) and non-basal (green) grains are nucleated in the regions of highest strain concentration in both materials. High levels of strain concentration in the non-RE alloy mean that nucleation is initially confined to relatively small areas of high stored energy b), while the homogeneous deformation in RE alloys causes SRX nucleation throughout the microstructure e). The growth of recrystallised grains is shown in c) and f) in which SRX grains quickly consume the small region of high stored energy which nucleated them. The growth of these grains into the deformed material is slow in the non-RE alloys as high strain concentration in the deformed material results in the surrounding grains having relatively low stored energy. In contrast the growth of recrystallised grains in the RE alloy happens more quickly as a result of the higher stored energy in surrounding grains and the close proximity of recrystallising grains to deformed material throughout the microstructure, due to homogeneous nucleation f). This explains why the RE alloy has a higher recrystallised fraction than the dilute alloy after equivalent deformation conditions and annealing time. In the non-RE alloys a combination of the slower growth of recrystallised grains into the surrounding deformed grains and the sparse distribution of recrystallising grains is likely to allow recrystallisation from the

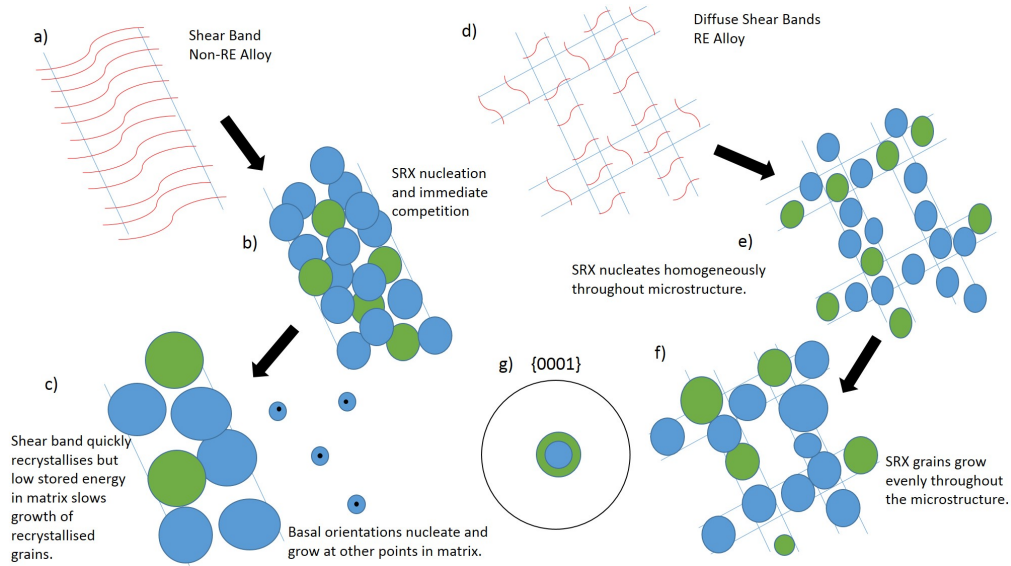


Figure 5.1: Schematic diagram showing SRX in a-c) non-RE and d-f) RE magnesium alloys. Red lines indicate stored energy density, blue circles indicate SRX grains with basal orientations and green circles SRX grains with non-basal orientations. g) $\{0001\}$ pole figure showing notional basal and off basal orientations.

deformed grains within the microstructure containing relatively low stored energy, both in comparison to equivalent sites in the RE alloy and the sites of initial recrystallisation in the non-RE alloy. As the stored energy in these recrystallising sites is relatively low the orientations nucleated from them are more likely to have basal orientations, which strengthens the basal texture thus limiting texture weakening.

In this way texture weakening in both RE and non-RE alloys is explained as a result of heavily deformed microstructures nucleating SRX grains with non-basal orientations. This texture weakening effect is strongest after cold rolling because this process increases the deformation within each grain, increasing the number of nucleation sites for off basal orientations. However, the texture weakens less in non-RE alloys because the inhomogeneous strain distribution allows many SRX grains to nucleate in regions of relatively low stored energy located between sparsely distributed shear bands and other areas of strong strain concentration. SRX in these regions nucleates grains with more basal orientations strengthening the basal texture and limiting texture weakening. By comparison homogeneous strain distribution in RE alloys means that such regions of low strain are less likely to recrystallise, as SRX grains from shear bands will grow into much of the deformed microstructure quickly as shear bands are evenly distributed and the deformed grains have a relatively high energy increasing the growth rate of SRX grains. Even in cases where these regions do nucleate SRX grains in RE alloys the higher stored energy of these regions is more likely to nucleate off basal orientations which would contribute to texture weakening.

5.1.3 Summary

Overall no strong evidence of a radically different SRX mechanism in RE alloys is found. In fact texture weakening is observed during SRX in both RE and non-RE alloys, this is attributed to regions of high strain concentration nucleating non-basal orientations which recrystallise weakening basal deformation textures. Texture is proposed to weaken less in non-RE alloys as a result of inhomogeneous strain distributions allowing more basal SRX orientations to nucleate in grains of low stored energy between sparsely distributed regions of high strain concentration. This occurs because the highly deformed regions which nucleate SRX first in non-RE alloys are distributed far apart and surrounded by regions of low stored energy (in comparison to the RE alloys). Slow growth of recrystallised grains into surrounding deformed grains allows time for nucleation of basal SRX grains in regions of low stored energy between the highly deformed regions ultimately limiting texture weakening. An increase in more uniform deformation in RE alloys has been reported by various authors and is discussed in detail in Section 1.8. The homogeneous deformation observed here cannot be specifically attributed to either increased non-basal slip or twinning however, we do observe an increased concentration of prismatic GND's, contraction and double twins which are frequently associated with this effect. The unique proposal made here is that texture weakening in cold rolled non-RE alloys is mediated by the same mechanism as RE alloys with the homogeneous deformed microstructure exacerbating the effect in RE alloys.

It is important to note that while these results do not explicitly disprove the operation of a unique RE texture weakening mechanism in these binary alloys, they do suggest that if one does exist it is a subtle effect. If a unique RE recrystallisation mechanism is operational its effects are exacerbated by cold rolling, probably as a result of the mechanism above, explaining why the recrystallised texture intensity in RE alloys is lower after cold rolling than after hot rolling. Although it is also possible that the RE effect in these binary alloys is simply due to more homogeneous deformation after rolling, as proposed above. An important distinguishing feature of the RE and non-RE texture weakening effects is that RE texture weakening occurs during DRX and SRX, while texture weakening in non-RE alloys only occurs during SRX where a significant amount of deformed material is retained post deformation. In practice this means non-RE texture weakening is only active after cold or warm rolling where little DRX occurs during processing as is the case here. If texture weakening in RE alloys operates by essentially the same mechanism then in order for it to be operational during DRX retarding of DRX could be critical in activating the effect. As by retarding DRX deformation and therefore non-basal orientations in the microstructure will be increased thus once DRX becomes active more non-basal orientations are available to nucleate non-basal DRX grains. If this were the

case then retarding DRX becomes critical in RE texture weakening as it allows non-basal orientations to develop in the microstructure which subsequently recrystallise weakening texture.

5.2 Formation Of Rare Earth Textures In ZEK100

In the binary magnesium-RE alloys discussed above the RE textures produced are essentially weak basal textures, this makes it difficult to identify when the RE effects are active. In the tertiary magnesium-zinc-Nd alloy ZEK100 the RE and zinc additions combine to produce an asymmetric texture with a characteristic split in the TD. It remains unclear to what extent the mechanism forming the TD split in ZEK100 is linked to the weak basal textures which form in the binary RE alloys, here this link is investigated by cold rolling ZEK100. The asymmetric nature of the TD split also provides an opportunity to examine the extent to which the deformed microstructure impacts the recrystallisation texture by observing SRX in transverse-cold rolled material.

In the following a texture split in the RD_{HR} refers to grains with basal orientations rotated from the ND towards the hot rolling direction of the as received material. A TD_{CR} texture split refers to basal orientations rotated towards the TD in cold rolled material. The TD_{CR} direction is defined by the cold rolling direction (RD_{CR}), which is parallel to RD_{HR} direction in straight cold rolling (SCR) and perpendicular to it in transverse cold rolling (TCR).

5.2.1 Recrystallisation in SCR and TCR Material

Recrystallisation of SCR and TCR ZEK100 led to the formation of the ZEK rare earth texture in which the basal texture is split into two lobes in the TD_{CR} direction, regardless of the direction of cold rolling. Significantly, unlike the recrystallised RE textures in binary magnesium-RE alloys, which are simply weakened deformation textures, the recrystallised ZEK texture appears to be unrelated to the deformation texture. Indeed, after TCR the TD_{CR} split in the recrystallised texture was rotated by 90° in comparison to the TD_{HR} split in the deformation texture of the as cold rolled TCR material, Figure 3.22 d,e).

Clearly the cold rolling direction is critical in generating nuclei oriented in the TD_{CR} which grow consuming the basally oriented deformed grains. In the following we focus on static recrystallisation within the transverse cold rolled material as in this material the recrystallising TD_{CR} texture component is easily distinguishable from the deformation texture, which is rotated by 90° about the ND. EBSD analysis on TCR material suggests

the primary nucleation site for recrystallising grains is shear bands in the microstructure Figure 3.24. In the as transverse rolled condition many of these shear bands are heavily deformed and do not produce clear Kikuchi patterns which can be indexed, Figure 3.24 a). Where these regions can be indexed they are found to have orientations primarily split towards the RD_{CR} , Figures 3.25 a) and 3.27, as might be expected in shear bands of this type following discussions in Section 1.3.4. However, while the majority of indexed orientations within shear bands are split in the RD_{CR} there are some isolated TD_{CR} orientations, Figure 3.30. Indeed, some TD orientations may also be hidden in the un-indexed areas of the shear bands. In any case the majority of deformed grains within the shear bands have RD_{CR} orientations which appear to nucleate similarly oriented recrystallised grains, this RD_{CR} component dominates the texture of recrystallising grains for the first two minutes of recrystallisation, Figure 3.25 b,c). After five minutes the TD_{CR} texture component becomes dominant in the recrystallised grains with grains of this orientation having the largest recrystallised grain sizes 3.25 d), the TD_{CR} component is retained in the fully recrystallised material. The advantage of TD_{CR} oriented recrystallising grains can be observed from the earliest stages of recrystallisation where after only one minute of annealing the largest recrystallising grains are found to have TD_{CR} orientations 3.26 b), however, there are so few of these grains at this stage that they do not contribute significantly to the overall texture of recrystallising grains.

Similar observations of RE orientations being present preferentially in large recrystallising grains have also been made in DRX grains in extruded magnesium-Mn- RE alloys [164] and in hot rolled magnesium-Zn-Zr- RE alloy systems [168]. Basu *et.al* attribute the dominance of the TD_{CR} component during recrystallisation to the higher boundary mobility of such TD_{CR} oriented grains [168] (Figure 1.38); the large number RD_{CR} grains within shear bands have, by definition, low misorientation angles between each other and therefore low boundary mobility. The small number of TD_{CR} oriented nuclei however, have high misorientation angles with surrounding RD_{CR} grains and thus high boundary mobility. They argue that the growth advantage of the TD_{CR} grains leads to their dominance after annealing for five minutes in the case of ZEK alloys. While boundary mobility is doubtless a contributory factor leading to the dominance of the TD_{CR} texture component, overall this explanation of RE texture formation is incomplete and does not account for the full range of RE effects; for example, provided TD orientations nucleated within shear bands in RE and non- RE alloys, the same logic regarding boundary high mobility of TD_{CR} orientations would apply but these non- RE alloys do not nucleate the TD_{CR} component during recrystallisation within shear bands. Perhaps a more fundamental question is how do the TD_{CR} orientations nucleate within the shear bands and why does this mechanism only appear to be active in RE -Zn magnesium alloys?

One of the simplest explanations for the nucleation of TD orientations in the deformed microstructure is the presence of TD oriented shear bands. Figure 3.28 shows two possible shear band orientations; those producing the RD texture component (red) and those which could potentially produce the TD component (green). In both cases the orientation of deformed grains within the shear band is suggested to be controlled basal slip which orientates basal planes parallel with the shear plane, these orientations recrystallise nucleating recrystallised grains with the same orientation. It is possible that the TD_{CR} orientations such as those in Figure 3.30 are nucleated by the TD_{CR} (green) shear bands and are detected in small numbers because the ND-RD_{CR} cross-section of our maps is likely to capture more of the RD oriented (red) than TD oriented (green) shear bands. As a result more TD_{CR} grains are expected to be observed in an EBSD map of the ND-TD_{CR} cross-section. Figure 3.29 compares ND-RD_{CR} and ND-TD_{CR} cross-sections in material after 5 minutes annealing, showing that if anything, the TD_{CR} split in recrystallising grains is reduced when observed in the ND-TD_{CR} orientation. The small number of recrystallised TD_{CR} grains in this ND-TD_{CR} cross-section may also be because less strain occurs in the TD_{CR} direction than the RD_{CR} during rolling and so shear banding in the TD is likely to be less acute and therefore less influential on nucleating RX grains than RD_{CR} shear bands (red) shear bands.

An increase in non-basal slip activity is also frequently cited as the source of the RE texture component in recrystallised textures. The mechanism of this effect must be either non-basal slip nucleating RE orientations or allowing those orientations to grow preferentially. In Section 4.5 the VPSC model was used to simulate SCR and TCR in ZEK100 and while it did not specifically account for RE additions changing the CRSS values of each slip system the simulation suggests the likely impact changing rolling direction has on slip system activity. Figure 4.9 and Table 4.2 give the percentage activities of each deformation mode during SCR and TCR assuming reasonable magnesium CRSS values, these simulations reproduce the deformation textures of both materials well, Figure 4.8 e,f). Notably during SCR the dominant slip systems are basal and prismatic slip, which both accommodate $\approx 45\%$ of strain, while under TCR $\approx 70\%$ of strain is accommodated by basal slip. Although the absolute numbers are best viewed as rough estimates the fact remains that the dislocation content of SCR and TCR material is likely to be significantly different with basal slip particularly influential under TCR. Unfortunately IGMA analysis on the EBSD maps of the as rolled ZEK material did not produce any conclusive results to support the prediction of a significant change in prismatic dislocation activity with rolling direction. In any case the mechanism producing the recrystallised TD_{CR} component is clearly operational in both SCR and TCR regimes regardless of the differences in the dislocation content of the material as a whole. A crucial point to consider is that the VPSC model does not account for shear banding in the material which is likely to

significantly impact deformation behaviour. Simulations of shear banding in magnesium may be required to explain the formation of the TD texture component as Figure 3.26 b) shows recrystallising grains with the TD_{CR} component have an advantage over those with the RD_{CR} component even before they have grown out of the shear banded region. This suggests that dislocation activity within the shear band is more influential than the material as a whole because once the recrystallised grains begin to consume deformed grains surrounding shear bands the TD_{CR} recrystallised grains already have a size advantage. This may also go some way to explaining the 90° rotation of the RE texture during TCR too, because the TD_{CR} orientations develop within shear bands which are oriented towards the RD_{CR} in both SCR and TCR. In other words the 90° rotation of the texture is caused by the orientation of the shear band nucleating the texture which is defined relative to the RD_{CR} in both SCR and TCR.

In summary the mechanism forming the TD_{CR} (RE) texture component in ZEK100 is found to be active during SRX after SCR and TCR. The TD_{CR} orientations are found to nucleate within shear bands at the early stages of SRX and have an advantage over recrystallised grains with RD_{CR} orientations which nucleate at the same time. Thus despite nucleating in smaller numbers than the RD_{CR} orientated grains the TD_{CR} grains come to dominate the recrystallised texture in both SCR and TCR material. The 90° rotation of the TD_{CR} texture component relative to the original hot rolled TD orientation during TCR is believed to be controlled by the orientation of the shear bands which dominate the microstructure after cold rolling and whose direction is clearly defined by the cold rolling direction. While the majority of deformed and recrystallised grains within these shear bands are found to have RD_{CR} orientations, as expected due to high levels of basal slip, a small number of TD_{CR} orientations are nucleated within the shear band by a currently unknown mechanism. Basu *et.al* [168] note that once nucleated TD_{CR} grains are likely to have a growth advantage over RD_{CR} grains due to the high mobility of the high angle boundaries between TD_{CR} and the majority RD_{CR} oriented grains in the shear band, accounting for the dominance of TD_{CR} in the final recrystallised texture.

Nucleation of the TD_{CR} orientations has been considered a result of a special group of TD_{CR} oriented shear bands forming during rolling, however no evidence of TD_{CR} oriented shear bands was found in the microstructure. Macroscopic dislocation content was also considered a possible source of the RE textures. However, although the VPSC model predicts rotating the material from SCR to TCR will cause a significant reduction in prismatic slip activity, this is not predicted to produce any orientations rotated 90° from the deformation texture which may act as nucleation sites for the rotated recrystallisation texture in TCR material. If a change in the macroscopic dislocation activities were responsible for the TD_{CR} split in ZEK textures such a significant change in dislocation activity between SCR and TCR would be expected to affect the recrystallised texture.

As the recrystallised texture merely rotates after TCR with no change in morphology another mechanism must be responsible for nucleating the TD_{CR} component. The orientation of the TD_{CR} texture is proposed to be controlled by the direction of the dominant shear bands in the material which form oriented towards the RD_{CR} , the dislocation behaviour and activities within these shear bands are therefore critical in nucleating the TD_{CR} components observed by a currently unknown mechanism.

5.2.2 Recrystallisation in ECR Material

Before considering possible mechanisms forming the TD_{CR} texture component within shear bands during SCR and TCR it is pertinent to discuss the SRX behaviour of the ECR material. During ECR almost equal strain was imparted in the material parallel and perpendicular to the RD_{HR} direction. The maximum compressive strain achievable during ECR, of $\epsilon = -0.24$, was less than that after SCR and TCR where much higher strains could be achieved ($\epsilon = -0.4$). This lower strain resulted in a slightly weaker basal deformation texture intensity in the ECR material which is still split in the TD_{HR} direction, like the SCR and TCR material, but with a wider misorientation from the $ND \approx 20^\circ$. Overall the deformation texture of the ECR material, like that of the SCR and TCR material was exactly as expected of a typical magnesium alloy and it can be reproduced well using the VPSC model, Figure 4.10 g,h). However, the recrystallisation behaviour of the ECR material is totally different to that of SCR and TCR material. Full recrystallisation after ECR produces a recrystallised texture with a slight split in the TD_{HR} orientation, Figure 3.31, but the misorientation of this split remains much lower than that in recrystallised SCR or TCR material. The ECR rolling schedule seems to have changed the recrystallisation mechanism in ZEK100.

VPSC simulations of the ECR process shown in Figure 4.10 reproduce the deformation texture well and suggest that the activity of each deformation mode in ECR is intermediate between the upper and lower limits set by SCR and TCR, Figure 4.9. As a large change macroscopic dislocation behaviour does not affect the recrystallisation morphology between SCR and TCR it seems unlikely that the intermediate values produced during ECR could explain a change in recrystallised texture in ECR material. More significant is a comparison between the as rolled microstructure in TCR and ECR ZEK100, Figure 3.32, where three primary differences are observed; first the grain size is larger after ECR, due to the lower strains achieved in this material. Second there are fewer shear bands visible after ECR, again this is probably due to the smaller compressive strains. Finally some areas of the ECR material contained unusual twinning behaviour comprising of wide intersecting twins, the usual twin-matrix relationship had broken down in the ECR material as a result of deformation slip in both rolling directions preventing

twin identification. However, ECR simulations predict the activity of compression twins during ECR is negligible, this is consistent with observations of wide twin morphologies typical of tension twins. Of these observations the most significant could be the absence of shear bands in the material, considering their proposed importance in SCR and TCR material in nucleating RX textures and controlling the rotation of the TD_{CR} component during TCR. In many ways the recrystallisation mechanism in ECR material is similar to that previously discussed in the binary magnesium alloys. In both ECR ZEK100 and the binary alloys SRX led to the formation of weakened deformation textures rather than a unique RE component as observed in the SCR and TCR ZEK100. The absence of this TD_{CR} component during ECR is thus explained by the absence of shear bands during rolling, without these bands the TD_{CR} orientation is not nucleated and may not grow as in SCR or TCR material. The ECR process is likely to impede shear band formation as shear bands of different orientation are needed to accommodate strain during rolling in each direction, thus rotations during rolling prevent one orientation of shear band from dominating (unlike in SCR or TCR).

In summary, the TD_{CR} recrystallised texture component found in SCR and TCR ZEK100 is not produced following ECR. Shear bands are thought to be required to generate the TD_{CR} texture component in ZEK100 during SCR and TCR. However, shear band formation is suppressed during ECR and is thus thought to prevent the nucleation of TD_{CR} orientations within shear bands. The recrystallisation texture in ECR ZEK100 is best described as a weakened deformation texture and in this respect the ECR material behaves similarly to the cold rolled binary RE alloys discussed in Section 5.1 which also recrystallise producing weakened deformation textures without unique RE texture components. In these binary alloys these weakened deformation textures are produced in spite of shear band formation, which in these materials does not appear to nucleate the TD_{CR} RE texture component typical of shear bands in ZEK alloys. Therefore in explaining the nucleation of the TD_{CR} component the Zn addition is influential as the RE alloying additions.

5.2.3 Formation of RE Texture Component in ZEK Alloys

The TD_{CR} RE texture component in ZEK alloys appears to nucleate within shear bands and does not originate either from the macroscopic deformation texture (which is a strong basal texture) or the dominant local orientation within shear bands (which is oriented towards the RD_{CR}). Fundamentally an explanation is required to describe how recrystallisation nuclei with basal orientations split towards the TD_{CR} form within the shear

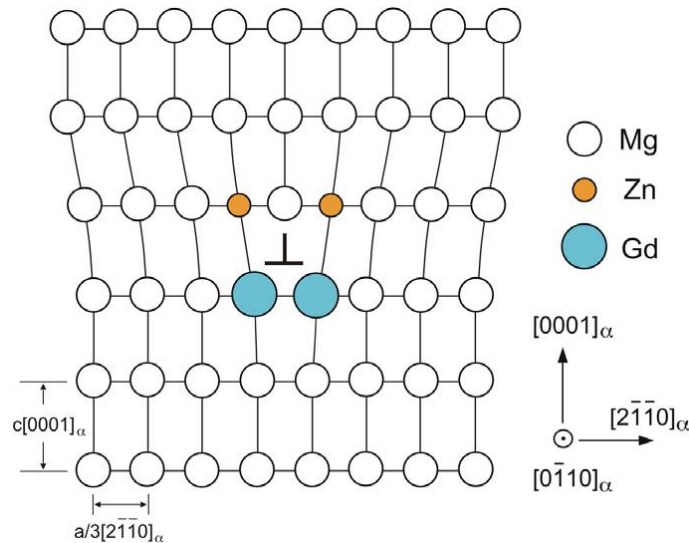


Figure 5.2: Schematic of the pinning of a basal edge dislocation by solute Zn and Gd additions [199].

bands because once these nuclei form Basu *et.al* [168] suggest they have far higher boundary mobilities than competing RD_{CR} nuclei, explaining why those orientations come to dominate the fully recrystallised texture.

An important consideration here is that these TD_{CR} orientations are not observed in the recrystallised textures in binary magnesium-RE alloys which also recrystallise from shear bands. If viable TD_{CR} oriented nuclei formed in the binary alloys then one would expect them to have the same growth advantage as in the tertiary alloys. Therefore the TD orientations either only form or only grow in the tertiary ZEK alloys.

The most obvious difference between the two alloy groups is the Zn addition in tertiary alloys which must facilitate the nucleation of the TD_{CR} orientations in some way. Importantly it is the combination of RE and Zn atoms that cause these effects, as other magnesium-Zn containing alloys (such as AZ31) do not display the same weak textures. One of the most significant effects Zn additions could have in RE alloys is the proposed formation of RE-Zn dimers in solution [197, 199] as discussed in Section 1.9. The driving force for dimer formation is believed to be the relaxation of misfit strains caused by replacing a magnesium atom in the lattice with a larger RE or smaller Zn atom. Nie *et.al* [199] note that such Gd-Zn dimers may segregate to dislocations as shown in Figure 5.2 pinning them more effectively than either element on its own. Pinning of dislocations could strongly affect recovery behaviour, especially the kinetics of subgrain formation, as dislocations are less mobile. The overall dislocation content of the material could also change if one deformation mode is pinned more effectively than others (see Section 4.4), although such changes were not predicted to nucleate significant TD orientations in the deformed texture by the VPSC model. Another key consideration is the potential effect

of tertiary alloying additions on the solubility of RE in solution. In section 3.5.2 EDX data found Nd additions, in an alloy with a Nd concentration below the solubility of Nd in magnesium, were preferentially located within O and Fe containing particles. However, the role of particles in the formation of RE textures is thought to be limited as RE effects were not reported in this binary magnesium-Nd alloy and in general particle concentrations are expected to be too low to have a significant pinning effect in many alloys showing RE effects (Section 1.9). This focuses attention on the potential pinning of dislocations by RE-Zn dimers and the subsequent effects on recrystallisation textures.

The TD texture component grows from nuclei within shear bands that have a TD orientation. The initial TD orientation may form during deformation, perhaps due to strain incompatibilities, subsequently recrystallising without requiring a significant orientation change. Or the TD orientations may form by rotation of the typical RD oriented shear bands as part of a recovery/recrystallisation mechanism. Examination of the deformed microstructure in Figure 3.30 does show some TD oriented regions in the deformed microstructure, however it is difficult to identify which of these regions will nucleate TD orientations during SRX. Indeed the most influential regions of the microstructure are also those with highest energy which are too deformed to be indexed by EBSD analysis, thus there is no way of knowing the orientation of the microstructure within these regions. Two possibilities are thus considered; either the TD orientations form via a rotation of the deformed RD orientations within the shear band by a recovery/recrystallisation mechanism or the TD orientations form in the shear bands during deformation.

In order to nucleate TD orientations from the RD orientated shear bands a mechanism such as rotational DRX is required. Such a mechanism was observed by Molodov *et.al* [132] within a compression twin as a result of the recovery of prismatic dislocations during cold deformation of a magnesium single crystal. Shear bands in RE alloys are often suggested to nucleate as a result of compression twinning and so RDRX within parts of the shear bands in ZEK100 might be expected to follow a similar mechanism. However, the RDRX nuclei nucleated by prismatic slip in this mechanism had orientations with a characteristic 30° rotation about the $\langle c \rangle$ axis of the compression twin parent. Such a rotation, caused by prismatic slip, cannot reorient the basal poles of the parent crystal from the RD_{CR} orientation of the shear band to the TD_{CR} orientations required for the TD texture, to achieve this rotation recovery of basal and/or pyramidal dislocations would be required. However, it is not clear why such a mechanism involving recovery basal or pyramidal dislocations would preferentially nucleate the TD_{CR} components.

On the other hand if the TD orientations were formed within shear bands during deformation then subsequent recrystallisation of these regions by typical mechanisms (including RDRX) would be expected to nucleate grains with a similar TD component to the parent

grain. In this case the question is why such TD orientations do not develop in binary RE alloys which produce weakened deformation textures during RX. Clearly the addition of Zn in ZEK100 is critical in facilitating this change. As the deformation textures of magnesium-RE and magnesium-RE-Zn alloys are reportedly very similar[168] and VPSC simulations suggest that small changes in the relative activity of each slip system (which may be caused by Zn addition) has minimal effect on nucleating TD oriented grain in the bulk, it is proposed a recovery related process is likely to account for the preferential nucleation of TD orientations in ZEK100. The Schmid factor for prismatic slip is high in TD oriented grains and so the prismatic dislocation content in these TD regions within shear bands is also likely to be higher than that of the RD oriented regions in the majority of the shear band, which are expected to contain primarily basal dislocations. If RE-Zn dimers are assumed to be more effective at pinning basal dislocations than prismatic dislocations then in a recovery based mechanism the RD oriented parts of the shear band would recover more slowly than the TD oriented parts because the basal dislocations are more effectively pinned by RE-Zn dimers. This would allow the (few) TD orientations in the shear bands to form viable nuclei before the RD orientations. Once the TD nuclei begin to grow the high boundary mobility of these orientations allows them to grow faster and subsequently dominate the recrystallisation texture. This also explains why TD orientations do not develop in non-RE alloys; because without the effective pinning of basal dislocations by RE-Zn dimers the recovery rate of prismatic dislocations is not fast enough to overcome the numerical advantage of the basal orientations in these alloys, even where TD orientations are present in the deformed shear band.

While highly speculative this mechanism does explain the preference for TD_{CR} orientations in recrystallising grains which is difficult to do without considering prismatic slip as a key factor. In support of this mechanism is that sparse TD_{CR} orientated regions within shear bands are observed in as cold rolled TCR material, Figure 3.30. Such orientations also appear to have a growth advantage over RD_{CR} oriented recrystallising grains from the very early stages of recrystallisation, Figure 3.26. In Section 4.4.1.2 we also noted that VPSC modelling suggests reduced activity of tension twinning in comparison to compression twinning (as experimentally observed in ZEK alloys) may lead to an increased number of TD_{CR} orientations in the deformation texture, although the typical basal texture remains dominant. It must be acknowledged though that there is currently no evidence suggesting that RE-Zn dimers should preferentially pin basal dislocations more than prismatic dislocations, which is a key component for this mechanism. High level DFT modelling beyond the scope of this work is likely required to reproduce this effect if it is present. Unfortunately the the limitations of the EBSD technique preventing indexing of the shear bands in the as rolled condition make it very difficult to determine with certainty the existence of TD oriented regions in the deformed state. Ideally an in

situe recrystallisation experiment would show the recovery and recrystallisation of such deformed TD regions of shear bands before RD oriented nuclei, however currently this is not possible.

5.2.4 Grain Growth In ZEK100

Once recrystallisation is complete after hot or cold rolling the TD texture component is fully established in ZEK alloys. Here it is argued that the formation of this component may be due to a combination of dislocation pinning by RE-Zn dimers and the high boundary mobility of the high angle boundaries between these TD oriented grains and the basal orientations of deformed grains. It is therefore interesting to discuss the effect of grain growth on the texture in these alloys, as the proposed mechanism of TD texture formation assumes no particular growth advantage of the TD orientations other than their high boundary mobility, caused by strong basal textures of most other grains in deformed magnesium. Figure 3.33 shows an EBSD map of ZEK100 after annealing for 30 days where significant abnormal grain growth has occurred. The texture of the material is still spread in the TD however, the TD oriented lobes present in the recrystallised material have been replaced with a smeared basal texture in the TD. Viewing the texture as function of grain size (Figure 3.34) fails to recover the TD lobes present in the recrystallised material however, it does suggest that larger grains are slightly more basally oriented than the smaller grains. Figure 3.35 shows that this smeared basal texture can also be found in grains with a smaller than average size within fully recrystallised ZEK100. In other words these smaller grains, which are at a growth disadvantage during recrystallisation, gain an advantage over larger grains which are split in the TD during grain growth. After the long annealing treatment used here these more basal orientations come to dominate the material texture.

Like the formation of the split TD texture component this can also be justified on the basis of a higher boundary mobility, in this case of basally oriented grains; At the end of recrystallisation the situation which leads to the dominance of TD orientations, high boundary mobility caused by high misorientation angles between TD grains and deformed grains, is reversed. Recrystallised basal grains, which are below average size, are low in number but have high misorientations between themselves and the dominant recrystallised TD orientated grains, which have a corresponding low boundary mobility due to their superior numbers in the recrystallised TD texture. As a result all other effects being equal one expects these basal orientations to have a growth advantage over grains oriented within the TD lobes during normal grain growth, which explains why the texture returns to a more basal morphology after significant grain growth. A similar mechanism explaining

changes in bulk texture during grain growth due to the boundary mobility between texture components has also been observed during grain growth in pure titanium [153].

However, this does not explain the abnormal grain growth also observed in the ZEK alloy. Abnormal grain growth is typically associated with strong textures, pinning of grain boundaries by second phase particles[21] and recently solute drag of grain boundaries[178]. In this case we note that the abnormally grown grains have various orientations spread about the TD of the material (Figure 3.34 j,k)) suggesting the abnormal grain growth is not related to the orientation of the grains. This might be expected as the recrystallised texture, although oriented in the TD, is quite weak and so unlikely to produce a growth advantage large enough to account for abnormal grain growth. Abnormal grain growth has also been reported by other authors in both binary [95] and tertiary [150] RE alloys. In these cases particle pinning and segregation of RE atoms to grain boundaries have been cited as the most probable causes. The cause of abnormal grain growth in this alloys is thus likely to be a complex function of both these factors, as this is not the focus of this thesis it is not explored further. In either case the most significant observation for the present discussion is that grains orientated within the TD lobes do not appear to a significant growth advantage over other orientations (other than boundary misorientations) during normal or abnormal grain growth. In turn this suggests that TD grains boundaries do not have a special growth advantage, which might otherwise have explained the formation of the TD texture component during primary recrystallisation.

5.3 Grain Boundary Segregation and Solute Drag

All of the mechanisms proposed above explain RE texture formation during static recrystallisation after cold rolling, however texture weakening in RE alloys also occurs during DRX. It is suggested this occurs only in RE alloys because RE additions delay DRX enough for the deformed microstructure to nucleate weak textures by the mechanisms proposed above. Importantly, as discussed in Section 1.9, RE texture weakening is deactivated at high temperatures, where segregation to grain boundaries is found to fall [194]. Recent modelling has also suggested that grain boundary drag, as a result of RE segregation, is likely to retard DRX in magnesium [193]. This analysis combines high resolution TEM imaging and EDX to determine the extent of RE segregation to grain boundaries at a higher resolution than has been achieved before, in magnesium-0.1523 at% Y, which produces RE effects, and magnesium-0.0243 at% Nd, which does not show RE effects. Y atoms are found to segregate strongly to grain boundaries forming clusters <2nm in diameter, peak concentrations at the boundary are found to be ≈ 1.5 at% Y. While in the Nd alloy no grain boundary segregation was observed, this alloy did not

produce significant texture weakening during hot rolling and is not a RE alloy by the definitions proposed in Section 5.1.1. Although the Nd concentration in this alloy is close to the critical concentration required for RE effects, as measured by Hantzsche *et.al* [149], Figure 3.10. EDX analysis shows that Nd resides primarily in a range of magnesium, iron and oxygen containing precipitates within the matrix. Precipitation of Nd with the impurity elements in magnesium was not expected on the basis of the magnesium-Nd phase diagram which indicates all Nd should be in solution in this alloy[7], suggesting that either this diagram is in error or even the low concentrations of impurities in these alloys (Table 2.2) are enough to change the solubility of Nd in magnesium. This could be very significant for the RE effects as precipitation of Nd depletes the matrix of Nd which is likely to reduce the activity of the solute RE effects including segregation of Nd atoms to grain boundaries and/or dislocations. Without the presence of solute Nd in the matrix the material behaves similarly to a non-RE magnesium alloy and does not produce texture weakening characteristic of RE alloys, as shown in Figure 3.8. Further work is needed to fully identify the Nd containing phases present in the Nd alloy, however if the presence of impurities such as Fe are found to significantly change the solubility of RE atoms this could significantly complicate the RE effects because RE atoms are only believed to be effective texture weakeners when in solution. A point supported by the observation that although RE particles are observed in both Y and Nd alloys texture weakening was only observed in the Y alloy where significant grain boundary segregation was observed. If impurities were found to significantly affect the solubility of RE elements then they could be one factor in explaining why some of the binary alloys considered here (e.g Nd, La, Ce) do not produce textures as weak as those observed in alloys with similar compositions examined by other authors. Figure 3.9 shows the texture strength of our 0.0349 at% Ce was 5 mrd stronger than that reported by Mackenzie [138] and Hantzsche [149] after similar processing, this may be partly due to a higher level of impurities in the alloy studied here.

In summary segregation of solute RE atoms to grain boundaries is believed to be critical in activating RE texture weakening through a grain boundary drag mechanism retarding DRX. High resolution EDX analysis showed Y atoms strongly segregated to grain boundaries in an alloy which showed RE effects, while Nd was not found to segregate in an alloy which did not show RE effects. In the Nd alloy the RE atoms were found to precipitate in the matrix, in fact both alloys contained a range of particles containing RE atoms and non-RE impurities. While the volume fraction of these particles is believed to be too low to cause significant boundary pinning, particle formation depletes the matrix of solute RE. This effect is likely to be exacerbated in low solubility elements, like Nd, as only a small amount of RE needs to precipitate to significantly reduce matrix concentrations. This could be significant in deactivating RE effects if the matrix concentration falls low

enough to prevent significant segregation to grain boundaries and dislocations which are believed to be required to activate the RE effects.

Chapter 6

Conclusions

- Texture weakening during recrystallisation has been reported in both RE and non-RE magnesium alloys. To qualify as RE texture weakening a definition is proposed requiring the recrystallisation texture to weaken during both DRX and SRX to less than 6 mrd.
- The critical concentration of RE required to activate these effects had been associated with the solubility of each RE in magnesium. EDX analysis in the TEM shows segregation of RE to grain boundaries in $\approx 4\text{nm}$ clusters only in alloys which produced the RE effect, indicating that segregation is critical to activating these RE effects. The critical concentration is therefore proposed to be related to the concentration of RE required to exert a significant pinning effect on these boundaries, which results in the retarding of DRX during processing. Retarded DRX is thought to be critical in RE texture formation as it allows the development of off basal orientations during deformation which nucleate the RE texture components.
- Non-RE alloying additions also have a significant effect on the critical concentration of RE. The binary Nd-magnesium alloy studied here did not produce RE effects unlike similar alloys in other studies. EDX analysis shows Nd atoms are primarily located in particles with impurities and not segregated to grain boundaries, despite Nd concentrations below the solubility limit in magnesium. Thus even very low concentrations of tertiary alloying additions could affect the solubility of RE in magnesium, preventing segregation to grain boundaries. This effect complicates determination of the critical concentration of RE as it is probably also a function of the concentration of other alloying additions. The impurity effects are likely to be more significant in low solubility RE alloys as the concentration of RE in solution of these alloys is low by definition and so even a small reduction in RE solubility

may be enough to deplete the matrix of RE preventing significant grain boundary segregation.

- Two different texture weakening mechanisms are observed; one in binary magnesium-RE alloys and another different mechanism in the tertiary magnesium-RE-Zn alloys. Texture weakening in the binary RE alloys is proposed to be due to the same mechanism as in the non-RE alloys after cold rolling and recrystallisation.
- After cold rolling and partial SRX the binary RE alloys are found to have a more homogeneous strain distribution and a finer recrystallising grain size than the non-RE alloys, despite similar SRX mechanisms observed in both materials. While both RE and non-RE alloys go on to produce texture weakening after cold rolling and complete SRX, the texture is found to be weaker in the RE alloys. In both cases texture weakening is proposed to be nucleated in regions of high strain localisation where off basal orientations are nucleated recrystallising first nucleating the weak RE textures. In the RE alloys these areas of strain localisation are homogeneously distributed maximising the texture weakening effect, while in non-RE alloys heterogeneous strain distribution allows SRX in regions between areas of high strain localisation with a lower stored energy and fewer off-basal orientations. These areas are likely to nucleate more basally oriented grains limiting the texture weakening effect in these non-RE alloys. Critically this texture weakening is not possible during DRX in non-RE alloys as recrystallisation occurs before enough strain concentration occurs to nucleate the off basal orientations required, while in RE alloys grain boundary drag by RE atoms delays DRX allowing such orientations to form.
- In ZEK100, a magnesium-Nd-Zn alloy, recrystallisation after cold rolling produces a unique TD split in the basal texture of the material which is not explained by the macroscopic deformation texture, which is similar to that of other magnesium alloys. The orientation of the TD split is determined by previous rolling direction as a result of recrystallisation within shear bands whose orientation is also controlled by the rolling direction. In ZEK100 which has been equal cold rolled shear bands are not dominant as a result of rotation of the sheet between rolling passes and so the recrystallised texture is similar to binary RE alloys, a weakened deformation texture. The mechanism nucleating the TD orientations from shear bands largely oriented toward the RD is unknown however, growth of TD orientations as a result of a special boundary relationship seems unlikely as during grain growth there is a resurgence of basal orientations. This is explained as a result of the higher boundary mobility of basal orientations amongst the majority of recrystallised grains split in the TD. A (largely hypothetical) mechanism is proposed in which TD orientations within shear bands recrystallise more quickly than the RD oriented bulk of the shear band

due to the preferential pinning of basal dislocations, possibly by RE-Zn dimers in solution. Once nucleated the high boundary mobility of recrystallising TD oriented grains leads to them growing larger faster than the majority of recrystallising RD grains.

Bibliography

- [1] I. J. Polmear: ‘Light Alloys: Metallurgy of the Light Metals’, Butterworth Heinmann, 1989.
- [2] B. L. Mordike and T. Ebert, 2001, **A302**, 37–45.
- [3] S. R. Agnew, P. Mehrotra, T. Lillo, G. Stoica and P. Liaw, *Acta Materialia*, 2005, **53(11)**, 3135–3146.
- [4] X. Huang, K. Suzuki, A. Watazu, I. Shigematsu and N. Saito, *Materials Science and Engineering: A*, 2008, **488(1-2)**, 214–220.
- [5] J. Hirsch and T. Al-Samman, *Acta Materialia*, 2013, **61(3)**, 818–843.
- [6] K. Oh-ishi, K. Hono and K. Shin, *Materials Science and Engineering: A*, 2008, **496(1-2)**, 425–433.
- [7] L. Rokhlin: ‘Magnesium Alloys Containing Rare Earth Metals’, 2003.
- [8] J. Nie and B. Muddle, *Acta Materialia*, 2000, **48(8)**, 1691–1703.
- [9] C. Antion, P. Donnadieu, F. Perrard, a. Deschamps, C. Tassin and a. Pisch, *Acta Materialia*, 2003, **51(18)**, 5335–5348.
- [10] M. Pekguleryuz and A. A. Kaya, *Advanced Engineering Materials*, 2003, **5(12)**, 866–878.
- [11] A. I. Murphy and R. J. M. Payne, *J. Inst. Metals*, 1946, **73(3)**, 105.
- [12] Y. C. Lee, A. K. Dahle and D. H. Stjohn, *Metallurgical and Materials Transactions A*, 2000, **31A**, 2895–2906.
- [13] G. Ling Song and A. Atrens, *Advanced Engineering Materials*, 2000, **(1)**, 11–33.
- [14] G. Wu, Y. Fan, H. Gao, C. Zhai and Y. P. Zhu, *Materials Science and Engineering: A*, 2005, **408(1-2)**, 255–263.
- [15] K. Grube, J. A. Davis and L. W. Eastwood, *Proc. ASTM*, 1950, **50**, 989.

- [16] W. Liu, F. Cao, L. Chang, Z. Zhang and J. Zhang, *Corrosion Science*, 2009, **51(6)**, 1334–1343.
- [17] R. Wu, Z. Qu and M. Zhang, *Materials Science and Engineering: A*, 2009, **516(1-2)**, 96–99.
- [18] H. E. Friedrich and B. L. Mordike: ‘Magnesium Technology’, Springer, 2006.
- [19] P. G. Partridge, *Metallurgical Reviews*, 1967, **12(1)**, 169.
- [20] D. Hull and D. J. Bacon: ‘Introduction to Dislocations’, Butterworth Heinmann, 1965.
- [21] F. J. Humphreys and M. Hatherly: ‘Recrystallization and Related Annealing Phenomena’, Elsevier, 1995.
- [22] R. Von Mises, *Z. Angew. Math. U. Mech*, 1928, **8(3)**, 161.
- [23] F. Kang, Z. Li, J. T. Wang, P. Cheng and H. Y. Wu, *Journal of Materials Science*, 2012, **47(22)**, 7854–7859.
- [24] K. Máthis, K. Nyilas, a. Axt, I. Dragomir-Cernatescu, T. Ungár and P. Lukáč, *Acta Materialia*, 2004, **52(10)**, 2889–2894.
- [25] S. R. Agnew and O. Duygulu, *International Journal of Plasticity*, 2005, **21(6)**, 1161–1193.
- [26] H. Wang, B. Raeisinia, P. Wu, S. R. Agnew and C. Tomé, *International Journal of Solids and Structures*, 2010, **47(21)**, 2905–2917.
- [27] W. B. Hutchinson and M. R. Barnett, *Scripta Materialia*, 2010, **63(7)**, 737–740.
- [28] A. Chapuis and J. H. Driver, *Acta Materialia*, 2011, **59(5)**, 1986–1994.
- [29] Y. B. Chun, M. Battaini, C. H. J. Davies and S. K. Hwang, *Metallurgical and Materials Transactions A*, 2010, **41(13)**, 3473–3487.
- [30] B. Li and E. Ma, *Physical Review Letters*, 2009, **103(3)**, 035503.
- [31] M. Yoo, *Metallurgical Transactions A*, 1981, **12A(3)**, 409–418.
- [32] J. W. Christian: ‘Encyclopedia of Materials: Science and Technology’, Elsevier Science Ltd, 2001.
- [33] B. C. Wonsiewicz and W. A. Backofen, *Trans AIME*, 1967, **239**, 1422.
- [34] A. Akhtar and E. Teghtsoonian, *Acta Metallurgica*, 1969, **17**, 1339.

- [35] S. Sandlöbes, M. Friák, J. Neugebauer and D. Raabe, *Materials Science and Engineering: A*, 2013, **576**, 61–68.
- [36] H. Conrad and W. D. Robertson, *Trans AIME*, 1957, **209**, 503.
- [37] R. E. Reed-Hill and W. D. Robertson, *Trans AIME*, 1957, **209**, 496.
- [38] P. Ward-Flynn, J. Mote and J. E. Dorn, *Trans AIME*, 1961, **221**, 1148.
- [39] T. Obara, H. Yoshinga and S. Morozumi, 1973, **21(July)**, 845.
- [40] J. F. Stohr and J. P. Poirier, *Philosophical Magazine*, 1972, **25(6)**, 1313–1329.
- [41] J. Koike, T. Kobayashi, T. Mukai, H. Watanabe, M. Suzuki, K. Maruyama and K. Higashi, *Acta Materialia*, 2003, **51(7)**, 2055–2065.
- [42] G. Martin, C. W. Sinclair and R. a. Lebensohn, *Materials Science and Engineering: A*, 2014, **603**, 37–51.
- [43] F. Xu, R. Holt and M. Daymond, *Acta Materialia*, 2008, **56(14)**, 3672–3687.
- [44] S. Graff, W. Brocks and D. Steglich, *International Journal of Plasticity*, 2007, **23(12)**, 1957–1978.
- [45] B. Hutchinson, J. Jain and M. R. Barnett, *Acta Materialia*, 2012, **60(15)**, 5391–5398.
- [46] A. Akhtar and E. Teghtsoonian, *Acta Metallurgica*, 1969, **17**, 1351.
- [47] A. Akhtar and E. Teghtsoonian, *Philosophical Magazine*, 1972, **25(4)**, 897–916.
- [48] A. Couret and D. Caillard, *Acta Metallurgica*, 1985, **33(8)**, 1447–1454.
- [49] A. Couret, D. Caillard, W. Püschl and G. Schoeck, *Philosophical Magazine A*, 1991, **63(5)**, 1045–1057.
- [50] J. Friedel: ‘Internal Stress and Fatigue in Metals’, Elsevier, 1959.
- [51] B. Escaig, *Phys. Stat. Sol.*, 1968, **28**, 463.
- [52] W. Puschl, *Progress in Materials Science*, 2002, **47**, 415–461.
- [53] H. Yoshinaga and R. Horiuchi, *Trans. J I M*, 1964, **5**, 14–21.
- [54] Y. Tang and J. A. El-Awady, *Acta Materialia*, 2014, **71**, 319–332.
- [55] M. Yoo, J. R. Morris, K. M. Ho and S. R. Agnew, *Metallurgical and Materials Transactions A*, 2002, **33(3)**, 813–822.
- [56] A. H. Cottrell and B. A. Bilby, *Proc.Phys.Soc.*, 1948, **62**, 4.

- [57] A. H. Cottrell, *London: Physica Society*, 1948, 30.
- [58] H. Suzuki, *Sci. Rep. Res. Inst. Tohoku Univ*, 1952, **4A**, 455.
- [59] J. Fisher, *Acta Metallurgica*, 1954, **2**.
- [60] R. Labusch, *Physica Status Solidi (B)*, 1970, **41(2)**, 659–669.
- [61] G. P. M. Leyson and W. A. Curtin, *Philosophical Magazine*, 2013, **93(19)**, 37–41.
- [62] R. L. Fleischer, *Acta Metallurgica*, 1961, **9**, 996–1000.
- [63] C. Cáceres and D. Rovera, *Journal of Light Metals*, 2001, **1(3)**, 151–156.
- [64] N. Stanford and M. R. Barnett, *International Journal of Plasticity*, 2013, **47**, 165–181.
- [65] H. Scharf, P. Lucac, M. Bocek and P. Haasen, *Z. Metallk*, 1968, **59**, 799.
- [66] J. Van Der Planken and A. Deruyttere, *Acta Metallurgica*, 1969, **17**, 451.
- [67] J. A. Yasi, L. G. Hector and D. R. Trinkle, *Acta Materialia*, 2010, **58(17)**, 5704–5713.
- [68] M. Chaturvedi, K. Tangri and D. J. Lloyd, 1972, **6**, 16–19.
- [69] M. C. Chaturvedi and D. J. Lloyd, *Philosophical Magazine*, 1974, **30(6)**, 1199–1207.
- [70] C. Wang, Y. Xu and E. Han, *Materials Letters*, 2006, **60(24)**, 2941–2944.
- [71] N. Stanford, I. Sabirov, G. Sha, A. La Fontaine, S. P. Ringer and M. R. Barnett, *Metallurgical and Materials Transactions A*, 2010, **41(3)**, 734–743.
- [72] C. Corby, C. Cáceres and P. Lukáč, *Materials Science and Engineering: A*, 2004, **387-389**, 22–24.
- [73] S. Couling, *Acta Metall*, 1959, **7**, 133.
- [74] S. M. Zhu and J. F. Nie, *Scripta Materialia*, 2004, **50(1)**, 51–55.
- [75] A. Ahmadiéh, J. Mitchell and J. E. Dorn, *Trans AIME*, 1965, 1130.
- [76] J. a. Yasi, L. G. Hector and D. R. Trinkle, *Acta Materialia*, 2011, **59(14)**, 5652–5660.
- [77] J. A. Yasi, L. G. Hector and D. R. Trinkle, *Acta Materialia*, 2012, **60(5)**, 2350–2358.
- [78] M. D. Nave and M. R. Barnett, *Scripta Materialia*, 2004, **51(9)**, 881–885.

- [79] M. R. Barnett, Z. Keshavarz, A. Beer and X. Ma, *Acta Materialia*, 2008, **56(1)**, 5–15.
- [80] M. R. Barnett, *Materials Science and Engineering: A*, 2007, **464**, 8–16.
- [81] L. Jiang, J. Jonas, R. Mishra, a.a. Luo, a.K. Sachdev and S. Godet, *Acta Materialia*, 2007, **55(11)**, 3899–3910.
- [82] A. Jain and S. R. Agnew, *Materials Science and Engineering: A*, 2007, **462(1-2)**, 29–36.
- [83] S. R. Agnew, M. H. Yoo and C. Tomé, *Acta Materialia*, 2001, **49(20)**, 4277–4289.
- [84] C. Tomé, R. A. Lebensohn and F. Kock, *Acta metall. mater*, 1991, **39(11)**, 2667–2680.
- [85] J. J. Jonas, S. Mu, T. Al-Samman, G. Gottstein, L. Jiang and Martin, *Acta Materialia*, 2011, **59(5)**, 2046–2056.
- [86] M. Yoo and J. K. Lee, *Philosophical Magazine A*, 1991, **63(5)**, 987–1000.
- [87] M. R. Barnett, *Materials Science and Engineering: A*, 2007, **464**, 1–7.
- [88] E. Schmid and W. Boas: ‘Plasticity of Crystals: With Special Reference to Metals’, Chapman and Hall, 1935.
- [89] M. R. Barnett, Z. Keshavarz, A. Beer and D. Atwell, *Acta Materialia*, 2004, **52(17)**, 5093–5103.
- [90] M. R. Barnett, *Materials Science and Engineering: A*, 2007, **464(1-2)**, 8–16.
- [91] W. Hartt and R. Reed-Hill, *Trans. Metall. Soc. AIME*, 1967, **239**, 1511.
- [92] M. R. Barnett, *Scripta Materialia*, 2008, **59(7)**, 696–698.
- [93] M. A. Meyers, O. Vohringer and V. A. Lubarda, *Acta Materialia*, 2001, **49**, 4025–4039.
- [94] S. Sandlöbes, S. Zaefferer, I. Schestakow, S. Yi and R. Gonzalez-Martinez, *Acta Materialia*, 2011, **59(2)**, 429–439.
- [95] J. Hadorn, K. Hantzsche, S. Yi, J. Bohlen, D. Letzig, J. A. Wollmershauser and S. R. Agnew, *Metallurgical and Materials Transactions A*, 2012, **43(4)**, 1347–1362.
- [96] N. Stanford and M. R. Barnett, *Materials Science and Engineering: A*, 2008, **496(1-2)**, 399–408.

- [97] J. Scott, M. Miles, D. Fullwood, B. Adams, A. Khosravani and R. K. Mishra, *Metallurgical and Materials Transactions A*, 2012, **44(1)**, 512–516.
- [98] X. Li, P. Yang, L.-N. Wang, L. Meng and F. Cui, *Materials Science and Engineering: A*, 2009, **517(1-2)**, 160–169.
- [99] M. R. Barnett and N. Stanford, *Scripta Materialia*, 2007, **57(12)**, 1125–1128.
- [100] M. Hatherly and A. S. Malin, 1984, **18(c)**, 449–454.
- [101] M. R. Barnett, M. Nave and C. Bettles, *Materials Science and Engineering A*, 2004, **386(1-2)**, 205–211.
- [102] W. Lee and K. Chan, *Acta Metallurgica et Materialia*, 1991, **39(3)**, 411–417.
- [103] J. Scott, M. Miles, D. Fullwood, B. Adams, A. Khosravani and R. K. Mishra, *Metallurgical and Materials Transactions A*, 2012, **44(1)**, 512–516.
- [104] F. W. Bach, B. A. Behrens, M. Rodman, A. Rossberg and G. Kurz, *Jom*, 2005, 57–61.
- [105] S. Ion, F. J. Humphreys and S. White, *Acta Metallurgica*, 1982, **30(10)**, 1909–1919.
- [106] A. Styczynski, C. Hartig, J. Bohlen and D. Letzig, *Scripta Materialia*, 2004, **50(7)**, 943–947.
- [107] Y. WANG and J. Huang, *Acta Materialia*, 2007, **55(3)**, 897–905.
- [108] R. Gehrman, M. M. Frommert and G. Gottstein, *Materials Science and Engineering A*, 2005, **395(1-2)**, 338–349.
- [109] Y. B. Chun and C. Davies, *Materials Science and Engineering: A*, 2011, **528(18)**, 5713–5722.
- [110] C. Leppin, J. Li, D. Daniel and A. Technology, *Numisheet*, 2008, **5**.
- [111] D. Letzig, L. Stutz, J. Bohlen and K. U. Kainer, *Materials Science Forum*, 2011, **690**, 298–301.
- [112] G. E. Dieter: ‘Mechanical Metallurgy’, 1928.
- [113] D. Li and A. Ghosh, *Materials Science and Engineering: A*, 2003, **352(1-2)**, 279–286.
- [114] N. Stanford, D. Atwell and M. R. Barnett, *Acta Materialia*, 2010, **58(20)**, 6773–6783.

- [115] C. John Neil and S. R. Agnew, *International Journal of Plasticity*, 2009, **25(3)**, 379–398.
- [116] H. Wang, P. Wu, K. Boyle and K. Neale, *International Journal of Solids and Structures*, 2011, **48(6)**, 1000–1010.
- [117] A. R. Antoniswamy, A. J. Carpenter, J. T. Carter, L. G. Hector and E. M. Taleff, *Journal of Materials Engineering and Performance*, 2013, **22(11)**, 3389–3397.
- [118] C. John Neil, S. R. Agnew and J. C. Neil, *International Journal of Plasticity*, 2009, **25(3)**, 379–398.
- [119] D. Sun, C. Chang and P. Kao, *Metallurgical and Materials Transactions A*, 2010, **41(7)**, 1864–1870.
- [120] X. Yang, H. Miura and T. Sakai, *Materials Transactions*, 2003, **44(1)**, 197–203.
- [121] M. R. Barnett, A. Sullivan, N. Stanford, N. Ross and A. Beer, *Scripta Materialia*, 2010, **63(7)**, 721–724.
- [122] O. Sitdikov and R. Kaibyshev, *Materials Transactions*, 2001, **42(9)**, 1928.
- [123] A. Galiyev, R. Kaibyshev and G. Gottstein, *Acta Materialia*, 2001, **49(7)**, 1199–1207.
- [124] T. Al-Samman and G. Gottstein, *Materials Science and Engineering: A*, 2008, **490(1-2)**, 411–420.
- [125] M. Myshlyaev, H. McQueen, a. Mwembela and E. Konopleva, *Materials Science and Engineering: A*, 2002, **337(1-2)**, 121–133.
- [126] R. Kaibyshev, A. Goloborodko, F. Musin, I. Nikulin and T. Sakai, *Materials Transaction*, 2002, **(10)**, 2408.
- [127] R. Kaibyshev, K. Shipilova, F. Musin and Y. Motohashi, *Materials Science and Engineering: A*, 2005, **396(1-2)**, 341–351.
- [128] C. Bettles and M. R. Barnett: ‘Advances in Wrought Magnesium Alloys’, Woodhead Publishing Ltd, 2012.
- [129] J. Tan and M. Tan, *Materials Science and Engineering A*, 2003, **339(1-2)**, 124–132.
- [130] E. Martin and J. J. Jonas, *Acta Materialia*, 2010, **58(12)**, 4253–4266.
- [131] O. Sitdikov and R. Kaibyshev, *Materials Science and Engineering: A*, 2002, **328(1-2)**, 147–155.

- [132] K. D. Molodov, T. Al-Samman, D. a. Molodov and G. Gottstein, *Acta Materialia*, 2014, **76**, 314–330.
- [133] D. Yin, K. Zhang, G. Wang and W. Han, *Materials Science and Engineering: A*, 2005, **392(1-2)**, 320–325.
- [134] M. Sanjari, A. Farzadfar, A. S. H. Kabir, H. Utsunomiya, I.-H. Jung, R. Petrov, L. Kestens and S. Yue, *Journal of Materials Science*, 2014, **49(3)**, 1408.
- [135] Q. Ma, B. Li, W. Whittington, a.L. Oppedal, P. Wang and M. Horstemeyer, *Acta Materialia*, 2014, **67**, 102–115.
- [136] T. Al-Samman, K. D. Molodov, D. A. Molodov, G. Gottstein and S. Suwas, *Acta Materialia*, 2012, **60(2)**, 537–545.
- [137] Q. Ma, B. Li, E. Marin and S. Horstemeyer, *Scripta Materialia*, 2011, **65(9)**, 823–826.
- [138] L. Mackenzie and M. Pekguleryuz, *Scripta Materialia*, 2008, **59(6)**, 665–668.
- [139] R. Doherty, D. Hughes, F. Humphreys, J. Jonas, D. Jensen, M. Kassner, W. King, T. McNelley, H. McQueen and a.D. Rollett, *Materials Science and Engineering: A*, 1997, **238(2)**, 219–274.
- [140] F. I. Humphreys, *Acta Metallurgica*, 1979, **27**, 1801–1814.
- [141] T. Al-Samman and X. Li, *Materials Science and Engineering: A*, 2011, **528(10-11)**, 3809–3822.
- [142] L. Mackenzie, B. Davis, F. J. Humphreys and G. W. Lorimer, *Materials Science and Technology*, 2007, **23(10)**, 1173–1180.
- [143] T. Al-Samman, *Materials Science and Engineering: A*, 2013, **560**, 561–566.
- [144] J. Robson, D. Henry and B. Davis, *Acta Materialia*, 2009, **57(9)**, 2739–2747.
- [145] X. Huang, K. Suzuki, Y. Chino and M. Mabuchi, *Journal of Materials Science*, 2012, **47(11)**, 4561–4567.
- [146] J. del Valle and O. Ruano, *Materials Letters*, 2009, **63(17)**, 1551–1554.
- [147] X. Huang, K. Suzuki and Y. Chino, *Materials Science and Engineering: A*, 2013, **560**, 232–240.
- [148] S. A. Farzadfar, E. Martin, M. Sanjari, E. Essadiqi and S. Yue, *J Mater Sci*, 2012, **47**, 5488.

- [149] K. Hantzsche, J. Bohlen, J. Wendt, K. Kainer, S. Yi and D. Letzig, *Scripta Materialia*, 2010, **63(7)**, 725–730.
- [150] M. Sanjari, S. A. Farzadfar, T. Sakai, H. Utsunomiya, E. Essadiqi, I.-H. Jung and S. Yue, *Materials Science and Engineering: A*, 2013, **561**, 191–202.
- [151] S. Yi, H.-G. Brokmeier and D. Letzig, *Journal of Alloys and Compounds*, 2010, **506(1)**, 364–371.
- [152] K. Zhu, D. Chaubet, B. Bacroix and F. Brisset, *Acta Materialia*, 2005, **53(19)**, 5131–5140.
- [153] N. Bozzolo, N. Dewobroto, T. Grosdidier and F. Wagner, *Materials Science and Engineering: A*, 2005, **397(1-2)**, 346–355.
- [154] F. Wagner, N. Bozzolo, O. Van Landuyt and T. Grosdidier, *Acta Materialia*, 2002, **50(5)**, 1245–1259.
- [155] T. Mayama, M. Noda, R. Chiba and M. Kuroda, *International Journal of Plasticity*, 2011, **27(12)**, 1916–1935.
- [156] I. J. Polmear, *Materials Science and Technology*, 1994, **10**, 1–16.
- [157] E. Ball and P. Prangnell, *Materials Science*, 1994, **31(2)**, 111–116.
- [158] J. Bohlen, M. R. Nürnberg, J. W. Senn, D. Letzig and S. R. Agnew, *Acta Materialia*, 2007, **55(6)**, 2101–2112.
- [159] N. Stanford, D. Atwell, a. Beer, C. Davies and M. R. Barnett, *Scripta Materialia*, 2008, **59(7)**, 772–775.
- [160] A. Farzadfar, E. Martin, M. Sanjari, E. Essadiqi, M. A. Wells, S. Yue and E. Martin, *Materials Science and Engineering: A*, 2012, **534**, 209–219.
- [161] Y. Chino, M. Kado and M. Mabuchi, *Materials Science and Engineering: A*, 2008, **494(1-2)**, 343–349.
- [162] S. Yi, J. Bohlen, F. Heinemann and D. Letzig, *Acta Materialia*, 2010, **58(2)**, 592–605.
- [163] N. Stanford, *Materials Science and Engineering: A*, 2010, **527(10-11)**, 2669–2677.
- [164] J. Bohlen, S. Yi, D. Letzig and K. U. Kainer, *Materials Science and Engineering: A*, 2010, **527(26)**, 7092–7098.
- [165] L. Mackenzie and M. Pekguleryuz, *Scripta Materialia*, 2008, **59(6)**, 665–668.

- [166] X. Li, T. Al-Samman, S. Mu and G. Gottstein, *Materials Science and Engineering: A*, 2011, **528(27)**, 7915–7925.
- [167] A. Farzadfar, M. Sanjari, I. H. Jung, E. Essadiqi and S. Yue, *Materials Science and Engineering: A*, 2011, **528(22-23)**, 6742–6753.
- [168] I. Basu and T. Al-Samman, *Acta Materialia*, 2014, **67**, 116–133.
- [169] N. Stanford, *Materials Science and Engineering: A*, 2010, **528(1)**, 314–322.
- [170] D.-W. H. Kim, B.-C. Suh, M.-S. Shim, J. H. Bae and N. J. Kim, *Metallurgical and Materials Transactions A*, 2013, **44(7)**, 2950–2961.
- [171] J.-Y. Lee, Y.-S. Yun, B.-C. Suh, N.-J. Kim, W.-T. Kim and D.-H. Kim, *Journal of Alloys and Compounds*, 2014, **589**, 240–246.
- [172] L. L. Rokhlin, *Journal of Phase Equilibria*, 1998, **19(2)**, 142–145.
- [173] Q. Ran, H. L. Lukas, G. Effenberg and G. Petzow, *CALPHAD*, 1988, **12(375)**.
- [174] N. Stanford and M. R. Barnett, *Scripta Materialia*, 2008, **58(3)**, 179–182.
- [175] R. Cottam, J. Robson, G. Lorimer and B. Davis, *Materials Science and Engineering: A*, 2008, **485(1-2)**, 375–382.
- [176] N. Stanford, *Materials Science and Engineering: A*, 2013, **565**, 469–475.
- [177] J. Hadorn, K. Hantzsche, S. Yi, J. Bohlen, D. Letzig and S. R. Agnew, *Metallurgical and Materials Transactions A*, 2012, **43(4)**, 1363–1375.
- [178] S. G. Kim and Y. B. Park, *Acta Materialia*, 2008, **56(15)**, 3739–3753.
- [179] N. Stanford, M. Callaghan and B. de Jong, *Materials Science and Engineering: A*, 2013, **565**, 459–468.
- [180] I. Basu, T. Al-Samman and G. Gottstein, *Materials Science and Engineering: A*, 2013, **579**, 50–56.
- [181] Y. Wang, *Materials Chemistry and Physics*, 2003, **81(1)**, 11–26.
- [182] U. F. Kocks and C. Tomé: ‘Texture and Anisotropy’, Cambridge University Press, 1998.
- [183] Y. Chino, M. Kado and M. Mabuchi, *Materials Science and Engineering: A*, 2008, **494(1-2)**, 343–349.
- [184] J. Hadorn, R. P. Mulay, K. Hantzsche, S. Yi, J. Bohlen, D. Letzig and S. R. Agnew, *Metallurgical and Materials Transactions A*, 2012, **44(3)**, 1566–1576.

- [185] M. Suzuki, H. Sato, K. Maruyama and H. Oikawa, *Materials Science and Engineering A*, 1998, **252(2)**, 248–255.
- [186] Y. Chino, M. Kado and M. Mabuchi, *Acta Materialia*, 2008, **56(3)**, 387–394.
- [187] S. Sandlöbes, Z. Pei, M. Friák, L.-F. Zhu, F. Wang, S. Zaeferrer, D. Raabe and J. Neugebauer, *Acta Materialia*, 2014, **70**, 92–104.
- [188] S. Sandlöbes, M. Friák, S. Zaeferrer, A. Dick, S. Yi, D. Letzig, Z. Pei, L. F. Zhu, J. Neugebauer and D. Raabe, *Acta Materialia*, 2012, **60(6-7)**, 3011–3021.
- [189] A. Urakami and M. E. Fine, *Acta Metallurgica*, 1971, **19**, 887.
- [190] A. Sato and M. Meshii, *Acta Metallurgica*, 1973, **21**, 753.
- [191] A. Couret and D. Caillard, *Acta Materialia*, 1985, **33(8)**, 1455–1462.
- [192] T. Tsuru, Y. Udagawa, M. Yamaguchi, M. Itakura, H. Kaburaki and Y. Kaji, *J Phys.: Condens Matter*, 2013, **25(2)**, 022202.
- [193] J. D. Robson, *Metallurgical and Materials Transactions A*, 2013, **45A(8)**, 3205–3212.
- [194] N. Stanford, G. Sha, J. Xia, S. Ringer and M. R. Barnett, *Scripta Materialia*, 2011, **65(10)**, 919–921.
- [195] J. Hu, K. Ikeda and T. Murakami, *Journal of Materials Processing Technology*, 1998, **73(1-3)**, 49–56.
- [196] E. Abe, a. Ono, T. Itoi, M. Yamasaki and Y. Kawamura, *Philosophical Magazine Letters*, 2011, **91(10)**, 690–696.
- [197] H. Kimizuka and S. Ogata, *Materials Research Letters*, 2013, **1(4)**, 213–219.
- [198] D.-H. Ping, K. Hono and J. Nie, *Scripta Materialia*, 2003, **48(8)**, 1017–1022.
- [199] J. Nie, K. Oh-ishi, X. Gao and K. Hono, *Acta Materialia*, 2008, **56(20)**, 6061–6076.
- [200] O. Instruments: Kikuchi, 2014.
- [201] R. Hielscher and H. Schaeben, *Journal of Applied Crystallography*, 2008, **41(6)**, 1024–1037.
- [202] D. B. Williams and B. C. Carter: ‘Transmission Electron Microscopy: A Textbook for Materials Science’, Springer, 2009.
- [203] K. Nakazima, T. Kikuma and T. Pokora, *Yamata Tech. Rep.*, 1968, **264**, 141–54.

- [204] M. Materials, S. Centre, G. Street, M. Manchester, J. Quinta Da Fonseca, P. Mumery and P. Withers, *Journal of Microscopy*, 2005, **218(April)**, 9–21.
- [205] D. Garcia, J. Orteu and L. Penazzi, *Journal of Materials Processing Technology*, 2002, **125-126**, 736–742.
- [206] B. Pan, K. Qian, H. Xie and A. Asundi, *Measurement Science and Technology*, 2009, **20(6)**, 062001.
- [207] J.-J. J. Orteu, *Optics and Lasers in Engineering*, 2009, **47(3-4)**, 282–291.
- [208] R. Hill and J. Rice, *Journal of the Mechanics and Physics of Solids*, 1972, **20(6)**, 401–413.
- [209] F. Roters, P. Eisenlohr, L. Hantcherli, D. Tjahjanto, T. Bieler and D. Raabe, *Acta Materialia*, 2010, **58(4)**, 1152–1211.
- [210] R. A. Lebensohn and C. N. Tome, *Acta metall. mater.*, 1993, **41(9)**, 2611–2624.
- [211] G. H. Campbell, S. M. Foiles, H. Huang, D. a. Hughes, W. E. King, D. H. Lassila, D. J. Nikkel, T. D. de la Rubia, J. Y. Shu and V. P. Smyshlyaev, *Materials Science and Engineering: A*, 1998, **251(1-2)**, 1–22.
- [212] G. I. Taylor, *J. Inst. Metals*, 1938, **62**, 307.
- [213] C. Tomé, *Modelling Simul. Mater. Sci. Eng*, 1999, **7**, 723.
- [214] R. A. Lebensohn, C. Tomé and P. P. Castañeda, *Philosophical Magazine*, 2007, **87(28)**, 4287–4322.
- [215] R. Hill, *J. Mech. Phys. Solids*, 1965, **13**, 89–101.
- [216] A. Molinari, G. R. Canova and S. Ahzi, *Acta Metallurgica*, 1987, **35(12)**, 2983–2994.
- [217] R. Masson, M. Bornert, P. Suquet and A. Zaoui, 2000, **48**, 1203–1227.
- [218] A. Molinari and L. S. Toth, *Acta metall. mater.*, 1994, **42(7)**, 2453–2458.
- [219] H. Wang, P. Wu, C. Tomé and Y. Huang, *Journal of the Mechanics and Physics of Solids*, 2010, **58(4)**, 594–612.
- [220] R. A. Lebensohn and C. Tomé, *Materials Science and Engineering: A*, 1994, **175(1-2)**, 71–82.
- [221] J. Eshelby, *Proceedings of the Royal Society of London. Series A, Mathematical and Physical Sciences*, 1957, **241(1226)**, 376–396.
- [222] E. Voce, *J. Inst. Met.*, 1948, **74**, 537.

- [223] P. Vanhoutte, *Acta Metall*, 1978, **26**, 591.
- [224] P. Turner and C. Tomé, *Acta Metallurgica et Materialia*, 1994, **42(12)**, 4143–4153.
- [225] S. R. Agnew, *Scripta Materialia*, 2003, **48(8)**, 1003–1008.
- [226] S. R. Agnew, D. Brown and C. Tomé, *Acta Materialia*, 2006, **54(18)**, 4841–4852.
- [227] B. Raeisinia, S. R. Agnew and A. Akhtar, *Metall. Mater. Trans. A*, 2011, **42A**, 1418.
- [228] A. Prakash, S. Weygand and H. Riedel, *Computational Materials Science*, 2009, **45(3)**, 744–750.
- [229] D. Peirce, R. J. Asaro and A. Needleman, *Acta Metall*, 1982, **30**, 1087–1119.
- [230] S. Balasubramanian and L. Anand, *Acta Materialia*, 2002, **50(1)**, 133–148.
- [231] A. Salem, S. Kalidindi and S. Semiatin, *Acta Materialia*, 2005, **53(12)**, 3495–3502.
- [232] A. Staroselsky and L. Anand, *International Journal of Plasticity*, 2003, **19(10)**, 1843–1864.
- [233] S.-T. Tseng and H.-T. Hu, *Transactions of Nonferrous Metals Society of China*, 2013, **23(11)**, 3372–3382.
- [234] O. Diard, S. Leclercq, G. Rousselier and G. Cailletaud, *International Journal of Plasticity*, 2005, **21(4)**, 691–722.
- [235] A. J. Beaudoin, K. K. Mathur, P. R. Dawson and G. C. Johnson, *International Journal of Plasticity*, 1993, **9**, 833–860.
- [236] K. W. Neale, 1993, **35(12)**, 1053–1063.
- [237] A. Fernández, M. T. Pérez Prado, Y. Wei and A. Jérusalem, *International Journal of Plasticity*, 2011, **27(11)**, 1739–1757.
- [238] S.-H. Choi, D. Kim, S. Park and B. You, *Acta Materialia*, 2010, **58(1)**, 320–329.
- [239] H. Abdolvand and M. R. Daymond, *Acta Materialia*, 2012, **60(5)**, 2240–2248.
- [240] S.-H. Choi, D. Kim, H. Lee and E. Shin, *Materials Science and Engineering: A*, 2010, **527(4-5)**, 1151–1159.